Collaborative System and Multi Robots Based on Pneumatic Muscle Actuator

Alaa Falah Abdulhasan Al-Ibadi

Autonomous Systems and Robotics Centre
School of Computing, Science & Engineering
University of Salford, Manchester, UK

Submitted in Partial Fulfilment of the Requirements of the Degree of Doctor of Philosophy July 2019

Contents

List of figures

List of tables

List of Abbreviations

PMA	Pneumatic Muscle Actuator
DC	Direct Current
AC	Alternating Current
EMI	Electromagnetic Interference
HIC	Head Injury Criterion
VC	Viscous Injury Response
GSI	Gadd Severity Index
WSUTL	The Wayne State University
VSA	variable Stiffness Actuators
DoF	Degree of Freedom
CWS	Collaborative Work Space
HRC	Human-Robot Collaboration
PNNP	Parallel Neural Network-Proportional ControlSsystem
SBCA	Self-Bending Contraction Actuator
CPMA	Circular Pneumatic Muscle Actuator
DB-PMA	Double-Bend Pneumatic Muscle Actuator
PID	Proportional-Integral-Derivative Controller
CC	Constant Curvature
IK	Inverse Kinematic
3D	Three Dimensional
R-R/ R-H	Robot-Robot/ Robot-Human
IMU/MPU	Inertial Measurement Unit

List of symbols

I	Integration
a	Acceleration (m/s^2)
n	Weighting Factor
t	Time (sec)
Δt_{max}	The difference of the Maximum time (sec)
â	acceleration in g's
g	acceleration of gravity (9.81 m/s^2)
M_{rob}	Robot Mass (kg)
M_{rotor}	Rotor Mass (kg)
M_{link}	Link Mass (kg)
v_{safe}	Safe velocity (m/s)
L	Pneumatic Muscle Actuator Length (m)
D	Pneumatic Muscle Actuator Diameter (m)
θ	The braided angle (Degree)
b	The Length of the Braided Strand (m)
n	Number of Strand Turns
P	Air Pressure (kPa)
V	Volume of The Actuator (m^3)
P_0	The Environment Pressure (P_0=103.36 kPa),

P_g	Gauge Pressure (The Relative Pressure) (kPa)
si	The Total Inner Surface (m^2)
dli	The Inner Surface Displacement (m)
dV	The Volume Change (m^3)
dW_{in}	The Input Work Change (Nm)
dW_{out}	The Output Work Change (Nm)
L_0	The Initial Value of The Actuator's Length (m)
D_0	The Initial Value of The Actuator's Diameter (m)
r	The Actuator's Radius (m)
r_0	The Initial Value of The Actuator's Radius (m)
ε	The Contraction Ratio
έ	The Extension Ratio
c_1, c_2	Positive Constants
F	Actuator's Force (N)
Ĺ	The Average Length (m)
L_{ndec}	The Contraction Length (m)
L_{ninc}	The Elongation Length (m)
a, b, c, d, and e	Constants
q	Correction Factor
δ	The Bending Angle of The Continuum Arm (Degree)
W	Load (kg)

D_{out}	The Outer Diameter of The PMA (m)
D_{in}	The Inner Diameter of The PMA (m)
Th_D	The Twice Value of The Rubber Tube and Sleeve Thicknesses (m)
f_{rs}	The Resistance Force (N)
s_r	The Stiffness of The Rubber Tube (N/m)
A_{in}	The Inner Area of The Rubber Cross Section (m^2)
F_c	The Loses Force Due to The Contactless Between The Inner Tube and The Sleeve (N)
s	The Stiffness of The Actuator (N/m)
K_p, K_I and K_D	The PID Constants
u	The Controlled Input
e	Error
p_r	Pressure Reference Value (kPa)
y_r	System ‘s Output Reference Value
Arc	Arc length (m)
β, γ, α	Angle (Degree)
β_{max}	Maximum Angle (Degree)
W	The Arc’s Width (m)
H	The Arc’s Hight (m)
F_t	Total Force (N)
F_{rt}	Total Resistance Force (N)

F_{rr}	The Rod resistance Force (N)
L_v	Vertical Actuator Length (m)
L_h	Horizontal Actuator Length (m)
λ	Hypotenuse Length of the DB-PMA (m)
ε_h	Horizontal Variation Ratio
ε_v	Vertical variation Ratio
L_{in}	Inner Length of CPMA (m)
L_{out}	Outer Length of CPMA (m)
DRR	Diameter Reduction Ratio

Dedication

I dedicate this work to my beloved wife Alya whose unconditional encouragement and support made it possible for me to finish this PhD. I wish to express my heartfelt love to my lovely son Mohammed Reda for coping with the undue paternal deprivation during four years of my study. To my family, I love you all.

And with special love to my mother and father to their love and blessings.

Acknowledgements

Completion of this thesis was possible with the support of several people. I would like to express my sincere gratitude to all of them. First of all, I would like to thank my supervisor and the chair of the Robotics and Autonomous System Centre Prof. Samia Nefti-Meziani. Special thanks to my co-supervisor Dr. Steve Davis for his support and guidance during my study. The thesis would not have to come to a successful completion, without the encouragement I received from my colleagues at the department. I would also thank the lab technician Mr. Andrew Baker for his logistics services and to Mr. Michael Clegg to his support.

I owe a lot to my wife, my son, my parents and sisters, who encouraged and helped me at every stage of my personal and academic life and longed to see this achievement come true.

Many thanks to the University of Basrah and the Ministry of Higher Education and Scientific Research in Iraq to support my PhD. Special thanks to the Iraqi Cultural Attaché in London for their support during my study.

Abstract

Designing a multi-robot system provides numerous advantages for many applications, such as low cost, multi-tasking and more efficient group work. While the rigidity of the robots used in industrial and medical application increase the probability of risk of injury. Therefore, many researches are done to increase the safety factor for robot-human interaction, as a result, either the separated between the human and robot is suggested or the force shutdown to robot system is applied. These solutions might be useful for industrial applications, nonetheless it is not for medical and the application require the direct interaction between the human and machine. To overcome the rigidity problem, a soft pneumatic muscle actuator PMA is used in this thesis to design a fully soft robot arm.

The performances and the behaviours of these actuators are tested to enhance the force formula for the contraction and the extension PMAs. General length formulas are proposed in terms of the initial length in addition to the structure-based formulas for the tensile force and length.

Three different novel actuators are proposed together with their kinematics. These actuators include: the self-bending contraction actuator SBCA, the double-bend pneumatic muscle actuator DB-PMA and the circular pneumatic muscle actuator CPMA. The presented actuators are used with the simple contraction and extension actuators to design different novel structures of continuum arms and end effectors. Then an efficient control system is proposed by using a parallel structure of the neural network NN and proportional P controller (PNNP controller). The presented continuum arms formed a multiple robot system to perform several tasks under the PNNP controller.

Chapter one:

1. General introduction

1.1 Main overview

Nowadays, there is a significant interest in robots in industrial, medical and space researches. Numerous challenges and difficulties have been found in such robot applications, including risk of injury, rigidity, position and force control problems, cost and a wide workspace requirement. Many solutions have been introduced to solve these problems; however, a number of difficulties are still being studied.

New controller processes are presented to overcome the position and force control problems of rigid robots, either for single robots or cooperation groups. Several researches are being done to modify the existing actuators or test new types to make the robot safer for human interaction, which is one of the main challenges in industrial application areas. Numerous types of variable stiffness actuators (VSA) have been presented during the last few years. Some of them reduced the probability of risk of injury. In spite of their excellent performance, the rigidity is a main characteristic of this type of actuators. This led to the invention of sufficiently soft, high stiffness actuators. The pneumatic muscle actuator (PMA) provides appreciable advantages over other types of actuators such as high power to weight ratio, variable stiffness, multi-degree of freedom (DoF), small workspace requirements and low cost. On the other hand, the nonlinearity is the major disadvantage of the PMA. Therefore, an exact force and position model does not exist yet. As a result, the control strategies have to be modified to overcome the difficulties for the single actuator as well as for the multi PMAs. The arm, which is made from a PMA, is called a continuum arm and provides new robotic behaviour and offers an infinite number of robot applications.

Use of the continuum arm in a multi-robot system represents additional model and control issues.

1.2 Aim and objectives

Using soft actuators such as a pneumatic muscle actuator (PMA) as well as building a fully soft robot, as part of a multiple robot system, is the main target of this project. In addition, this project aims to modify and find the appropriate models for the single or multiple actuators robot system, as well as design a suitable control system for single or multiple actuators structure systems. This work involves many tasks, including to design, test, build continuum arms, model and control the robot system.

The main objectives of this research are:

1. Study the performance of the pneumatic muscle actuator including its advantages and disadvantages.
2. Modify the existing force models and find the proper formula to describe both the tensile and extension forces.
3. Formulate a mathematical model to describe the length of the single actuator as well as multi actuator schemes.
4. Formulate a mathematical model for the end effector position angle.
5. Design and construct a multi robot system based on the PMA including continuum arms and suitable end effectors.
6. Design the efficient control system for the collaborative system.

1.3 Research Methodology

Throughout this research, numerous tasks have been involved, such as design several dimensions of contraction and extension pneumatic muscle actuators, design novel soft pneumatic actuators, study the kinematics for each type, design several continuum arms and soft grippers and design and applied a novel control for single and multiple arms. The overall research methodology during the various stages of this research can be illustrated as follows:

1- Reviews the literatures of the wide used actuators in robotic systems, starting from the electric motors, variable stiffness actuators and finally study the pneumatic

muscle actuators. Furthermore, the literature includes continuum manipulators, end effectors and control systems to understand current research efforts.

2- Design several dimensions of both types of PMAs to study their characteristics.

3- Review the previous researches of air muscle's force and modify the force formula to enhance its accuracy for the contraction actuators and make it suitable to the extension PMAs.

4- Design and construct continuum arms and study their performances.

5- Modify the structure of the PMA to establish new behaviours.

6- Design several continuum arms and end effectors.

7- Design efficient control systems for all prototypes.

8- Applied a collaborative control system to multiple robot arm to perform several tasks.

1.4 Research contributions

This research introduces several contributions either in mathematical models for the single, series, and parallel actuators, or in new actuators and continuum arms. The main contributions in this research can be listed as follows:

1- Force, length and bending angle models:
   a. Enhance the tensile force formula for the contraction actuator by consider the required amount of air pressure to produce the tensile force.
   b. Make the modified tensile force formula suitable for the extension actuators.
   c. Formulate experimentally general length models for both types of the PMA depend on the initial length of the actuators.
   d. Present novel force and length formulas depend on the structure and the material properties of the air actuators.

2. Propose a parallel structure of control system by using a neural network and proportional control system (PNNP) to enhance the precession and the speed to control such type of systems.
3. Novel actuators and soft grippers:
    a. Design a novel self-bending contraction actuator (SBCA) which introduces an efficient bending behaviour. Furthermore, the kinematics and the force formula for this actuator are presented in terms of its dimensions and air pressure and validated experimentally.
    b. A novel circular pneumatic muscle actuator (CPMA) is presented by the inspiration of special types of human facial muscles. The kinematics and the radial force formula are presented and validated.
    c. A new design of double-bend pneumatic muscle actuator (DB-PMA) is presented together with its kinematics. The DB-PMA is inspired by the lateral undulation motion of a snake.
    d. Design an active soft gripper by using a small size of the SBCA as fingers. the grasping for the presented gripper can be easily performed by applied an equal air pressure to all fingers simultaneously.
    e. Design a circular-extension soft griper by using three identical extension actuators and CPMA. The proposed gripper has the ability of extension, bending and grasping. The grasping is too high, and it is developed by the radial force of the CPMA.
4. New design of two segments continuum arm is presented. The position of the free end is illustrated according to different patterns of the applied air pressure. Then an open-loop control system is applied to control the position of the end effector of the presented robot arm. Furthermore, a novel control strategy is applied to control the position of the free end by distribute the axes on the actuators and make each actuator is responsible on one axis. This strategy shows a high control accuracy for such type of systems.
5. Applied a collaborative control system to several Robot-Robot (R-R) and Robot-Human (R-H) systems to validate the presented actuators, continuum arm, soft grippers and the PNNP controller system. Moreover, shows the performances of the soft actuators and the continuum arms.

1.5 List of publications

1- Al-Ibadi, A., Nefti-Meziani, S. and Davis, S., 2016, August. Valuable experimental model of contraction pneumatic muscle actuator. In *Methods and Models in Automation and Robotics (MMAR), 2016 21st International Conference on* (pp. 744-749). IEEE.

2- Al-Ibadi, A., Nefti-Meziani, S. and Davis, S., 2016, October. 3D position mapping of continuum arm. In *Students on Applied Engineering (ICSAE), International Conference for* (pp. 1-6). IEEE.

3- Al-Ibadi, A., Nefti-Meziani, S. and Davis, S., 2017, September. Cooperative project by self-bending continuum arms. In *Automation and Computing (ICAC), 2017 23rd International Conference on* (pp. 1-6). IEEE.

4- Al-Ibadi, A., Nefti-Meziani, S. and Davis, S., 2017, September. Novel models for the extension pneumatic muscle actuator performances. In *Automation and Computing (ICAC), 2017 23rd International Conference on* (pp. 1-6). IEEE.

5- Al-Ibadi, A., Nefti-Meziani, S. and Davis, S., 2017, October. Efficient structure-based models for the McKibben contraction pneumatic muscle actuator: the full description of the behaviour of the contraction PMA. In *Actuators* (Vol. 6, No. 4, p. 32). Multidisciplinary Digital Publishing Institute.

6- Al-Ibadi, A., Nefti-Meziani, S. and Davis, S., 2018. Design, implementation and modelling of the single and multiple extensor pneumatic muscle actuators. *Systems Science & Control Engineering*, *6*(1), pp.80-89.

7- Al-Ibadi, A., Nefti-Meziani, S. and Davis, S., 2018. Active soft end effectors for efficient grasping and safe handling. *IEEE Access, 6, pp.23591-23601*.

8- Al-Ibadi, A., Nefti-Meziani, S. and Davis, S., 2018. Design, Kinematics and Controlling a Novel Soft Robot Arm with Parallel Motion. Robotics, 7(2), p.19.

9- Al-Ibadi, A., Nefti-Meziani, S., & Davis, S. (2018, April). A circular pneumatic muscle actuator (CPMA) inspired by human skeletal muscles. In *2018 IEEE International Conference on Soft Robotics (RoboSoft)*. IEEE.

10- Al-Ibadi, A., Nefti-Meziani, S., Davis, S. and Theodoridis, T., 2018. Novel design and position control strategy of a soft robot arm. *Robotics*, *7*(4), p.72. Multidisciplinary Digital Publishing Institute.

11- Al-Ibadi, A., Nefti-Meziani, S. and Davis, S.T., 2018, September. Human-robot shared control for split-site interaction and disabled assistance. In *8th Joint*

Workshop on New Technologies For Computer/Robot Assisted Surgery (CRAS 2018).

12- Al-Ibadi, A., Nefti-Meziani, S., Davis, S.T. and Theodoridis, T., 2018, September. Design of two segments continuum robot arm based on pneumatic muscle actuator (PMA). In *Proceedings of the 24th International Conference on Automation & Computing*.

13- Irshaidat, M., Soufian, M., Al-Ibadi, A., & Nefti-Meziani, S. (2019, April). A novel elbow pneumatic muscle actuator for exoskeleton arm in post-stroke rehabilitation. In 2019 2nd IEEE International Conference on Soft Robotics (RoboSoft) (pp. 630-635). IEEE.

1.6 Thesis organisation

This Thesis is divided into ten chapters. The main overview, aim, objectives, research contributions, Publications, and thesis organisation are described in chapter one. Chapter two discusses the main types of actuators that are used in robots, and studies the main positives and negatives including the structure and modelling of the pneumatic muscle actuators (PMA). In chapter three, the brief overview is explained for the collaborative robot systems, their types and the main challenges to achieve the efficient control system. The existing force formula for the contractor PMA is modified in chapter four and an important change is applied to make it suitable for the extensor actuator. Moreover, the length change of both types of the PMA is modelled mathematically in addition to the arm free end position angle. Then a structure based formulas for the contraction actuator is presented for the length, force, and stiffness. Chapter five introduces the types of controllers for the PMA. And a parallel structure of neural network NN controller and Proportional (P) controller are used to provides an efficient controller for single and multiple actuators. Novel structures of PMAs are presented in chapter six; including the self-bending contraction actuator (SBCA) of an efficient bending behaviour, the double-bend PMA (DB-PMA) which is inspired by lateral undulation movement by a snake. Unless the contraction and the extension actuators, the DB-PMA has the ability of vertical and horizontal movements. Special type of human facial muscles inspired us to design a circular pneumatic muscle actuator (CPMA). The biological muscles have a circular shape, and it controls the opening and the closing of human's eyes and mouth. The unique feature of the proposed CPMA is the variation of its inner diameter with applied air pressure, and

it provides high radial force. Furthermore, the kinematics for each actuator is presented. Two different soft grippers are presented in chapter seven with different structures and grasping abilities. These grippers are designed using the extension PMA, the SBCA, and CPMA. Chapter eight presents a multiple degrees of freedom (DoF) continuum arm with two control strategies to adjust the position of the end-effector. The collaboration of a multiple robot system is proposed in chapter nine of two or three robots and a human for various tasks and collaborative forms. The summary of this thesis, the conclusion and future work are given in chapter ten.

Chapter Two:

2. Types of actuators used in robotics

2.1 Introduction

The process that converts the energy to a mechanical form is called actuation. An actuator is a device that achieves this conversion (Poole & Booker, 2011). "An actuator is a mechanism for activating process control equipment by the use of pneumatic, hydraulic, or electronic signals" (O'Halloran, O'malley, & McHugh, 2008) and has to ensure that the energy conversion is useful. Actuators are principally the "driver" of a robot. They provide the necessary forces and movement to direct the robot from one position to another, and they have properties that significantly affect the overall performance of any mechanical systems (Vanderborght et al., 2013). Numerous actuators can be used in the design of a robotic system, though obviously they will require some level of control (Kamrani & Nasr, 2008). The actuators available depend on the load involved. The term "load" is associated with many factors including force, torque, the speed of operation, accuracy and power consumption (Gieras, 2008).

2.2 Rigid actuators

Synchronous actuators such as brushless direct current (DC) motors, Stepper motors, and brushed servo DC motors, and asynchronous actuators including traction motors, alternative current (AC) servo motors, pneumatic, and hydraulic are common used in rigid robots. These actuators provide the requirement motion and displacement for these machines. Several differences can be noticed between these actuators, but, in general, the main advantages are easy installation and control. While the rigidity, high weight, and the high cost are main disadvantages (Küçük, 2012).

2.3 Actuator effect on robot-human interaction

An interaction between the robot arm and humans represents an important issue in the industrial and medical application, which has to be safe and compliant during all probable situations such as control failure, human error, or any unexpected error in the

robot arm itself. On the other hand, the performance of the robot, including accuracy and rapidity, remains necessary as the task requirement (Bicchi et al., 2005). Tonietti, Schiavi, and Bicchi (2005) explain that the machines must be safe against all conceivable accidents whilst they interact with humans. Another important target is their behaviour, which can frequently be expressed as a speed of motion. The designers used to consider the safety and the performance as two separate features (Schiavi et al., 2008). A machine is more dangerous when it moves fast compared with a slow machine, however, the speed is one of the important requirements in applications; therefore, slow machines are unacceptable. To overcome this problem, many sensors are used in the rigid robot arm and active control. This solution is costly and not adequately dependable (Tonietti et al., 2005).

2.3.1 Safety

In recent years, there is increasing interest in using robots in numerous services such as industrial, medical and domestic applications. The robot-human interactions increase because of wide uses of robots (Haddadin, Albu-Schäffer, & Hirzinger, 2007b). Whilst at work, there is a risk that an accident could develop at any time due to a robot body or its moving manipulator having a fault (A. Bicchi & Tonietti, 2004). Several standards indicates have been developed by researchers for hazard severity, including; the Head Injury Criterion (HIC), the Viscous Injury Response (VC), the Gadd Severity Index (GSI), and the "3 ms" criterion. The Wayne State University (the WSUTL) developed a basic tolerance limit curve and most of the methods above are related to its work. The WSUTL is a head acceleration curve on impact duration (A. Bicchi & Tonietti, 2004).

Gadd (1966) shows that the threshold of possible injury can be defined as an integer number:

$$I = \int a^n \, dt \tag{2.1}$$

Where:

a: acceleration, force, or pressure.

n: weighting factor ≥ 1.

t: time (sec).

Two factors are affected in this indexing threshold; the value of n, which is signed by 2.5 based on the WSUTL animal impact data indicating a hazardous concussion, and the

maximum pulse intensity which can be continued without risk to life must also be carefully chosen if absolute, rather than relative evaluations. The number 1000 is selected as a maximum threshold value. ISO-10218 illustrates new collaborative operation requirements for industrial robots; one of the following factors always has to be satisfied: The TCP/flange velocity desires to be ≤ 0.25m/s, the maximum dynamic power ≤ 80W, or the maximum static force ≤ 150N. These values are based on heuristics, proposing to give a human the possibility to avoid risky conditions (Gao & Wampler, 2009; Haddadin, Albu-Schäffer, & Hirzinger, 2007a; Haddadin et al., 2007b; Haddadin, Albu-Schäffer, & Hirzinger, 2010).

The head injury criterion (HIC) is derived from GSI, and it is defined as:

$$\mathrm{HIC}(\Delta t_{max}) = \max_{t_1,t_2}\left[\left(\frac{1}{t_2-t_1}\int_{t_1}^{t_2} \hat{a}\, dt\right)^{2.5}(t_2 - t_1)\right] \tag{2.2}$$

Where $\Delta t_{max} \geq (t_2\text{-}t_1)$, t_1 is the start time, t_2 is the time required to reach the maximum velocity and they measure in seconds, and $\hat{a}$ is the acceleration in g's (acceleration of gravity) and it is defined by:

$$\hat{a} = \frac{a}{g} \tag{2.3}$$

Where a is the head acceleration in (m/s^2), and g is approximately (9.81 m/s^2).

Depending on the time the HIC is called (HIC_{15}) if (Δt_{max}=15 ms) and (HIC_{36}) if (Δt_{max}=36 ms). The HIC unit is (sec) because the â is unitless (Gao & Wampler, 2009) . A single rigid joint is a simple case to study the HIC when it moves by velocity v (m/s). Figure 2.1 shows the structure of the rigid joint with practical factors.

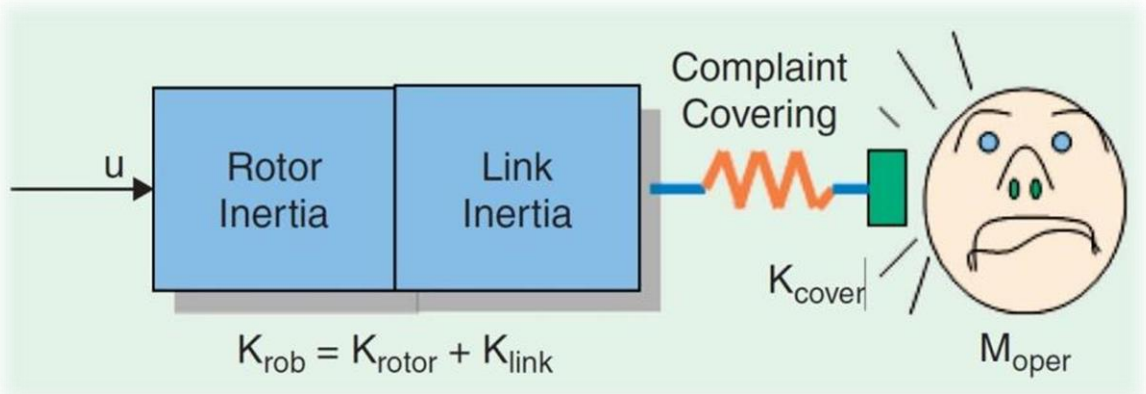

Figure 2.1 A single rigid joint. (A. Bicchi & Tonietti, 2004).

By integral eq. (2.2) we get the following expression:

$$\mathrm{HIC} = 2\left(\frac{2}{\pi}\right)^{\frac{3}{2}}\left(\frac{K_{cov}}{M_{oper}}\right)^{\frac{3}{4}}\left(\frac{M_{rob}}{M_{rob}+M_{oper}}\right)^{\frac{7}{4}} v^{\frac{5}{2}}$$

$$\stackrel{\text{def}}{=} \rho\left(M_{rob}, M_{oper}, K_{cov}\right) v^{\frac{5}{2}} \tag{2.4}$$

Where the total mass $M_{rob} = M_{rotor} + M_{link}$, M_{rotor} and M_{link} are the rotor and link respectively, the impacted operator mass is M_{oper}, and K_{cov} is the stiffness of the arm cover (A. Bicchi & Tonietti, 2004). For each system ρ is constant, therefore HIC depends on the velocity, so the safe velocity can be defined as a function of maximum allowed HIC.

$$v_{safe} = \left(\frac{HIC_{max}}{\rho(.)}\right)^{\frac{2}{5}} \tag{2.5}$$

To verify these formulas, the data which is given by A. Bicchi and Tonietti (2004) are used as follows: (M_{rotor}=1.2 kg, M_{link}=0.1 kg, K_{cov}= 5 kN/m and M_{oper}= 4 kg), for HIC=100, the safe velocity =2 m/s. Another example is introduced by Gao and Wampler (2009) for the following PUMA 560 robot parameters (M_{rob}=25 kg, K_{cov}= 25 kN/m, M_{oper}= 4 kg, and v =1 m/s); from (2.4) the HIC=2 s, this value is too low, so that the system is safe for robot-human interaction.

2.3.2 Series elastic actuation

Pratt and Williamson (1995) and D. W. Robinson (2000) developed a type of actuator called a series elastic actuator (SEA) to solve the high impedance problem. The basic SEA configuration is illustrated in Figure 2.2.

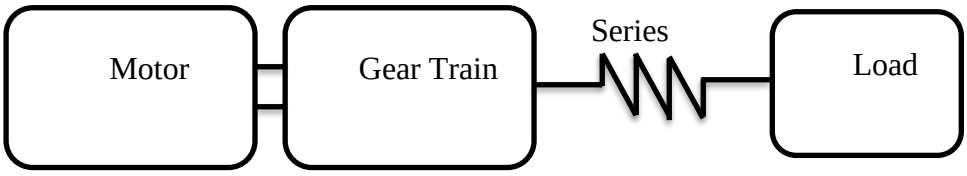

Figure 2.2 A basic diagram of series elastic actuator.

Pratt and Williamson (1995) show that the ESA reduce the pack value of load force and work as low pass filter (LPF). Furthermore, the series elasticity converts the force control problem, which is difficult, into a position control problem. In this case, the force values are proportional to the SEA position difference multiplied by the spring constant. The main

advantage of the series elastic actuator method is that it provides low output resistance through the frequency domain (Zinn et al., 2004).

At low frequencies that are less than the closed loop bandwidth of the SEA, the most common impedance reduction is 10 to 100 times, however, the impedance is reduced to the stiffness of the elastic coupling if the frequency is more than the SEA closed loop bandwidth (Pratt & Williamson, 1995; D. W. Robinson, 2000; Zinn et al., 2004).

2.3.3 Distributed micro-mini actuator

To address the performance limitation problem of the series elastic actuator and the control of robot joint torque, a new actuator known as distributed micro-mini actuator (DM^2) is developed (Zinn et al., 2004). Bicchi et al. (2005) explain that the DM^2 divides the generated torque between two actuators. These actuators work in different frequencies, one for the low and the other for the high frequency. The two actuators are connected to the same joint in parallel at a different location. A proper work for the Dm^2 occurs when the low and high motors have a zero or small impedance to ensure that these actuators do not add any disturbance to the system (Zinn et al., 2004). Figure 2.3 shows the connected method for the DM^2 with the robot manipulator.

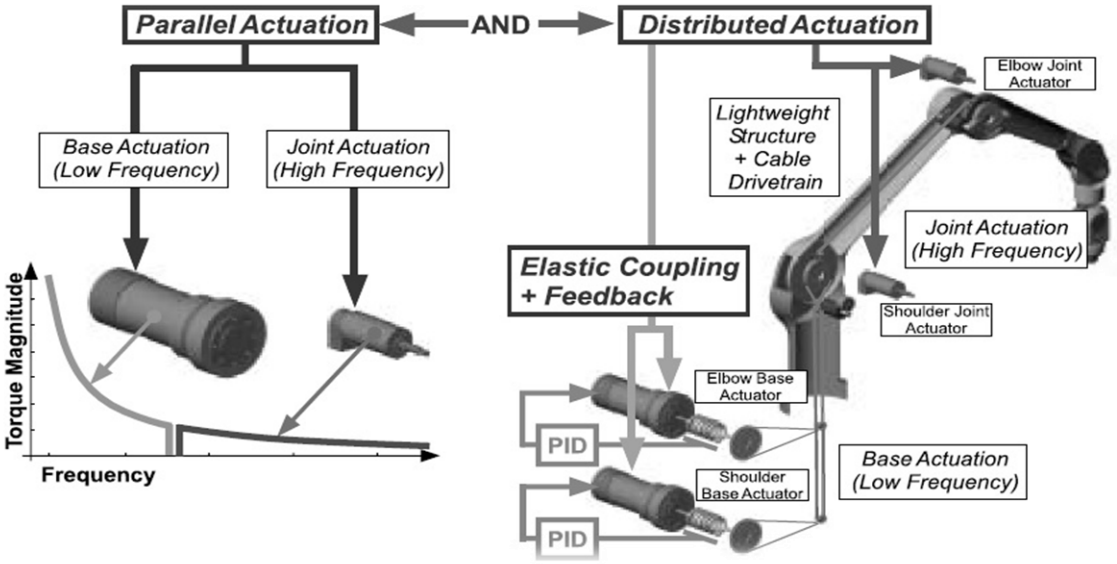

Figure 2.3 Location of low and high frequency actuators (Zinn, Roth, Khatib, & Salisbury, 2004).

2.3.4 Variable stiffness actuator (VSA-I)

Bicchi et al. (2005) developed a new design of variable stiffness actuator (VSA) in their lab, as seen in Figure 2.4. Two independent brushless controlled motors are used, connected by a trimming belt. Passive elastic elements are used to link the VSA cover.

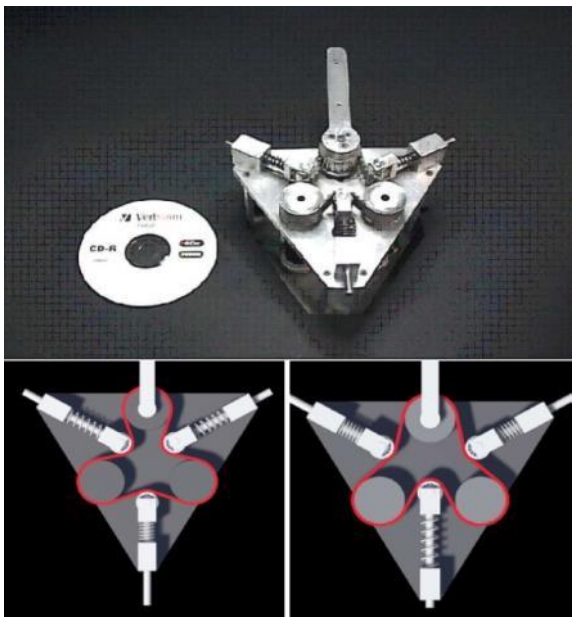

Figure 2.4 Variable stiffness actuator prototype (Bicchi, Tonietti, Bavaro, & Piccigallo, 2005).

The length of the timing belt ($L \approx 0.35$ m), is tensioned by the spring constants ($k=3$ N/m and $K_m=4$ N/m). The position controlled brushless motors are connected to the pulleys q_1 and q_2 which are connected non-linearly to the main shaft q_m by the timing belt (Tonietti et al., 2005). The torque capacity for this actuator is limited and it has a limited implementation performance in the robot arm (Schiavi et al., 2008).

2.3.5 Variable stiffness actuator (VSA-II)

This new type of actuator is developed by Schiavi et al. (2008) to overcome the limitation on torque capacity and the lack of robot joint performance. The short lifetime for the timing belt which is used in VSA-I, is replaced by four bar mechanisms which provide massive torque and make the actuator more robust. Figure 2.5 illustrates the structure of VSA-II.

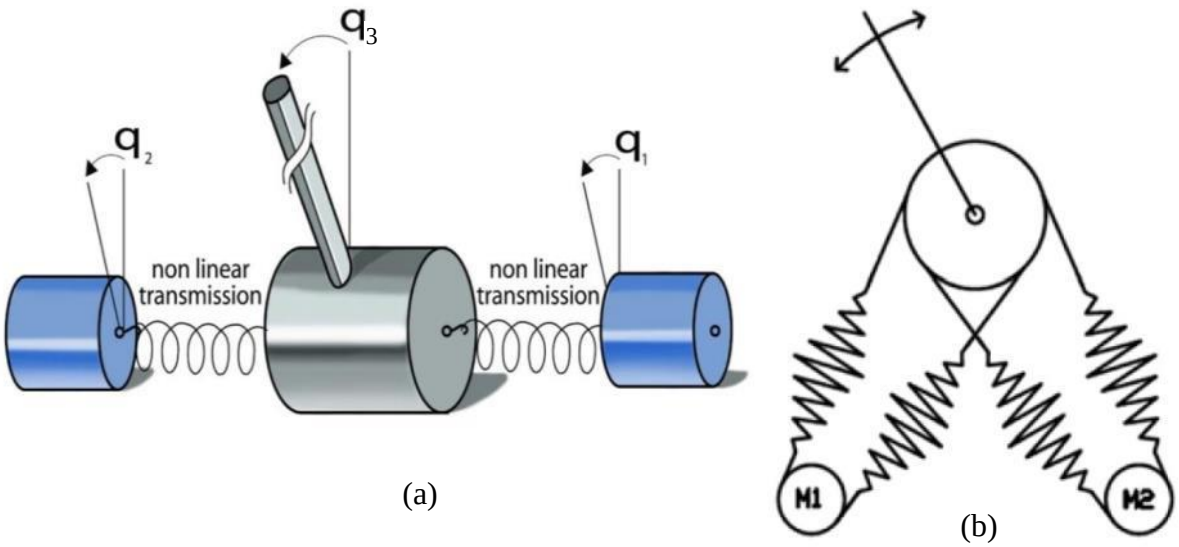

(a) (b)

Figure 2.5 Variable stiffness actuator VSA-II

(a) VSA-II schematic: q_1 and q_2 are the angle of the motors, q_3 is the joint shaft displacement (Schiavi, Grioli, Sen, & Bicchi, 2008).

(b) The four spring bar configuration of VSA-II (Vanderborght et al., 2013).

The transmission system in this actuator aims to provide a nonlinear torque-displacement between the motor torque and the shaft. The desired transmission ratio between input and output is achieved by a suitable design of the four-bar mechanism.

2.3.6 CompAct-VSA

N. G. Tsagarakis et al. (2011) present a new variable stiffness actuator, which is known as CompAct-VSA. The performance of this type of actuator is based on utilising the mechanism of the lever arm with the changeable axis. Figure 2.6 shows the prototype structure of the CompAct-VSA.

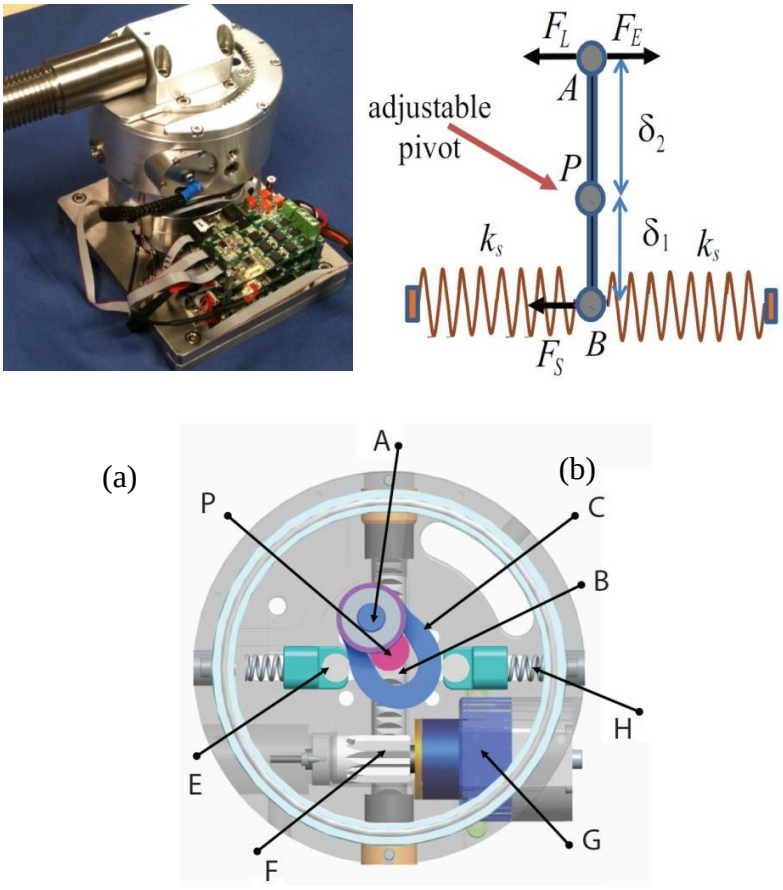

Figure 2.6 CompAct VSA (N. G. Tsagarakis, Sardellitti, & Caldwell, 2011)

(a) The CompAct unit. (b) Lever arm mechanism and variable pivot point diagram. (c) A 3D assembly of CompAct VSA: A) Joint connecting the link and the cam, B)Joint axis, C) Cam shaped lever arm, P) Pivot, E) Cam roller, F)Rack and pinion transmission, G) Motor, and H) Spring.

The stiffness is adjusted by changing the pivot and is achieved in a shorter time, as this actuator uses a short lever arm and small spring to decrease its size.

2.3.7 VSA-CubeBots

Catalano et al. (2011) developed a new variable stiffness servo actuator, known as VSA-CubeBots. The word servo applies to the overall system, which is comprised of the

major mover, the sensors for position control and the electronic board for the control system. Figure 2.7 a photograph of a VSA-Cube.

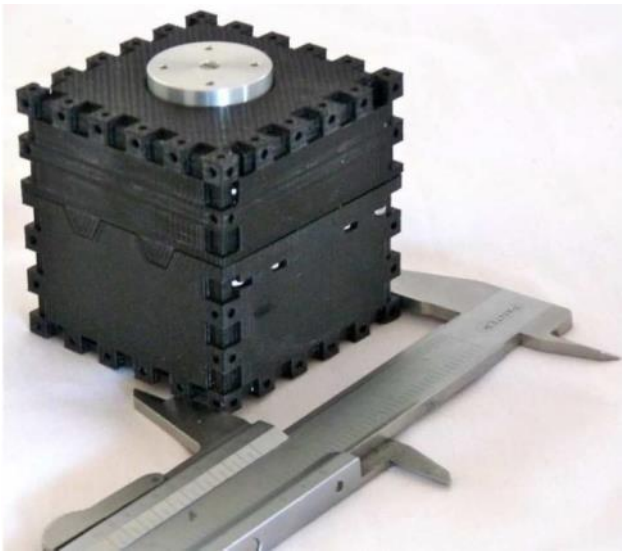

Figure 2.7 A VSA-CubeBots photograph (Catalano et al., 2011).

The small size, the low price, and the high modularity represent the most important design consideration for this actuator (Melo et al., 2014). Catalano et al. (2011) explain that the main advantage of this type of actuator is the low cost which represents one of the important issues in variable stiffness actuation.

2.3.8 Robustness of variable stiffness actuators

Wolf and Albu-Schaffer (2013) discuss the mechanical robustness of the variable stiffness actuators, which is defined as the rare probability of risk at a precise situation. This risk is dependent on two main factors: the severity of the consequences and the likelihood of them occurring. For a rigid robot manipulator, adding a spring to the actuator to change its behaviour to be a variable stiffness actuator means adding an additional part to the actuator, which leads to mechanical complexity and the complex behaviour of the spring itself. The VSA robustness is low when it is working at a limited performance. Internal and external risks may affect the robustness of the actuator as well as the robot's performance.

Ozparpucu, Haddadin, Albu-Schäffer, and Center (2014) studied the optimal control for VSA as shown in Figure 2.8 which it constructed using a nonlinear spring to connect the fixed motor to the link.

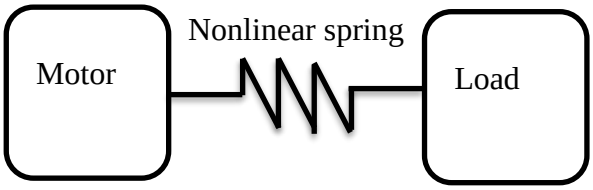

Figure 2.8 Variable stiffness actuator.

They presented a novel optimal control method for VSA. The main advantage of this process is the direct physical relation to the system but this method is only applied to one flexible joint and is still open for further research on the multi-joint system (Albu-Schäffer et al., 2010).

2.4 Pneumatic muscle actuator

In recent years there has been a substantial increase in designing, modelling and constructing (biological based) continuum robots (Bartow, Kapadia, & Walker, 2013; Godage, Branson, Guglielmino, & Caldwell, 2012b; McMahan et al., 2006a; McMahan et al., 2005).

The PMA has positives over standard pneumatic cylinders such as the high power to weight ratio, low workspace requirement, flexible structure (Jamwal & Xie, 2012; B.-S. Kang, Kothera, Woods, & Wereley, 2009; Kelasidi, Andrikopoulos, Nikolakopoulos, & Manesis, 2011; Leephakpreeda, 2011; Ranjan, Upadhyay, Kumar, & Dhyani, 2012; Wickramatunge & Leephakpreeda, 2010), infinite degrees of freedom (DoF) (Godage & Walker, 2015; Trivedi, Rahn, Kier, & Walker, 2008; Zheng, Branson III, et al., 2012), variable installation options, no mechanical wear, slight compressed-air consumption, availability of dimension, low cost and robust reliability for human use (B.-S. Kang et al., 2009; Wickramatunge & Leephakpreeda, 2010). A part from these advantages, PMA has been regarded as a suitable substitute for other actuators such as electrical and hydraulic (Anh, 2010; Ranjan et al., 2012). Furthermore, the robot is expected to be safer and more

flexible (Davis, Tsagarakis, Canderle, & Caldwell, 2003; Jamwal & Xie, 2012; Wickramatunge & Leephakpreeda, 2010).

Despite its distinct advantages, PMA exhibits highly nonlinear features (Anh, 2010; Jamwal & Xie, 2012; B.-S. Kang et al., 2009; Nakamura & Shinohara, 2007; Szepe, 2011; Thanh & Ahn, 2006; Tondu & Lopez, 2000), which are time dependent. The showing of nonlinearity in the PMA is due to the compressibility of air, the inner tube elastic-viscous properties and geometrically complex behaviours of the PMA outer covering (Jamwal & Xie, 2012; Kelasidi et al., 2011; Wickramatunge & Leephakpreeda, 2010). Moreover, the hysteresis behaviour is caused by the inner tube, which produces different characteristics of PMA during contracting and expanding (Godage et al., 2012b; B.-S. Kang et al., 2009; Leephakpreeda, 2011). This makes the modelling and controlling of pneumatic muscles more difficult (Andrikopoulos, Nikolakopoulos, & Manesis, 2014; Kelasidi et al., 2011; More & Líška, 2013; Ranjan et al., 2012; Wickramatunge & Leephakpreeda, 2010).

Current models do not fully explain every stage of the mechanical performances; therefore an enhanced model is still required (Wickramatunge & Leephakpreeda, 2010). Different models have been proposed to describe the behaviours of the PMAs. Among these models, the Chou and Hannaford model (Chou & Hannaford, 1996) and the Tondu and Lopez model (Tondu & Lopez, 2000) are widely used. These models are based on the assumption of the virtual works of the cylindrical shape and the small thickness of the inner tube (Chou & Hannaford, 1996; Kelasidi et al., 2011; Tondu & Lopez, 2000). Even though there are excellent initial descriptions of the mechanical behaviours, these models are still limited in predicting the performance of the PMA, at least in no-load situations. Furthermore, the force of pulling, length change, air pressure supply, radius and material properties are the major parameters of the PMA. Dynamic performances and the relationships between these parameters differ greatly from one PMA to another.

2.4.1 Structure of pneumatic muscle actuator

The pneumatic muscle actuator (PMA), which was first developed by Joseph L. McKibben in the 1950's, is made from an inner rubber tube surrounded by a braided sleeve (Chou & Hannaford, 1996). The McKibben artificial muscle is the most widely used, due to its simple structure. Its working principle is very simple: The surface stress of the inner tube is transformed into an axial contraction force (Tondu, 2012). The amount of this force

depends on the amount of air pressure. Figure 2.9 illustrates the structure of the PMA, in addition to the material and parts used to build it.

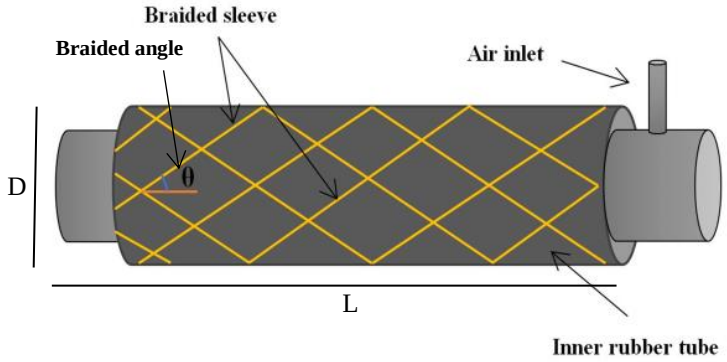

Figure 2.9 The structure of the pneumatic muscle actuator.

Where L & D represent the length and the diameter of the air muscle without air pressure and θ is the braided angle, which is the angle between the vertical line and the braided strand (b). The value of this angle varies from 0^o to 180^o based on the structure and is a major factor in muscle behaviour.

There is a similarity in behaviour between the human muscle and the pneumatic muscle; they contract by thickening due to the pressure in the inner tube. The Bridgestone Company introduced it again as a rubber actuator in the late 1980s. Since then, the robots are actuated by PMAs especially for medical applications (Ranjan et al., 2012).

2.4.2 Operation of PMA

Kelasidi et al. (2011) and Takosoglu, Laski, Blasiak, Bracha, and Pietrala (2016) explain the principle of operation of the contraction pneumatic muscle under the following conditions: a) varying the input pressure at constant load to determine the isotonic characteristics of the PMA, b) under constant pressure and changing the attached load to find the isobaric characteristics of the pneumatic muscle, and c) the constant contraction ratio operation by changing both the applied pressure and the attached load to determine the isometric performances. The diameter of the braided sleeve will maximize by increasing the air pressure whilst the length of muscle will decrease, additional air will lead to contracting the muscle and increasing in thickness (Ranjan et al., 2012).

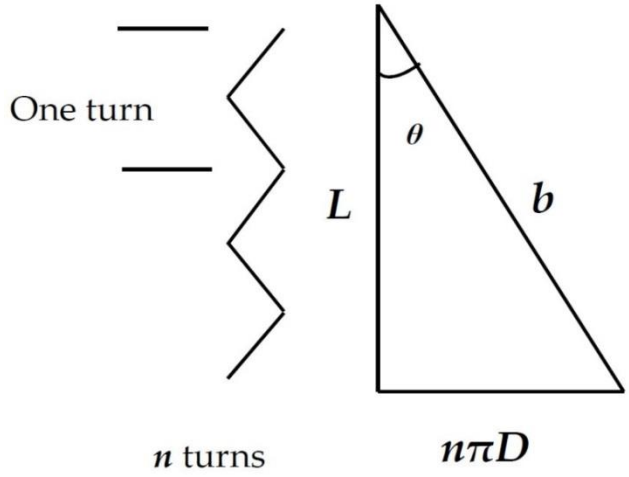

Figure 2.10 The parameters of the PMA.

In Figure 2.10, *n* is the number of strand turns from end to end of the muscle, which is constant for each muscle. The other parameters (*L*, *D* and θ) are changed due to air pressure and the shape of the PMA. In the first case, as is shown in Figure 2.11, PMA is fixed at one end and a constant load is attached to the other end. The gauge pressure gradually increases from zero bar. At a certain pressure value P_1, pulling force will develop and lift the attached load until it reaches the equilibrium point, where the pulling force is equal to the mass weight (Kelasidi et al., 2011).

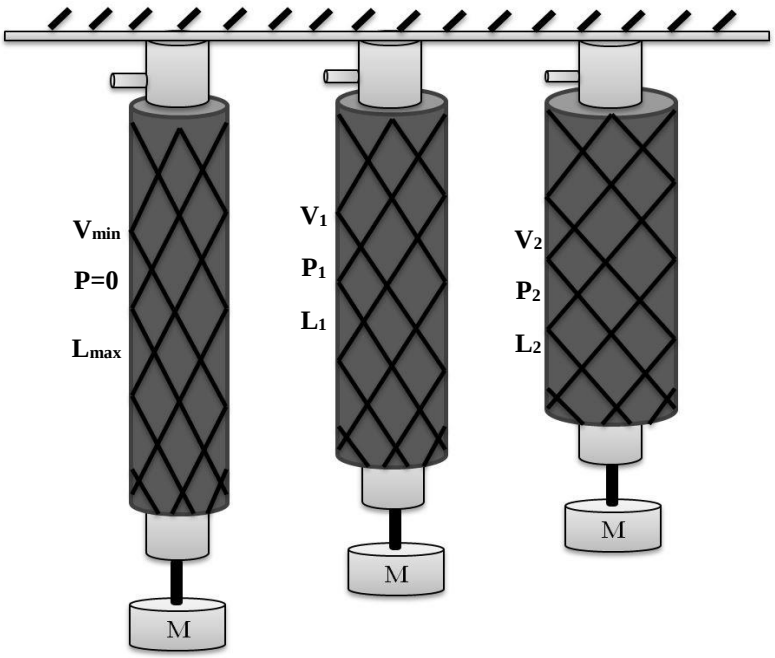

Figure 2.11 Constant load test of the PMA.

At this point, the volume will increase to V_1 and the length reduces to L_1. Supply more air to the muscle at pressure P_2 and it will increase the volume and make the PMA contract more to L_2 until the air pressure reaches its maximum value, which depends on the construction of the PMA.

The second operation case is pressurising the PMA at constant air pressure P, then various loads are attached as shown in Figure 2.12.

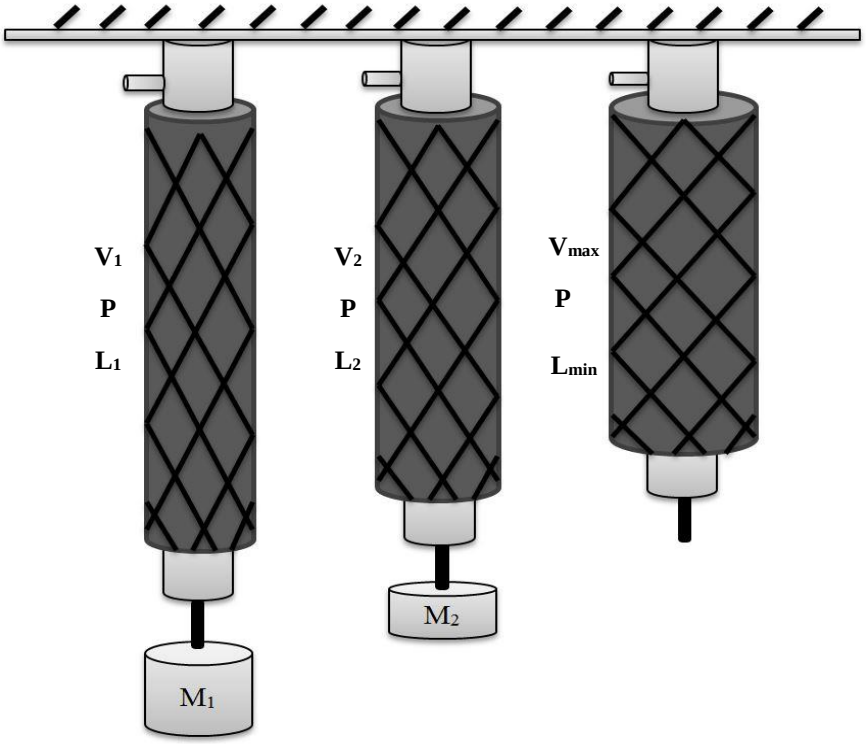

Figure 2.12 Constant pressure test of the PMA

Reducing the load from M_1 will increase the volume and decrease the length of the muscle (Davis et al., 2003; Kelasidi et al., 2011; Ranjan et al., 2012).

R. Kang, Branson, Zheng, Guglielmino, and Caldwell (2013) argue that in most applications, the PMA is used as a contraction muscle in order to establish a tensile force due to increasing the air pressure, whilst there is another common use in behaviour as an extending mode. Interest in soft robotic manipulators has significantly increased due to their ability to configure with surrounding environments, acting with a wide range of objects which are different in size. The extensor actuators (see Figure 2.13) are related to contractor McKibben actuators; both are operated by supplying air pressure to the rubber tubes encased in a braided sleeve. Where McKibben actuators have a braided angle $\theta <$

54.7°, this resulted in them contracting due to the air pressure, the extensor soft actuators have $\theta > 54.7°$. This type of actuator is extended in length and contract diameter which is caused by the air pressure (Trivedi, Lotfi, & Rahn, 2008).

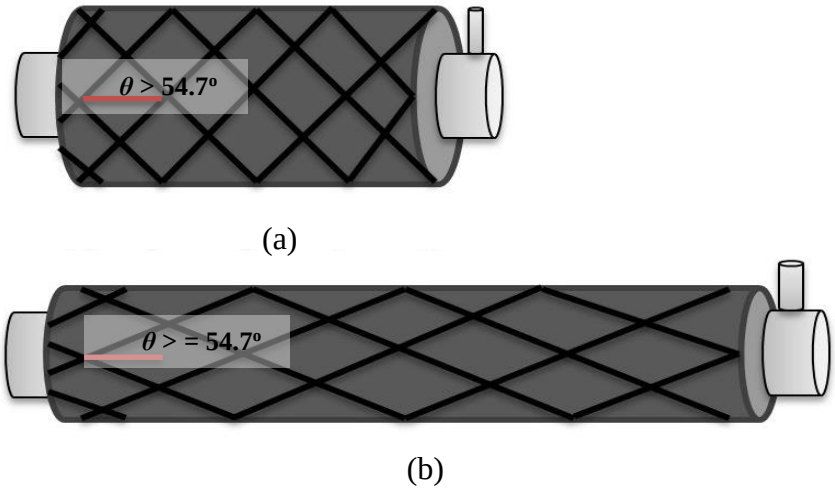

Figure 2.13 Extension PMA. (a) Before pressurizing, (b) After pressurizing.

2.4.3 Modelling of the PMA

Tatlicioglu, Walker, and Dawson (2007) show that in the most engineering systems it is important to have an accurate model to improve the behaviour of the system. In recent years there has been interesting research done to mathematically model the PMAs. The work was done to relate both the air pressure and the length of PMA to the generated tensile force of contraction muscles. Numerous factors are having major effects on the model, such as the properties of material used in PMA construction, length, diameter, braided angle, air pressure and contraction force. Understanding the relationships between these factors leads to driving accurate models, especially for control requirements (Kelasidi et al., 2011).

Important work was done by Chou and Hannaford (1996). They derived a model for the contraction pneumatic muscle actuator under the following assumptions: (1) the shape of an actuator is cylindrical; (2) there is always a contact between the braided sleeve and the surface of the inner tube; (3) neglecting the friction between the tube and the braided sleeve; and (4) ignoring the latex forces of the tube. Referring to Figure 2.10, the input work (W_{in}) for the McKibben's muscle under air pressure supply is:

$$dW_{in} = \int_{s_i}(P - P_0)dl_i.\,ds_i = (P - P_0)\int_{s_i} dl_i.\,ds_i = P_g dV \tag{2.6}$$

Where P is the absolute pressure, P_0 is the environment pressure (P_0=1.0336 bar), P_g is the gauge pressure (the relative pressure), s_i is the total inner surface, dl_i is the inner surface displacement, and dV is the volume change. The output work W_{out} occurs when the actuator shortens with the volume change.

$$dW_{in} = -FdL \tag{2.7}$$

Where F is the contractor (tensile) force and L is the axial (actuator) length. Assuming the lossless actuator has no storage energy, the input work must equal the output work, then:

$$dW_{out} = dW_{in} \tag{2.8}$$

thus,

$$-F\,dL = P_g dV$$

or,

$$F = -P_g \frac{dV}{dL} \tag{2.9}$$

To evaluate the dV/dL, the authors assumed the braided strand b length was fixed during the pressurizing process. Therefore, the volume of an actuator depends on its length. L and D can be computed as a function of θ.

$$L = b\,cos\theta \tag{2.10}$$

$$D = \frac{b\,sin\theta}{n\pi} \tag{2.11}$$

Where b and n are constant, the volume of the actuator under cylindrical shape assumption is:

$$V = \frac{1}{4}\,\pi D^2 L \tag{2.12}$$

From equations 2.10 and 2.11:

$$V = \frac{b^3}{4\pi n^2}\,sin^2\theta\,cos\theta \tag{2.13}$$

Return to (2.9):

$$F = -P_g \frac{dV}{dL} = -P_g \frac{dV/d\theta}{dL/d\theta} = \frac{P_g b^2(2cos^2\theta - sin^2\theta)}{4\pi n^2} = \frac{P_g b^2(3cos^2\theta - 1)}{4\pi n^2} \quad (2.14)$$

Or

$$F = \frac{\pi D_0^2 P_g}{4}(3cos^2\theta - 1) \quad (2.15)$$

Where: $D_0 = {}^{b}/_{n\pi}$, is the diameter when θ=90°. From this model the maximum contraction will occur when F=0, and that happen when θ=54.7°.

The second widely used model was made by Tondu and Lopez (2000). Their contraction force formula derived under the following assumptions: 1- The shape of PMA is a perfect cylinder with zero wall thickness. 2- There is a contact between the inner rubber tube and the braided sleeve. 3- The braided strand length is constant. 4- There is no friction between the tube and the sleeve. 5- The latex tube force is neglected. Figure 2.14 illustrates the PMA parameters under initial and pressurized conditions.

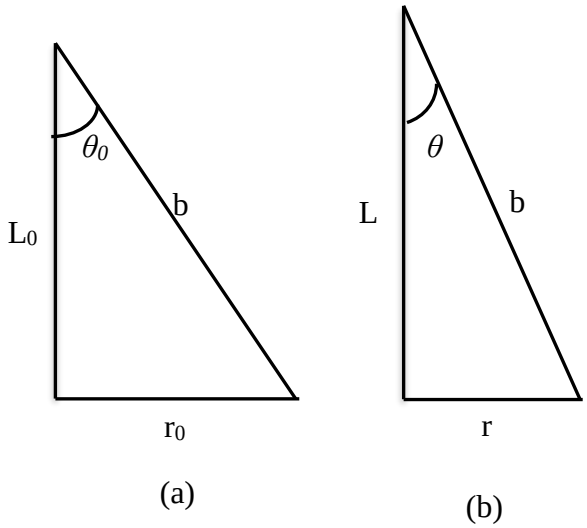

Figure 2.14 Parameters of contraction PMA. (a) Initial values, (b) under pressure values.

Mathematically:

$$r_0^2 + L_0^2 = b^2 \quad (2.16)$$

$$r^2 + L^2 = b^2 \quad (2.17)$$

Where: r_0 and L_0 represent the initial value of actuator radius and length respectively, r and L are the radius and length under pressurizing conditions; the strands length b is constant.

And

$$L_0 = b\ cos\theta_0 \tag{2.18.a}$$

$$r_0 = b\ sin\theta_0 \tag{2.18.b}$$

$$L = b\ cos\theta \tag{2.18.c}$$

$$r = b\ sin\theta \tag{2.18.d}$$

Or

$$L = L_0\ \frac{cos\theta}{cos\theta_0} \tag{2.19.a}$$

$$r = r_0\ \frac{sin\theta}{sin\theta_0} \tag{2.19.b}$$

From above

$$r = r_0\ \frac{\sqrt{1-cos^2\theta_0(^L/_{L_0})^2}}{sin\theta_0} \tag{2.20}$$

By using the virtual work equation, the contraction force can be written as a function of pressure P_g and the contraction ratio ε:

$$F(P_g, \varepsilon) = \pi r_0^2\ P_g[\alpha(1-\varepsilon)^2 - \beta] \tag{2.21}$$

Where

$$\varepsilon = \frac{L_0 - L}{L_0} \tag{2.22}$$

And

$$\alpha = \frac{3}{tan^2\theta_0} \tag{2.23.a}$$

$$\beta = \frac{1}{sin^2\theta_0} \tag{2.23.b}$$

Other research is being done to overcome the above assumptions for the presented contractor force models. Tondu and Lopez (2000) modified their model by adding the correction factor (q≤1) as following:

$$F(P_g, \varepsilon) = \pi r_0^2\ P_g[\alpha(1-q\varepsilon)^2 - \beta] \tag{2.24}$$

There are two options to select the correction factor: (1) Constant value, which depends on the material and (2) Variable value, which depends on the pressure.

B.-S. Kang et al. (2009) drive a formula to the correction factor as follows:

$$q(P_g) = 1 + c_1\, e^{-c_2 P_g} \tag{2.25}$$

Where: c_1 and c_2 are positive constants. From this equation, the correction factor becomes "1" at maximum air pressure, where the actuator shape is cylindrical.

Another work was done by Doumit, Fahim, and Munro (2009) to re-drive the volume formula for the incorrect cylindrical actuator shape. Figure 2.15 illustrates the irregular actuator form at zero pressure.

L_0 represents the actuator length, L_1 is the horizontal length of the cone, L_2 is the cone generator length, φ is the cone angle, L_3 is the middle length, D is the middle diameter and d is the ends diameter.

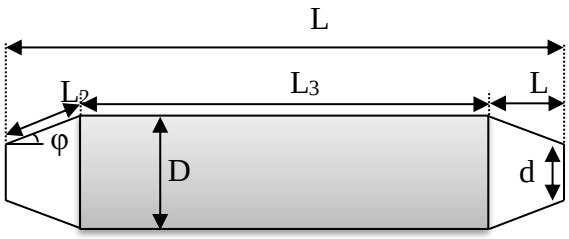

Figure 2.15 Actual geometrical model of PMA.

By using (2.11) the diameter is calculated by:

$$D = \frac{(b^2 - L_m^2)^{1/2}}{\pi n} \tag{2.26}$$

To overcome the contact between inner-tube and braided shell assumption N. Tsagarakis and Caldwell (2000) replaced the gauge pressure P_g by P_a which is equal to:

$$P_a = P_g - P_r \tag{2.27}$$

Where P_r is the (pressure to overcome the radial elasticity of the rubber liner), and it is equal to:

$$P_r = K_r(Dsin\theta - D_0) \tag{2.28}$$

K_r is a constant equal to 20 if D sin θ < 0.033 m. and it is equal to 5 if D sin θ > 0.033 m.

and D_0 is the initial diameter.

Wickramatunge and Leephakpreeda (2010) define the force formula as a function of stiffness parameter K and the stretched length L_s, which is defined as the difference between the instantaneous length L and the minimum length at maximum pressure L_u. Figure 2.16 shows these lengths at a certain contraction force.

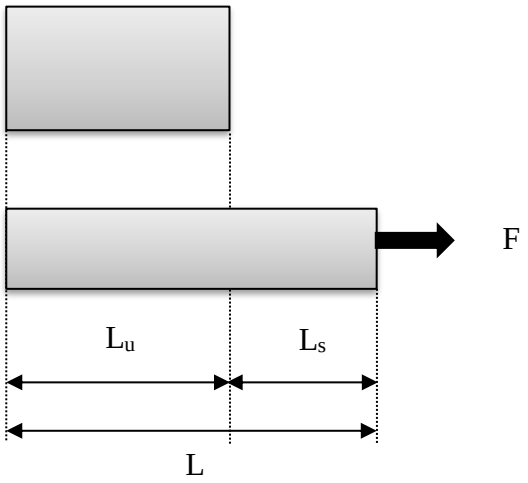

Figure 2.16 Length definition of the PMA under certain force.

$$F = K(P_g, L_s)L_s \tag{2.27}$$

K is represented by a polynomial function, which means its parameters are computed from the experimental data for each actuator.

$$K(P_g, L_s) = c_3P_g^2 + c_2P_gL_s + c_1L_s^2 + c_0 \tag{2.28}$$

Furthermore, the authors define a mathematical formula for L_u as a function of gauge pressure as following:

$$L_u = h_2P_g^2 + h_1P_g + h_0 \tag{2.29}$$

Ranjan et al. (2012) presents another force formula as a function of contraction ratio ε.

$$F = 12970\ (f_0\varepsilon^{-1} + f_1 + f_2\varepsilon + f_3\varepsilon^2) \tag{2.30}$$

The parameters (f_0, f_1, f_2, and f_4) are evaluated experimentally by attaching different loads to the actuator and recording ε each time.

Artificial Neural Network (ANN) was used by Jamwal and Xie (2012) to design an identifier of pleated pneumatic muscle actuator (PPMA), which connected pressure, length and force together as three main factors of the air actuator.

Davis et al. (2003) argue that the braided strand is not fixed and it changes during the pressurizing process by about 5.1 % for 1.77 m muscle length and diameter 20 mm at 450 kPa.

Chou and Hannaford (1996) suggested adding 2.5 N to the force formula to represent the fiction at elongation and -2.5 N at shortening. And they modified the force formula (2.21) by considering the sleeve thickness. Tondu and Lopez (2000) neglected the friction between the inner tube and the sleeve and considered only the friction between threads, which depends on the friction constant, the pressure, number of thread turns, and the contact surface. Davis and Caldwell (2006) used similar approach of Tondu and Lopez and drive a more accurate model for friction.

2.4.4 Soft robot continuum arms

A new generation of robots have been proposed during recent decades, using this type of soft actuator. Continuum robots, with distinctive capabilities, reach places that are typically unreachable for rigid machines and risky for individuals.

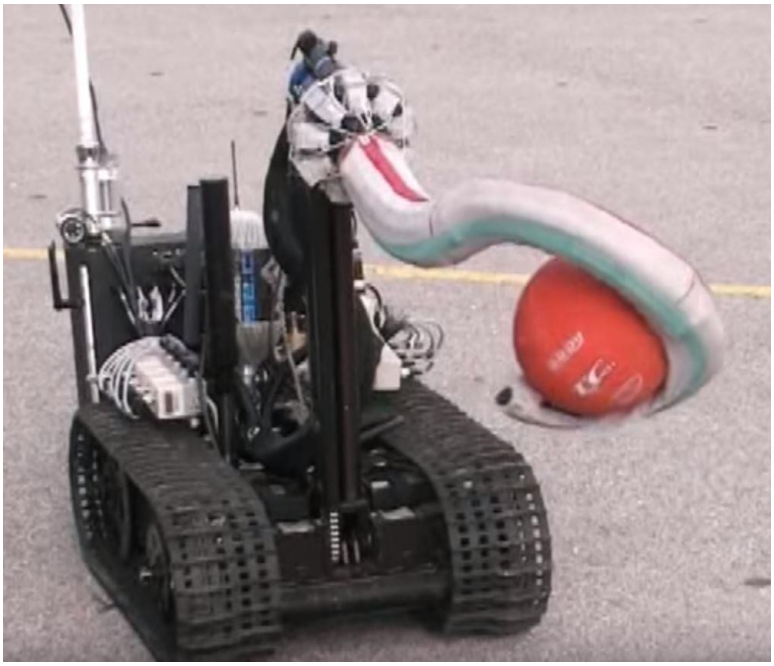

Figure 2.17 Multiple directional continuum arm with suction cup (Neppalli et al., 2007).

The low cost of the material used to build the soft robot arm makes the losses in case of an accident negligible. The continuum arms are also recognized for their varied range of grasping capabilities. They can definitely grasp objects of different forms and dimensions, as shown in (Neppalli et al., 2007). The grasping can also be achieved by numerous naturally inspired approaches; for example, the continuum robot featured in (Neppalli et al., 2007) can grasp a plastic box like an elephant trunk (see Figure 2.17).

Several prototypes have been designed to achieve a unique application, such as McMahan et al. (2005) presented the Air-Octor continuum arm with less complexity in terms of build and control due to the single central soft actuator and the use of tendons as actuators. However, it lacks flexibility and force because of the friction of the cable. It is difficult to overcome the friction effect caused by low pressure in the central member, which leads to cable binding and, consequently, unwanted actions of the soft arm (see Figure 2.18).

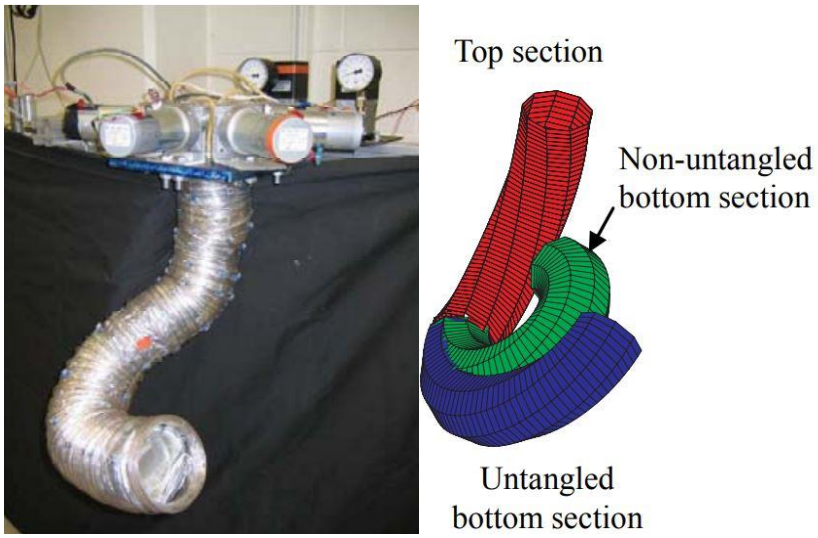

Figure 2.18 Two-section Air-Octor (McMahan, Jones, & Walker, 2005).

OctArm by McMahan et al. (2006a), which is elastic, flexible and has good power, but is difficult to construct and control because of the multiple pressurised central actuators which increase the mechanical challenges for the design (see Figure 2.19).

Figure 2.19 OctArm V- continuum manipulator (McMahan et al., 2006a).

Another design has been implemented by Neppalli and Jones (2007) by using a single extensor pneumatic actuator and three cables to arrange the direction of the free end. This design provides bending in an arc of constant curvature, is easy to control by motors, and can work with an air pressure of up to 483 kPa (see Figure 2.20). However, they do not provide any data about the load conditions and the grasping performance for the presented soft arm.

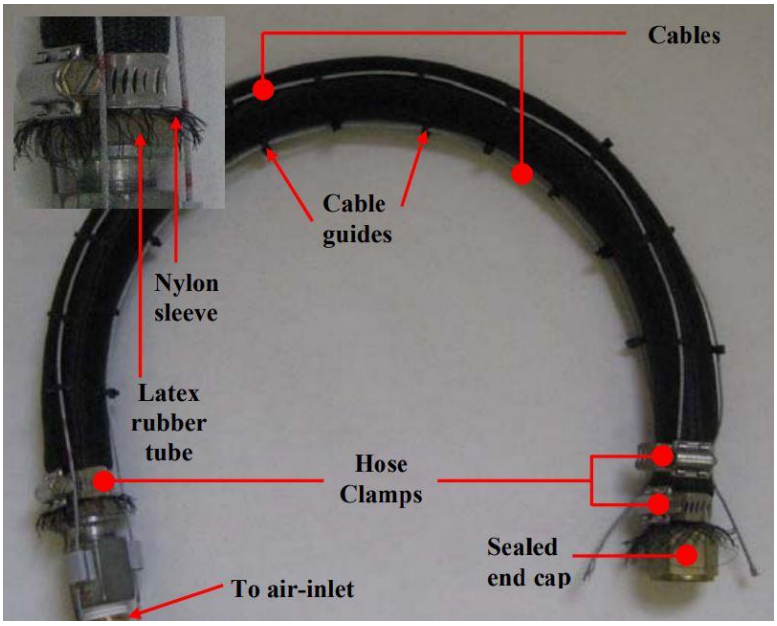

Figure 2.20 Cable actuated of single extensor continuum arm (Neppalli & Jones, 2007).

Zheng, Branson, et al. (2012) presented a design and model for an underwater continuum manipulator inspired by *Octopus vulgaris* (see Figure 2.21).

Figure 2.21 Octopus inspired underwater continuum manipulator (Zheng, Branson, et al., 2012).

Giannaccini et al. (2018) designed a variable stiffness continuum arm by using two layers of three contraction actuators and single extensor core actuator. Activate any of the two contraction PMAs bend the arm in one direction while the extensor actuator controls the arm stiffness (see Figure 2.22).

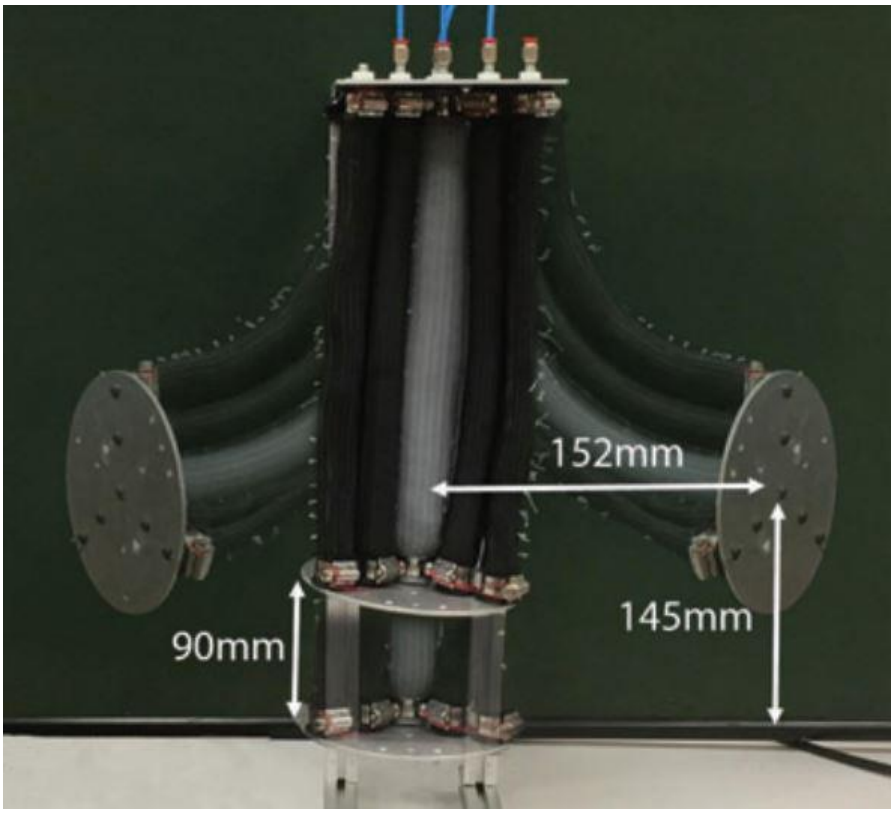

Figure 2.22 Variable stiffness, bending continuum robot arm (Giannaccini et al., 2018).

Despite the number of prototypes and the constructed commercial continuum robots (G. Robinson & Davies, 1999), numerous difficulties continue to surface in the design and kinematics of continuum robots. First, the development of a robust soft robot arm that is easy to implement and control (Neppalli & Jones, 2007). Secondly, one that performs multiple actions, making it suitable for several applications.

2.5 Summary

An actuator is the major part of a robot; its type and performance identify the type, performance and efficiency of the robot. Many types of actuators are used in industrial robots; the rigidity, flexibility and the stiffness are its classification base. The high risk factors of the rigid actuators motivated the researchers to search for new types which are more flexible and variable in stiffness. Numerous kinds of adaptable actuators have been invented and modified in more than one place in the world; nevertheless, the pneumatic muscle actuator (PMA) is the type which incorporated the main advantages of the various styles, including force, variable stiffness, multi degree of freedom, low cost, small work space requirement and easy implementation. However, the high level of nonlinearity is the main disadvantage of the PMA and this is where the dynamic model of this actuator still needs enhancement to reach the optimal form. Moreover, the nonlinearity and hysteresis make the desired control difficult to achieve. Therefore, a modified model has to be developed and suitable controller methods used to reach the performance goals.

Chapter Three:

3. Multiple Robot System

3.1 Introduction

Multiple Robots systems can achieve many requirements in an industrial application such as dividing the desired force among the arms and sharing multi-tasks at the same time (Adorno, Fraisse, & Druon, 2010; Tinós, Terra, & Ishihara, 2006). Moreover, the multi-robot system is faster, reliable and more powerful than the single robot system in the same application, and it maximizes the efficiency of the collaborative team (Roy & Dudek, 2001). In addition, using several cheap robots provide redundancy and the system is expected to be more reliable (Burgard, Moors, Fox, Simmons, & Thrun, 2000). However, numerous problems related to dynamic control such as multi-robot coordination mechanisms (Gerkey & Matarić, 2004), grasping, position, and force control remain unsolved (Liu & Abdel-Malek, 2000). Furthermore, the complexity of the system is increased due to the number of robots and humans in the project area (Roy & Dudek, 2001).

3.2 Task requirements

Task defines the type, specifications, size and number of robots required. An object movement between two positions which are small apart without an obstacle require a single robot arm, while, a task such as car manufacturing may require more than two robot manipulators.

3.2.1 Tasks that required multiple robot arms

A large, high-speed robot arm can perform many tasks individually. However, this type of robots is expensive, high weight, and requires a wide work space. Consequently, the human-robot interaction is impossible due to the high risk of injury. The example of two keys apart and need to turn at the same time is given by Dudek, Jenkin, and Milios (2002). For this example, two synchronized or communicated robot arms are required.

3.2.2 Tasks that need multiple robots

Tasks that involve multiple subtasks need several robots in which they called parallel robots. The term “parallel robots” is used to define the robot that has several parallel links from the base till the end effector. In contrast, the serial robot has a single manipulator of several links connected together by several joints serially.

In case of using multiple robots in parallel a communication is required between them in order to make sure that the task is completed properly (Dudek et al., 2002), unless it increase the system cost, not suitable, or risky for secure application such as military tasks (Berman, Halász, Hsieh, & Kumar, 2009).

3.2.3 Task sharing

Sharing a task between two or more robots decreases the required time and increase the reliability. Moreover, using multiple simple robots is another advantage instead of using one complex and expensive robot (Zlot & Stentz, 2005).

3.3 Robot-Human interaction

Nowadays, the robots can be found anywhere in our life, either in factories or in the normal life of people (Severinson-Eklundh, Green, & Hüttenrauch, 2003). While the human workers need to be continue, the robot validates its efficiency in product quality, flexible in work and high reliability in manufacturing process (Jeff Fryman & Bjoern Matthias, 2012; Jörg Krüger, Lien, & Verl, 2009). Depending on the type of task, the multi-robot system may classify into many taxonomies (Yanco & Drury, 2004). Figure 3.1 illustrates the collaboration possibilities between robots and humans individually or as a team, where H refers to human and R refers to the robot.

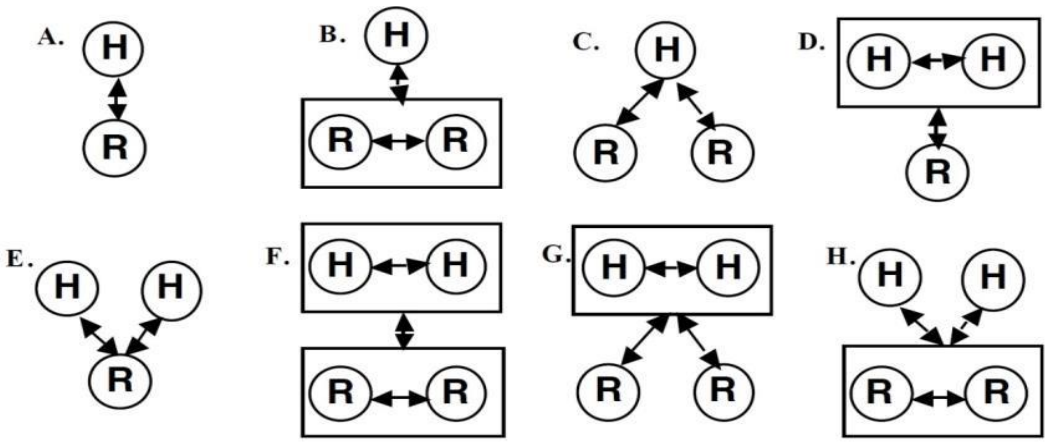

Figure 3.1 Possible taxonomies of robot-human interaction (Yanco & Drury, 2004)

The context where the robot will be used leads to understanding the interaction requirement among the robots and between the human and robot. This includes the number of humans and robots to be used, the task to be solved, and in several cases the human is expected to assist the robot to overcome the limitation in robot performance (Severinson-Eklundh et al., 2003). A number of factors are nominated for the robot to be successful, such as the repetition to reach regular quality, the speed and the force of manufacturing robots, reduction of the task hazards, decrease of the force required and flexibility in programming (Jeff Fryman & Björn Matthias, 2012).

The estimated number of multi-task robots around the world is about 1,664,000 as reported by the International Federation of Robotics (IFR) statistical analysis (IFR International Federation of Robotics, 2015). The industrial robots continue to develop in both safety and productivity, moreover, while they have evolved in their functionality, safety is an extremely significant concern (Jeff Fryman & Björn Matthias, 2012).

3.3.1 Application of Human-Robot Collaboration

In recent years, numerous applications between human and robot have been classified in different ways. However, all classifications are based on the same work space, which is physically accessible for human and robot. This space is defined as collaborative work space (CWS). The most important applications which affect either the risk ratio or the efficiency of project are (Jeff Fryman & Björn Matthias, 2012):

1- Prevent robot moving

While the user is in the CWS the robot is not allowed to move and it has to stop in its position.

2- Speed limitation

Speed limitation must be defined to reduce the human injury probability, and it is adaptable for the human position.

3- Force limitation

Force and power limited values must define when the contact between the human and the robot should occur.

4- Mechanical interaction

Mechanical contact between human and robot through an object is one of the common applications of human-robot collaboration (HRC) (Kosuge et al., 1994). Figure 3.2 gives an example of this application.

Figure 3.2 Human robot interaction through an object.

5- Using a robot as a tool

Using the robot as a tool is an easy way to support the achievement of the physical project; Bechar and Edan (2003) used the human-robot collaboration to increase the efficiency of harvesting.

3.3.2 Distribution of tasks between humans and robots

Normal industrial robot systems pose a threat on human life due to its high force, inertial and the rigidity (Jeff Fryman & Bjoern Matthias, 2012). The tasks in CWS need to distribute between human and robot according to what is suitable for each in terms of load, risk and application.

3.3.3 Industrial robots

For over thirty years robots have been used in many industrial applications (Adorno et al., 2010; Heyer, 2010). The most common tasks had done by industrial robots include welding, sorting, soldering, painting, casting and stacking. In the early years the robots were designed to work in static environments with joint torque feedback only, which limited this type of robots to working individually and not close to the human (Heyer, 2010).

Workspace, where high performance robots are working together with human in the same environment, have numerous difficulties and risks either on both the human side and on the manufacturing side. The commercial robots available these days have acceptable levels of speed, accuracy, repeatability and dexterity (Gudiño-Lau & Arteaga, 2005; Heyer, 2010). The dynamic models and control methods are slightly difficult to achieve the desired requirement in compression with a single robot system (Gudiño-Lau & Arteaga, 2005).

3.4 Multi-arms robot system

The multi-tasking, cost saving and low space requirement are the main advantages for using the multi-arms robot instead of multi robots (J Krüger, Schreck, & Surdilovic, 2011). Tinós et al. (2006) mention that based on the human, using two arms is better than using one. Two or three arms can execute complex tasks, which is difficult or impossible to do

with a single robot arm, see Figure 3.3. It is important to study the performance of the hand to increase the manipulation and gripper capability of the robot as well as increase the desired force for task completion (Gudiño-Lau & Arteaga, 2005).

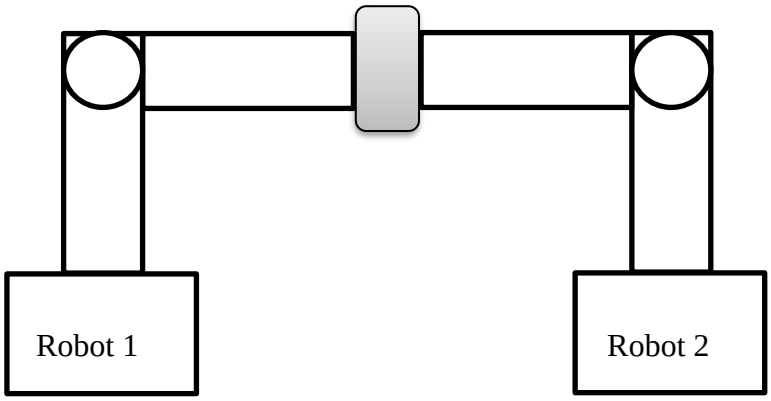

Figure 3.3 Two robots holding an object.

3.5 Levels of collaboration

Different levels of collaboration between humans and robots can be classified depending on the nature of the work.

3.5.1 Low level

At this level of collaboration, there is no direct contact between the human and the robot (Shi, Jimmerson, Pearson, & Menassa, 2012), and the human is totally out the work space from the start to the end of the task time. The risk of injuries at this level is significantly high, and the example of this task is the welding robot (Kaipa, Morato, Liu, & Gupta, 2014).

3.5.2 Medium level

The full automatic operation of the robot occurs at this level of collaboration, and the human may enter into the CWS at any time of the task but outside the restriction area (Shi et al., 2012).

3.5.3 High level

The risk of injury at this level is high since the human is within the CWS while the robot is in operation. The robot speed, force and path must be synchronized with human motion and forced shutdown could happen to prevent accidents (Jeff Fryman & Björn Matthias, 2012; Shi et al., 2012).

3.6 Communication in collaboration environment

Communication between the human and the robot represents one of the major keys to success in collaborative systems. Moreover, the sensors which have been built in the robot or in the environment, can also be a type of communication in the CWS (Ende et al., 2011; Gleeson, MacLean, Haddadi, Croft, & Alcazar, 2013).

3.7 Summary

Collaborative work between humans and robots is widely used these days because of application and environmental challenges. Hazards and risk of injuries are at the top of the motivating factors for using the robot in the most dangerous areas in the work space, while the human has the controller position. Many controller problems have been solved including position and force problems. However, a list of problems is still under study at the base of rigid robot systems. Risk of injuries, cost of multi robot systems and coordinators are examples of such problems.

Chapter Four:

4. Modelling of pneumatic muscle actuator

4.1 Introduction

The first and most important step to an efficient control is the perfect model system. During recent years, numerous researches have been done to model the tensile force of the contractor pneumatic muscle actuator (PMA). The widely common force formulas were developed by Chou and Hannaford (1996) and Tondu and Lopez (2000) as mentioned in chapter two. To enhance the models presented, experiments are being done to study the affected factors and improve the formula of contraction force.

Both types of PMA are considered in this chapter by designing a set of contraction and extension actuators, and then study the performances at different pressure and load conditions. The length of the contraction PMA is formulated as a function of air pressure and the initial length by set of equations. Then, the tensile force for Tondu and Lopez (2000) is modified to reduce the error between the experimental and the model data. Serial and parallel structures of the contraction actuators are implemented, then, the length and the force of each configuration are studied.

The length and force for single and multiple extensor actuators are formulated to explain the performances to such type of actuators.

4.2 Contractor pneumatic muscle actuator

4.2.1 Construction

Many PMAs are constructed in different lengths and diameters. Each actuator is basically made from a braided sleeve covered rubber tube and the two ends are closed with pieces of any solid material, and left with a small hole as an air input in one end. Actuator nominal lengths between (10 cm and 40 cm) are used by numerous researchers such as Anh (2010), Chou and Hannaford (1996), Tondu and Lopez (2000), Wickramatunge and Leephakpreeda (2010), and Ranjan et al. (2012). In this section, 20 cm, 30 cm and 40 cm

actuators are constructed with about 1.76 cm diameters. Table 4.1 shows the used material for each actuator, and **Error! Reference source not found.** illustrates the construction p rocess. These actuators are set to be the contractor type by choosing the braided angle θ to be less than 54.7^{o}.

Table 4.1 Description of material used in the PMA contraction

Material	Model/Type
Rubber tube	700c * 18-25
Braided sleeve	RS 408-215
Plastic 3D printed ends	/
Air muscle kit	/
Cable tie	/

(a)

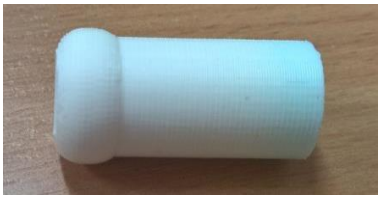

(b)

(c)

(d)

(e)

(f)

(g)

(h)

Figure 4.1 Parts and construction of the pneumatic muscle actuator.

(a) Air muscle kit, (b) Close end, (c) Opened end, (d) Braided sleeve, (e) Rubber tube, (f) Cable tie, (g) Inner rubber tube with the two ends,(h) The contraction PMA

4.2.2 Practical experiments

Air pressure is applied to the actuators above; the pressure is increased from 0-500 kPa by a manual valve at 50 kPa step. Table 4.2 gives the specification of the PMAs under study.

Table 4.2 Specifications of the contractor PMAs under study

Nominal length L_0 (cm)	Diameter D (cm)	Braided angle θ (degree)
20	1.767	31.35
30	1.752	30.02
40	1.764	30.28

4.2.2.1 Length change experiment

In this experiment, the air pressure is applied to each actuator simultaneously and it is regulated by a valve from 0-500 kPa in 50 kPa steps, then it is decreased backwards to zero, to observe the hysteresis. At each value of the air pressure, the length L, the percentage of length change, the braided angle θ, the diameter D and the contraction ratio ε of the actuators are recorded. Table A.1, Table A.2, and Table A.3 show the results of the each PMA separately.

Where P is the applied air pressure, L is the length of the actuator, $\acute{L}$ is the average length of the actuator at the same increment and decrement pressure values, length difference is the percentage of contraction ratio, θ is the braided angle, D is the diameter and ε is the contraction ratio.

To avoid the explosion of the air muscle, and since the contraction ratio has a slight difference; the maximum air pressure is set to 400 kPa for the 20 cm PMA and 500 kPa for 30 cm and 40 cm PMAs. The constructed PMAs are configured to be as identical in diameter and braided angle as possible. The results are plotted as a function of air pressure as shown in the figures below. Figure 4.2 illustrates the change in length for P varies from zero to its maximum value and from maximum to zero for the three actuators.

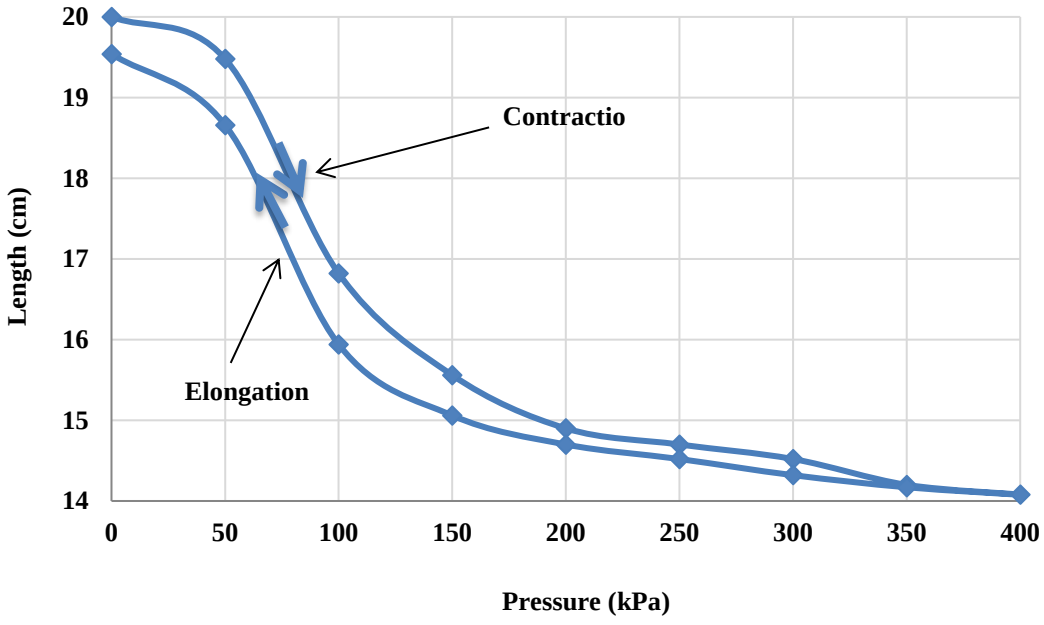

(a)

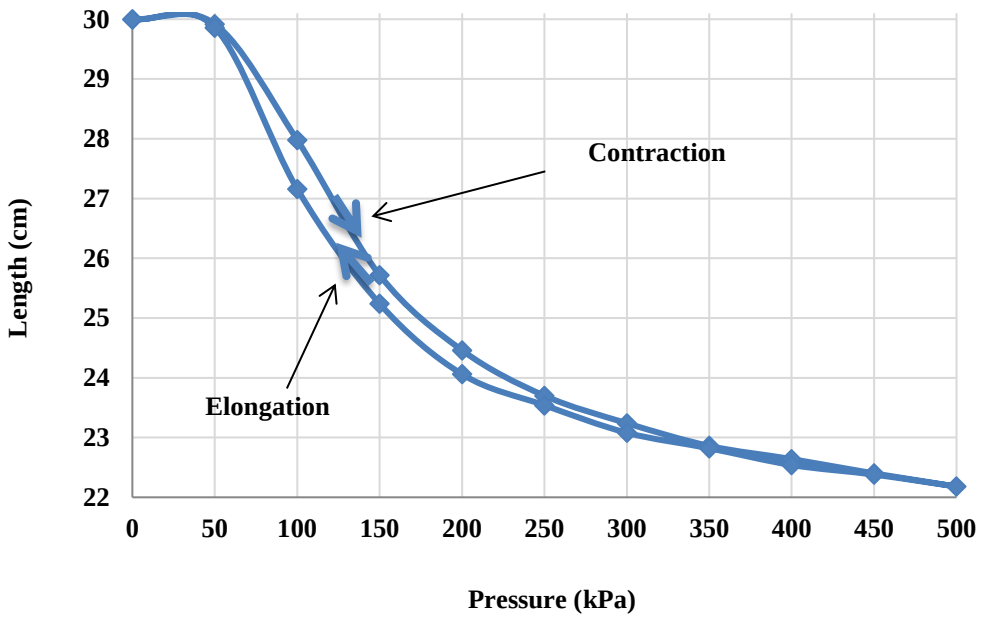

(b)

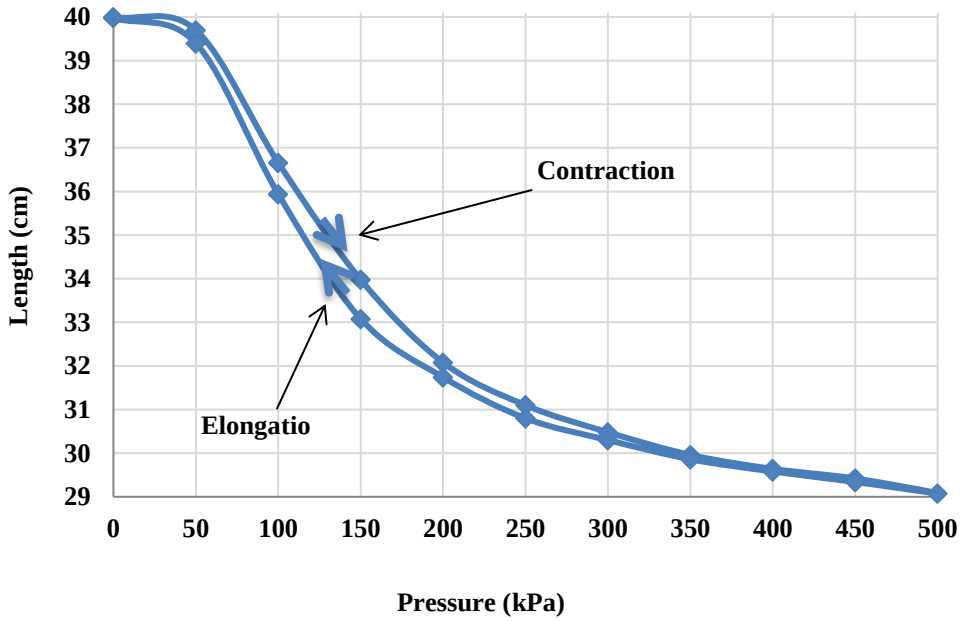

(c)

Figure 4.2 Plots of actuator length change against air pressure.

(a) 20 cm PMA, (b) 30 cm PMA, (c) 40 cm PMA

Both the hysteresis and the elasticity behaviours of the air muscle appear in Fig. 4.2. This performance, due to the variety of the input air pressure, makes the control system of this type of actuator more difficult. In Figure 4.3 below the plot of the length average value $\acute{L}$ is illustrated, where:

$$\acute{L} = \frac{L_{n_{dec}} + L_{n_{inc}}}{2} \tag{4.1}$$

Where $0 \leq n \leq P_{max}$, $L_{n_{dec}}$ and $L_{n_{inc}}$ are the contraction and elongation lengths respectively. In the following explanation of the experiment, $\acute{L}$ will represent the actuator length.

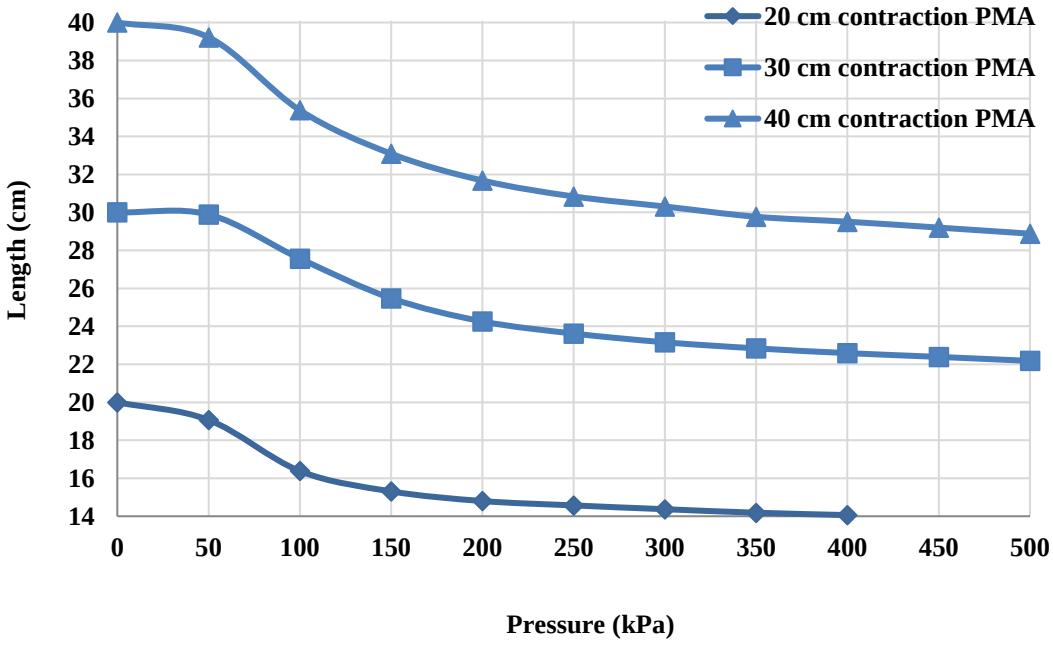

Figure 4.3 The experimental data of the contractor PMAs

From these results, a set of equations is derived to model the actuator length as a function of P and L_0 as follows:

$$L = a + \frac{b}{[1+(\frac{p}{c})^d]^e} - 0.009L_0\sqrt{p} \tag{4.2}$$

$$\text{Where: } \begin{bmatrix} a \\ b \\ c \\ d \\ e \end{bmatrix} = \begin{bmatrix} 0.4351 & 0 & 0.0183 & -0.0003 \\ 0.5649 & 0 & -0.0183 & 0.0003 \\ -0.0141 & 0 & 0.0031 & -0.00006 \\ 0.5487 & 0 & -0.0136 & 0.00007 \\ 0 & 0.3694 & 0 & 0 \end{bmatrix} \begin{bmatrix} L_0 \\ L_0^{-0.248} \\ L_0^2 \\ L_0^3 \end{bmatrix} \quad (4.3)$$

The sigmoidal function was firstly considered for each muscle individually, then we added ($-0.009L_0\sqrt{p}$) as an error correction. The final step is finding the parameters (a, b, c, d and e) as a function of L_0. Figure 4.4 gives the validation plots for the model compare with experimental results.

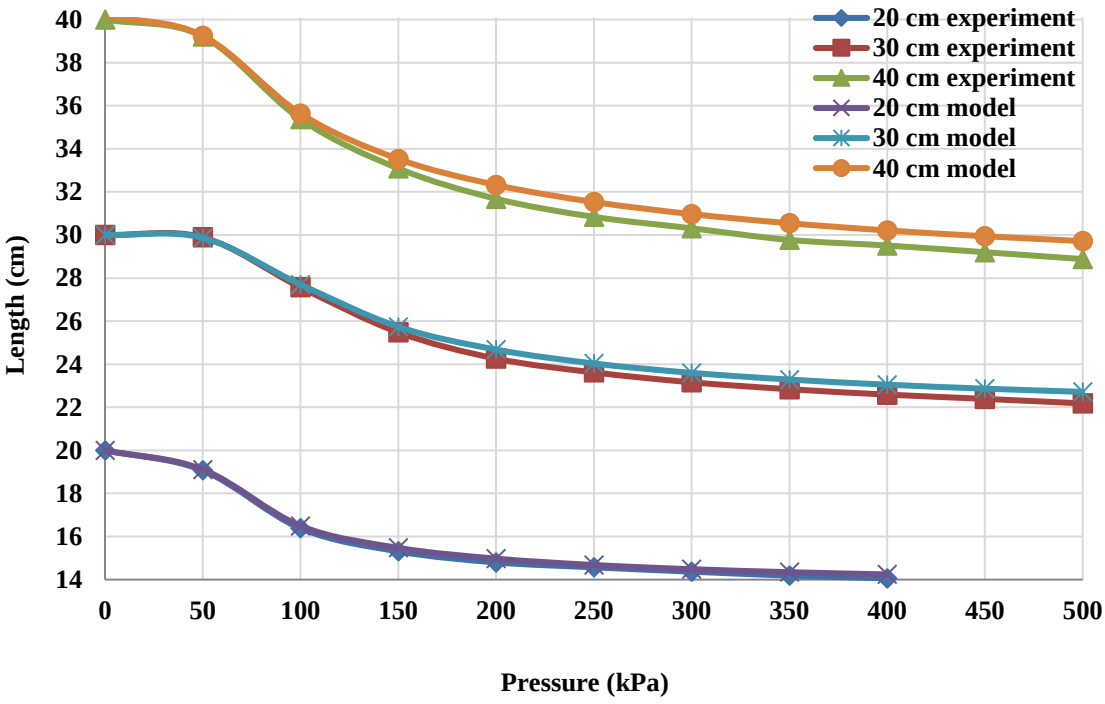

Figure 4.4 The validation results of the model for the three actuators

Figure 4.4 shows the significant matching between the lab result and the mathematical model result for all actuators under study.

To ensure the reliability of this model, one muscle is constructed for lengths (25 cm); the same model is applied for this PMA and the result is plotted in **Figure 4.5**. From these

results, we can consider this model as a valuable mathematical model for PMAs which have the nominal lengths (20 cm ≤ L_0 ≤ 40 cm), therefore, the position control for a single PMA can be achieved.

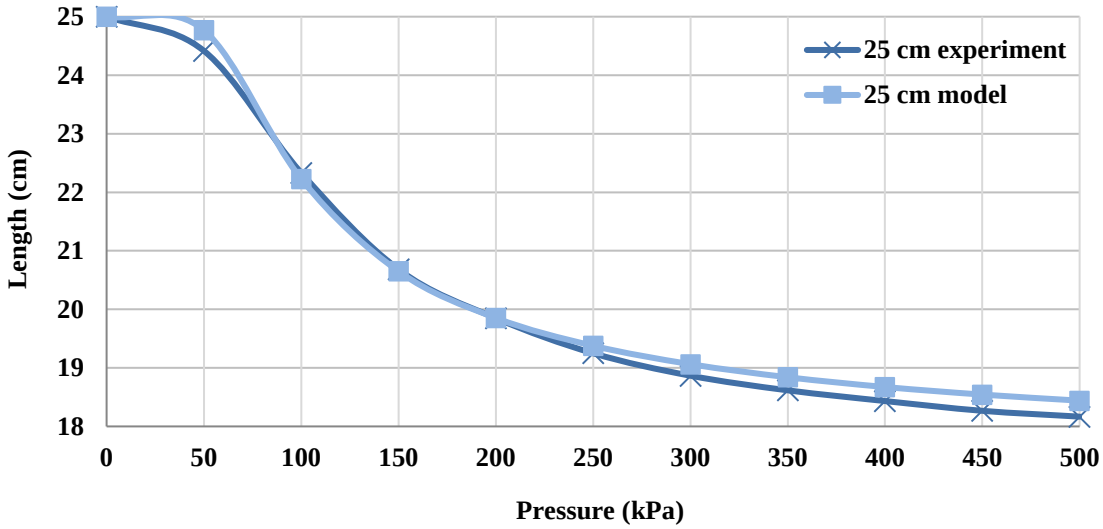

Figure 4.5 The validation results of the 25 cm PMA

4.2.2.2 Modelling of tensile force of a single PMA

Numerous works are done for modelling the force of the contractor PMA, In this section the model of Tondu and Lopez (2000) is selected to overcome some of the assumptions and to modify the existing model. To achieve this aim, a load is attached to the free end of the actuator and it varies from 0 kg to 10 kg by 0.5 kg steps. At each weight, the pressure from 0 to P_{max} is applied, then the length of the actuator is recorded.

Table A.4, Table A.5, and Table A.6 show the given data from these experiments for the three PMAs, which explains the length of the actuator due to the change in air pressure supply and the attached load.

The results are plotted in figures below in two forms; Figure 4.6 gives the length against the pressure at a fixed load, at load steps (0, 1, 2… 10) kg., while Figure 4.7 shows the actuator length against the weight at supply pressure from 0 bar to P_{max}.

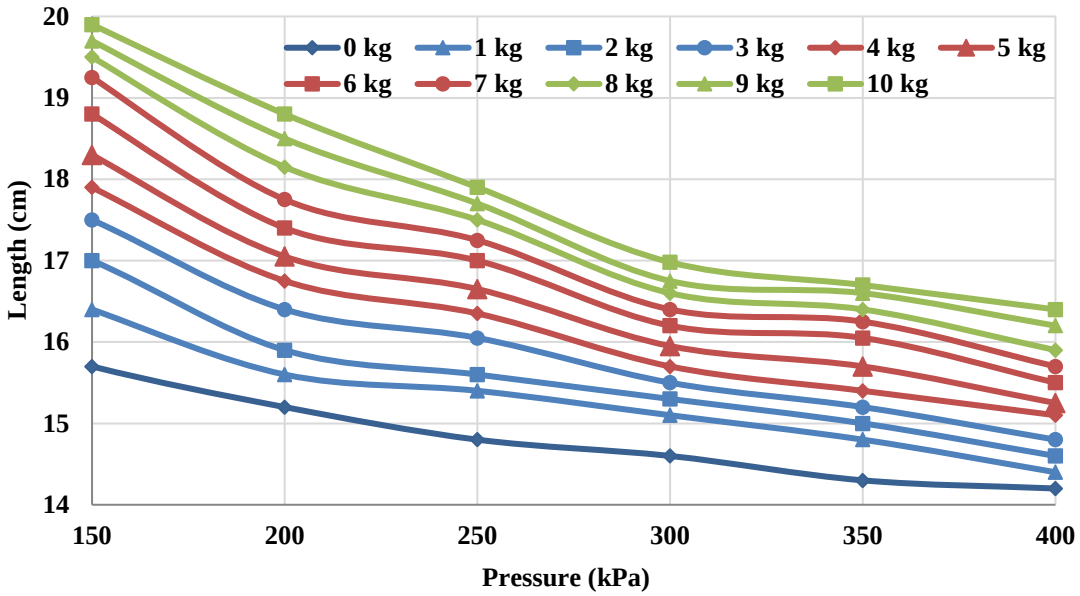

(a) 20 cm contractor PMA

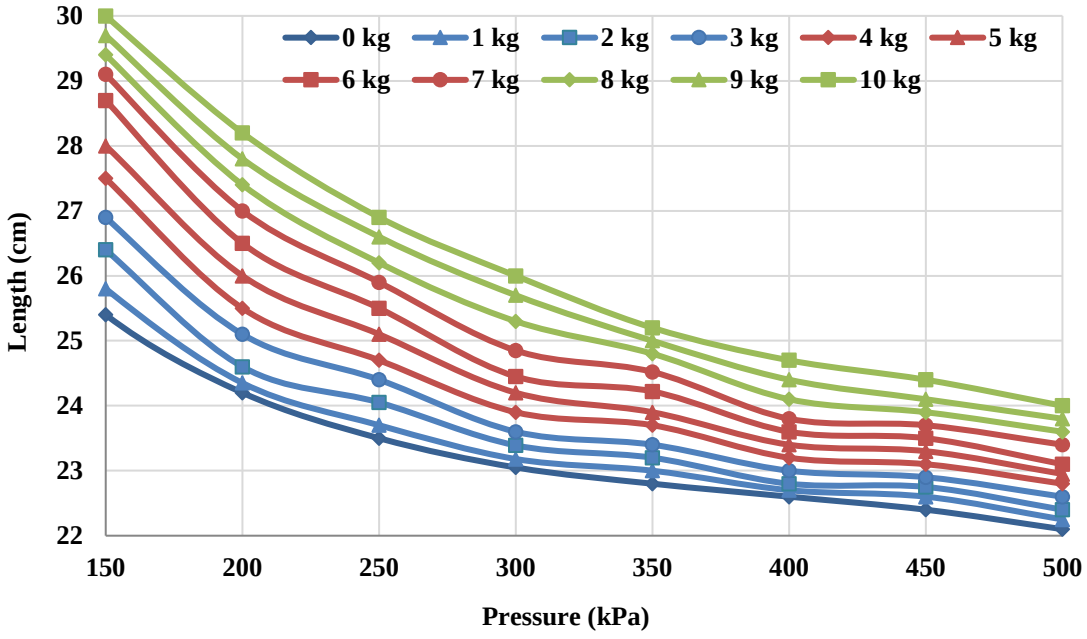

(b) 30 cm contractor PMA

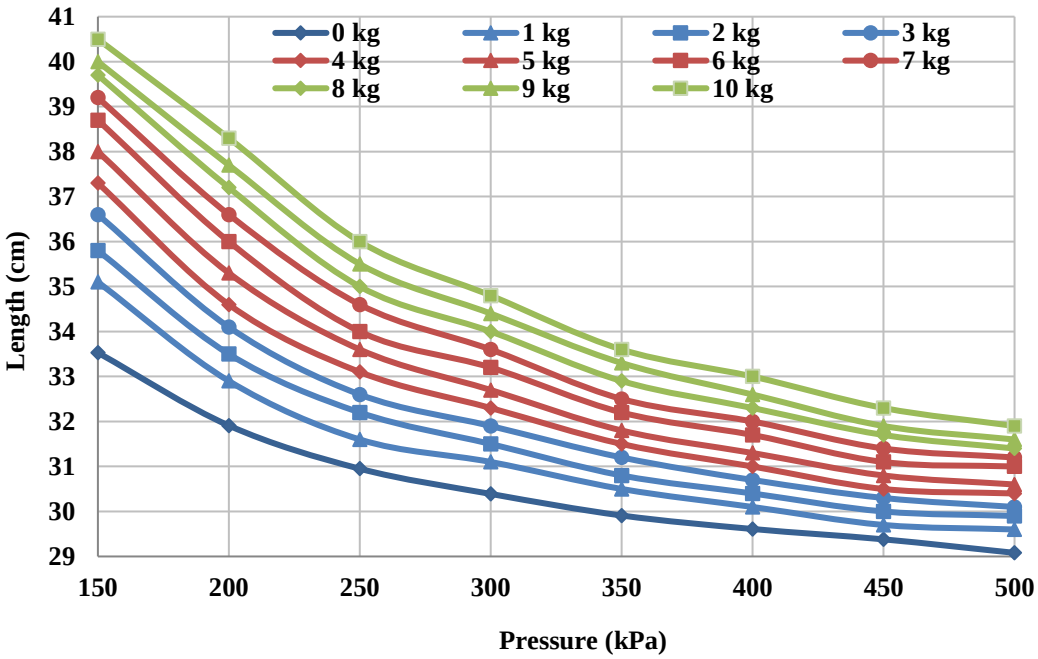

Figure 4.6 The length of the actuators against the pressure at fixed weight values.

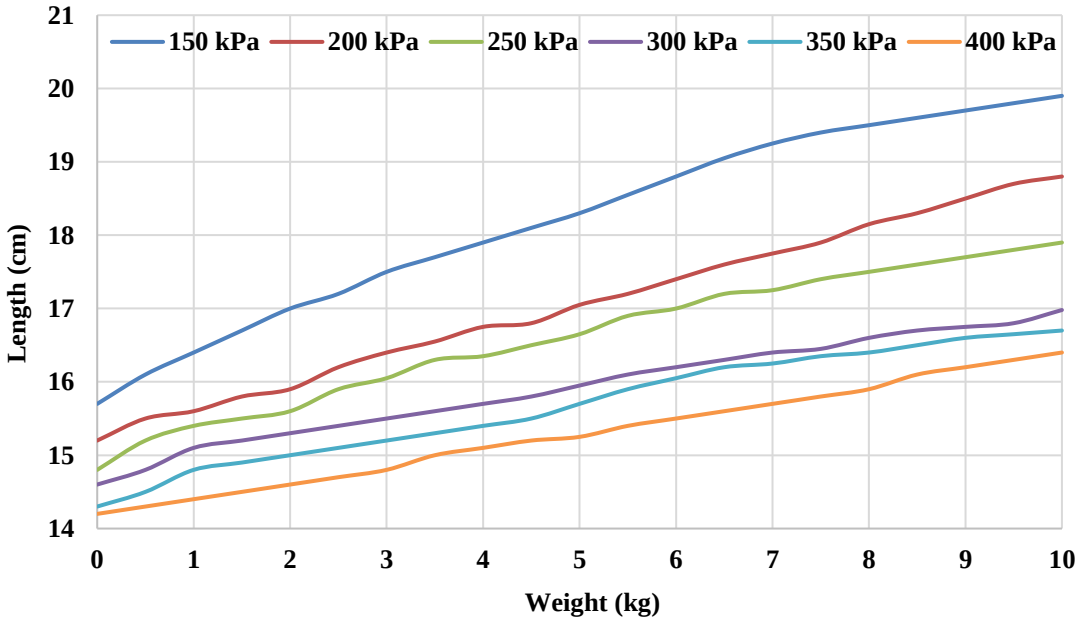

(a) 20 cm contractor PMA

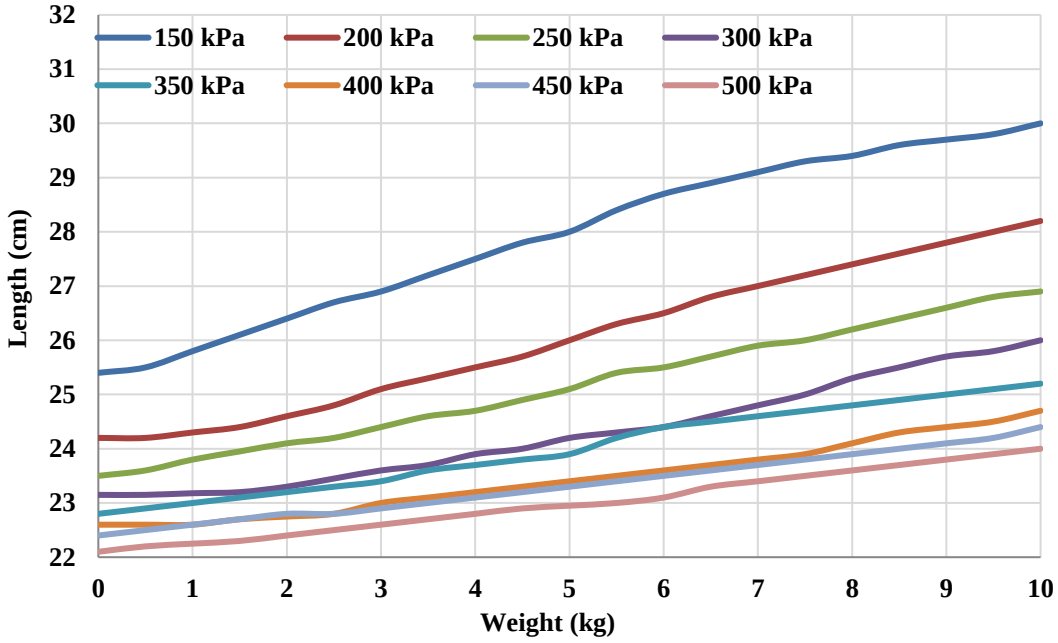

(b) 30 cm contractor PMA

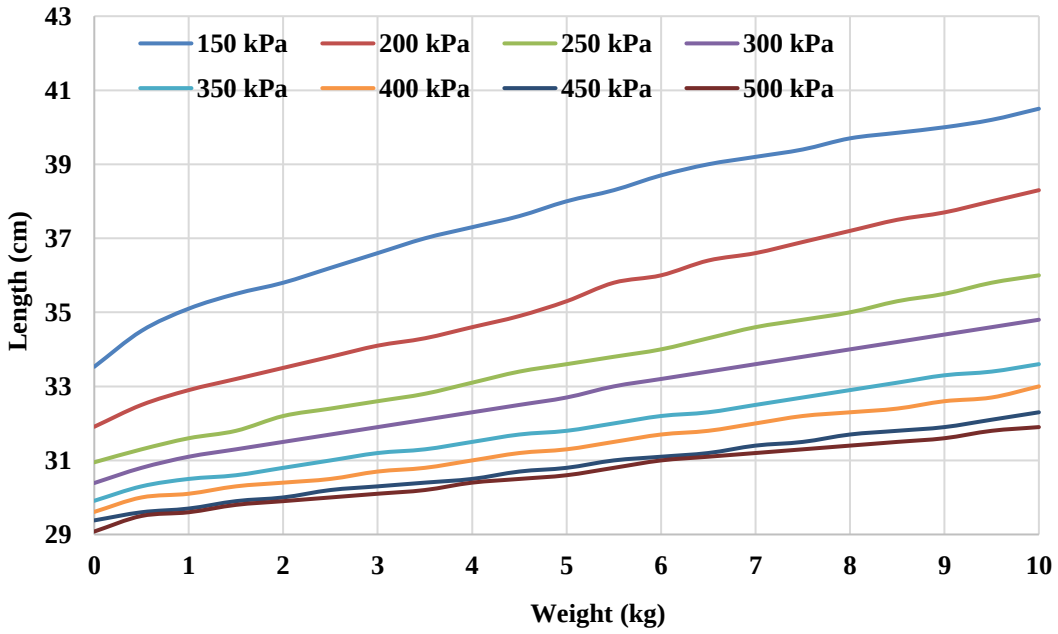

(c) 40 cm contractor PMA

Figure 4.7 The length of the actuators against the weight at fixed pressure values

Figure 4.6 shows that the loaded actuator has the same behaviour when it is pressurised but the contraction ratio at high load is less than its value at low load values. Meanwhile, Figure 4.7 illustrates that at a certain air pressure, the length of the actuator increases when the load increases. However, this increment keeps the contraction performance to the actuator and its value is small once the high pressure is applied.

Two of the Tondu and Lopez (2000) assumptions are described here; the cylindrical shape of the PMA and the contact between the rubber inner tube and the braided sleeve. Selecting the proper formula for the correction factor (2.25) depends on the design of the actuators. In this section the following formula is used for our muscles.

$$q(P) = 1 + 1e^{-0.5P} \tag{4.4}$$

A digital weight indicator is used to note the first force when the air pressure is slightly increased from 0 bar, in the whole experiment and for the all muscles, the first force value appears at P equal to 45 kPa. At this time the full contact between the inner tube and the braided sleeve occur. From this, the force of the air muscle could be assumed to be zero for the $P \leq 45$ kPa; and then subtract this value from P for $P \geq 45$. The modified force formula will be as following:

$$f = 0 \quad , \qquad 0 \leq p \leq 45 \text{ kPa}$$

$$f = \pi r_o^2 (p - 45)[\alpha(1 - q\varepsilon)^2 - \beta] \, , \; p \geq 45 \text{ kPa} \tag{4.5}$$

α and β are given in (23.a) and (23.b) respectively, and to explain the presented force formula, the 30 cm PMA is used as an example. Figure 4.8 shows the force against the pressure for the theoretical data (2.24) and the experimental data. From this figure there is a significant difference between the two plots, this variation due to the simplified assumptions. The modified formula is validated in Figure 4.9, which gives the important matching between the theoretical data of (4.5) and the same experimental results.

Figure 4.9 shows that the modification of the force formula brings the theoretical force plot back to be more matching with the actual experimental results.

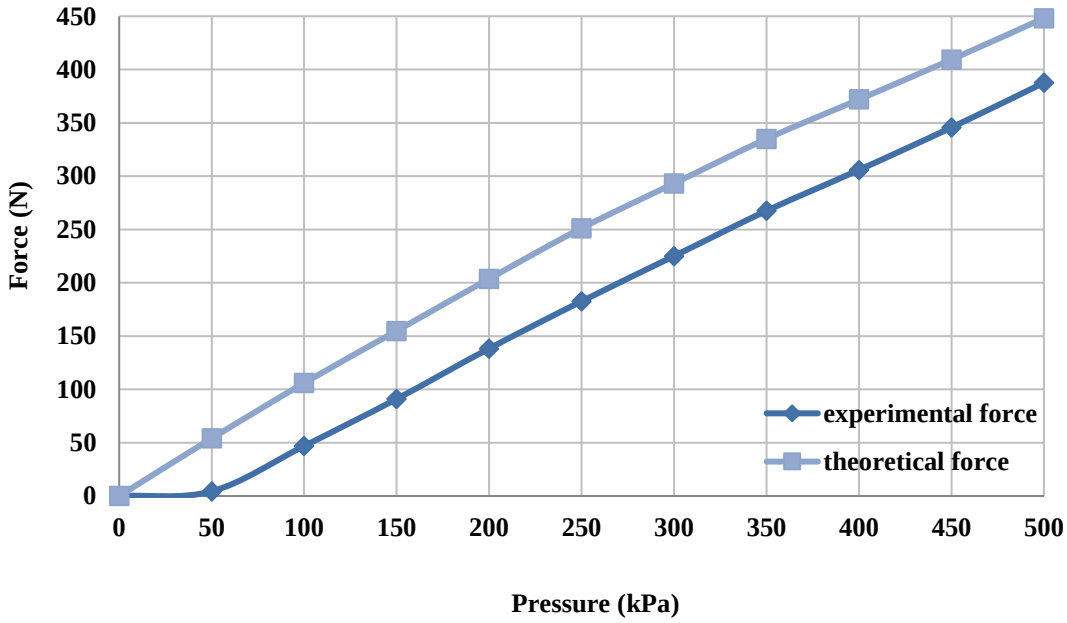

Figure 4.8 The experimental and theoretical force for the 30 cm PMA from (2.24).

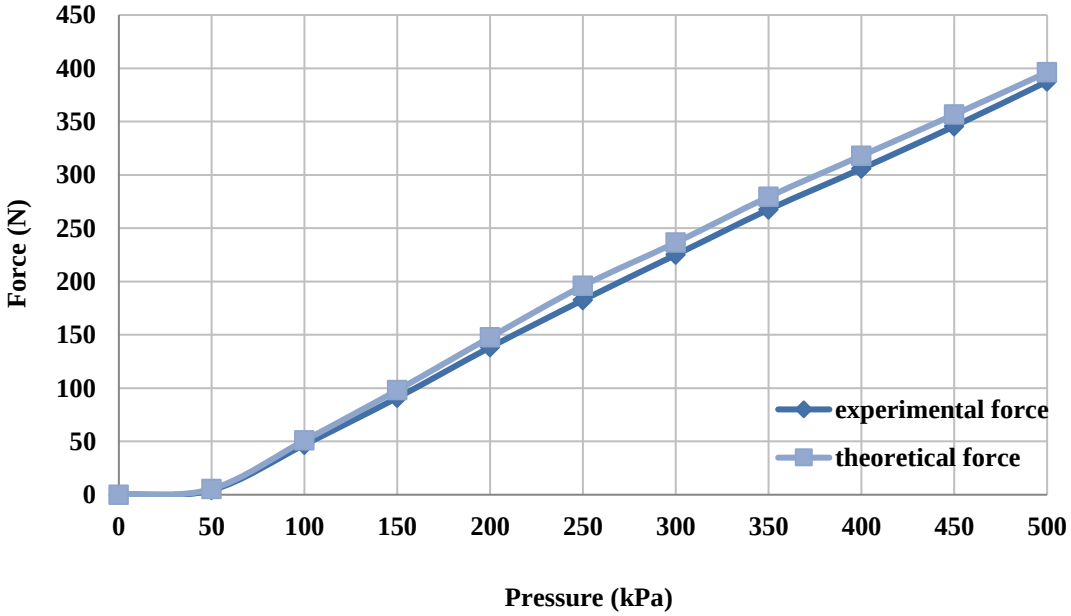

Figure 4.9 The experimental and presented theoretical force for the 30 cm PMA from (4.5).

4.2.2.3 Force of two PMAs in series

Experiments are done for two 30 cm PMAs constructed in series as in Figure 4.10 and the results are compared with the results of one 60 cm PMA as in Figure 4.11. Referring to (4.5), the force depends on the radius, the braided angle and the contraction ratio. Hence these parameters are chosen to be identical and the contraction ratio for a single 60 cm actuator is similar to the contraction ratio if two 30 cm actuators are in series, therefore the force is equivalent.

Figure 4.10 A photograph of 2-sections 60 cm PMA.

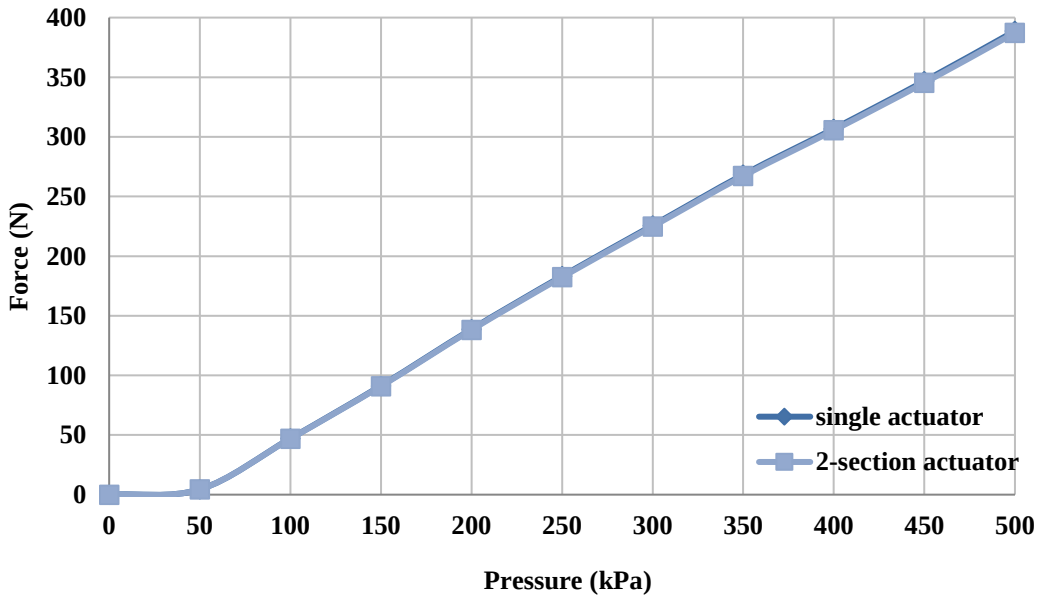

Figure 4.11 The experimental force for single 60 cm and 2-section 60 cm PMAs.

4.2.2.4 Force of the parallel contractor PMAs

Numerous structures could be designed as parallel PMAs. In this section, four identical 30 cm contractor PMAs are constructed as an arm with two ends as shown in Figure 4.12.

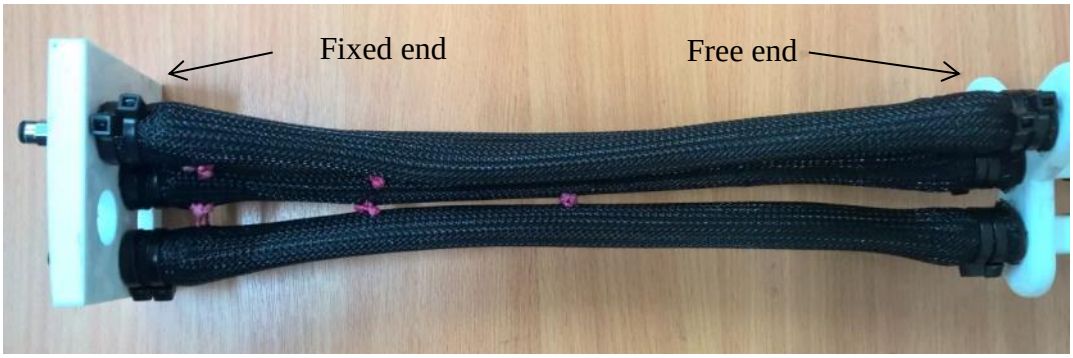

Figure 4.12 Four 30 cm PMAs laying in parallel.

The two ends are designed by Solidworks 2015 and they are printed by a 3D printer. The fixed and the free ends are shown in Figure 4.13.

(a) Fixed end (b) free end

Figure 4.13 Solidworks design of the arm two ends.

As shown in Figure 4.12, there is one muscle in the centre of the arm, and the other three are located as a 120^{o} displacement. The distance between each muscle's centre and the centre of the arm is 30mm. The same tests are applied to the arm for contraction and force characteristics. Figure 4.14 illustrates the change in length with respect to pressure

input, comparing individual muscles. The slight differences between the two plots are due to the friction between muscles. Furthermore, it is clear that the arm is acting as a single PMA for contraction characteristics whilst adding many features such as pending and multi positions of its end. With reference to (4.5), both input pressure and contraction ratio have an effect on the force of each PMA. Therefore, the expected force characteristics for the arm will be four times that of a single muscle.

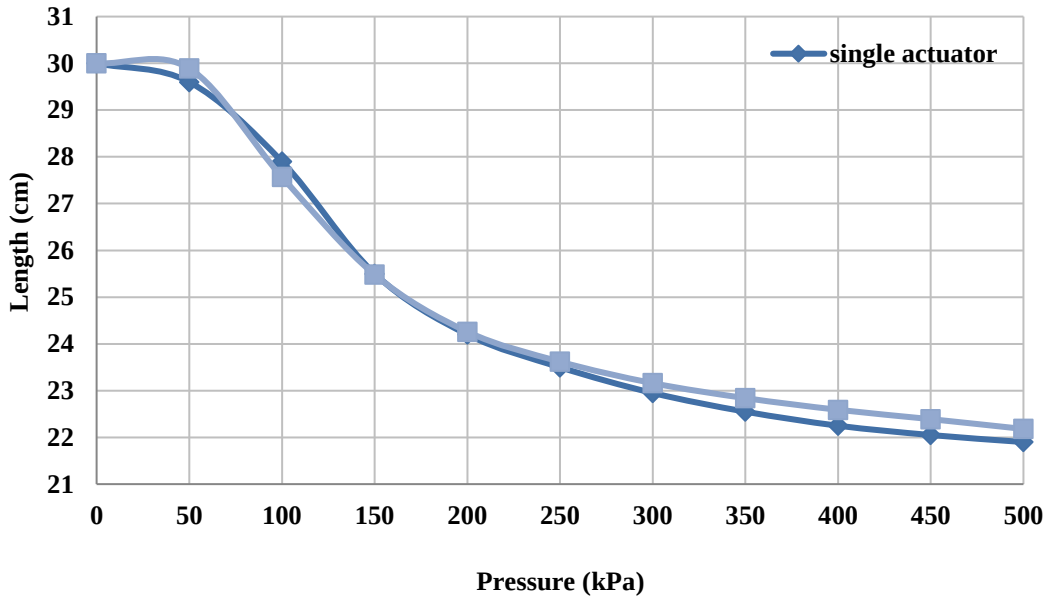

Figure 4.14 Length – pressure characteristic of single PMA and 4-PMAs in parallel.

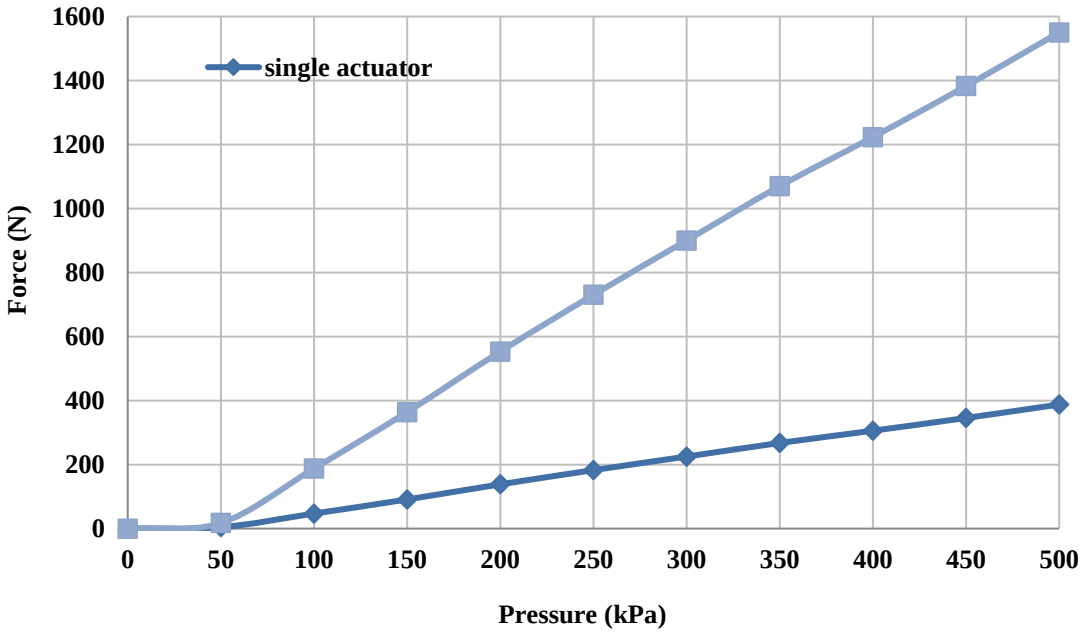

Figure 4.15 Force – pressure characteristic of single PMA and 4-PMAs in parallel

Figure 4.15 clearly explains this idea. Consequently, the force of multi PMAs in parallel can be calculated as in (4.6).

$$F = Kf \tag{4.6}$$

Where *F*: is the total force (N), *K*: is the number of parallel muscles, and *f*: is the force of single muscle (N).

4.2.2.5 Modelling of the arm free end angle

The pneumatic muscle actuator arm has a smooth bending behaviour when it is actuated by air (Godage, Branson, Guglielmino, Medrano-Cerda, & Caldwell, 2011). There have been a number of researches done on curvature (Godage, Branson, Guglielmino, & Caldwell, 2012a; Godage et al., 2011). In this section the free end angle of a 4-PMAs 30 cm arm shown in Figure 4.16 is studied as a function of actuated air pressure; no load and load states are considered.

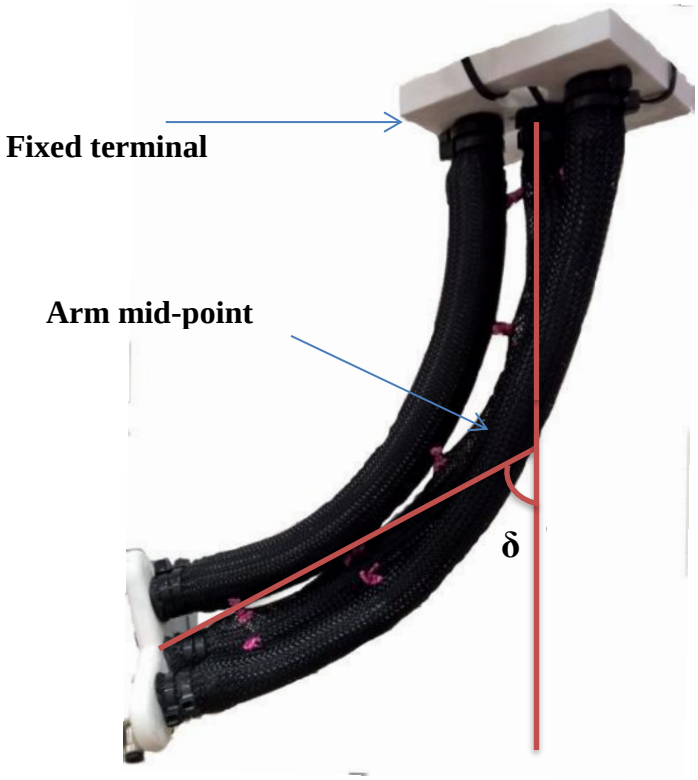

Figure 4.16 Pressurized arm at certain pressure with δ degree angle.

Firstly, the experiments are done by recording the initial angle of the free end δ, which is equal to zero degrees due to a straight-line arm. Secondly, all PMAs are actuated by 45 kPa, then the pressure is increased in the corner of one of the PMAs. The arm will then bend into another position, depending on the amount of P in the muscle; and δ is recorded each time. Figure 4.16 shows the contraction arm under actuation from certain pressure between 0-500 kPa.

The maximum angle value δ_{max} depends on the amount of the attached load w to the arm end. Table 4.3 below shows different maximum angles with different load values.

Table 4.3 maximum angle with different loads.

Load (Kg)	**Pressure (kPa)**	**δ_{max} (degree)**
0.0	380	84.333
0.1	340	84.0
0.2	380	75.5
0.3	340	66.0
0.4	300	57.0
0.5	280	47.0

Figure 4.17 illustrates the test data for δ as a function of actuated air pressure in one muscle within the arm at different loads, and it is clear that the maximum angle depends on the load value. From these records, (4.7) models the position angle with any load (w) as a function of pressure (p).

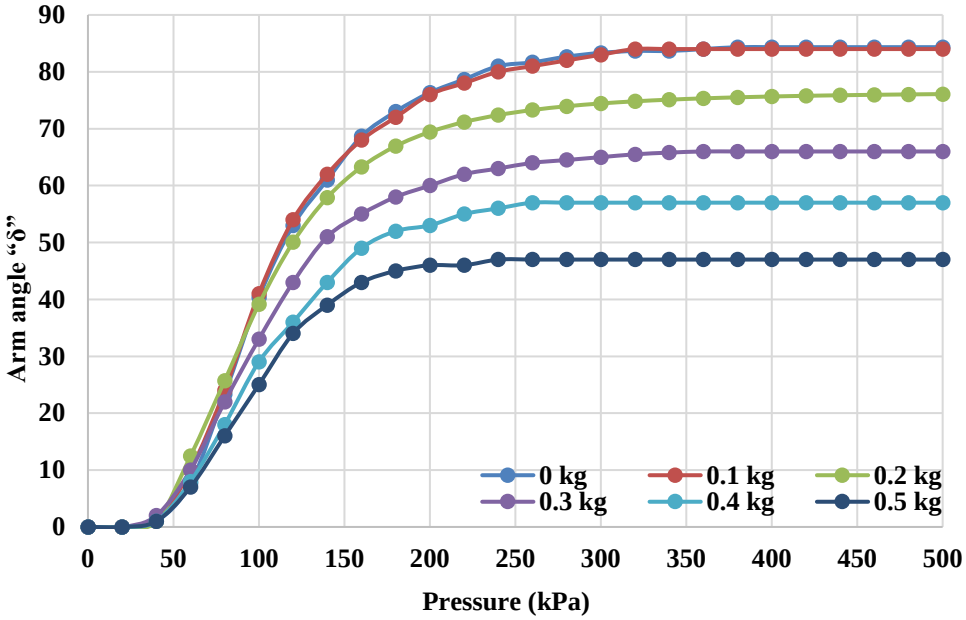

Figure 4.17 Experimental arm angle at multi load values.

$$\delta = a + \frac{b}{1+(\frac{p}{c})^d} \tag{4.7}$$

$$\begin{bmatrix} a \\ b \\ c \\ d \end{bmatrix} = \begin{bmatrix} 85.109 & 68.4155 & -915.4121 & 2145.117 & -1779.245 \\ -86.195 & -69.7074 & 940.9097 & -2210.206 & 1837.185 \\ 1.047706 & 0.1331478 & -4.69328 & 18.98427 & -21.75253 \\ 3.459321 & 0.7990463 & -24.19429 & 84.25137 & -67.01067 \end{bmatrix} \begin{bmatrix} 1 \\ w \\ w^2 \\ w^3 \\ w^4 \end{bmatrix} \tag{4.8}$$

Comparisons between experimental and theoretical data are given in Figure 4.18 for two states (no load and 0.3 Kg) using (4.7) and (4.8). The figure shows that the slight difference between experimental and theoretical plots can be ignored for *P* equal or more than 2.6 bar.

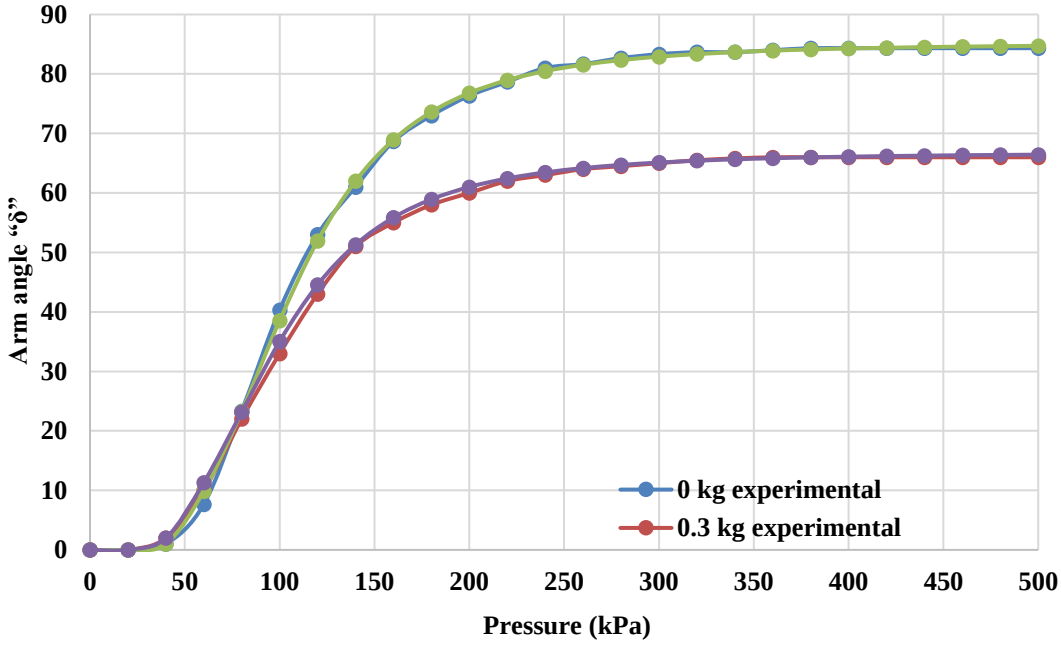

Figure 4.18 Experimental and theoretical angle values.

4.2.3 Structure-based models for the contractor muscle actuator

In recent years there has been numerous of research done to mathematically model the PMAs. The work was done to relate both the air pressure and the length of the PMA to the generated pulling force of contraction muscles. Numerous factors have major effects on the model, such as the properties of the material used in PMA construction, length, diameter, braided angle and air pressure. Understanding the relationship between these factors leads to constructing accurate models, especially for control requirements (Kelasidi et al., 2011).

4.2.3.1 Contraction force based on structure of the actuator

Referring to Figure 2.10 and under the virtual work theory, the input work (W_{in}) for the McKibben's muscle under air pressure supply is:

$$dW_{in} = \int_{s_i}(P - P_0)dl_i.ds_i = (P - P_0)\int_{s_i} dl_i.ds_i = P_g dV \qquad (4.9)$$

Where s_i is the total inner surface, dl_i is the inner surface displacement, and dV is the volume change. The output work (W_{out}) occurs when the actuator shortens with the volume change.

$$dW_{in} = -FdL \tag{4.10}$$

Where F is the contractor (pulling) force and *L* is the axial (actuator) length. Assuming the lossless actuator has no storage energy, the input work must equal the output work as assumed before, then:

$$dW_{out} = dW_{in} \tag{4.11}$$

thus,

$$-F\,dL = P_g dV \tag{4.12}$$

or,

$$F = -P_g \frac{dV}{dL} \tag{4.13}$$

The authors are assumed that the braided strand *b* length fixed during the pressurising process, and the volume of the actuator under cylindrical shape assumption is:

$$V = \frac{1}{4}\,\pi D^2 L \tag{4.14}$$

Referring to the assumption above for the Chou and Hannaford (1996), Tondu and Lopez (2000) model, the type of material and its thickness, and as a result its stiffness plays a major factor in the force production. For that reason, the volume of the actuator is redefined as follows:

$$V = \frac{1}{4}\,\pi D_{in}^2 L \tag{4.15}$$

And

$$D_{in} = D_{out} - Th_D \tag{4.16}$$

Where *V* is the volume in (m^3), D_{in} is the inner diameter in (m), *L* is the length of the PMA in (m), D_{out} is the outer diameter in (m) and Th_D is twice the value of both the inner rubber tube and the braided sleeve thickness. Figure 4.19 shows the cross section of the actuator structure.

From (4.15) and (4.16) the volume of the PMA is less than the volume of the actuator in (4.14). Moreover, the w_{in} will be less, and depends on the thickness of the rubber tube and the braided sleeve.

Increasing the rubber tube stiffness leads to increasing its resistance and the w_{out} will decrease, while the generated pulling force affects it longitudinally. The resistance force of the actuator will be defined as follows:

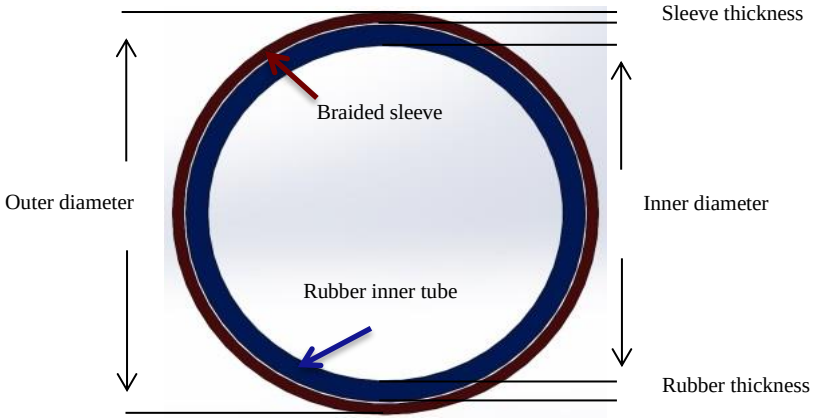

Figure 4.19 The cross section of the PMA structure.

$$f_{rs} = \frac{s_r A_{in}}{\Delta L} \tag{4.17}$$

Where f_{rs} is the resistance force (N), s_r is the stiffness (N/m) of the rubber tube, A_{in} (m^2) is the inner area of the rubber cross section and ΔL (m) is the change of the actuator length at each pressure step.

The losses force due to a contactless between the surfaces of the rubber tube and the braided sleeve is found experimentally as shown in (4.18).

$$f_c = \frac{0.641}{\Delta L} \tag{4.18}$$

Under the principle of virtual work, the pulling force F can be defined as follows:

$$F = \frac{P_g \Delta V}{\Delta L} - f_{rs} - f_c \tag{4.19}$$

Where ΔV represents the volume change between the initial and new value each time the pressure is changed.

To validate this equation, a 20 cm contraction actuator has been built to the specifications shown in Table 4.4.

Table 4.4 The initial specifications of a 20 cm contraction PMA.

L_0 (m)	Rubber thickness (m)	Braided thickness (m)	Inner diameter (m)	Rubber stiffness (N/m)
0.2	1.1×10^{-3}	0.5×10^{-3}	12×10^{-3}	363.33

The actuator is pressurised from zero to 500 kPa by 50 kPa steps; at each step the length of the PMA is recorded. From (4.17), the resistance force of the inner rubber tube is illustrated in Figure 4.20, as a function of the input pressure.

Figure 4.20 shows that the resistance force is very high at low-pressure values (P_g< 50 kPa) and its value has been decreased dramatically at P=50 kPa.

The contactless losses at each air pressure step are also calculated and are illustrated against the pressure in Figure 4.21. The lose value at P < 50 kPa is significantly high.

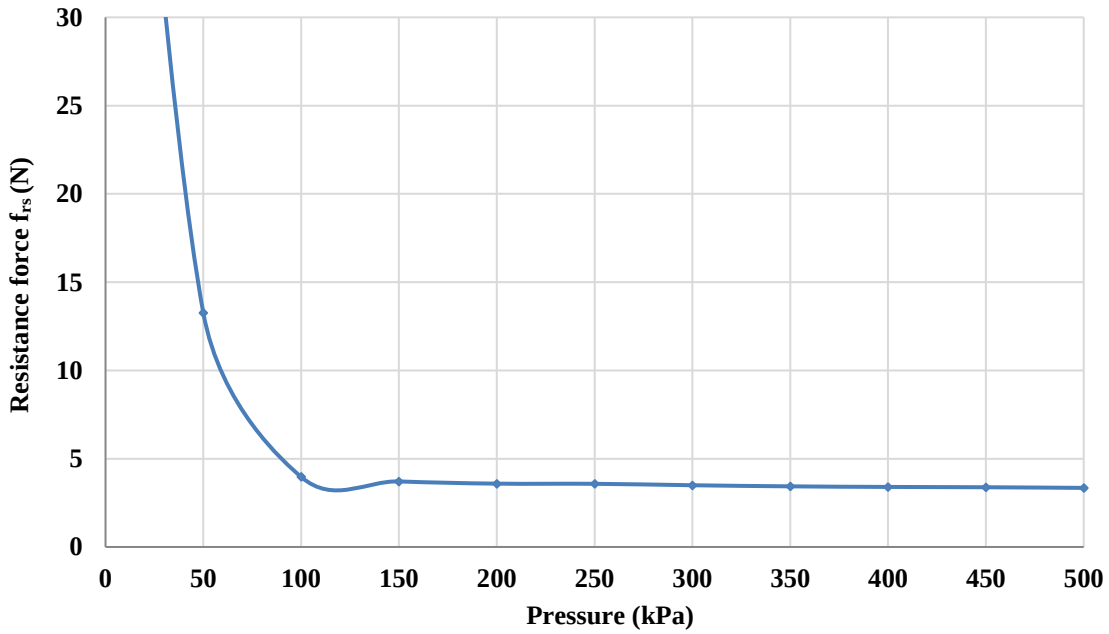

Figure 4.20 The resistance force of the rubber tube against air pressure.

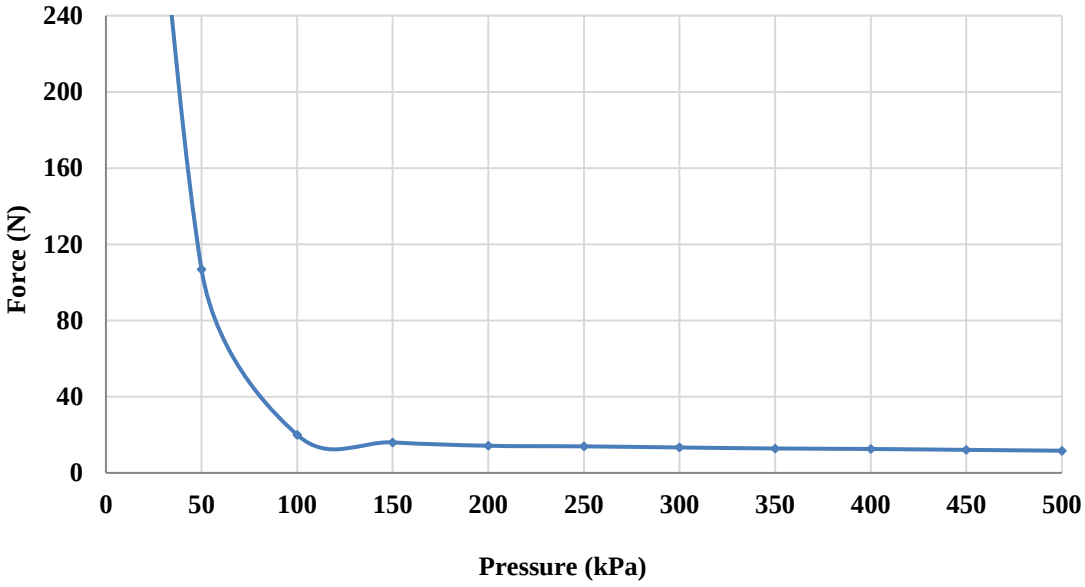

Figure 4.21 The contact less losses between the rubber tube and the braided sleeve against air pressure

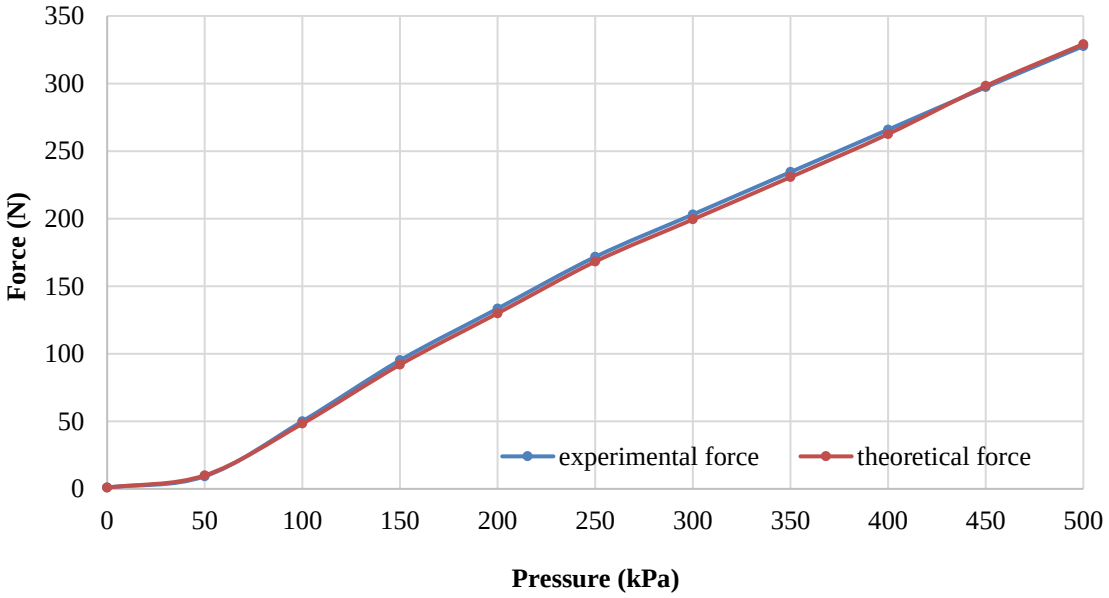

Figure 4.22 The experimental and theoretical force of the PMA against air pressure.

Figure 4.22 shows the force of both the experimental and theoretical pulling force and it is explained that there is a substantial matching between them.

Since the value of f_{rs} and f_c is high at $P_g < 50$ kPa, the pulling force F cannot be produced, and the generated force increases when the opposite forces are decreased.

To ensure that the (4.19) can fit for all contraction actuators, another actuator for the following specification is constructed (Table 4.5).

Table 4.5 The initial specifications of a high stiffness, 20 cm contraction PMA.

L_0 (m)	Rubber thickness (m)	Braided thickness (m)	Inner diameter (m)	Rubber stiffness (N/m)
0.2	2.2×10^{-3}	0.5×10^{-3}	12×10^{-3}	1090

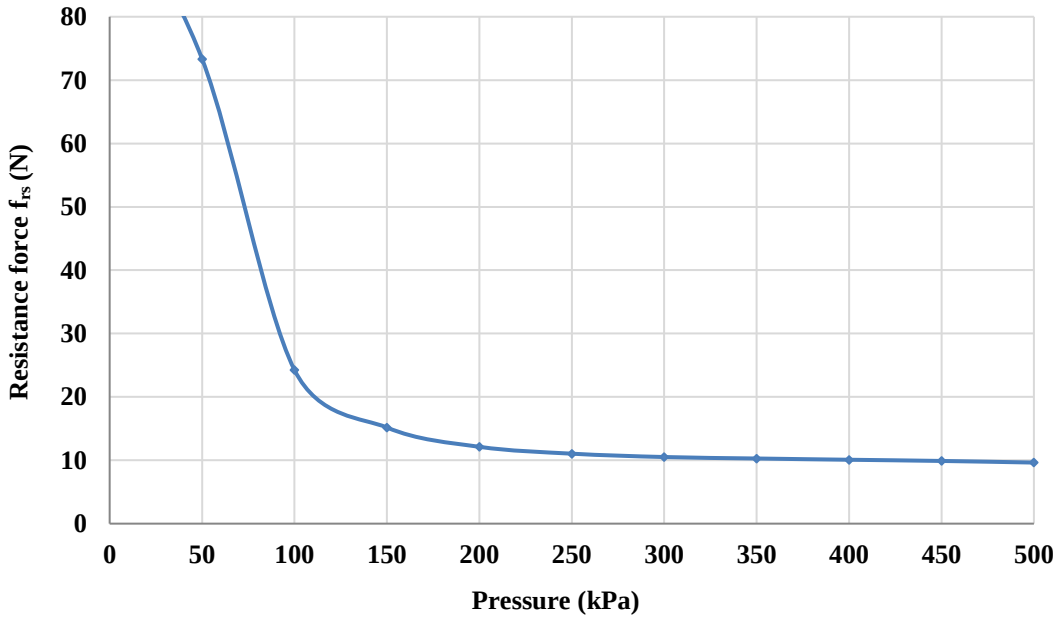

Figure 4.23 The resistance force of the high stiffness rubber tube against air pressure.

The contactless losses f_c for this muscle has the same values as the pressure seen in Figure 4.22, while the resistance force f_{rs} is different because it is dependent on the rubber's stiffness. Figure 4.23 shows the resistance force against the air pressure for the second actuator.

The force of this actuator is higher than the force of the first PMA while the losses are increased because the stiffness is increased.

Increasing the stiffness of the rubber leads to increasing the resistive force, on the other hand it decreases the contraction ratio ε and as a result the input work will be higher.

The two PMAs above are made from the same rubber tube diameter but with different stiffness values. Therefore, to further verification, an actuator is made to the specifications listed in Table 4.6.

Table 4.6 The initial specifications of the new contraction PMA.

L_0 (m)	Rubber thickness (m)	Braided thickness (m)	Inner diameter (m)	Rubber stiffness(N/m)
0.2	1.1×10^{-3}	0.5×10^{-3}	26.5×10^{-3}	545

The losses force a cause to contactless has almost the same values because the material types are the same for both the rubber and the sleeve. Whereas, the resistance force is different because of the differences in diameter and stiffness of the actuators. From (4.17) the f_{rs} can be given as in Figure 4.24. The mean square error (MSE) is listed in Table 4.7 and it gives the error between the experimental and the proposed force formula to the actuators under study for the pressure steps from 0 to 500 kPa.

Table 4.7 The MSE of the three actuators.

Actuator	MSE
1	7.23
2	9.31
3	22.68

Figure 4.22 and the table. 4.13 verify that the proposed force formula in (4.19) can be used for a variety of actuators, which differ in rubber stiffness and inner diameter.

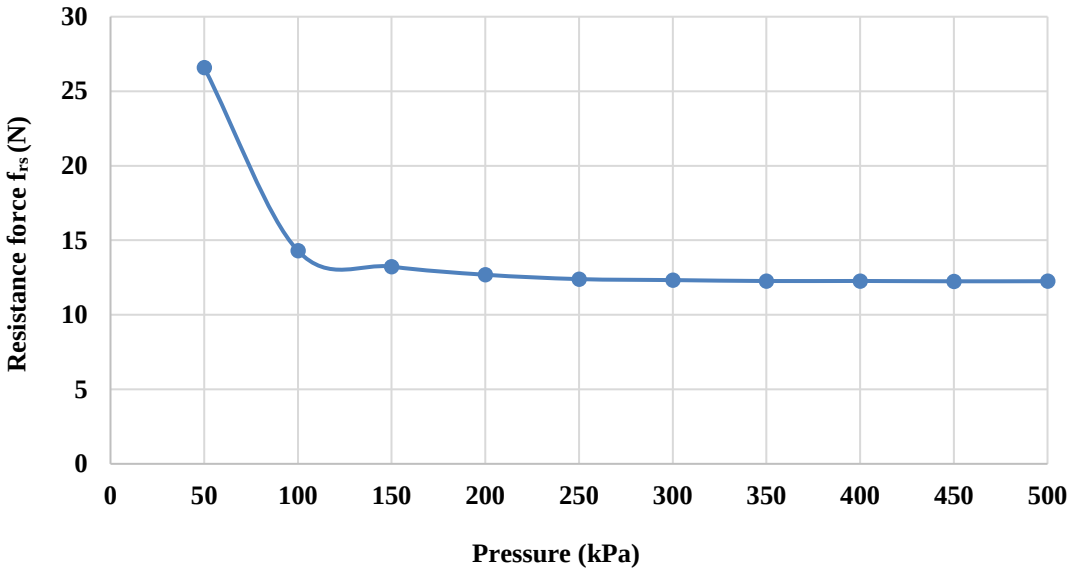

Figure 4.24 The resistance force of the third actuator against air pressure.

4.2.3.2 Structure-based length formula for contraction PMAs

The length of the contraction PMA decreases while the applied pressure is raised. However, the contraction ratio ε is not fixed for all actuators and it depends on the type of inner rubber tube, the diameter of the PMA and the maximum diameter of the braided sleeve.

To formulate an efficient length formula that is able to track the actual length of the PMA, the initial length L_0, initial diameter D_0 and the rubber stiffness must be considered. While the contraction ratio increases as a pressure increase, and the highest rubber stiffness is the lowest stretchable ability, then:

$$L \; \alpha \; \frac{1}{P} \tag{4.20}$$

$$L \; \alpha \; s_r \tag{4.21}$$

And to avoid divided by zero, an exponential form will consider as following:

$$L = L_0 - \frac{aL_0}{(1+e^{-b\frac{D_o}{sr}P_g})^{6.214}} \tag{4.22}$$

Where (a) and (b) are constants for a fixed structure and the expression to find them depend on the diameter and stiffness of the PMA.

$$\begin{bmatrix} a \\ b \end{bmatrix} = \begin{bmatrix} 0.0126 & 14882 & -2 \times 10^{8} \\ 2 \times 10^{-5} & -0.5375 & 11777 \end{bmatrix} \begin{bmatrix} 1 \\ \left(\frac{D_0}{s_r}\right) \\ \left(\frac{D_0^2}{s_r^2}\right) \end{bmatrix} \tag{4.23}$$

To improve the efficiency of this equation, four actuators are made to the specifications listed in Table 4.8.

Table 4.8 The specifications of the contraction PMAs.

PMA	L_0 (m)	Actuator diameter (m)	Rubber stiffness (N/m)
A	0.2	0.0152	363.33
B	0.2	0.0174	1090
C	0.2	0.0297	545
D	0.3	0.0152	363.33

Both the experimental and the theoretical length data for the muscle in table 4.14 are shown in Figure 4.25.

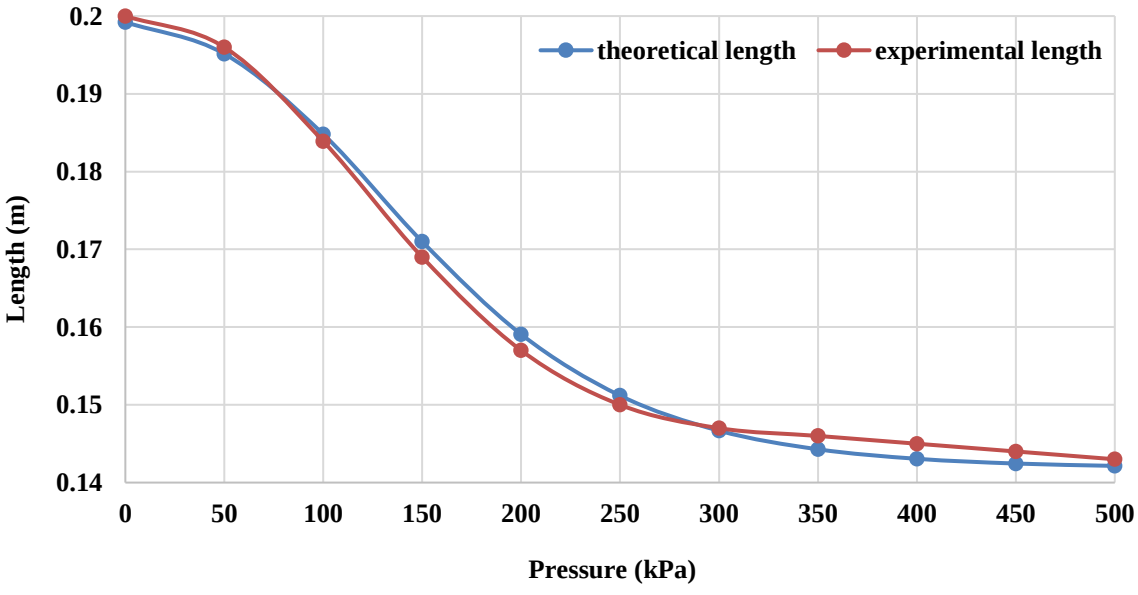

(A)

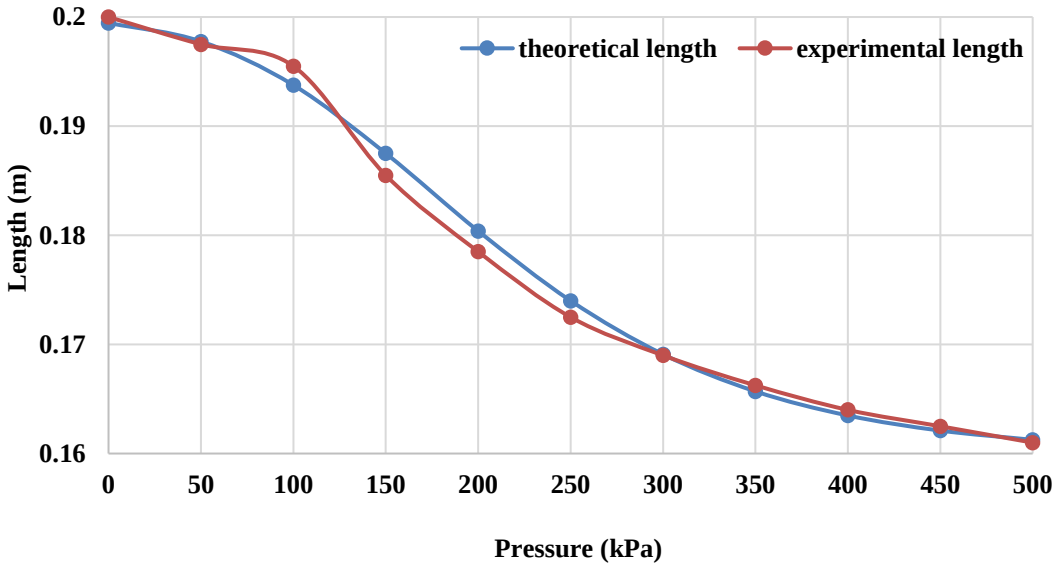
theoretical length
experimental length
Length (m)
0.2
0.19
0.18
0.17
0.16
0
50
100
150
200
250
300
350
400
450
500
Pressure (kPa)

(B)

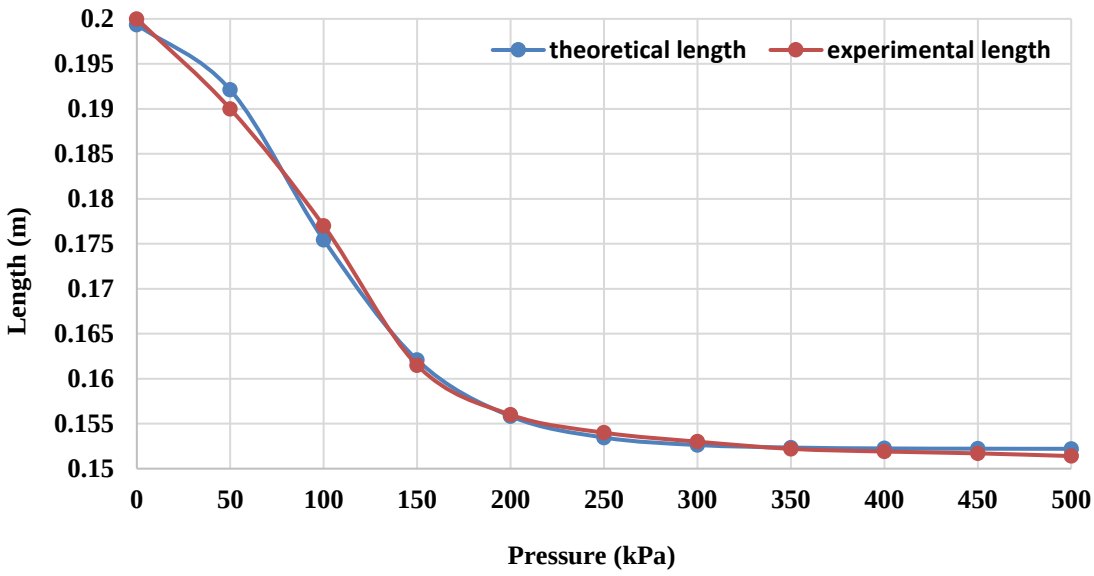
theoretical length
experimental length
Length (m)
0.2
0.195
0.19
0.185
0.18
0.175
0.17
0.165
0.16
0.155
0.15
0
50
100
150
200
250
300
350
400
450
500
Pressure (kPa)

(C)

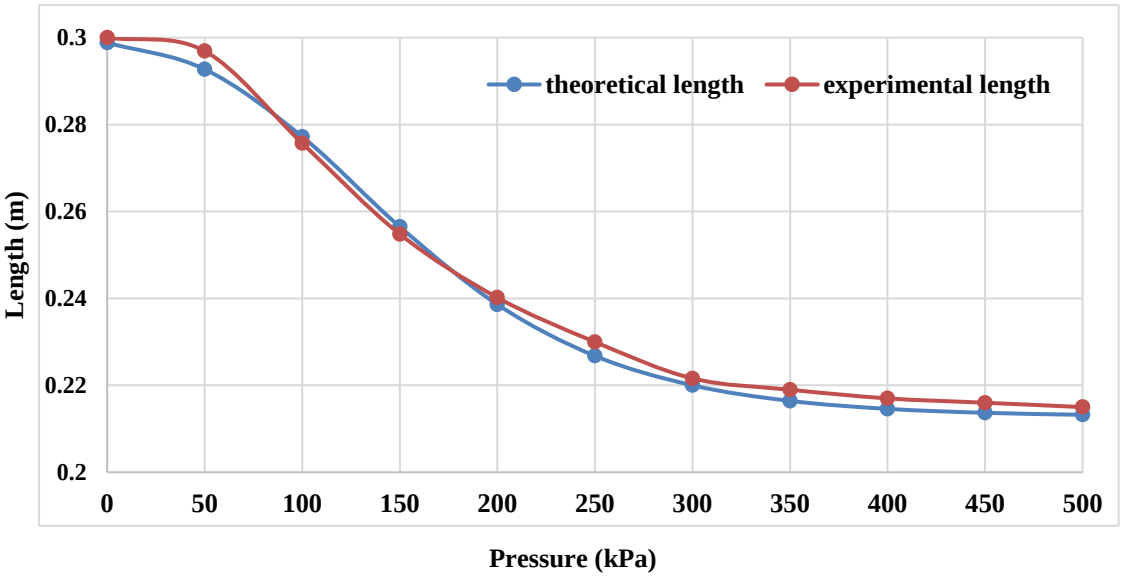

(D)

Figure 4.25 The experimental and theoretical length of the PMAs are listed in table 4.14.

While the experimental length is recorded as an average for the length during contraction and elongation, the small deviation is remaining inside the whole curve.

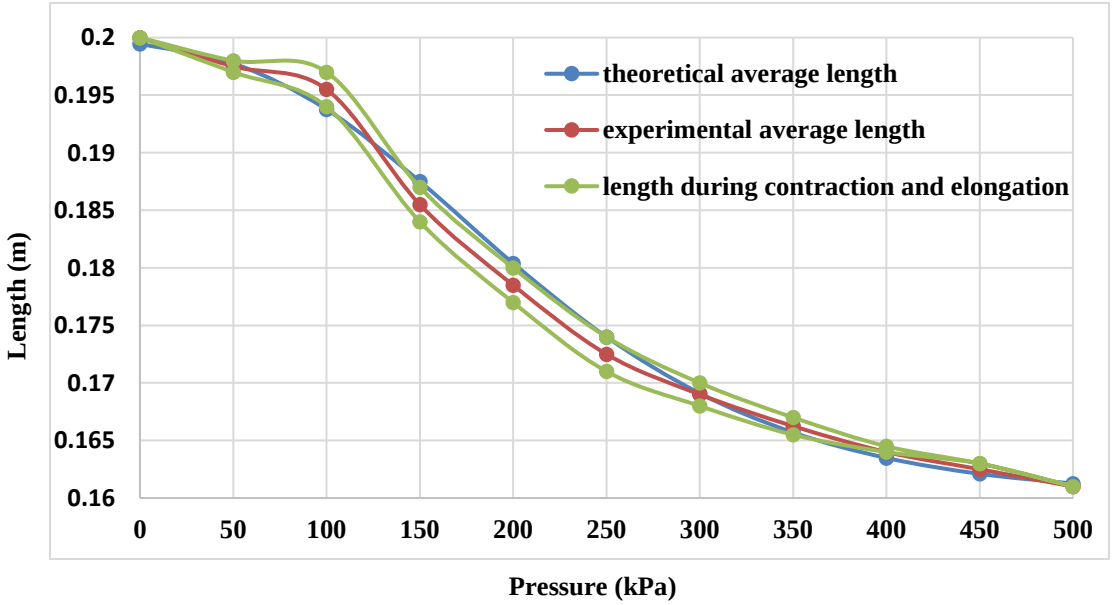

Figure 4.26 the length of the actuator B with contraction and elongation curve.

As an example, Figure 4.26 shows the length of the actuator B with a contraction and elongation curve.

The length formula in (4.23) can be used in (4.19) at any air pressure value to detect the contractor force. Furthermore, the position of a single actuator can be defined at any time for all PMAs under their structure specification.

Sárosi, Bíró, Németh, and Cveticanin (2015) argue that the maximum contraction ratio is about 25%. However, from (4.23) and as illustrated in Figure 4.25, the contraction ratio depends on the stiffness and diameter of the actuator and is not fixed. Table 4.9 lists the contraction ratio of the actuators (A, B, C and D), which are according to the specifications given in Table 4.8.

Table 4.9 The contraction ratio of the PMAs.

PMA	**contraction ratio (ε)**
A	29 %
B	19.5 %
C	24.3 %
D	28.6 %

Since (4.23) is derived from fitting the length of the actuator at no-load, Table 4.10 lists the MSE at different load values for the 20 cm contraction PMA fit for centimetres for 11 steps of pressure from 0 to 500 kPa.

Table 4.10 The MSE of the 20 cm contraction ratio PMA at different load values.

Load (kg)	**MSE**
0.0	0.0198
0.5	0.1405
1.0	0.1995
2.0	0.2363
3.0	0.431
4.0	0.9697

4.2.3.3 The Stiffness of the contraction PMA

One of the major advantages of the PMA is the variable stiffness performance (Vanderborght et al., 2013). The stiffness is defined as the length change due to changes in applied force.

From (4.19) and (4.23) the stiffness can be defined as in (4.24).

$$s = \frac{P_g \, \Delta V}{\Delta L^2} - \frac{f_{rs}}{\Delta L} - \frac{f_r}{\Delta L} \tag{4.24}$$

While both the length and the force of the actuator depend on the structure of the PMA, the stiffness (s) is determined by the structure of the PMA correspondingly. Figure 4.27 below describes the stiffness for the actuators (A, B and C) in table 4.14 as a function of air pressure.

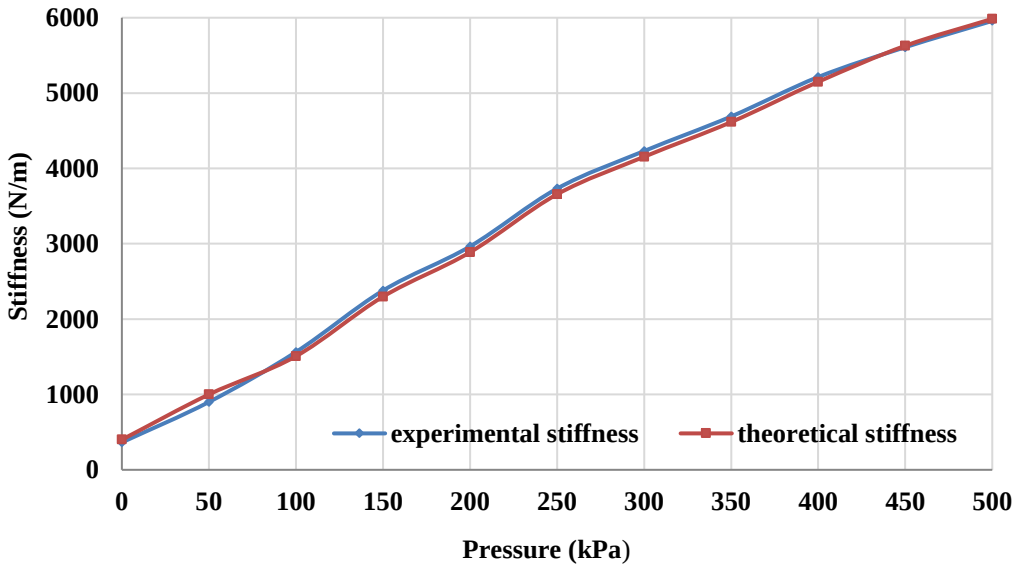

(A)

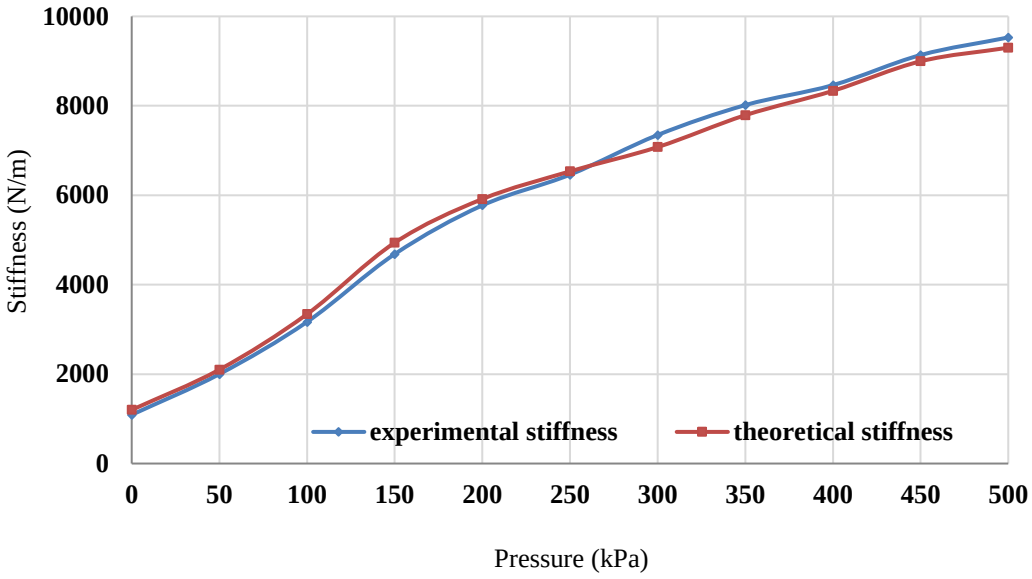

(B)

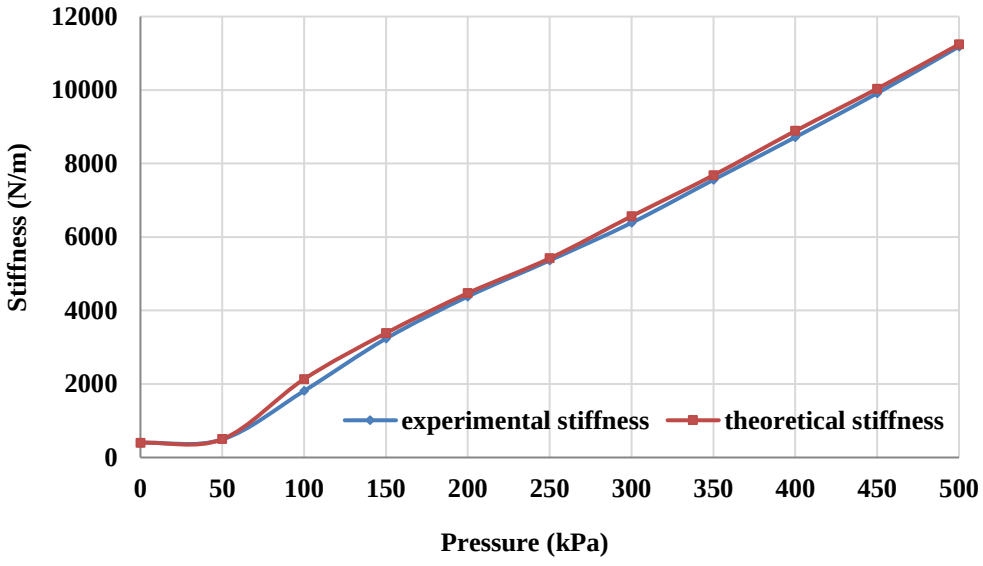

(C)

Figure 4.27 The experimental and theoretical stiffness of the three different PMAs.

4.3 Extensor pneumatic muscle actuator

4.3.1 Construction

A similar procedure is used to construct the extensor actuator as above in **Error! R eference source not found.**, the only difference is in **Error! Reference source not found.**.h. In this section, the length of the braided sleeve is triable the length of the inner tube to set the braided angle more than the threshold value. The photograph of the 30 cm extensor PMA is shown.

4.3.2 Practical experiments

Three actuators are designed for lengths 20 cm, 30 cm and 40 cm with about 3.0 cm in diameter. The pressure is increased from 0-500 kPa by a manual valve. Table 4.11 gives the specification of the PMAs under study.

Table 4.11 Specification of the extensor PMAs under study.

Nominal length L_0 (cm)	Diameter D (cm)	Braided angle θ (degree)
20	3.0	70.21
30	3.0	71.51
40	3.0	72.43

4.3.2.1 Length change experiment

Air pressure is applied from 0-500 kPa and then reduced to 0 bar by 50 kPa steps at the same time for all actuators. The results are listed in Table A.7, Table A.8, and Table A.9. The results are illustrated in Figure 4.28.a-c that shows the opposite behaviour of the contractor actuators. The length of the extensor muscles increases whilst the air pressure increases and vice versa. However, these types of PMAs have similar nonlinearities and hysteresis performance. Moreover, the extension ratio reaches to 50% or more, depends on its construction.

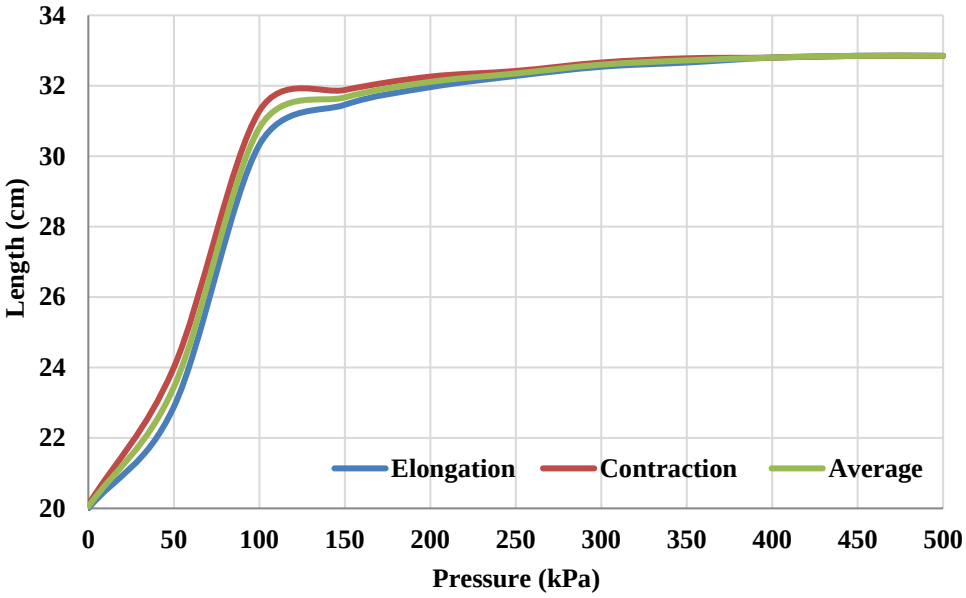
34
32
30
28
26
24
22
20
Length (cm)
0
50
100
150
200
250
300
350
400
450
500
Pressure (kPa)
Elongation
Contraction
Average

(a)

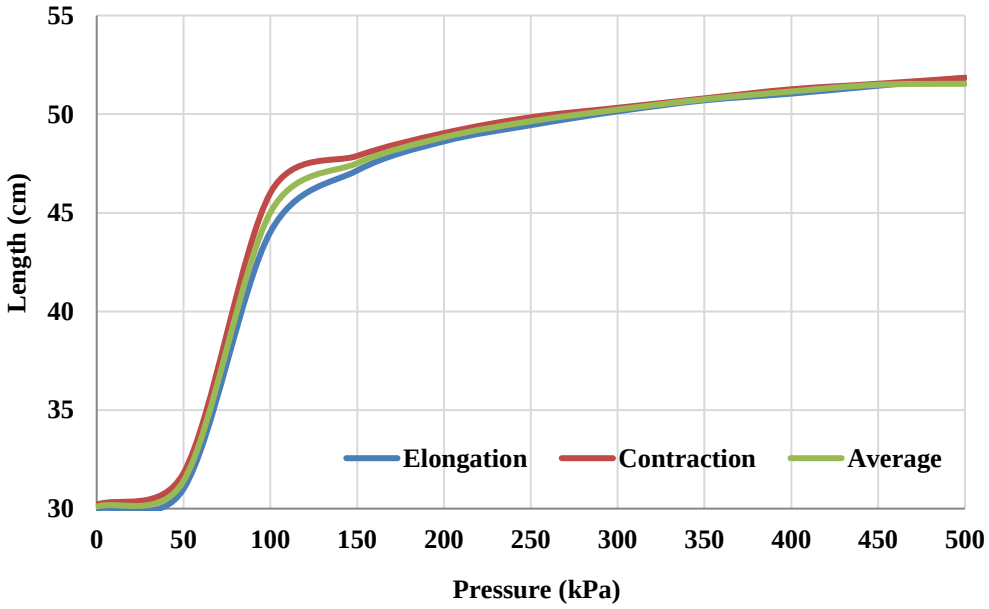
55
50
45
40
35
30
Length (cm)
0
50
100
150
200
250
300
350
400
450
500
Pressure (kPa)
Elongation
Contraction
Average

(b)

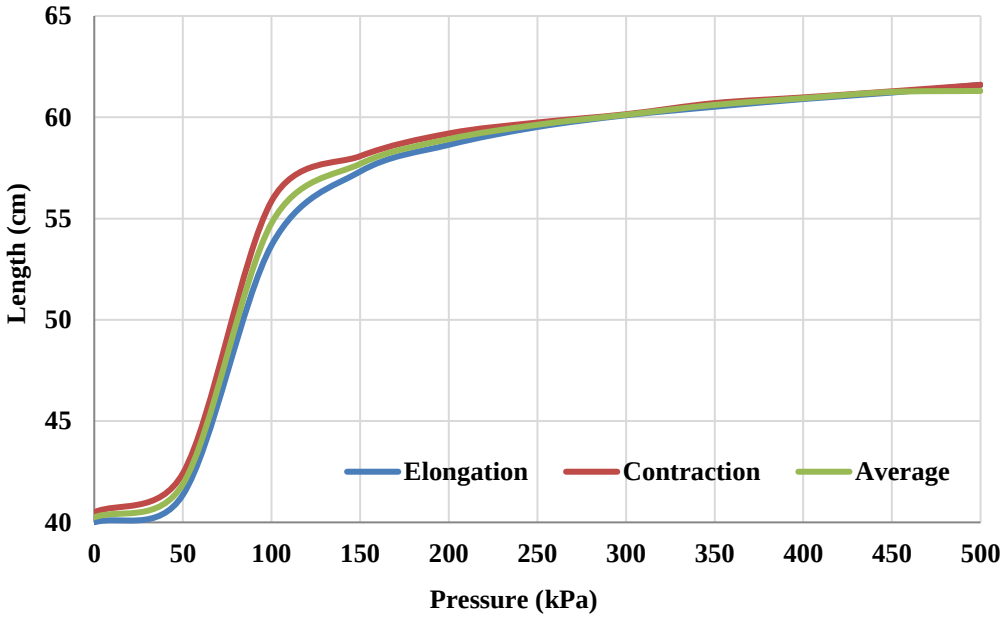

(c)

Figure 4.28 Plots of actuator length change against air pressure.

(a) 20 cm PMA, (b) 30 cm PMA, (c) 40 cm PMA

From the data above, a mathematical formula is derived to model the length $\acute{L}$ with respect to P and L_0. A similar procedure to the contraction length formula is used here to model the extension length. (4.7) gives the relationship between the actuator length and the pressure input to any muscle nominal length.

$$L = a - \frac{b}{1+(\frac{P}{c})^d} + 0.0009L_0P^2$$

$$\begin{bmatrix} a \\ b \\ c \\ d \end{bmatrix} = \begin{bmatrix} 0.2281 & 0.084598 & -0.0013189 \\ -0.94047 & 0.095934 & -0.0014863 \\ 0.014934 & 0.0012083 & -0.000026277 \\ 0.2080174 & -0.0032043 & 0.0000106189 \end{bmatrix} \begin{bmatrix} L_0 \\ L_0^2 \\ L_0^3 \end{bmatrix} \quad (4.7)$$

Figure 4.29 shows the experimental and the theoretical length against the pressure for the three actuators.

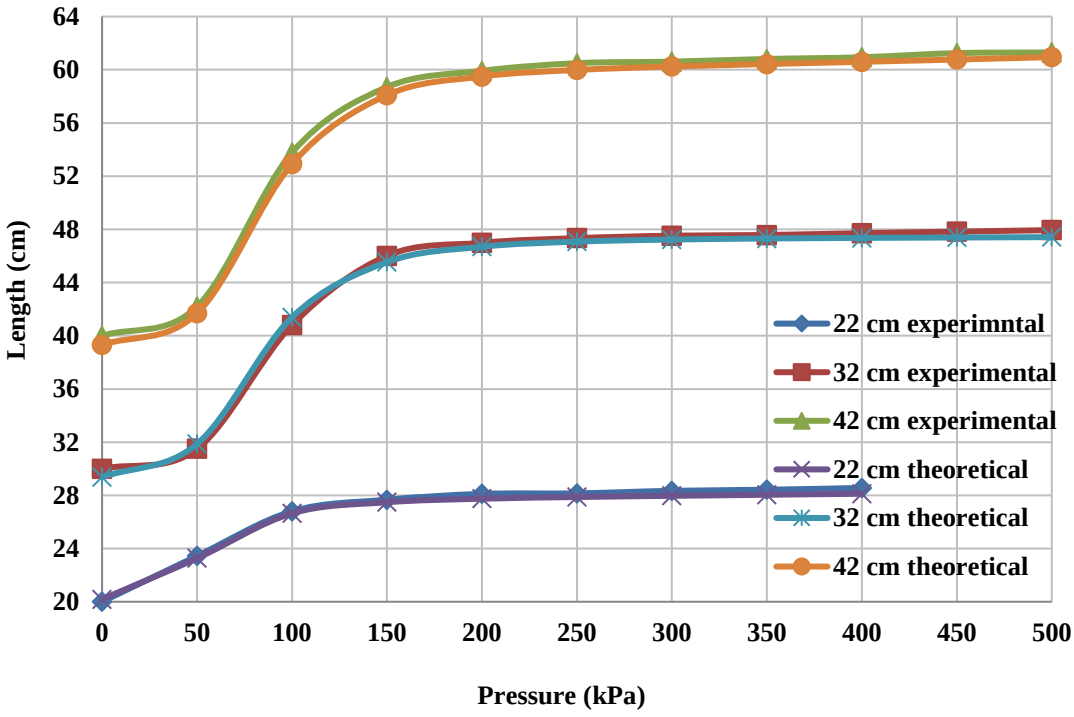

Figure 4.29 Experimental and theoretical length against air pressure.

4.3.2.2 Modelling of the extension force

Numerous works are done to model the PMA force for the contraction type. In this section, the force model for the extension actuator is found by modifying the Tondu and Lopez (2000) tensile force formula. A load is attached to the free end of the actuator varying from 0 kg to 10 kg by 0.5 kg steps. At each weight, the pressure from 0 to P_{max} is applied, then the length of the actuator is recorded.

Table A.10, Table A.11, and Table A.12 shows the given data from these experiments for the three PMAs, which explains the length of the actuator due to the change in supply of air pressure and the attached load.

(4.8) shows the modified force formula for the extensor PMA by accounting for the 45 kPa as a zero force pressure value.

$$f = 0 \ , \ 0 \leq p \leq 45 \text{ kPa}$$

$$f = -\pi r_o^2 (p - 45)[\alpha(1 - q\varepsilon)^2 - \beta] \ , \ p \geq 45 \qquad (4.8)$$

Where: $\acute{\varepsilon} = \frac{L-L_0}{L_0}$, $\alpha = \frac{3}{tan^2(\theta_0)}$, and $\beta = \frac{1}{sin^2(\theta_0)}$.

Multiply (4.8) by -1 to change the direction of force from a tensile to extension behaviour. Moreover, r_0 and θ_0 represent the initial values of radius and angle of the PMA respectively; and έ is the extension ratio.

Figure 4.30 illustrates the force against pressure plots for the experimental and theoretical data.

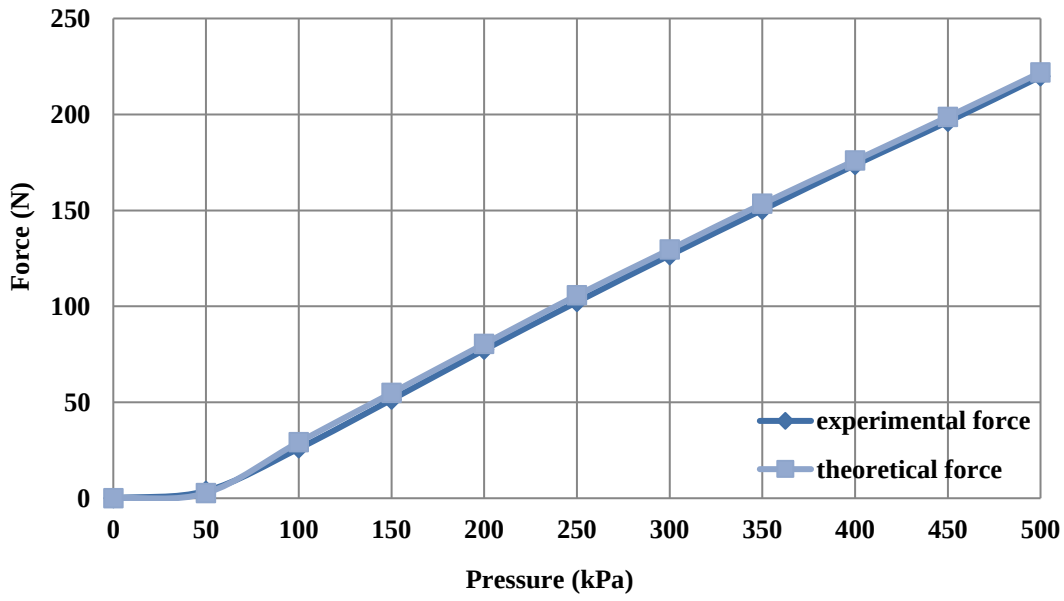

Figure 4.30 The experimental and the presented theoretical force for the 30 cm extensor PMA.

This figure proves the accuracy of the presented force model and gives the idea that the shape and contact between the inner tube and the covered sleeve of the pneumatic muscle actuator are the main affected parameters.

The results in table 4.8 above are plotted in figures below in two forms; Figure 4.31 gives the length against the pressure at fixed loads, at load steps (0, 1, 2… 10) kg., while Figure 4.31 shows the actuator length against the weight at supply pressure from 0 bar to P_{max}.

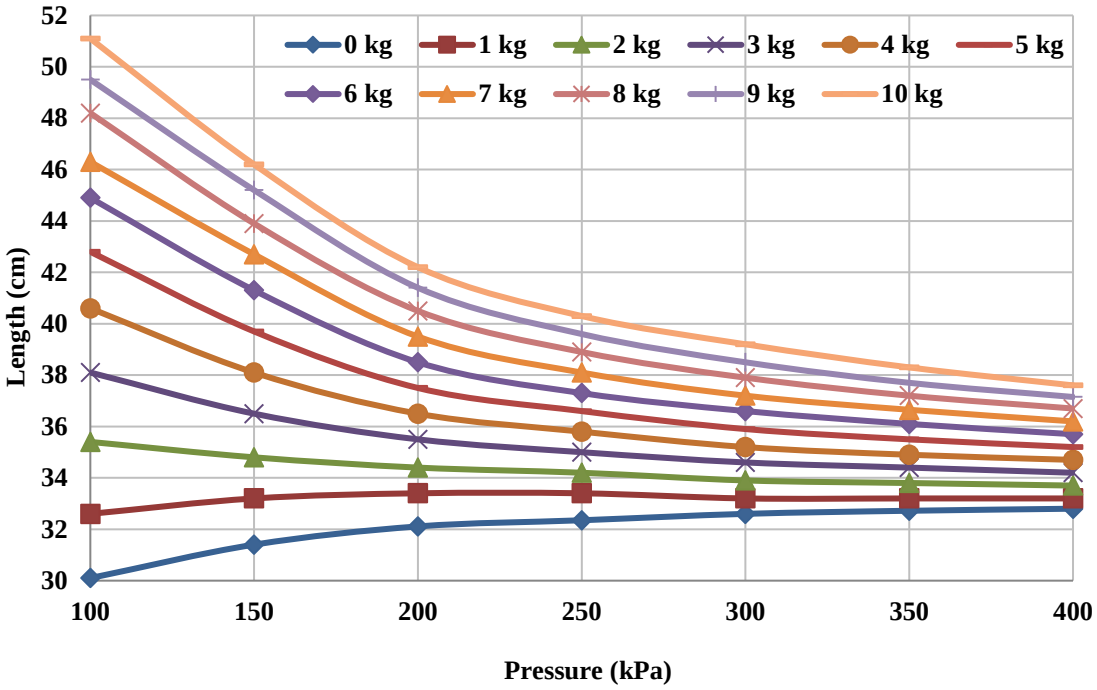

(a) 20 cm extensor PMA

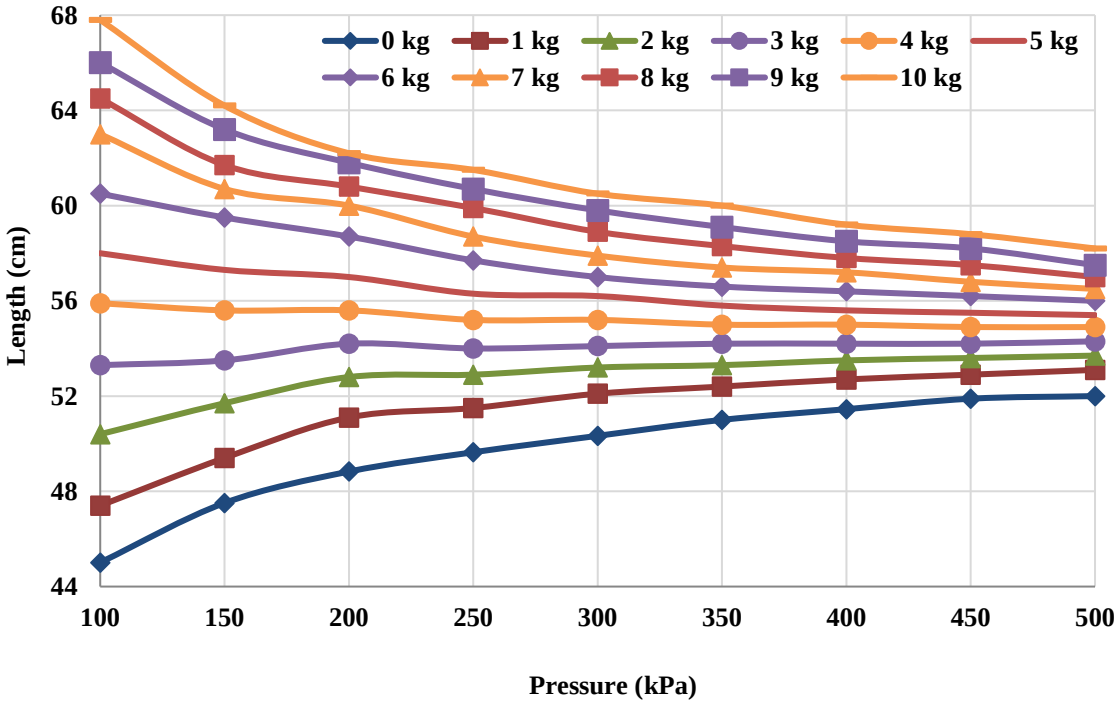

(b) 30 cm extensor PMA

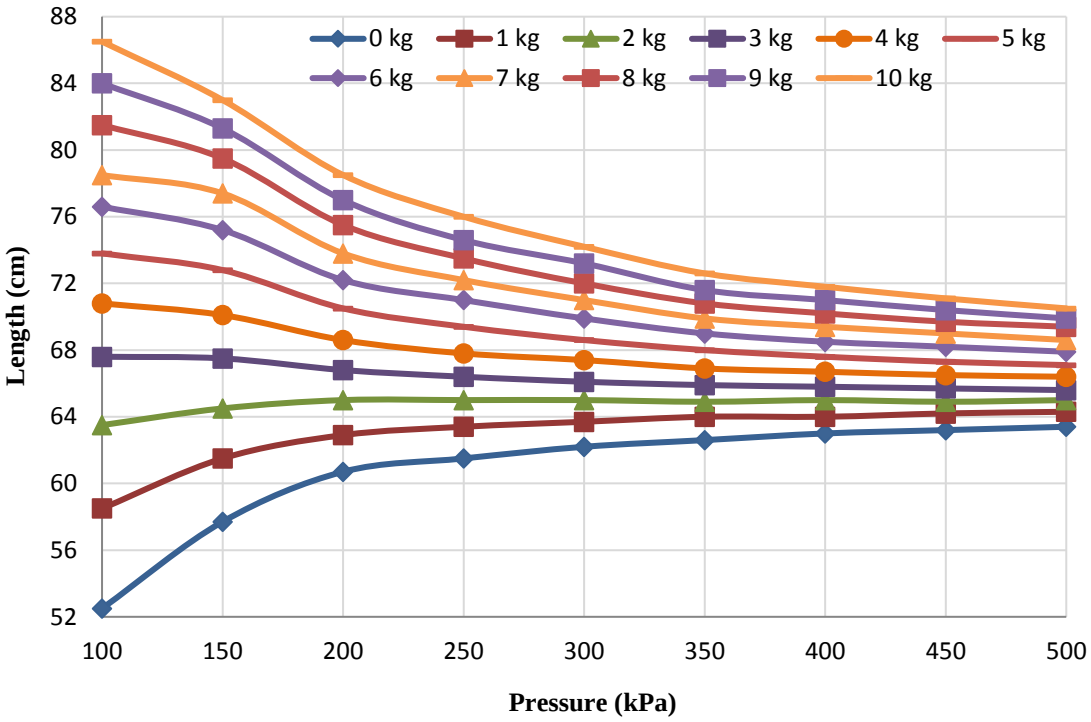

(c) 40 cm extensor PMA

Figure 4.31 The length of the actuators against the pressure at fixed weight values.

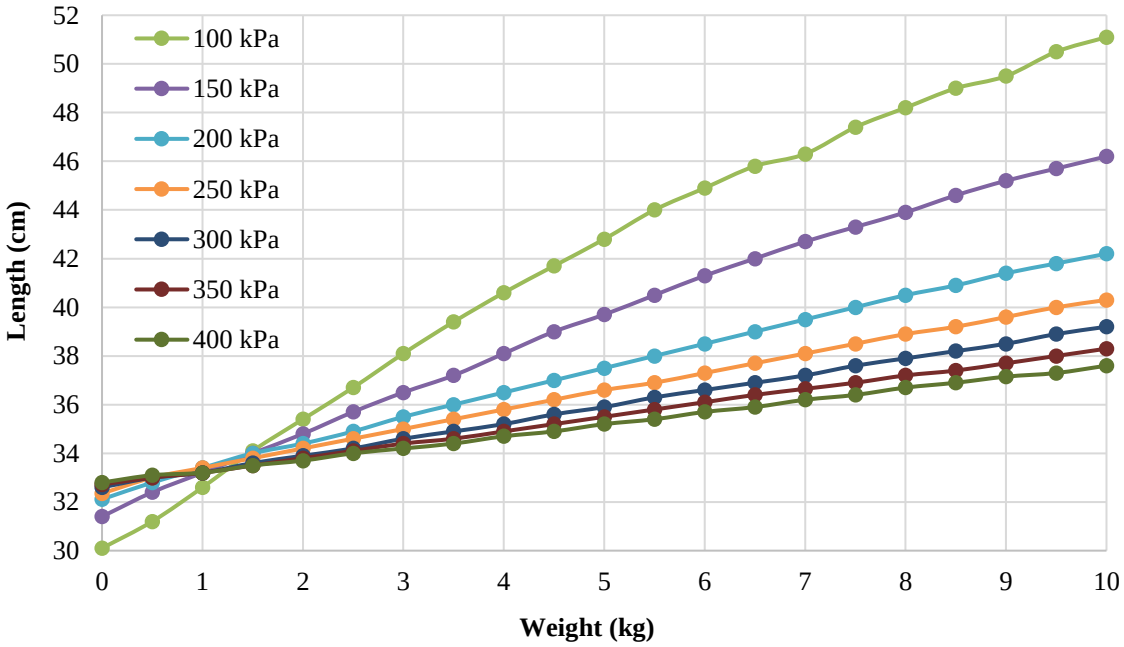

(a) 20 cm extensor PMA

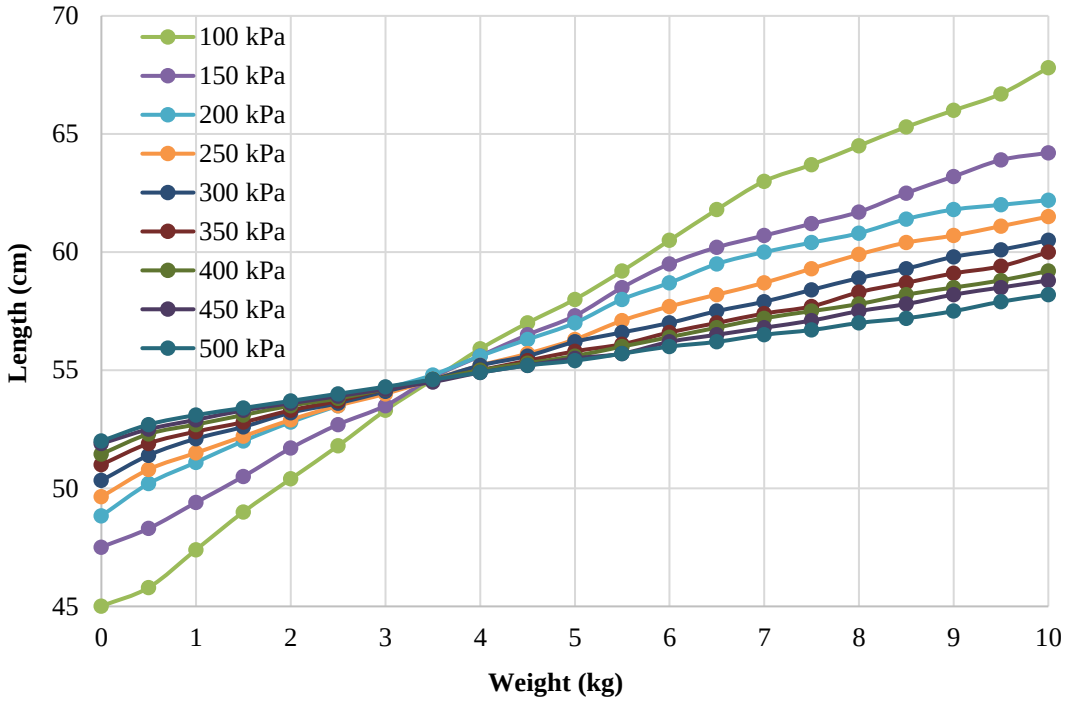

(b) 30 cm extensor PMA

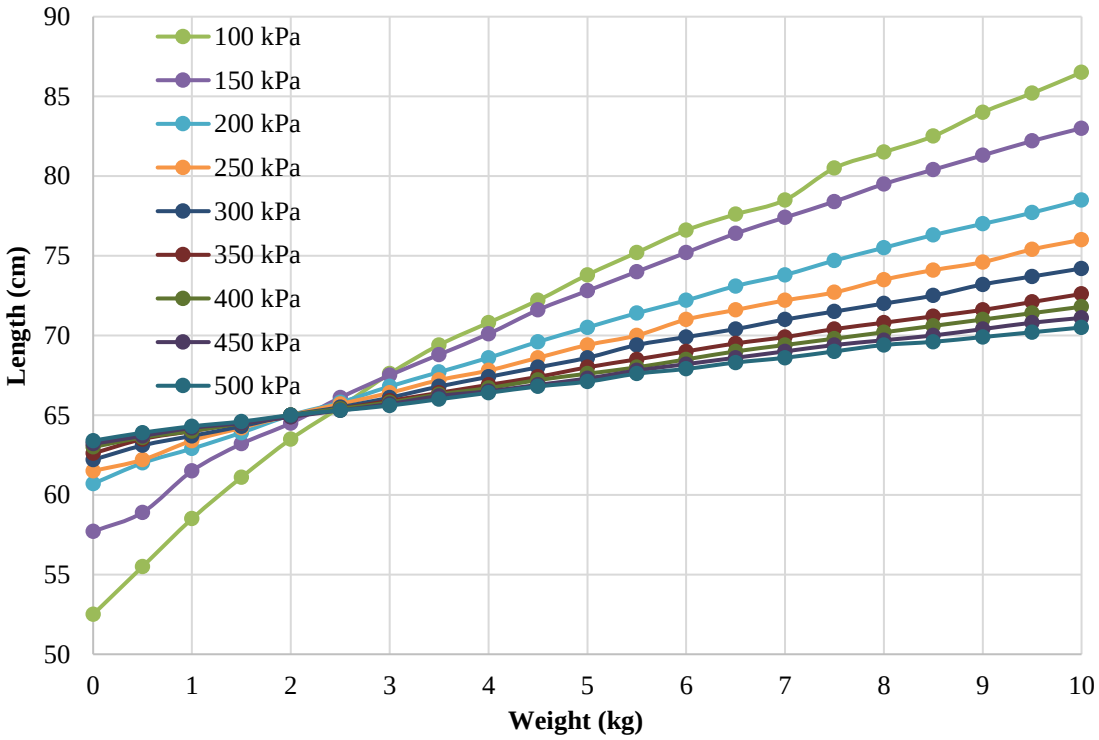

(c) 40 cm extensor PMA

Figure 4.32 The length of the actuators against the weight at fixed pressure values.

Figure 4.32 illustrates that the behaviour of the actuator changed from extensor to contractor because of the attached load. It is clear that the 20 cm actuator acts as an extensor PMA at loads less than 2 kg and otherwise as a contractor, whiles the 30 cm actuator in Figure 4.31.b acts as a normal extensor PMA at loads less than 4 kg and as a contractor when the load is high. Figure 4.31.c shows the behaviour for the 40 cm PMA; in this figure it works as extensor at loads less than 3 kg and as a contractor elsewhere. This performance provides additional advantages for the extensor PMA. It is first able to extend at a definite pressure without a load, then picks it up at certain weight, then lifts it at high pressure.

4.3.2.3 Bending angle model of an extensor continuum arm

By fixing one side of the extensor muscle and prevent it to extend at pressurised condition, the actuator will bend related to the air pressure (Walker, 2013) as shown in Figure 4.33. In this figure, a thread is used to fix the length of the actuator longitudinally.

(a

(b)

Figure 4.33 A 30 cm extensor PMA (a) one side sewed actuator (b) bending under 300 kPa air pressure.

To develop the bending in all directions a 4-PMAs continuum arm is designed and constructed as shown in Figure 4.34. Four extension actuators 30 cm each are used; one in the centre and the others are located at 3 cm from the centre and 120^0 between each other.

Figure 4.34 Four 30 cm extensor PMAs continuum arm.

A Solidworks 2015 is used to design the two ends, and a 3D printer is used to print them. Then the centre actuator is connected to others individually. Equal air pressure in all PMAs makes the arm extend in a straight direction, while, the different pressure inside the four actuators make the free end move in all direction in the space at almost constant curvature (Walker, 2013). The position angle is observed as a function of the supplied pressure and the attached load.

Firstly, the experiments are done by recording the initial angle of the free end (δ), which it is equal to (zero) degree due to a straight-line arm. Secondly, all PMAs are actuated by 45 kPa, then the pressure is increased in one of the PMAs in the corner. The arm will then bend into another position, depending on the amount of the pressure in the muscle. And δ is recorded each time. Figure 4.35 shows the extension arm under actuation from certain pressure between 0-500 kPa.

The maximum angle value (δmax) depends on the amount of the attached load (w) to the arm end. Table 4.12 below shows different maximum angles with different load values.

Figure 4.35 An extensor continuum arm at certain pressure.

Table 4.12 the maximum bending angle with different loads.

Load w (Kg)	**Pressure P (kPa)**	**δ_{max} (degree)**
0.0	500	164.833
0.1	500	163
0.2	500	155
0.3	500	135.2
0.4	500	126.1
0.5	500	116.2

The bending angle against the air pressure at different load values is illustrated in Figure 4.36 which it represents the position of the free end at any pressure step.

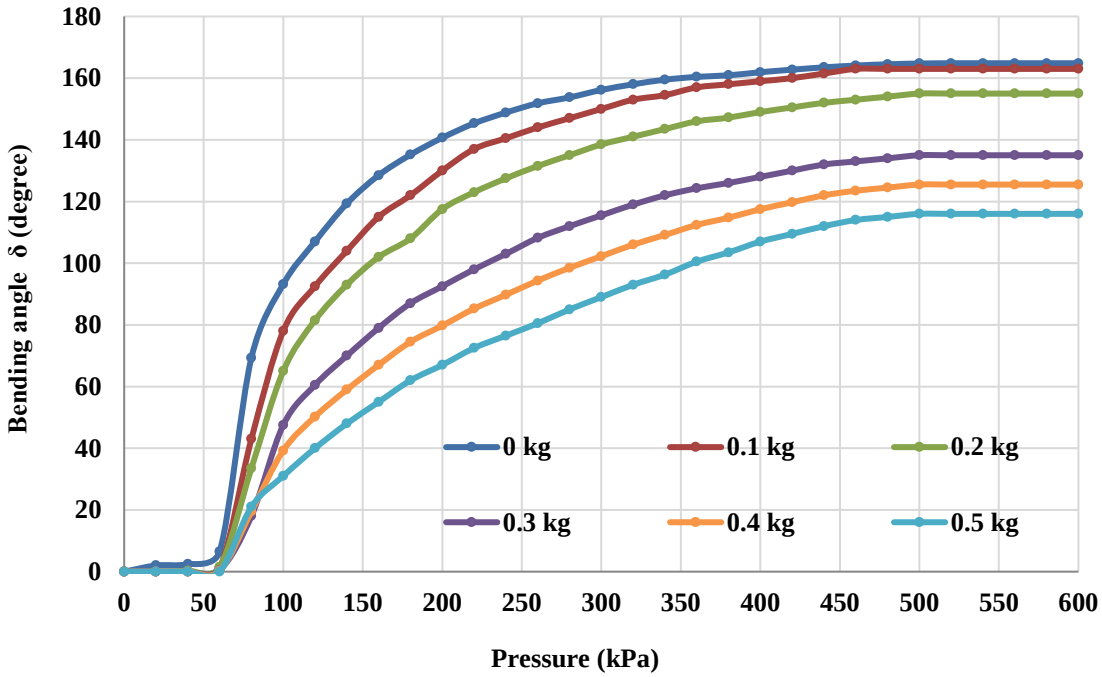

Figure 4.36 The bending angle against the pressure at different load conditions.

From these data, the bending angle increase when the applied pressure increases and its value at each air pressure step depends on the attached load. In our experiment, various loads from 0 to 0.5 kg are attached. Furthermore, the arm starts to bend when the air pressure reaches 80 kPa and the angle has a fixed value (δ_{max}) over 520 kPa. As a result, the operation range will be at pressure values from 80 kPa to 520 kPa.

A new formula of bending angle is presented as a function of the input air pressure and the amount of attached load as follows:

$$\delta = a - \frac{b}{[1+(\frac{p}{c})^d]^e} \tag{4.9}$$

Where: $\begin{bmatrix} a \\ b \\ c \\ d \\ e \end{bmatrix} =$

$$\begin{bmatrix} 173.57 & -350.13 & 9014 & -62973 & 167422 & -148110 \\ -172.1 & 312.6 & -8667.6 & 61529 & -164591 & 145972 \\ 0.5798 & 2.2097 & -33.363 & 201.17 & -499.34 & 431.94 \\ 303.74 & -5310.1 & 36922 & -118935 & 183790 & -111871 \\ 0.0045 & -0.0727 & 6.4529 & -43.867 & 103.32 & -81.375 \end{bmatrix} \begin{bmatrix} 1 \\ w \\ w^2 \\ w^3 \\ w^4 \\ w^5 \end{bmatrix}$$

Equation (4.9) above gives the bending angle at any air pressure amount from 0 – 600 kPa, while, the value of the parameters (a, b, c, d and e) depends on the attached load.

This formula is validated for all load conditions and Figure 4.37 gives the validation results for three conditions (0 kg, 0.2 kg and 0.5 kg). This figure shows a significant matching between the experimental results and the presented formula.

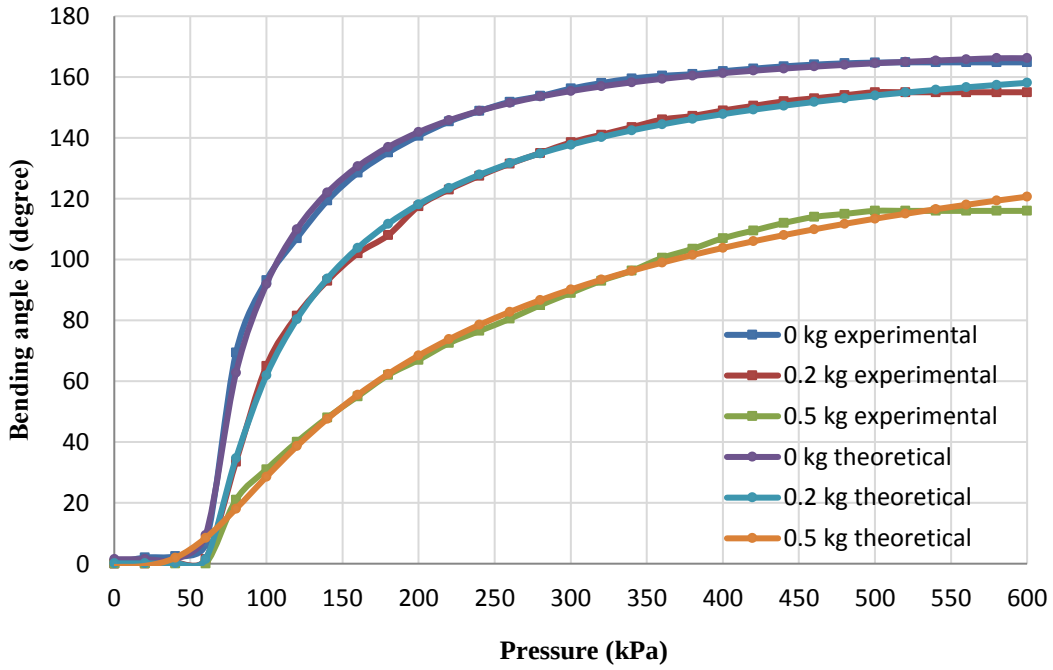

Figure 4.37 The validation results for the bending angle at three different load conditions.

4.3.3 Kinematics of the extensor continuum arm

The bending direction of the proposed arm depends on which extensor actuator is activated. Figure 4.38 shows the geometrical analysis of the actuators positions and the bending directions.

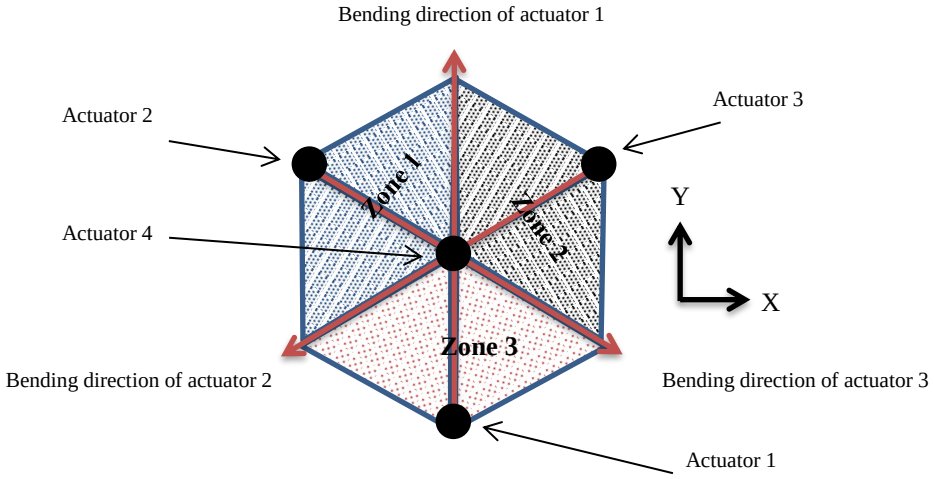

Figure 4.38 The geometrical analysis of the extensor continuum arm.

From Figure 4.38 the bending of the first extensors actuator is according to (4.9) and the direction of this bending is in the direction of the positive Y-axis (i.e. the extensor continuum arm will bend towards 90^0). The bending due to the first actuator can be written as: ($\delta_1 \angle 90^0$). Similarly, the bending angles of the second and third actuators are defined as: ($\delta_2 \angle 330^0$) and ($\delta_3 \angle 210^0$) respectively. And the resultant bending angle of the arm can be defined as:

$$\delta \angle \theta = \delta_1 \angle 90^0 + \delta_2 \angle 330^0 + \delta_3 \angle 210^0 \qquad (4.10)$$

Where δ_1, δ_2 and δ_3 are the bending angles of the soft arm due to the pressurised condition of the actuators 1, 2 and 3 respectively, and they calculated according to (4.9). The bending angle δ of the proposed extensor continuum arm in the direction of θ can be found anytime by applying (4.10).

Figure 4.38 shows three operation zones, each one represents the operation area for two actuators. The presented arm covers (zone1) when the actautor1 and actuator3 are activated. Similarly, pressurising actuators 1 and 2 cover (zone2), and (zone3) is covered by actuators

2 and 3. Consequently, pressurising the three actuators by different air pressure values makes the continuum arm moves to any of these zones according to (4.10).

Chapter Five:

5. Controlling of pneumatic muscle actuator

5.1 Introduction

The movement of soft actuators and continuum arms can be specified by different translations and rotations, elastic deformation of soft robotic manipulators results in virtually infinite degrees-of-freedom (DoF) motions, (bending, extension, contraction, torsion, buckling, etc.) Furthermore, the wide range of design and actuation techniques which makes each of these robots have unique properties (Manti, Cacucciolo, & Cianchetti, 2016) and the value mechanism and the high rubber material nonlinearity of the PMA make the control process difficult and rule out simple controllers. Therefore, to overcome these difficulties the high robust control has to be considered (Leephakpreeda, 2011; Tondu & Lopez, 2000). Numerous types of control strategies were used to control position and force of the PMA. Among them, adaptive pole-placement techniques for position and proportional-integral-derivative (PID) controllers was applied by Bowler, Caldwell, and Medrano-Cerda (1996). Sliding mode control was used by Cai and Yamaura (1996); Carbonell, Jiang, and Repperger (2001). A combination of PID controllers and ANN (Nonlinear PID) were used by Thanh and Ahn (2006) for physical rehabilitation by using multi-joint actuate based on pneumatic muscles as shown in Figure 5.1.

5.2 Nonlinear PID controller

The PID controller has been one of the important used strategies in industrial application because of its simplicity and robustness. The requirements for high-performance control with changes in operating conditions or environmental parameters are often beyond the capabilities of simple PID controllers (Su, Sun, & Duan, 2005). Moreover, the high nonlinearity of the PMAs makes the PID controller insufficient to solve this complex control problem. In order to improve the performance of linear PID to control the performances of PMA, many approaches have been established to enhance the adaptability and robustness by using the self-tuning method, general predictive control, fuzzy logic and neural networks strategy (Cervantes & Alvarez-Ramirez, 2001; Su, Duan, & Zheng, 2004).

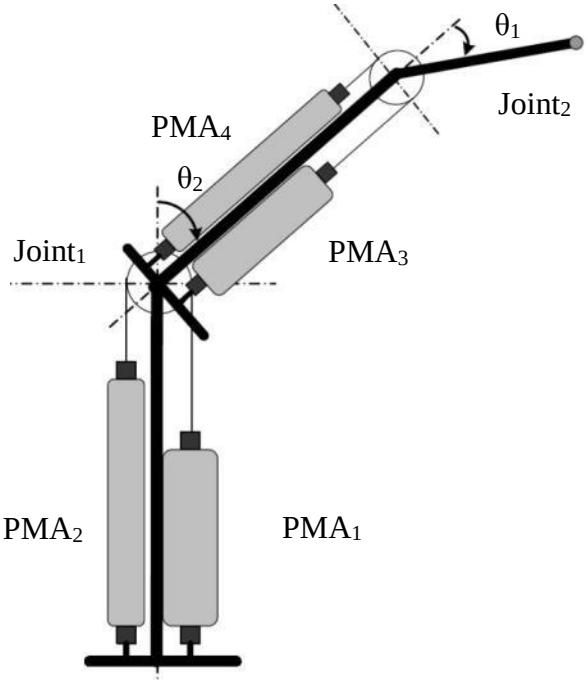

Figure 5.1 Two joints arm for rehabilitation process based on PMAs Thanh and Ahn (2006)

Figure 5.2 shows the nonlinear PID by connecting it serially to the ANN.

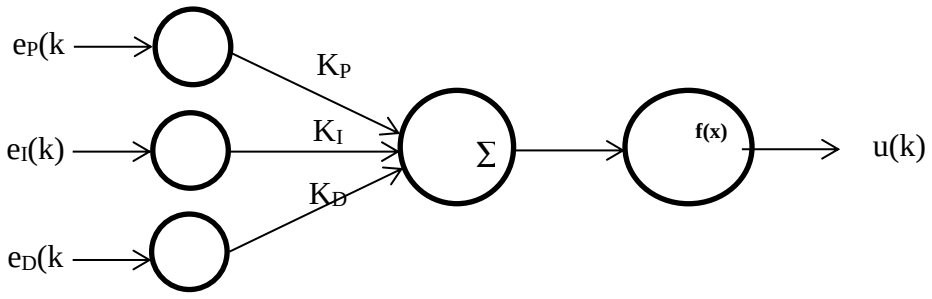

Figure 5.2 PID-ANN control structure (Thanh & Ahn, 2006)

Multi-layer ANN is used for 3- inputs, one neuron in one hidden layer and one output neuron with:

$$e_P(k) = \theta_{ref}(k) - \theta(k) \quad (5.1)$$

$$e_I(k) = e_P(k).\Delta T \quad (5.2)$$

$$e_D(k) = \frac{e_P(k)(1-z^{-1})}{\Delta T} \quad (5.3)$$

Where θ_{ref} and θ are the set points and the actual output for each joint respectively, ΔT is the sampling time, z is the Z-transform operator, K_p, K_I and K_D are PID constants which have to modify to find the optimal value, f(x) is a sigmoid function and u(k) is the controller output.

Other work was done by Anh (2010) using the same technique PID-ANN with added bias input to the hidden and output neurons.

5.3 Other controller approaches

The inverse control strategy for PMA motion control was presented by R. Kang, Guo, Cheng, and Chen (2014) and R. Kang, Guglielmino, Branson, and Caldwell (2013). By using this idea, they were able to define an inverse kinematic model for control application. Furthermore, they assumed that the dynamics of the system could be ignored because the speed of these types of actuators is low. Meanwhile, Nakamura and Shinohara (2007) presented a control scheme based on the mathematical model of PMA, which drive the inverse relationship between both the position and force of the PMA and the pressure input where P is the function of L and F.

The Fuzzy control based on bang-bang control strategy is used by Leephakpreeda (2011) with a combination of proportional control to adjust the system output around the desired points either for the length or the contraction force. Figure 5.3 shows the diagram of this control system.

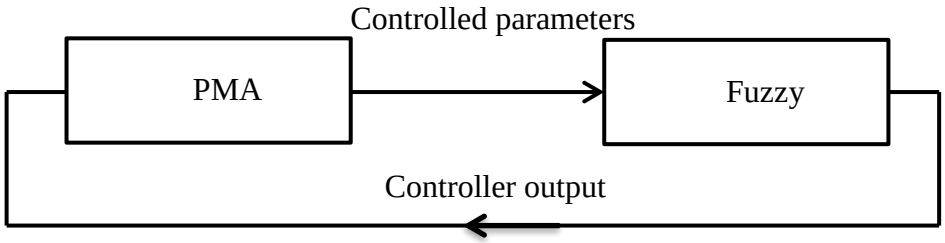

Figure 5.3 Block diagram of Fuzzy logic control system

In this method, the author used the pulse width modulation (PWM) technique as a variable time on-off controller to adjust the air valve outlets.

5.4 Static and dynamic controllers

Whether the robot system is under movement conditions or not, the control can be classified to static or dynamic.

5.4.1 Static control system

Under force equilibrium, the full configuration of the soft manipulator can be defined by a low dimensional state space representation. This assumption leads to interchangeably use the term ‘statics’ and ‘kinematics’ even though this is not a common practice in traditional robotics.

Model based statics controller is used by Camarillo, Carlson, and Salisbury (2009) for a 5-DoF per section model by formulate an inverse kinematics (IK). Bajo, Goldman, and Simaan (2011) presented a space controller configuration, by using external and internal sensors information

The most commonly used of model (IK) based static control system uses the constant curvature (CC) approximation (Hannan & Walker, 2003).

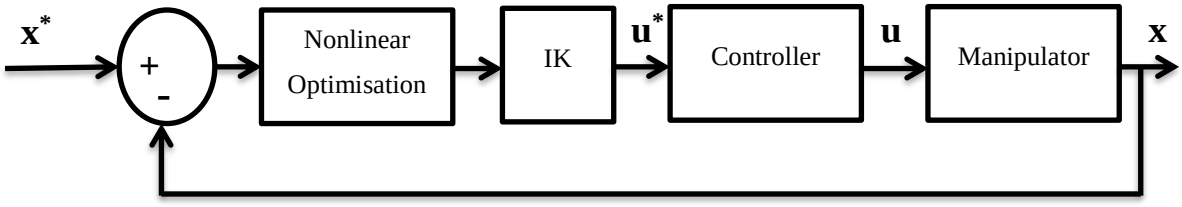

Figure 5.4 A block diagram of a model-based static controller system.

On the other hand, model-free based approaches for control of continuum/soft robots is a relatively new field and offers a wide range of possibilities. Although, these data dependent methods have been used effectively in the field of rigid manipulators (Nguyen-Tuong & Peters, 2011), the same cannot be said for continuum manipulators even though model-free approaches intuitively should fare better in this case.

The first usage of a model-free approach for development of a static controller was proposed in Giorelli, Renda, Ferri, and Laschi (2013) and by Michele Giorelli et al. (2015) for a two DoF and a three DoF (M Giorelli et al., 2015) cable driven soft manipulator. An efficient exploration algorithm for generating samples for IK learning was proposed in (Rolf & Steil, 2014). The main idea for the this controller system is applying a closed-loop controller system with an efficient sensory feedback system.

5.4.2 Dynamic control system

Design a dynamic control system to control a single PMA or a continuum arm of combination of soft actuators is a challenge. The exact dynamic model and a high number of sensors are required (Renda, Giorelli, Calisti, Cianchetti, & Laschi, 2014). Even that, there are some parameters are uncontrolled due to their nature properties (Gravagne, Rahn, & Walker, 2003).

Numerous researches have been done on the dynamic control of soft robotic systems including (Gravagne et al., 2003) (Gravagne et al., 2003). However, these papers proposed simplified models which do not provide a full description of the system nonlinearity.

The closed loop dynamic control system has been proposed by (A. Kapadia & Walker, 2011), although, only by simulations. A various control methods for the similar kinematics and dynamic models, in simulation, were done using a sliding mode controller by A. D. Kapadia, Walker, Dawson, and Tatlicioglu (2010), however, only for closed loop configuration space control. A first order sliding surface is defined as the filtered tracking error for this purpose. The advantage of a sliding mode controller over a simple inverse dynamics based PD controller is the higher robustness to model uncertainties; the downside being the slower error convergence, chattering and higher gain requirements. An experimental evaluation of this method was conducted with a planar three section continuum arm by A. D. Kapadia, Fry, and Walker (2014).

Similar to the static control system, the dynamic control system can either be model-based or model-free, and in both cases the high accuracy and efficient sensor and feedback system is required in order to track the dynamic behaviour of the soft robotic systems.

5.5 Parallel Neural Network-Proportional Controller

The neural network-proportional (PNNP) controller is suggested in this section in parallel structure. The NARMA-L2 NN-controller is used of 9-neurons in one hidden layer, 3-delayed plant inputs, 2-delayed plants outputs and it is trained by (trainlm) for 100 Epochs. The mean square error (MSE) for the training, testing and validating data is about 10^{-7}. To enhance the speed of the controller system, a proportional controller has been used in parallel to the NN controller. In this structure, the PNNP controller provides efficient performances in terms of precision and speed. The structure of the controller is shown in Figure 5.5. In spite of the controller is used to control the static of the PMA systems, the dynamic neural network is used due to the high nonlinearity of the PMA and the time variants.

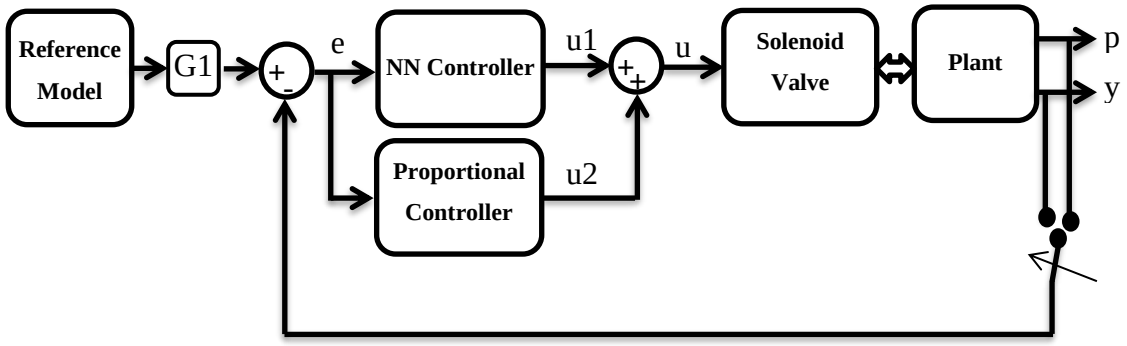

Figure 5.5 The schematics of the suggested controller

The reference model states the required target such as length, position, bending angle, and so on. Moreover, since the air pressure in single or multiple PMA defines the system performances, G1 can be either the inverse kinematics (IK) of the plant, and in this case, the proposed controller will adjust the pressure p; or G1 equal to 1, and in this case the controller system will track the error in the output y.

The error e can be defined as:

$$e = p_r - p \quad \text{, if G1 is IK} \tag{5.4}$$

Or

$$e = y_r - y \quad \text{, if G1 is 1} \tag{5.5}$$

p_r and y_r are the reference (set point) for the pressure and the system's output respectively.

The controller outputs *u1* and *u2* represent the duty cycle of the pulse width modulation signal (PWM) for the NN-Controller and P-controller respectively. Where, *u* is:

$$u = u1 + u2 \tag{5.6}$$

The NARMA-L2 NN-controller output *u1*can be defined as:

$$u1(k) = \frac{y_r(k+1) - f[y_n(k), u1_m(k-1)]}{g[y_n(k), u1_m(k-1)]} \tag{5.7}$$

where *f*( ) and *g*( ) are approximated using neural networks. And:

$$y_n(k) = [y(k), \dots, y(k-n+1)]^T \tag{5.8}$$

$$u1_m(k-1) = [u1(k-1), u1(k-2), \dots, u1(k-m)]^T \tag{5.9}$$

Where *n* and *m* equal to 2 and 3 respectively according to the proposed controller structure.

While the proportional controller output has been defined as:

$$u2(k) = k_p \frac{(y_r(k+1) - y(k+1))(u_{max})}{x} \tag{5.10}$$

The PWM signal controls the airflow for the valve output in fill and vent directions. Therefor two PNNP controllers are required; one to control the airflow in fill direction and the other controls the vent process.

According to the error, the proposed controller activates either the filling controller (positive error) or the venting controller (negative error). On other hand, two possible methods are used to train the NN. The first method is using an approximate relationship between the output and the duty cycle as in (5.11):

$$y^* = y_0 + \frac{x\,u}{98} \tag{5.11}$$

In case of the pressure controller of the single or multiple actuators, y^* and y_0 represent the air pressure in the actuator p and the initial pressure in the actuator. x is the maximum applied pressure p_{max} (p_{max} is subject to the actuator size and material), and u is the duty cycle of PNNP controller.

In most cases:

$$p_{max} = 500\ kPa \tag{5.12}$$

$$0 \leq p \leq p_{max} \tag{5.13}$$

$$x = p_{max} \tag{5.14}$$

$$0 \leq u \leq 100 \tag{5.15}$$

In order to prevent a continuous applied voltage (100% duty cycle) we chose 98% as a maximum operating duty cycle.

The formula (5.11) provides an acceptable linear approximation between the duty cycle of the controlled PWM signal and the actuator air pressure.

Alternatively, the actual relationship between the output and the duty cycle can be found experimentally as follows:

A contraction actuator of 30 cm length and 1.7 cm in dimeter is chosen. A source of 600 kPa is used to apply an air pressure to this actuator via a solenoid valve by different duty cycles from 0% to 100% during 1 sec. firstly, a 10% duty cycle is selected, and the air pressure is measured by a pressure sensor, then the vent process is activated. This process is repeated for 20%, 30%…, 100% respectively. The result for this experiment is shown in Figure 5.6. The trained line to this data is utilized to train the NN.

The (5.11) is used due to the similarity in the performances of the NN and to decrease the complexity of the control system. Moreover, the PNNP controller is tracking the desired behaviour online; therefore, the controller is adjusting the duty cycle to minimize the error.

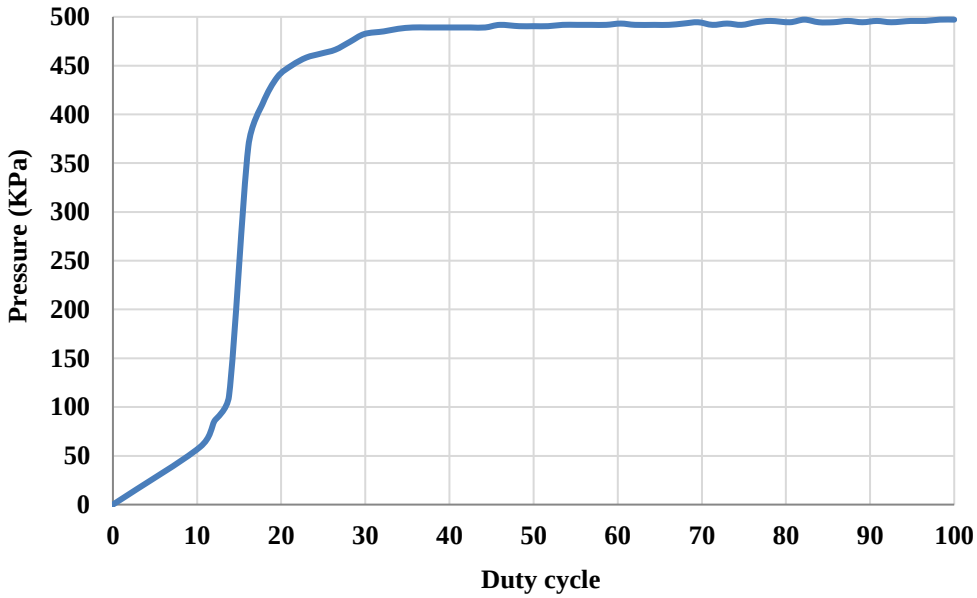

Figure 5.6 The relation between air pressure and duty cycle

5.5.1 Length control of single extensor PMA

In order to validate the proposed controller, a 30 cm extensor actuator is chosen. And an ultrasound HC-SR04 sensor is attached to the end of the actuator to measure its length. According to the (5.4): y^* is the length of the actuator L, y_0 is the initial length L_0 of the extensor PMA (30 cm) and x is the maximum extension ratio (50% of L_0).

The PNNP controller sends the controlled input u to the (3/3 Matrix MK 754.8E1D2XX) solenoid valve via Arduino Mega 2560. The Arduino acts as an interface between the PC and the valve-actuator system. It is reading the pressure and the distance from the pressure sensor and the ultrasound sensor and sending them to the Matlab via USB port. Then, The PNNP controller adjusts the duty cycles for both the filling and the venting and sends them back to the valve.

The length of the actuator is controlled under three different load values. At each time, a square wave between 30 and 45 cm is applied as a reference at 0.5 Hz. The extensor actuator and the control performance are illustrated in Figure 5.7 and Figure 5.8 respectively for 200 g.

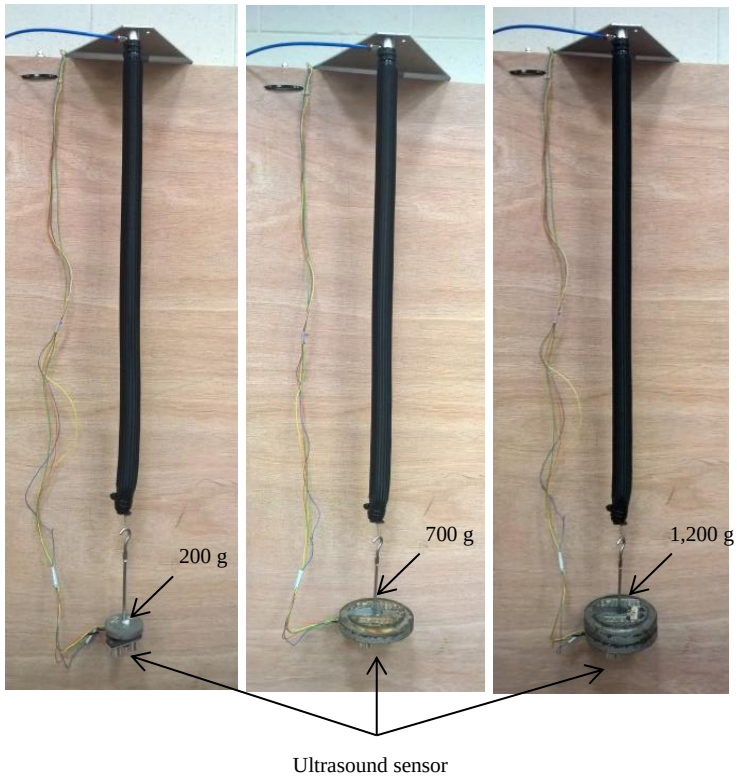

Figure 5.7 The extensor PMA at different attached load and the position of the ultrasound sensor

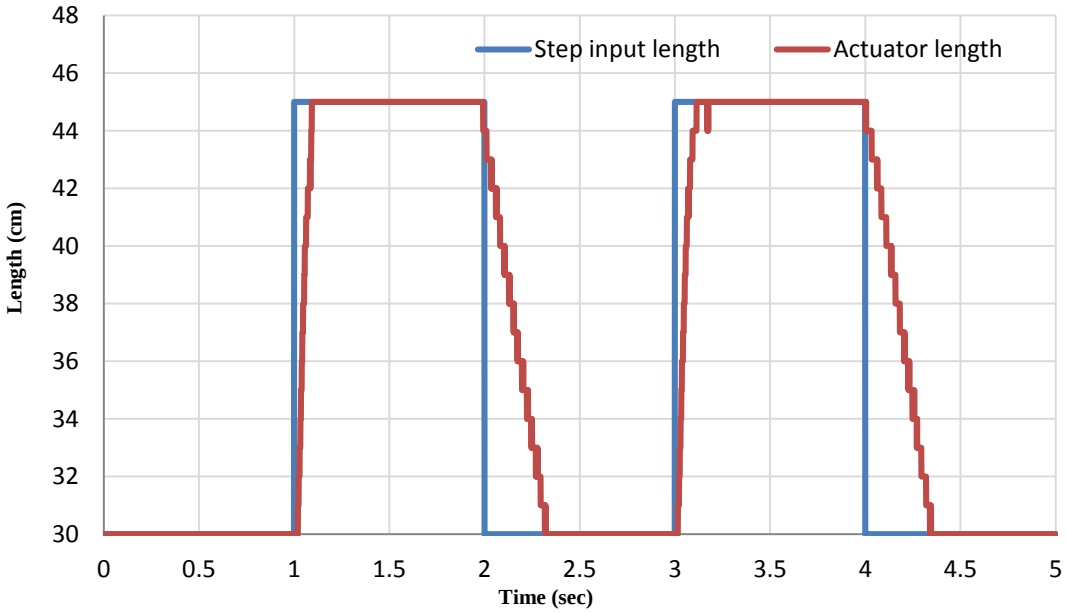

Figure 5.8 The step response of the 30 cm extensor actuator at 0.5 Hz.

Figure 5.8 shows that the contracting time is more than the elongation time because of the hysteresis of the actuator material. The air pressure of the extensor PMA is recorded during the controlling process and it is applied to the modelling formula in (4.7) in order to further validation of the proposed length model. The result of this validation is illustrated in Figure 5.9 and it shows the considerable matching between the two plots at the maximum error of 3 mm.

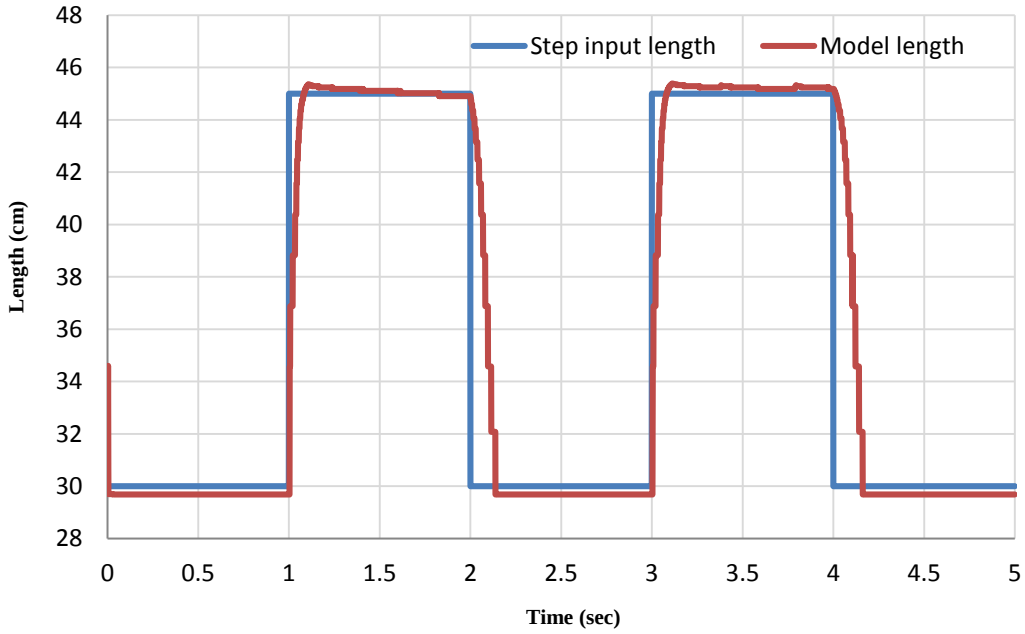

Figure 5.9 The step input and the model length of the 30 cm extensor actuator.

The proposed controller system shows a high accuracy of the actuator length and the applied pressure is used for extra validation to the model of the extensor length in (4.7). The PNNP controller will used in next chapters to control different performances according to the structure and the function of the single actuators and the continuum arm.

Chapter Six:

6. Novel structures of pneumatic muscle actuator

6.1 Introduction

The basic construction of the pneumatic muscle actuator (see Figure 2.9) results either contraction or extension behaviours according to the length of the inner tube and the braided shell. Several modifications are done to establish a bending behaviour to the single PMA. Among these Razif, Bavandi, Nordin, Natarajan, and Yaakob (2014) presented and analysed (M. Razif et al., 2014) a modified approach bending behaviour by using double chambers. Natarajan et al. (2014) designed a soft finger that can bend in various ways by controlling the form of the coverage sleeve. Wang, Aw, Biglari-Abhari, and McDaid (2016), Nordin, Razif, Natarajan, Iwata, and Suzumori (2013) and Faudzi et al. (2012) developed a bending actuator by using different braided angles.

In this chapter, a new approach will propose to establish a one direction bending behaviour for single actuator using the basic principle to design both the contraction and the extension PMA by modified the construction. Then, the inspiration of the lateral undulation motion of the snake is used to design a double bend pneumatic muscle actuator (DB-PMA). Finally, a novel circular pneumatic muscle actuator (CPMA) inspired by the human fascial muscles will explain in details.

6.2 Self-bending contraction actuator (SBCA)

Figure 4.16 and Figure 4.35 show a bending performance for a parallel structure of PMA, nonetheless, increasing the number of actuators increases the complexity of the control system and increases the weight of the robot arm and that leads to decrease the weight to force ratio. McMahan et al. (2006b) explain that using the principle of the constant-volume creates the bending behaviour of the PMA, where the dimensional adjustment on one side leads to a dimensional modification on another side.

6.2.1 The design of the SBCA

In this section, a thin (2 mm) flexible but incompressible reinforcing rod is used to partially fix the length of the contraction actuator.

Firstly, the rod is sewed at the outer covering of the actuator as shown in Figure 6.1. applying an air pressure forces the actuator to contract from all the free sides, while, the rod preventing the contraction along its length. This method offered a bending behaviour of single contraction actuator and the rod is laying on the outer arc.

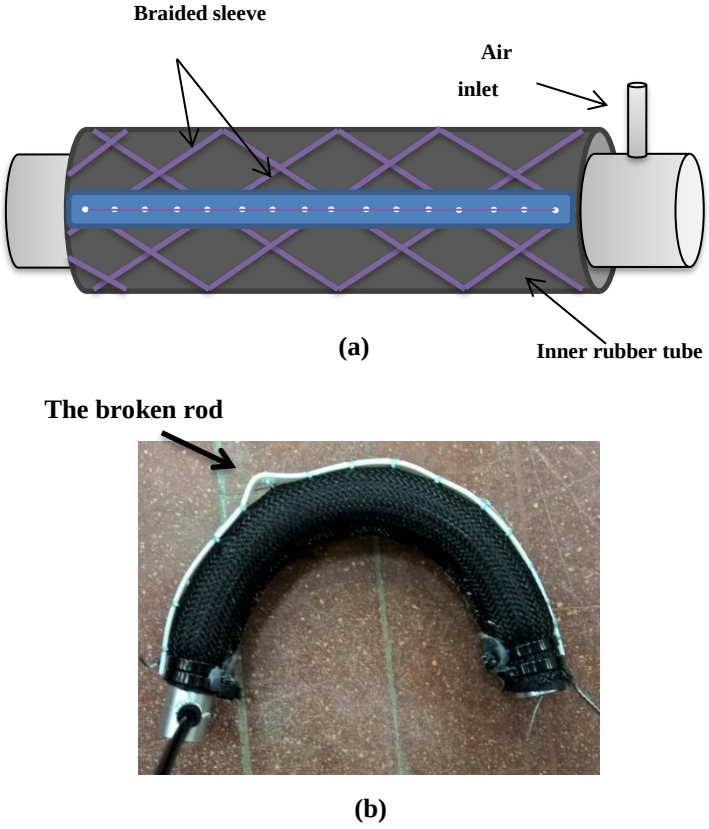

Figure 6.1 The structure of the self-bending contraction actuator version (1).

As shown in Figure 6.1, the actuator applied high force on the rod that leads to break it after several bending iterations. Moreover, the external shape of the actuator with laying rod decreases the softness appearance of the PMA. On the other hand, and again the biological concepts inspired me to copy the idea of our body. The rigid parts in human body (bones) are covered by a soft tissue (skin), and that make the external appearance soft.

Therefore, the reinforcement rod is inserted between the inner rubber tube and the braided sleeve. This method achieves biological concepts and increase the age of the rod because both the rubber tube and the covered shell applying force from both sides. Figure 6.2 illustrates the SBCA at new construction approaches.

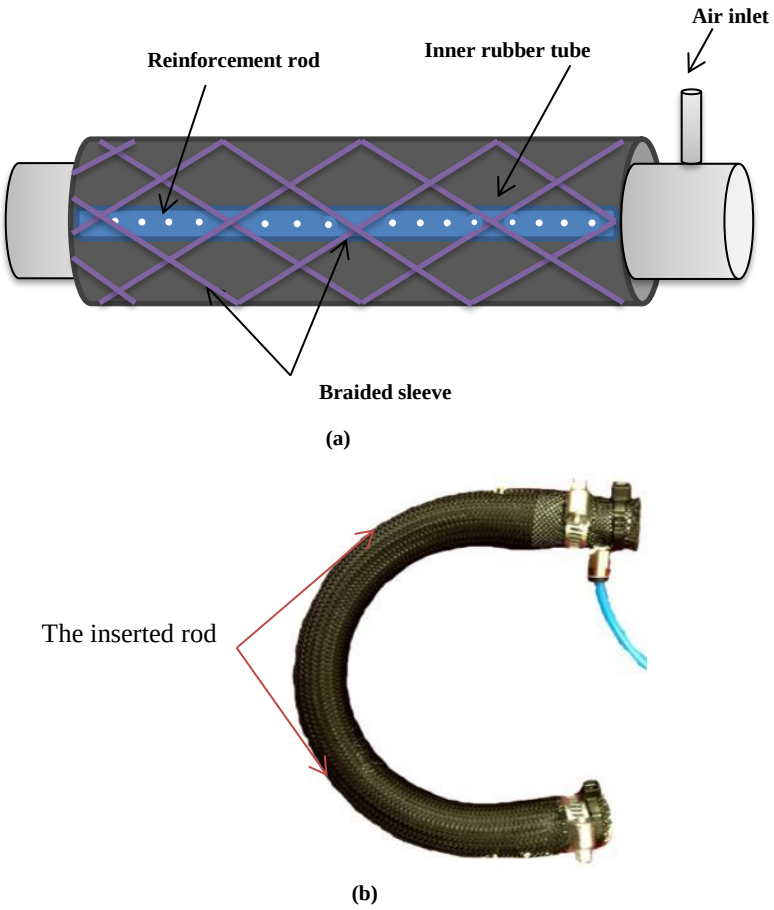

Figure 6.2 The novel structure of the SBCA version (2). (a) The structure of the SBCA showing the inserted rod. (b) The 30 cm SBCA at 300 kPa.

An experiment is done to study the bending angle of the proposed actuator at different values of the attached load as follows:

1- Fix the SBCA from the air inlet side vertically.

2- Connect a 9-axis motion tracking (BNO055) sensor to the free end to measure the bending angle.

3- Attach a load support to adjust the load value.

4- Applying an air pressure via (3/3 solenoid valve).
5- Measuring the air pressure by a pressure sensor.
6- Using Arduino Mega 2560 to control the experiment process.

The experimental components are shown in Figure 6.3 and Table 6.1 lists the maximum bending angle at different loads.

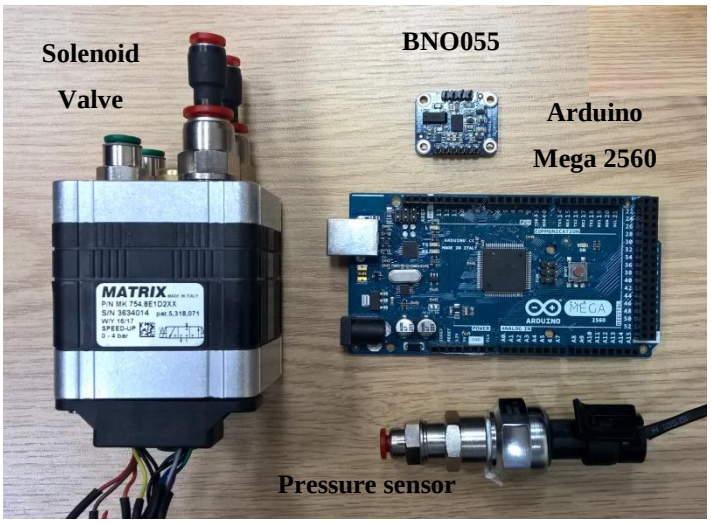

Figure 6.3 the experiment components

Table 6.1 The maximum bending angle at different loads

Load (kg)	Bending angle (degree)
0.0	213.1
0.5	136.2
1.0	73.0
1.5	49.3
2.0	34.1

From Table 6.1, the bending angle at load 0.5 kg is 136.2^0, while it is 47^0 for the 4-PMAs contraction arm in Figure 4.16 and 116.2^0 for the 4-PMAs extensor arm in Figure 4.35 and at similar load values. The payload for the SBCA is more than the payload for

previous arms. As a result, this actuator is more suitable for industrial applications that require efficient bending angles. Figure 6.4 shows the bending angle as a function of air pressure at different load values. Furthermore, the dimensions of the used material in this bending actuator are listed in Table 6.2

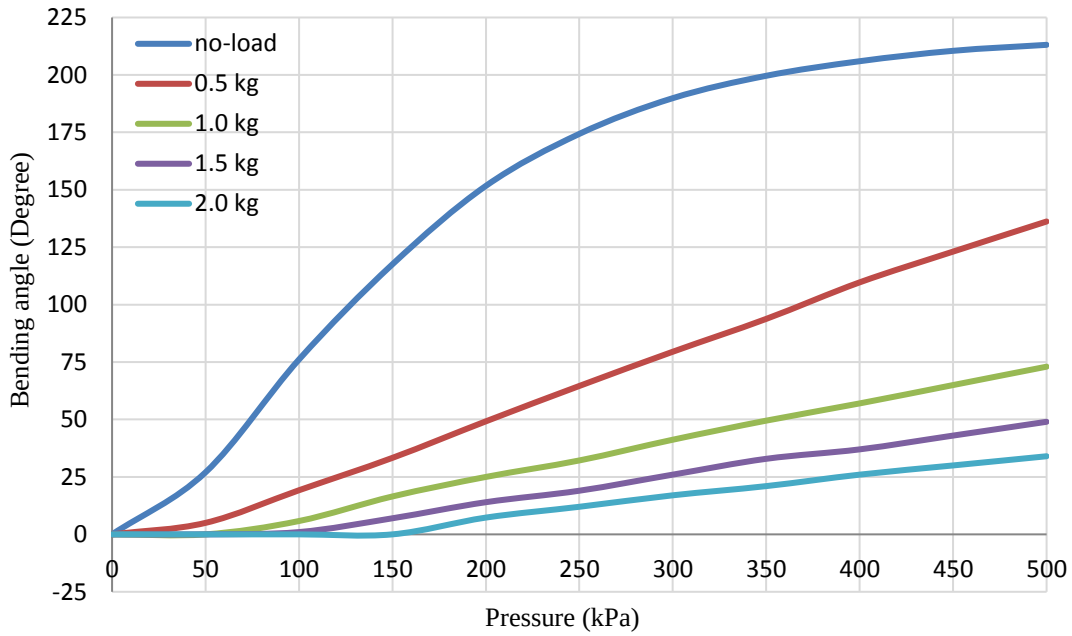

Figure 6.4 The bending angle at different attached load.

Table 6.2 The dimensions of the bending PMA

L_0 (m)	Rubber thickness (m)	Braided thickness (m)	Inner diameter (m)	Rubber stiffness(N/m)	Rod length (m)	Rod thickness (m)	Rod width (m)
0.3	1.1×10^{-3}	0.5×10^{-3}	12×10^{-3}	363.33	0.3	0.002	0.006

6.2.2 Kinematics of the SBCA

In general connecting the two ends of a line with length L results a circle (Figure 6.5). The dimension for this circle can be calculated as:

$$circumference = L = \pi D = 2\pi r \tag{6.1}$$

Where: D is the diameter and r is the radius of the circle.

Or:

$$D = \frac{L}{\pi} \tag{6.2}$$

Or:

$$r = \frac{L}{2\pi} \tag{6.3}$$

The angle of the circle is fixed at 360°.

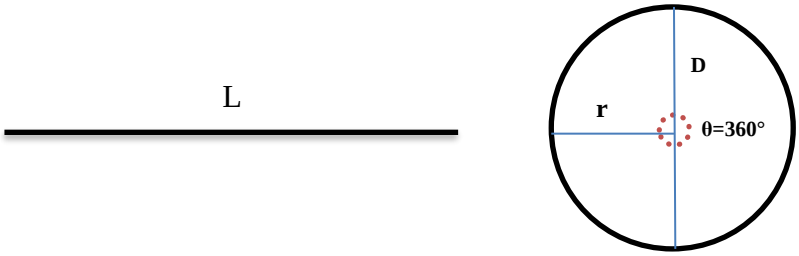

Figure 6.5 Line to circle conversion

Since, the maximum bending angle of the SBCA is not constant and it depends on the resting length (L_0) of the actuator, the bending angle can be measured using the arc length formula as follows:

$$Arc = \frac{\beta^{\circ}}{360^{\circ}} 2\pi r \tag{6.4}$$

Alternatively:

$$\beta^{\circ} = \frac{360^{\circ}\, Arc}{2\pi r} \tag{6.5}$$

Figure 6.6 illustrates the geometrical analysis of the SBCA at bending behaviour.

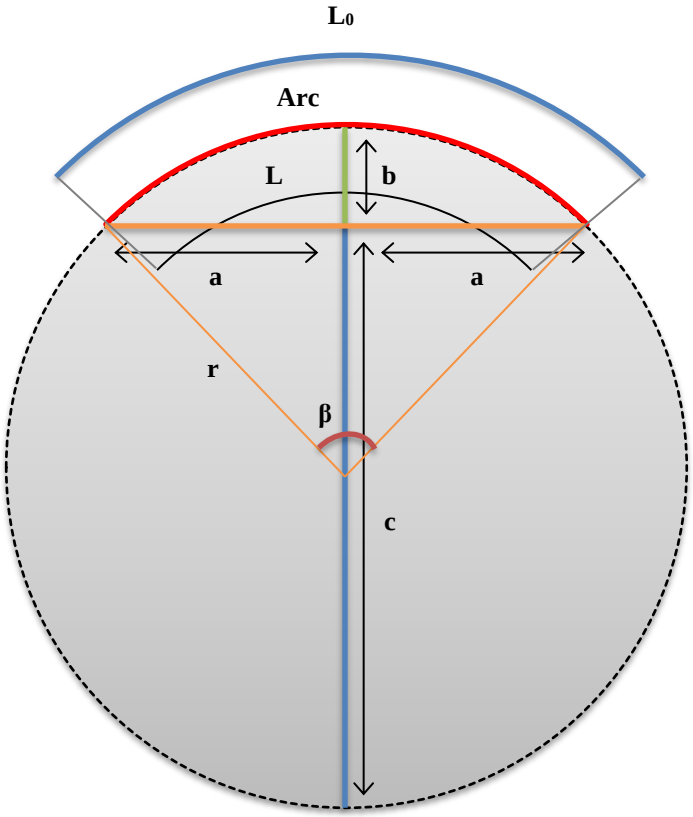

Figure 6.6 The geometrical analysis of the SBCA

Since, the rear length L_0 is constant due to the reinforcement rod; therefore, the only change will be in the length L because of the contraction performance. The bending angle β of the SBCA will be calculated according to the middle *Arc* (see Figure 6.6) as follows:

$$Arc = \frac{L_0 + L}{2} \tag{6.6}$$

Since:

$$\varepsilon = \frac{L_0 - L}{L_0} \tag{6.7}$$

Alternatively:

$$L = L_0(1 - \varepsilon) \tag{6.8}$$

Substituting (6.8) in (6.6):

$$Arc = \frac{L_0(2 - \varepsilon)}{2} \tag{6.9}$$

And:

$$\beta^{\circ} = \frac{360^{\circ} L_0(2-\varepsilon)}{4\pi r} \tag{6.10}$$

From (6.10) the bending angle β depends on the initial length of the actuator L_0, the contraction ration and the radius. From chapters two and four, the maximum contraction ratio is about 30%.

Hence, from (6.10) and Figure 6.6, the maximum bending angle β_{max} occurs at the maximum contraction ratio ε_{max} and the minimum radius r_{min} for a constant initial length.

Then:

$$\beta^{\circ}_{max} = \frac{360^{\circ} L_0(2-\varepsilon_{max})}{4\pi r_{min}} \tag{6.11}$$

Or:

$$\beta^{\circ}_{max} = \frac{360^{\circ} L_0(2-0.3)}{4\pi r_{min}}$$

Or:

$$\beta^{\circ}_{max} = \frac{48.7 L_0}{r_{min}} \tag{6.12}$$

Again from Figure 6.6 and using the intersecting Chords theorem (Shawyer, 2010):

$$a.a = b.c \tag{6.13}$$

Alternatively:

$$c = \frac{a^2}{b} \tag{6.14}$$

The diameter of the circle is:

$$Diameter = b + c \tag{6.15}$$

Or:

$$Diameter = b + \frac{a^2}{b} \tag{6.16}$$

Then, the radius is:

$$r = \frac{b}{2} + \frac{a^2}{2b} \tag{6.17}$$

Or:

$$r = \frac{a^2+b^2}{2b} \tag{6.18}$$

Since, a is the half the Arc's width W and the b is the Arc's height H, then:

$$r = \frac{W^2+4H^2}{8H} \tag{6.19}$$

From (6.19), the radius of the Arc can be found from its height and the width.

- Special case 1:

At β equal to 360°, the SBCA shapes as a circle. Therefore, the width of the *Arc* is zero and the radius is constant, and it is equal to H/2.

- Special case 2:

If the *W* is zero, the radius is constant and it equal to H/2 and β is equal or more than 360°, the value of the bending angle depends on the initial length of the SBCA only.

6.2.3 The bending force of the SBCA

The volume of Cylinder is:

$$V = \frac{\pi D^2 L}{4} \tag{6.20}$$

From Figure 6.6, The volume of the SBCA can be define as:

$$V = \frac{\pi D^2 Arc}{4} \tag{6.21}$$

And:

$$Arc = b\ cos\theta \tag{6.22}$$

$$D = \frac{b\ sin\theta}{n\pi} \tag{6.23}$$

Then:

$$V = \frac{b^3\ sin^2\theta\ cos\theta}{4n^2\pi} \tag{6.24}$$

From the virtual work theorem, the total force (F_t) can be calculated as:

$$F_t = P\ \frac{dV}{dArc} \tag{6.25}$$

Or:

$$F_t = P\ \frac{b^2}{4n^2\pi}(sin^2\theta - 2cos\theta) \tag{6.26}$$

The increment of the actuator diameter applies a radial force on the inserted rod, this force can be calculated by using the virtual work theorem as follows:

$$F_{rt} = P\frac{dV}{dD} \tag{6.27}$$

Or:

$$F_{rt} = P\frac{b^2}{4ncos\theta}\ (2sin\theta\ cos\theta - sin^3\theta) \tag{6.28}$$

Where: F_{rt} is the total resistance force.

The circumference of the actuator is:

$$C = n\pi D \tag{6.29}$$

Since the resistance force affects only on the rod, then the resistance force on the rod is:

$$F_{rr} = \frac{F_{rt}}{(\frac{C}{W_r})} \tag{6.30}$$

Where: W_r is the width of the rod. Then, the net force of the SBCA is the vertical force and can be calculated as:

$$F = F_t\ cos\beta - F_{rr} \tag{6.31}$$

6.2.4 Experiments and validation

To validate the proposed kinematics, three different bending actuators are designed and built in initial lengths (20 cm, 30 cm, and 50 cm) respectively (see Table 6.3).

A MPU 6050 sensor is mounted to the free end of the actuator to measure the bending angle. While the force is recorded by attach a load till the bending angle reaches zero degree. The both experiments done at 500 kPa.

Table 6.3 The bending angle and the bending force for the SBCA.

Length of SBCA (cm)	The maximum bending angle (degree)		The maximum bending force (N)	
	Experimental	Theoretical	Experimental	Theoretical
20	135	137.5	45.126	44.27
30	215	217.38	68.67	66.48
50	462	463.8	107.91	110.09

6.3 Double bend pneumatic muscle actuator (DB-PMA)

This section presents a novel design for a double bend pneumatic muscle actuator (DB-PMA) inspired by snake lateral undulation. The presented actuator has the ability to bend in opposite directions from its two halves. This behaviour results in horizontal and vertical movements of the actuator distal ends. The kinematics for the proposed actuator are illustrated and experiments conducted to validate its unique features.

Snake propulsion patterns are used to design snake robots to achieve several goals, such as rescue missions after natural and man-made disasters, inspections, investigations, and maintenance for dangerous or narrow areas (Erkmen, Erkmen, Matsuno, Chatterjee, & Kamegawa, 2002; Hopkins, Spranklin, & Gupta, 2009; Transeth, Pettersen, & Liljebäck, 2009). The multiple links snake robot was designed by Shan and Koren (1993) by using direct current (DC) motors to control the angles between the links and solenoids with sharp tip pins to generate a push force to the ground, and provide forward movement by moving the joints in a lateral direction. A wheel snake-like robot, SAM, was presented by Yamakita, Yamada, and Tanaka (2003) The friction between the wheels and the ground was ignored. A series of multi-module snake robots were designed by Wright et al. (2007), and the joint angle was controlled by a servo motor via a proportional–integral–derivative (PID) control system. Wright et al. (2012) designed a serial-linkage snake robot that contained several rigid modules with a DC motor and a gear box for each, resulting in an extendable 16 degrees of freedom (DoF).

6.3.1 Snake motion

Snake propulsion can be classified into four patterns: lateral undulation (serpentine), rectilinear locomotion, sidewinding, and concertina progression (Transeth et al., 2009) (Hopkins et al., 2009) (Hirose & Yamada, 2009). Lateral undulation is the most effective locomotion mode and it is widely perceived in almost all kinds of snakes. For this reason, we chose this pattern for our research. The snake forms its body into several curves, positioning in the X-Y planes during the lateral undulation. Figure 6.7 shows the lateral undulation locomotion of a snake.

Figure 6.7 The lateral undulation locomotion of a snake.

6.3.2 Structure of the Double-Bend Actuator

The basic structure of the contraction PMA is shown in Figure 6.8. The length of the braided sleeve was assumed to be similar to the length of the inner rubber tube to ensure that the braided angle θ is less than 54.7°. Figure 6.7 shows how the snake bends its body several times in two directions. The shape and the performance of this bending pattern were used to design a double bend pneumatic muscle actuator (DB-PMA) by inserting two thin reinforcement rods between the rubber tube and the sleeve. Each rod was placed on opposite sides of the two halves of the contraction actuator as illustrated in Figure 6.9. Each rod was three-dimensional (3D) printed with length of 28 cm, width of 0.6 cm, and thickness of 0.1 cm.

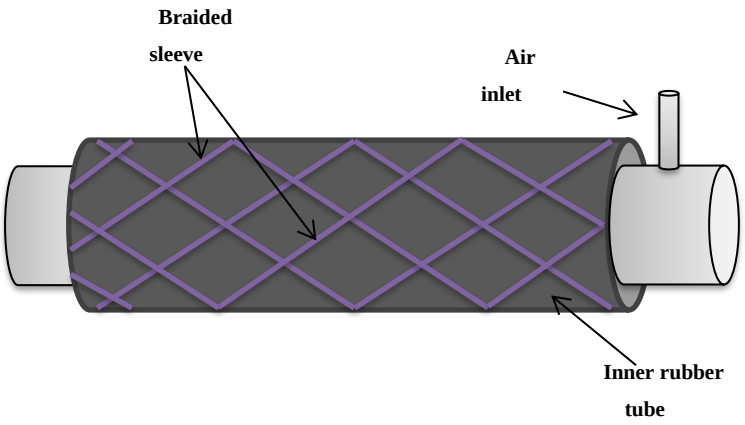

Figure 6.8 The structure of the contraction pneumatic muscle actuator (PMA).

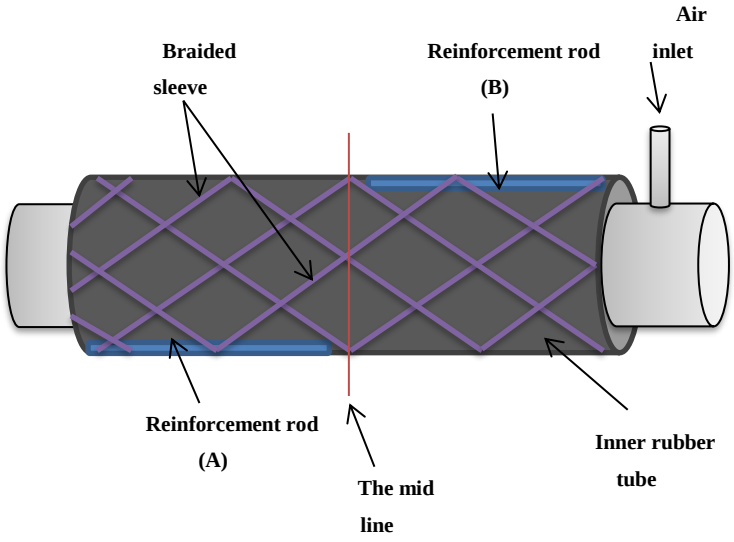

Figure 6.9 The structure of the double-bend pneumatic muscle actuator (DB-PMA).

The contraction occurs on the free sides while the rods prevent it, which leads to a bending behaviour as shown in Figure 6.10.

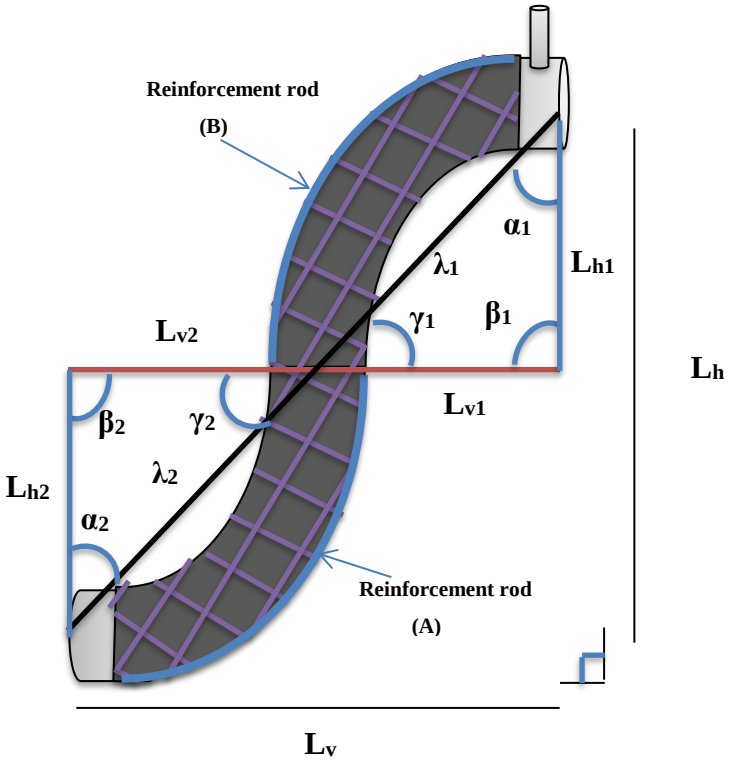

Figure 6.10 The bending behaviour and the geometrical analysis of the DB-PMA.

6.3.3 Kinematics of the DB-PMA

The geometrical analysis of the proposed arm is illustrated in Figure 6.9 and Figure 6.10 in two conditions according to the applied pressure: a relaxed and a pressurized condition.

6.3.3.1 Relaxed Condition

The length of the DB-PMA at zero pressure can be described in (6.32):

$$L_v = \lambda = L_0 \tag{6.32}$$

Where:

$$\lambda = \lambda_1 + \lambda_2 \tag{6.33}$$

where L_v is the vertical actuator length and L_0 is the actuator length at zero pressure. Hence, the length of the double-bend actuator is divided into two components: the vertical length and the horizontal length. Due to the relaxed condition, the horizontal length of the DB-PMA is zero.

6.3.3.2 Pressurised condition

Figure 6.10 shows both the vertical and horizontal lengths of the DB-PMA under pressurised conditions. The proposed actuator moves horizontally by the summation of the horizontal components of the first and the second halves, as shown in (6.34).

$$L_h = L_{h1} + L_{h2} \tag{6.34}$$

Where; L_h is the total horizontal movement with respect to the section area of the actuator, L_{h1} is the horizontal length of the first half, and L_{h2} is the horizontal length of the second half.

Both the vertical and horizontal movements can be calculated by using the cosine law as shown in (6.35):

$$\lambda_1^2 = L_{v1}^2 + L_{h1}^2 - 2L_{v1}L_{h1}cos\beta_1 \tag{6.35}$$

Where; λ_1 is the distance between the first end and the mid line of the actuator and β_1 is the angle between the direction of the vertical and horizontal distances of the first half.

Similarly, the distance between the second end and the mid line (λ_2) of the actuator under a pressurised condition is described in (6.36):

$$\lambda_2^2 = L_{v2}^2 + L_{h2}^2 - 2L_{v2}L_{h2}cos\beta_2 \tag{6.36}$$

From Figure 6.10, both the vertical and the horizontal lengths of the proposed actuator can be found as follows:

$$L_v = (\lambda_1^2 + L_{h1}^2 - 2\lambda_1 L_{h1}cos\alpha_1)^{\frac{1}{2}} + (\lambda_2^2 + L_{h2}^2 - 2\lambda_2 L_{h2}cos\alpha_2)^{\frac{1}{2}} \tag{6.37}$$

and:

$$L_h = (\lambda_1^2 + L_{v1}^2 - 2\lambda_1 L_{v1}cos\gamma_1)^{\frac{1}{2}} + (\lambda_2^2 + L_{v2}^2 - 2\lambda_2 L_{v2}cos\gamma_2)^{\frac{1}{2}} \tag{6.38}$$

Alternatively, the angles can be calculated in terms of the distances as follows:

$$\beta_i = \cos^{-1}\frac{L_{vi}^2 + L_{hi}^2 - \lambda_i^2}{2L_{vi}L_{hi}}, (i \in R) \tag{6.39}$$

where i is either 1 or 2 according to which half of the angle is being calculated.

$$\alpha_i = \cos^{-1}\frac{\lambda_i^2 + L_{hi}^2 - L_{vi}^2}{2\lambda_i L_{hi}}, (i \in R) \tag{6.40}$$

and:

$$\gamma_i = \cos^{-1}\frac{\lambda_i^2 + L_{vi}^2 - L_{hi}^2}{2\lambda_i L_{vi}}, (i \in R) \quad (6.41)$$

6.3.3.3 Special Condition1

For identical reinforcement rods with similar material and dimensions, the lengths and angles of the presented actuator at pressurised conditions are:

$$L_{v1} = L_{v2} \quad (6.42)$$

$$L_{h1} = L_{h2} \quad (6.43)$$

$$\lambda_1 = \lambda_2 \quad (6.44)$$

$$\beta_1 = \beta_2 = 90^0 \quad (6.45)$$

$$\alpha_1 = \alpha_2 \quad (6.46)$$

$$\gamma_1 = \gamma_2 \quad (6.47)$$

6.3.3.4 Special Condition2

If the bending angles of the first and the second halves equal 90°, then:

$$\alpha_1 = \alpha_2 = \gamma_1 = \gamma_2 = 45^0 \quad (6.48)$$

And:

$$L_{v1} = L_{v2} = L_{h1} = L_{h2} \quad (6.49)$$

Or:

$$L_v = L_h = \frac{L_0}{2} \quad (6.50)$$

Or:

$$L_v + L_h = L_0 \quad (6.51)$$

6.3.4 Experiments and Validations

Two identical 28 cm reinforcement rods were placed in the two halves of a 60 cm contraction actuator to create a DB-PMA. Special case 1 was used to calculate the angles and distances for the DB-PMA. Two (HC-SR04) ultrasonic sensors by (ElecFreaks, Shenzhen, China) were used to measure the vertical (L_v) and the horizontal (L_h) distances for the presented actuator. Figure 6.11 illustrates the presented actuator at two different pressures.

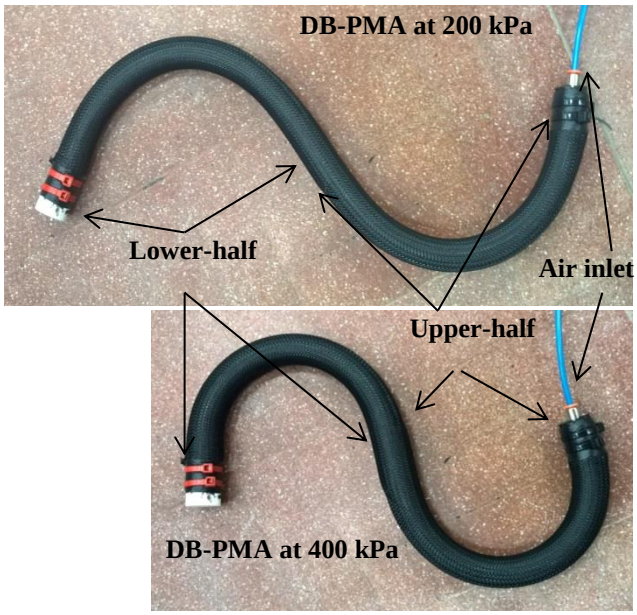

Figure 6.11 The presented DB-PMA at two different air pressures.

The pressure was applied by using a Matrix 3/3 solenoid valve in 50 kPa steps. At each pressure step, both the vertical and horizontal distances were measured by sensors and the angles were manually measured for several repeats and the average was recorded.

Figure 6.12 a–f shows the experiment and validation results for the distances and angles of the presented actuator.

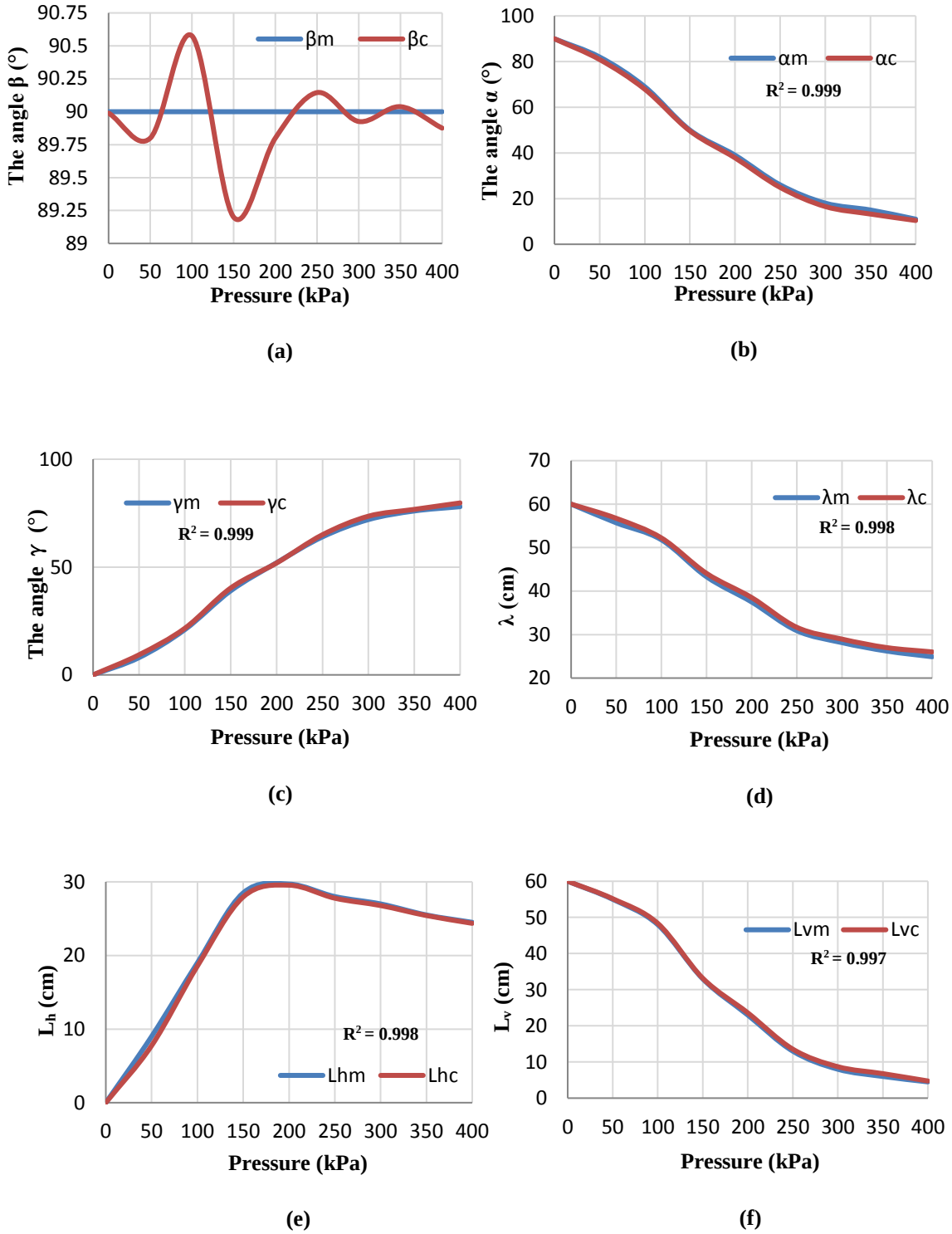

Figure 6.12 The parameters of the DB-PMA as a function of air pressure: (**a**) β_m and the calculated β_c angle, (**b**) α_m and the calculated α_c angle, (**c**) γ_m and the calculated γ_c angle, (**d**) λ_m and the calculated λ_c distance between the two ends, (**e**) L_{hm} and the calculated L_{hc} horizontal distance, and (**f**) L_{vm} and the calculated L_{vc} vertical distance.

Figure 6.12.a shows the calculation and the measurement value of β. Since the actuator is designed under special case 1, β has to be 90°. The measured angle is similar to the designed angle, with a maximum error of 0.6°. Because β is constant, α decreases from 90° to 10° (Figure 6.12.b), whereas γ increases from 0° to 80°, as shown in Figure 6.12.c, so that the summation of the triangle angles is 180° at each pressure step.

Figure 6.12.d illustrates the performance of λ with the increase in the applied air pressure. This distance decreases when the pressure increases from the original length of the actuator to about 25 cm at 400 kPa. When the horizontal distance in Figure 6.12.e was changed from 0 to 24.3 cm, through to its maximum value of 30 cm, the maximum change in horizontal direction occurred with special case 2 when both α and γ were about 45°. Figure 6.12.f shows that L_v decreases continuously with pressure increase.

The maximum variation ratio in the horizontal (εh) and vertical (εv) distances are defined in Equations (33) and (34) as follows:

$$\varepsilon h = \frac{L_0 - L_h}{L_0} \tag{6.52}$$

And:

$$\varepsilon v = \frac{L_0 - L_v}{L_0} \tag{6.53}$$

where L_0 is the initial length of the actuator at relaxed conditions according to the designed dimensions. The maximum ratios for the horizontal and vertical distances are 0.5 and 0.83, respectively. In comparison with the simple contraction PMA, the DB-PMA can be considered an efficient alternative in terms of the contraction ratio between the two ends of the actuator.

6.4 Circular pneumatic muscle actuator CPMA

Special types of facial muscles control the opening of the human eyes and mouth. The unique circular shape of these muscles provides an inspiration of circular pneumatic muscle actuator (CPMA) which has the ability to reduce the inner diameter by shrunk the inner circumference and increment the diameter of the actuator itself. The diameter

reduction of the CPMA causes a radial force on the object inside the actuator. The design and the kinematics of the presented actuator are explained and validated in this section.

6.4.1 Human facial muscles

Human facial muscles have unique features. They lie on the top of the body joints and their function is either to open and close the orifices of the face, or to pull the skin into intricate actions, creating facial expressions (Goodmurphy & Ovalle, 1999).

Martini, Timmons, and Tallitsch (2008) argue that muscle tissues share four basic properties:

1- Excitability: the ability to respond to stimulation.
   - Skeletal muscles normally respond to stimulation via the nervous system.
   - Cardiac and smooth muscles respond to the nervous system and circulating hormones.
2- Contractility: the ability to actively shorten and exert a pull or tension that can be harnessed by connective tissues.
3- Extensibility: the ability to continue to contract over a range of resting lengths.
4- Elasticity: the ability of a muscle to rebound toward its original length after a contraction.

A special shape of the human muscles has been noticed around the eyes (Orbicularis Oculi) and around the mouth (Orbicularis Oris). Each of these muscles has a circular shape. Figure 6.13 shows the shape of the human circular muscle. The contraction of this muscle decreases the mouth slot, while the resting causes the mouth to open. Similar effects occur in the human eyes.

This singular type of human skeletal muscle inspired us to design the CPMA, which has an ability to decrease its inner area by shrinking the outer and inner circumference and increase its diameter.

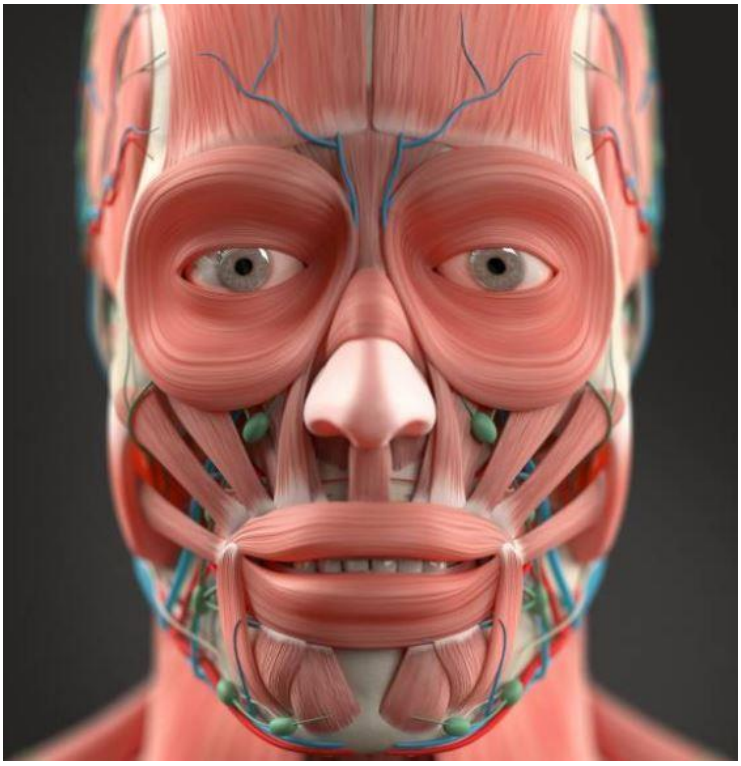

Figure 6.13 The human facial muscles including the circular muscles around the mouth and the eyes (Pinterest, 2019, June 14).

6.4.2 The design of the CPMA

The way to build a contraction PMA is also used to design and implement the CPMA. Similar lengths of a braided sleeve and an inner rubber tube are used to build the CPMA. The two ends are connected together by a solid aluminium cylinder. By pressurising the actuator, both the outer and the inner diameter of the CPMA will reduce, while the diameter of the actuator itself will increase until the braided angle reaches its critical value or the maximum value of the sleeve diameter is achieved. The triple diameter changes lead to decrement in the opening area. The opening area at relaxed condition (zero air pressure) depends on the rest length of the braided sleeve and its diameter.

6.4.3 The kinematics of the CPMA

Figure 6.14.a-b illustrates the geometrical analysis of the PMA and the contractor actuator of length *L* and diameter *D*. By bending this actuator until the two ends connect to each other, the resulting shape is two overlapping circles as shown in Figure 6.14.c.

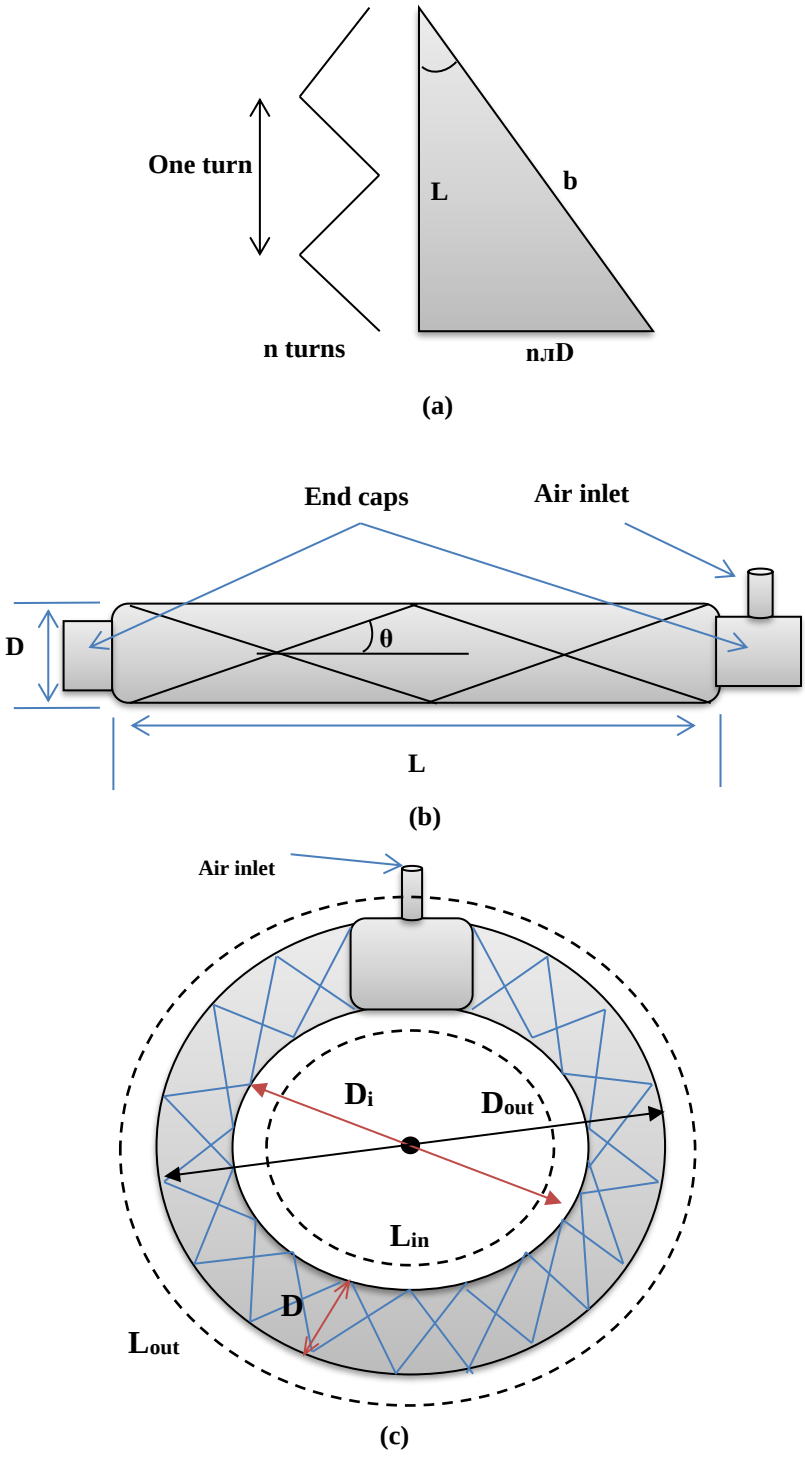

Figure 6.14 The geometrical structure of the CPMA. (a) the geometrical of the PMA. (b) The contraction actuator. (c) The circular actuator.

From Figure 6.14.a:

$$\tan\theta = \frac{n\pi D}{L} \tag{6.54}$$

Where θ is a braided angle and n is the turn numbers of strand length b.

Assuming that the diameter D of the contraction actuator in Figure 6.14.b is equal to the diameter of the CPMA and from Figure 6.14.c:

$$D_{in} = D_{out} - 2D \tag{6.55}$$

Where D_{in} is the inner diameter of CPMA and D_{out} is the outer diameter. The outer circumference (L_{out}) and the inner circumference (L_{in}) of the CPMA are defined in (6.56) and (6.57) as follows:

$$L_{out} = \pi D_{out} \tag{6.56}$$

$$L_{in} = \pi D_{in} \tag{6.57}$$

Assuming:

$$L_{out} = L \tag{6.58}$$

By substituting (6.58) in (6.56):

$$D_{out} = \frac{L}{\pi} \tag{6.59}$$

By substituting (6.54) and (6.59) in (6.55):

$$D_{in} = \frac{L}{\pi} - 2\frac{L\tan\theta}{n\pi} \quad (6.60)$$

Or:

$$D_{in} = \frac{L}{\pi}(1 - 2\frac{\tan\theta}{n}) \quad (6.61)$$

From (6.57):

$$L_{in} = L(1 - 2\frac{\tan\theta}{n}) \quad (6.62)$$

The contraction ratio for the contractor PMA is defined by:

$$\varepsilon = \frac{L_0 - L}{L_0} \quad (6.63)$$

Or:

$$L = L_0(1 - \varepsilon) \quad (6.64)$$

Where; L_0 is the length of the contraction actuator in the relaxed condition. By substituting (6.64) in (6.62):

$$L_{in} = L_0(1 - \varepsilon)(1 - 2\frac{\tan\theta}{n}) \quad (6.65)$$

From (6.61) and (6.65) the inner diameter and the inner circumference of the CPMA can be determined from the geometrical analysis of the contraction actuator.

6.4.4 The radial force of the CPMA

At pressurised conditions, the CPMA applied a force towards the centre of the actuator, along the radius. This force is created due to the shortness of the inner diameter.

By applying a virtual work law, the derivative of the input work (W_{in}) of the actuator is:

$$dW_{in} = p.dV \quad (6.66)$$

Where: p is the actuator pressure in (kPa) and V is the actuator volume in (m^3). Figure 6.15 shows the CPMA as a cylinder. The base area is a circular diameter D_{in} and the height is the actuator diameter D.

Both the inner diameter and the actuator diameter are changing with pressure which causes force (F) towards the centre, and the derivative of the output work (W_{out}) is:

$$dW_{out} = F.dD \tag{6.67}$$

Assuming that the losses are zero, the change in input work is equal to the change in output work:

$$dW_{in} = dW_{out} \tag{6.68}$$

Or:

$$F = p\frac{dV}{dD} \tag{6.69}$$

The volume of the cylinder V equal to:

$$V = \frac{\pi D_{in}^2 D}{4} \tag{6.70}$$

From (6.54) the height of the cylinder is:

$$D = \frac{L\tan\theta}{n\pi} \tag{6.71}$$

Substituting (6.60) and (6.71) in (6.70):

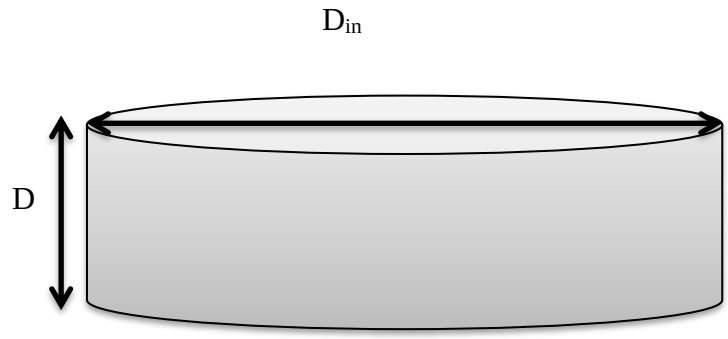

Figure 6.15 The geometrical structure of the CPMA as a cylinder.

$$V = \frac{1}{4}\left(\frac{L}{\pi}\left(1 - 2\frac{\tan\theta}{n}\right)\right)^2\left(\frac{L\tan\theta}{n}\right) \tag{6.72}$$

Differentiation in both the volume and the height with respect to θ gives:

$$\frac{dV}{dD} = \frac{dV}{d\theta} \times \frac{d\theta}{dD} \tag{6.73}$$

Then:

$$\frac{dV}{d\theta} = \frac{L}{n\pi cos^2\theta}\left(\frac{3L^2 tan^2\theta}{n^2\pi} - \frac{2L^2 tan\theta}{n\pi} + \frac{L^2}{4\pi}\right) \tag{6.74}$$

And:

$$\frac{dD}{d\theta} = \frac{L}{n\pi cos^2\theta} \tag{6.75}$$

Substituting (6.74) and (6.75) in (6.73) gives:

$$\frac{dV}{dD} = \frac{3L^2 tan^2\theta}{n^2\pi} - \frac{2L^2 tan\theta}{n\pi} + \frac{L^2}{4\pi} \tag{6.76}$$

The force in (6.57) can be found as follows:

$$F = p\frac{L^2}{4n^2\pi}(12\ tan^2\theta - 8n\ tan\theta + n^2) \tag{6.77}$$

Since the effective circumference is less than the actual length due to the length of the solid cylinder, then:

$$L = \acute{L} + L_s \tag{6.78}$$

Where: $\acute{L}$ is the effective outer circumference and L_s is length of the solid cylinder. Furthermore, assuming the required pressure to get a contact between the inner tube and the braided sleeve is p_0, then:

$$F = (p - p_0)\frac{\acute{L}^2}{4n^2\pi}(12\ tan^2\theta - 8n\ tan\theta + n^2) \tag{6.79}$$

6.4.5 Experiments and validations

A circular actuator is made by using a 38 cm expandable braided sleeve with a diameter variation of 2.5 to 4.5 cm. An inner rubber tube of 38 cm length and a diameter of 1.1 cm is fixed to the end of 5 cm solid aluminium cylinder which has a small inlet for the air. Both the rubber tube and the solid cylinder are covered by the braided sleeve makes the length of the braided sleeve similar to the length of the tube to ensure getting a braided angle less than 54.7^0. The other end of the tube and the sleeve is fixed to the second end of the solid cylinder to make a circular shape as in Figure 6.14.c. The *n* number for the selected sleeve dimensions is 2.75.

Several experiments are done to demonstrate the dimensions and the force for the CPMA and validate its kinematics. Air pressure is applied by solenoid (3/3 Matrix) valve and it is increased gradually from zero to 500 kPa by steps of 50 kPa. At each step, L_{out} and D are measured, and then the braided angle is calculated from (6.54). Figure 6.16 shows these dimensions as a function of pressure.

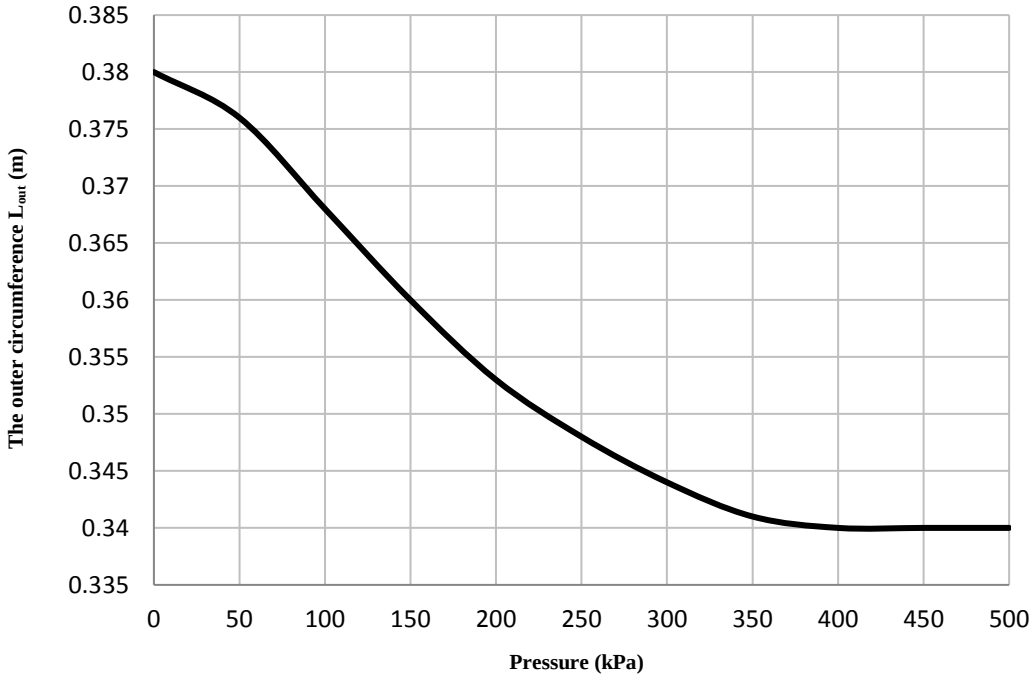

(a)

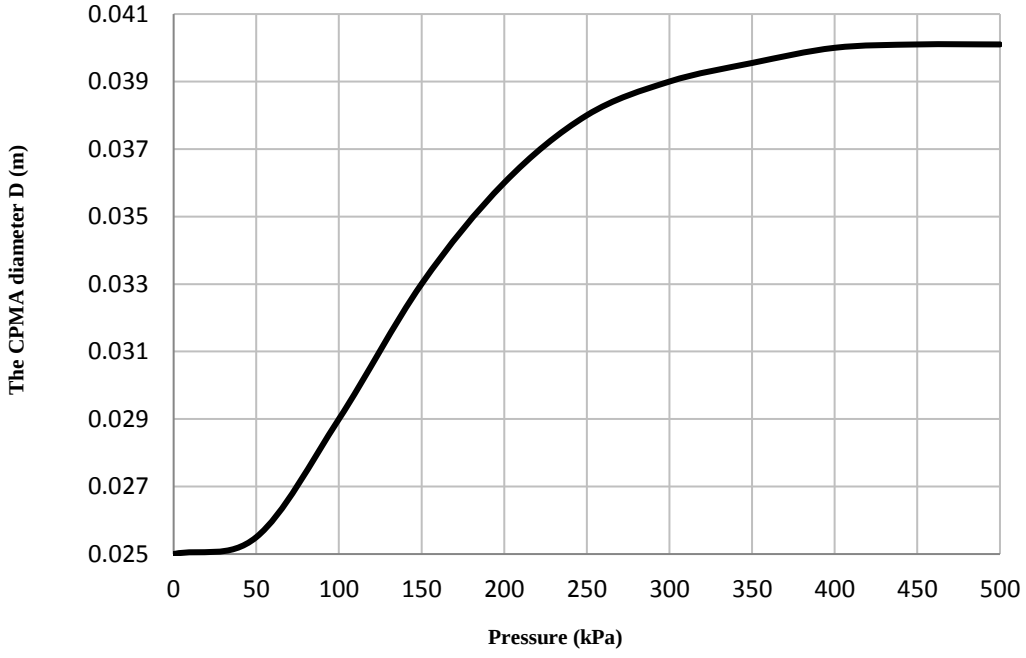

(b)

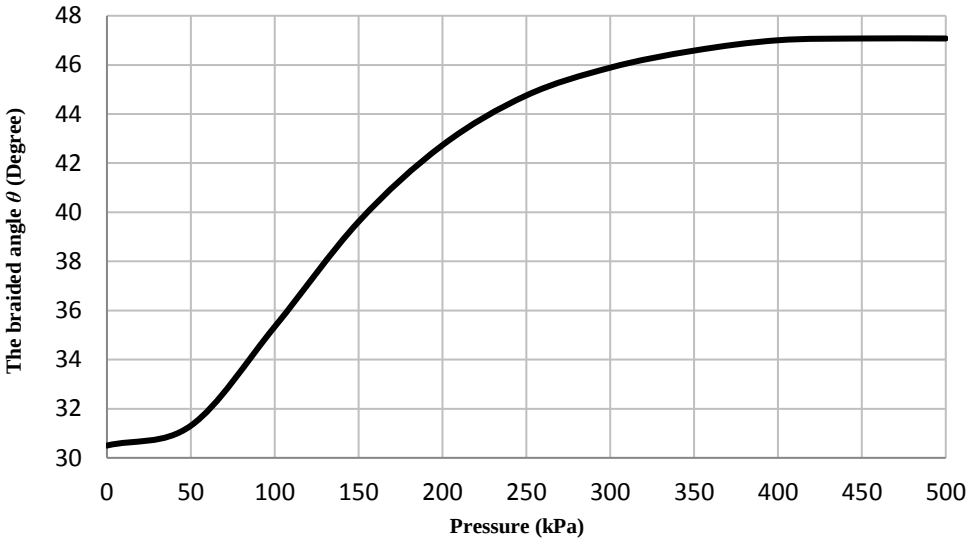

(c)

Figure 6.16 The variation of the CPMA's parameters according to the applied air pressure. (a) The outer circumference. (b) The diameter of CPMA. And (c) is the braided angle.

Figure 6.16.a shows that the outer circumference is reduced when the pressure is increased and that because of the value of the braided angle which it is below the critical value. As well as that mean, the L_{out} is under the contraction force but the contraction ratio is not as a simple contraction actuator due to the raise in the actuator diameter D (see Figure 6.16.b). The increment in D makes the outer circumference longer, and that reduces the contraction ratio. Figure 6.16.c illustrates the variation of the braided angle as a function of the applied air pressure. θ increased from its initial value 31.3^0 (according to the design's dimensions) to about 47^o and that met the design criteria to ensure that θ is less than 54.7^0.

Figure 6.17.a-b shows the reduction in the inner diameter D_{in} and the inner circumference L_{in} respectively. From (6.61) and (6.62), rising in the braided angle (the tangent value) leads to decreasing D_{in} and L_{in}, and that validate the presented kinematics of the CPMA.

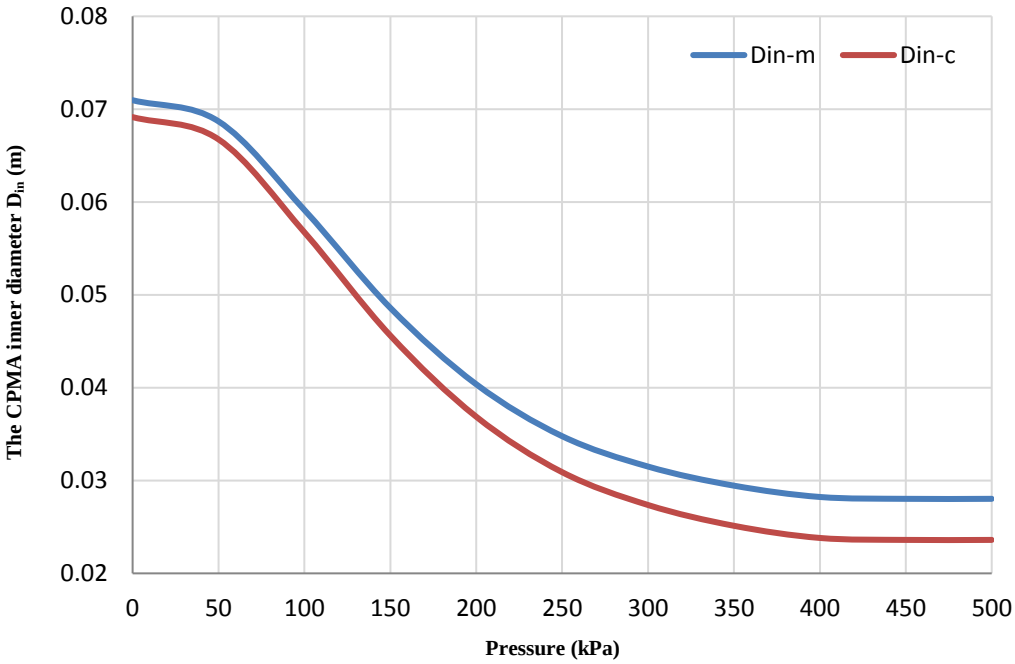

(a)

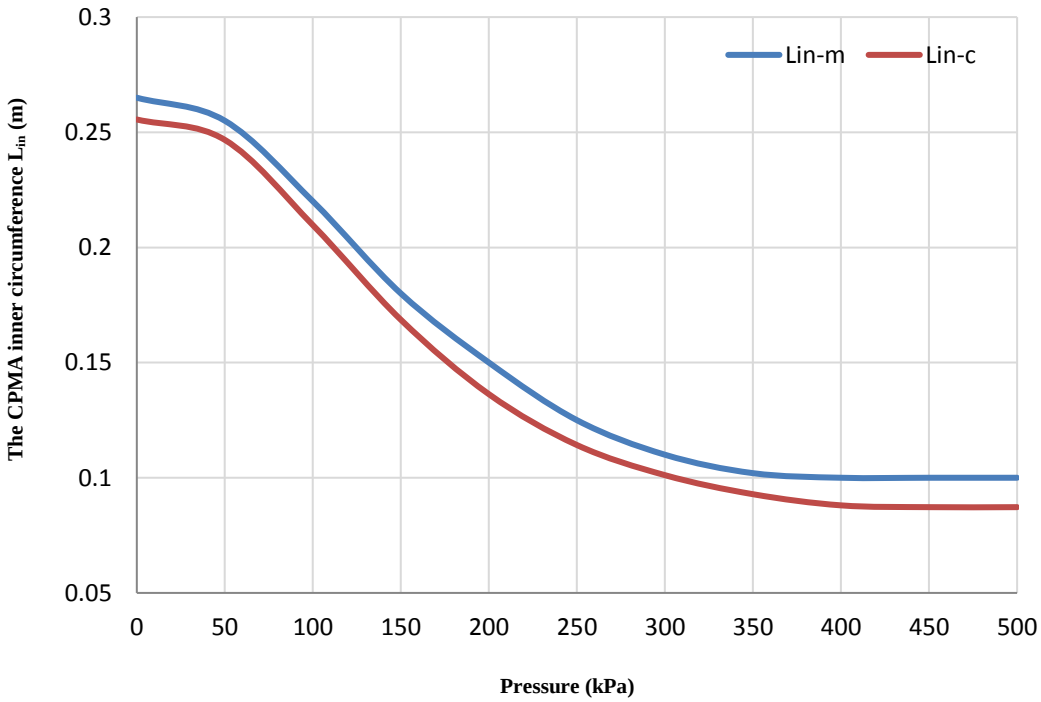

(b)

Figure 6.17 The validation of the CPMA's parameters. (a) The measured and the calculated inner diameter. (b) The measured and the calculated inner circumference.

The different contraction behaviour between the outer and the inner circumference explain the variation in the measured and the calculated D_{in} and L_{in} in Figure 6.17. While, in the presented kinematics, we assumed that the braided angle has a single value everywhere.

According to (6.77) and (6.79), the CPMA apply a force towards its centre due to the reduction in the inner diameter. To evaluate this force experimentally, a cylinder object of 6 cm in diameter is chosen with an ability to adjust its weight as shown in Figure 6.18. The applied air pressure is increased from zero to 500 kPa at 50 kPa steps. At each step the load is increased and the maximum value is recorded (the maximum load at non slipping). Figure 6.19.a-b illustrates the measurement and the calculated load for (6.77) and (6.79) respectively.

Figure 6.18 The experiment's equipment for actuation force.

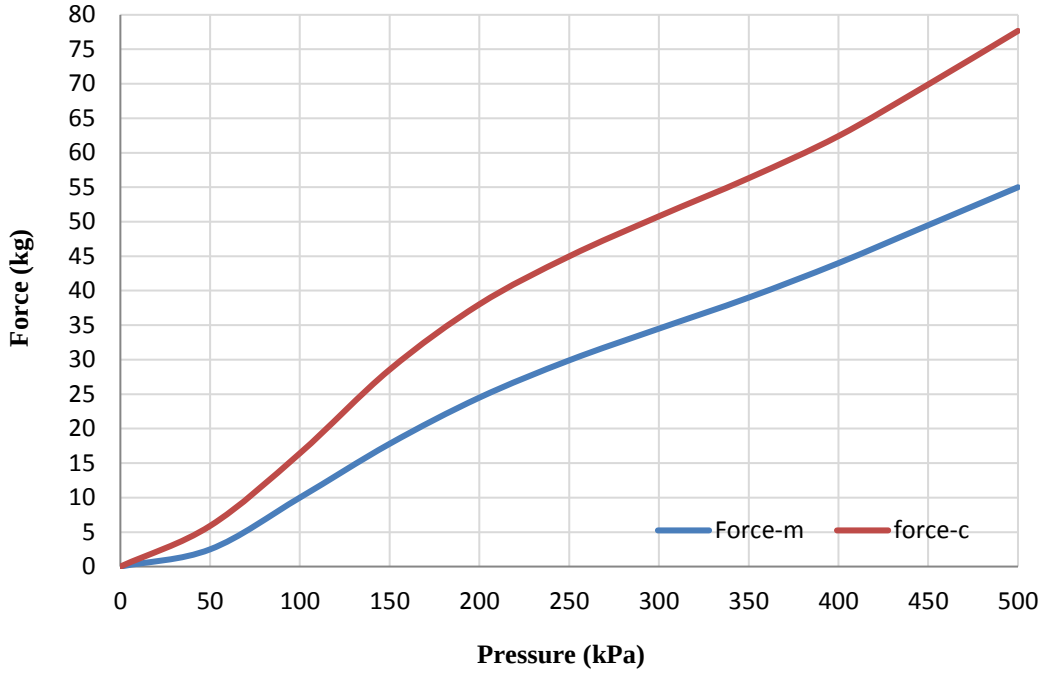

(a)

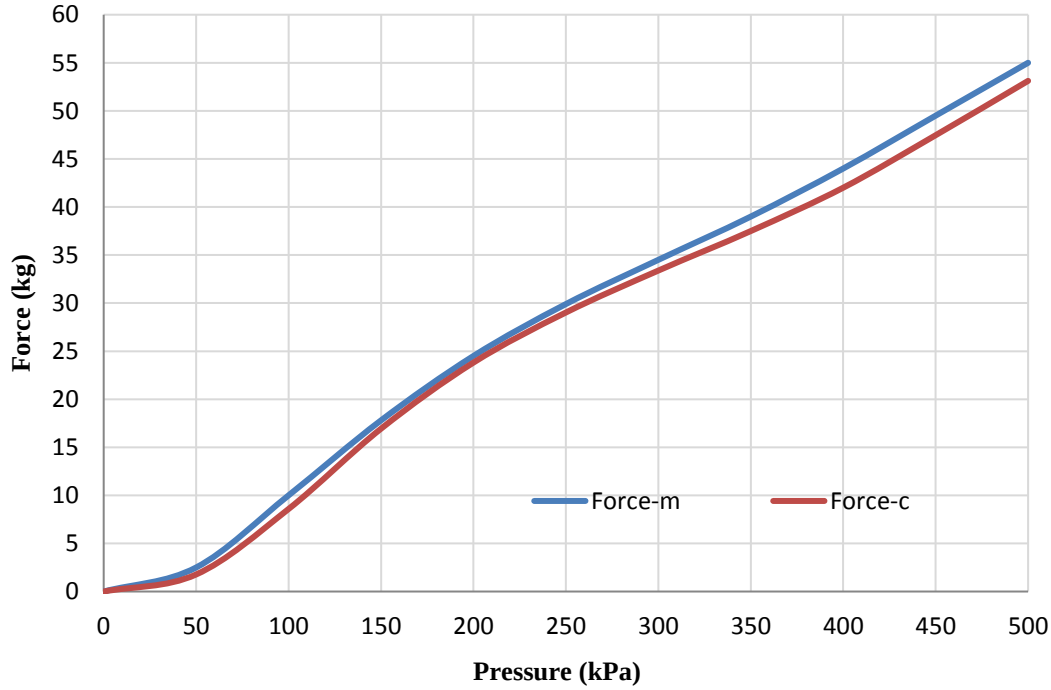

(b)

Figure 6.19 The measurement and the calculation force in kg. (**a**) The force according to (6.77). (**b**) The force according to (6.79).

The variations between the measurement force and the calculation force in Figure 6.19.a explain the effectiveness of the solid cap and the pressure need to establish the actuation force. For the structure of the presented CPMA, L_s is 5 cm and p_0 is 30 kPa. While Figure 6.19.b shows a slight difference between the experimental and the model force.

Chapter Seven:

7. Active soft end effectors for efficient grasping and safe handling

7.1 Introduction

Over recent years, several factors have driven researchers in both industry and academia to develop new grippers and robot end effectors. These factors include the need to decrease the cost of the systems and increase the range of products and materials a gripper can handle as robots are used in sectors other than traditional manufacturing (Fantoni et al., 2014). When the human hand grips an object, the grasp is determined based on expectations of the object's weight and using feedback from the fingertips to prevent the object slipping by adjusting the grasp force (Wettels, Parnandi, Moon, Loeb, & Sukhatme, 2009). In contrast, a typical mechanical robot gripper applies a fixed high force to the object to avoid slipping. This is inefficient in terms of energy use as often the grasp is firmer than is required and can also lead to damage if the object to be grasped is fragile. Similar techniques to that used by the human hand can be used in robots by attaching slip sensors to the robot gripper. The feedback from the tactile sensors reduces the experience reliability on robot operators and improves the end effector performance (Wettels et al., 2009) (Shimoga, 1996).

The cost of a gripper can represent more than 20% of the cost of the whole robot system and is subject to the task requirements and the complexity of the part to be handled. It may also add additional complexity to the control system (Choi & Koc, 2006). Typical traditional robot grippers were designed for predefined jobs and could not be used for different object dimensions, weights or shapes other than where variations were small. If a system is to be re-tasked to handle different objects, this can require modification of, or indeed entire replacement of, the gripper. Various dexterous or multi-use gripper designs have been proposed to overcome this issue. However, the high cost of such types of grippers and maintenance problems make its use limited to a few applications (Shimoga, 1996) (Choi & Koc, 2006).

While the cost is considered a minor issue for some industrial applications, innovative new actuators, such as pneumatic muscle actuators (PMA), which are low cost, low weight, flexible and soft (in addition to the many other advantages), make it a potential alternative to previous robot end effectors. From this biologically inspired artificial muscle, human-like robot hands have been created with both industrial and medical applications (Martell & Gini, 2007).

A range of varies actuated methods is recently used to design the soft robot grippers. Among these designs, Hassan et al. (2015) and Rateni, Cianchetti, Ciuti, Menciassi, and Laschi (2015) proposed a tendon-actuated soft three-fingers gripper made by using soft deformable materials. Giannaccini et al. (2014) proposed tendons soft gripper to deform and move a fluid-filled soft deformable container. Katzschmann, Marchese, and Rus (2015) and Mosadegh et al. (2014) presented soft continuum fingers made as two different extensible layers to establish a bending behaviour. A multiple bending directions micro gripper is developed by Wakimoto, Ogura, Suzumori, and Nishioka (2009), the actuators bend according to the pressurised internal chambers. A very different structure of continuum soft hand was presented by Niiyama et al. (2015). The gripper uses recently developed hinged pouch motors, which when pressurized bending in joints. Generally, these types of grippers are not able to vary their stiffness. While extremely compliant fingers may be required for grasping some objects. Stilli, Wurdemann, and Althoefer (2014) and Maghooa, Stilli, Noh, Althoefer, and Wurdemann (2015). Al Abeach, Nefti-Meziani, and Davis (2017) designed a variable stiffness gripper by varying a pressure inside the soft fingers which are made by an extension actuator and the grasping is occurred by tendons powered by contraction PMA.

Other types of soft grippers have been designed to provide compliant and safe grasping. The RBO hand by Deimel and Brock (2013) provides compliance which allows the hand to face its surfaces to that of an object in response to contact forces. Due to the softness, the RBO offers shape matching to increment the contact surface between hand and object without the requirement for obvious sensing and control. The hand's fingers are based on similar principles to that of the PneuNet actuator (Ilievski, Mazzeo, Shepherd, Chen, & Whitesides, 2011). The grasping force for this hand is up to 0.5 kg for three fingers. Deimel and Brock (2016) present the RBO hand-2, which is made similar to the human hand of five fingers. The weight of this hand is 178 g and it can grasp objects up to 0.5 kg. A three finger soft hand is designed by Homberg, Katzschmann, Dogar, and Rus (2015)

which is able to grasp a range of objects and can be mounted on existing robots used for grasping.

Several soft grippers have been presented in terms of safe grasping, among them, Amend, Cheng, Fakhouri, and Culley (2016) presented different commercial sizes of vacuum soft grippers varying from 1 mm to 1 m in diameter and able to grasp up to 3 kg, while, the gripper weight is varying from 1.1 kg to 2.9 kg. Wang et al. (2016), Nordin et al. (2013) and Faudzi et al. (2012) developed a bending actuator by using different braided angles and this idea has been used by Wang, McDaid, Giffney, Biglari-Abhari, and Aw (2017) to design a two-finger gripper to grasp an object by bending around it. The maximum experimental grasping force for their gripper is 61 g. Guo et al. (2018) presented a stretchable electroadhesion soft gripper by using a combination of the electrostatic force and a pneu-net (Mosadegh et al., 2014) soft bending actuator. Shintake, Rosset, Schubert, Floreano, and Shea (2016) designed an electrostatically actuated bending soft gripper able to grasp different object shapes.

In this chapter A three-fingers gripper has been designed based on SBCA (section 6.2.1) presented and its characteristics have been illustrated. Moreover, another three fingers are added to build a six-fingers gripper of two layers of contact points to increase the grasping performance. The CPMA is used together with basic extensor PMA to design an extensor-circular gripper, which provides an extraordinary grasping force in comparison to its weight, and then the design is developed by increasing the number of CPMAs to three. The modified design provides an extremely strong force able to grasp an object weighing up to 100 kg. The proposed new grippers are built to adapt to the shape of the object being grasped, allowing many different shaped objects to be grasped with a single device. They also seek to enhance efficiency by increasing the amount of payload that can be grasped whilst minimising power requirements and decreasing the control complexity when grasping objects.

7.2 Three fingers gripper base on SBCA

The proposed bending contractor actuator has been used to build a three-finger gripper as shown in Figure 7.1. Three identical actuators of 14 cm resting length were constructed using a 14 cm thin reinforcing rod placed along one side.

To maximize the range of motion in the fingers, a thin ribbon of elastomeric material is placed on the rear of each finger which causes the fingers to spread when the actuator is unpressurised. The top base of the gripper is made by a 3D printer and the complete gripper is shown in Figure 7.1.

The presented gripper can spread its fingers so that they are at a maximum of 20 cm apart and close them to the point where all fingers touch each other. This allows the gripper to grasp a large range of different object sizes.

In addition to the other advantages of the PMA, the proposed gripper has more benefits than other grippers for numerous reasons, such as low cost, which is about 10 dollars, easy to manufacture, wide dimension grasping ability, safe to low stiffness objects and it has a low mass (0.18 kg). Its inertia is also low, which potentially makes it safer for operation around humans.

In addition, it is easy to control by adjusting the air pressure in all fingers simultaneously, and the closed loop control is not needed to ensure that the three fingers make contact with the object because the fingers are compliant and will automatically bend around objects. To do this with a rigid noncompliant hand would require grasp planning and precise control of each finger.

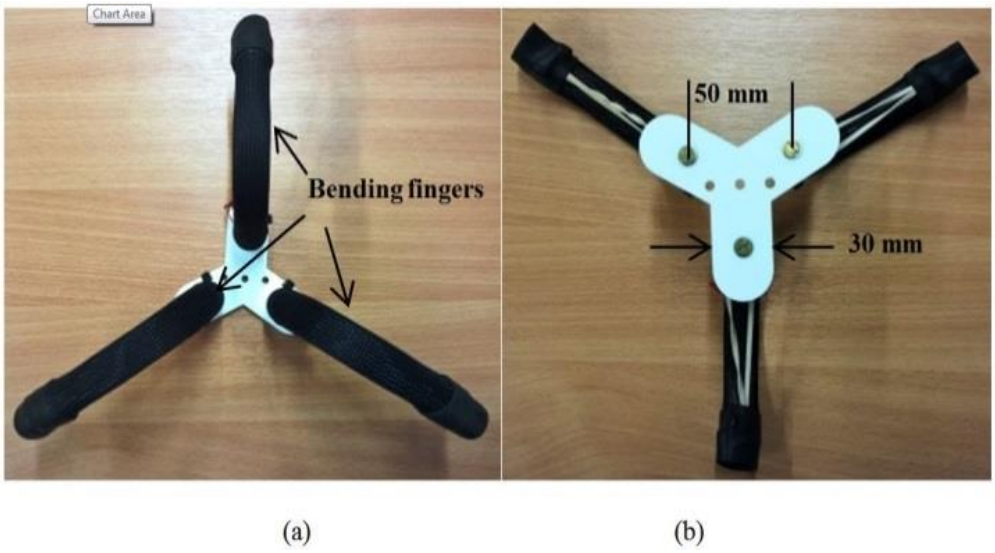

Figure 7.1 A three fingers gripper based on self-bending contraction actuator

Figure 7.2 shows that for cylindrical objects, the fingertips form a circle shape at different diameters, which depends on the diameter of the object. While different object shapes lead to putting the fingertips at different positions. The bending angle of the

proposed fingers is illustrated in Figure 7.3. This figure shows that the maximum bending angle for each finger is 72^0, which is more than is required to put them together at the centre of the gripper. Therefore, the force can be adjusted to grasp small objects such as the pen in Figure 7.6.

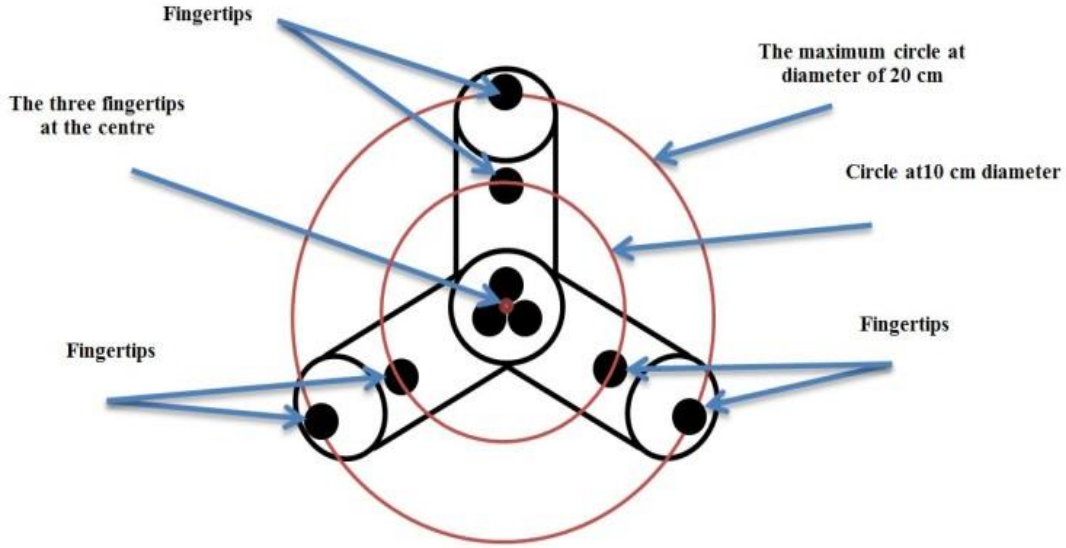

Figure 7.2 The fingertips of the gripper at different positions.

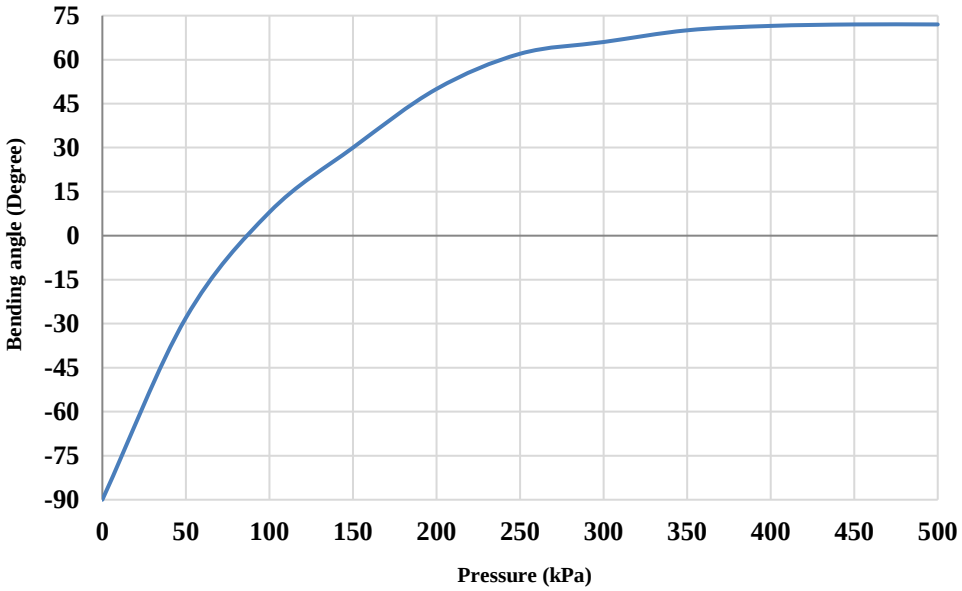

Figure 7.3 The bending angle –pressure characteristics for each finger.

Figure 7.4 shows that the force of a single finger is high at large cylinder diameters and decreases for smaller sizes. Because the finger's pressure for the small diameter is higher than the pressure for the big size, the pressure difference from the touch point to the maximum value (500 kPa) is reduced when the diameter is decreased since the finger needs more pressure to bend more. That reduces the force applied by the finger. Table 7.1 lists the minimum air pressure required to touch different diameter objects.

The maximum force for each finger is found at different bending angles, as follows:

- Cylindrical objects of different diameters are used for grasping by the proposed gripper.
- A force sensor is fixed at the fingertip to find the force value at each position.
- The pressure is increased manually from zero to the point of the force sensor start reading. This pressure has been recorded, by a pressure sensor, as a minimum required pressure to touch the object.
- The pressure then increases until it reaches the 500 kPa. At this point, the maximum force value is recorded.

Figure 7.5 shows the maximum force of each finger at different diameters.

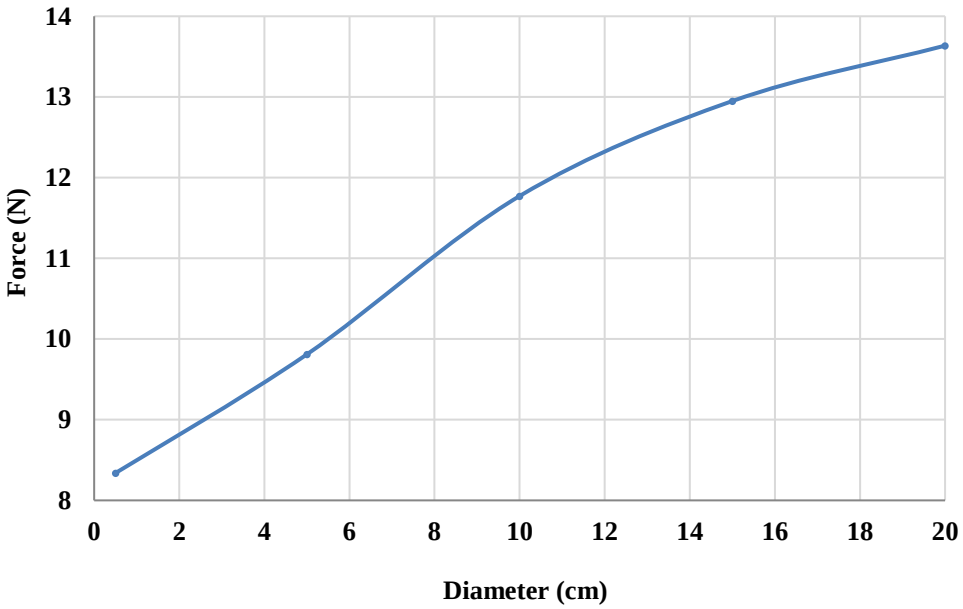

Figure 7.4 The force of a single finger at different positions.

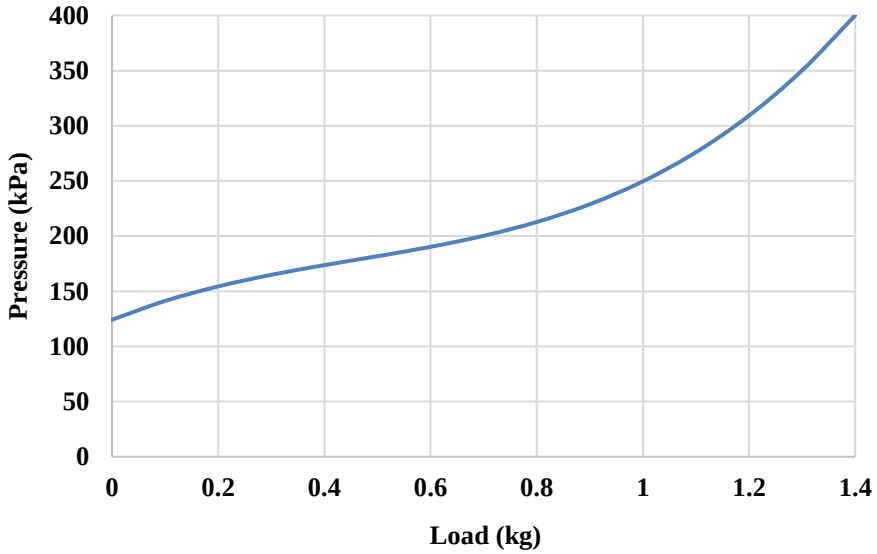

Figure 7.5 The payload–pressure characteristics for the three-fingers gripper.

Table 7.1 The maximum bending angle at different loads.

Object diameter (cm)	*Minimum required pressure (kPa)*
0.5	126
5	110
10	76
15	55
20	47

An experiment was undertaken to discover the maximum gripper payload with a 6 cm diameter cylindrical object of different weights. At each load value, the pressure was applied until the grasping operation occurred without slipping, then the experiment was repeated and the corresponding air pressure amount recorded. As a result, the payload for this gripper at this specific diameter is 1.4 kg but the grasping payload differs depending on the object's dimensions, as shown in Figure 7.4. The experiment results are illustrated in Figure 7.5, which shows that the grasping force is increased by applying more pressure to the fingers. The presented gripper has an advantage over the designed gripper in (Deimel & Brock, 2013), (Deimel & Brock, 2016) and (Homberg et al., 2015) due to its

increased grasping load. While the proposed gripper has a similar weight to the RBO hand and RBO hand 2, it provides an about three times of grasping weight.

Different object shapes could be grasped as shown in Figure 7.6. The pressure required to ensure contact between the fingertips when grasping depends on the dimensions of the target objects. However, the force needed can be defined as:

$$F = \frac{m(g+a)}{\mu\, n} \times s \tag{7.1}$$

Where F is the required grasping force in (N), m works part weight (kg), g is the gravitation acceleration and is approximately equal to 9.81 (m/s^2), a is the acceleration of movement, μ is the friction coefficient and is dependent on the material of both the finger and the object, n represents the number of fingers and is equal to 3 in this case, and s is the safety factor.

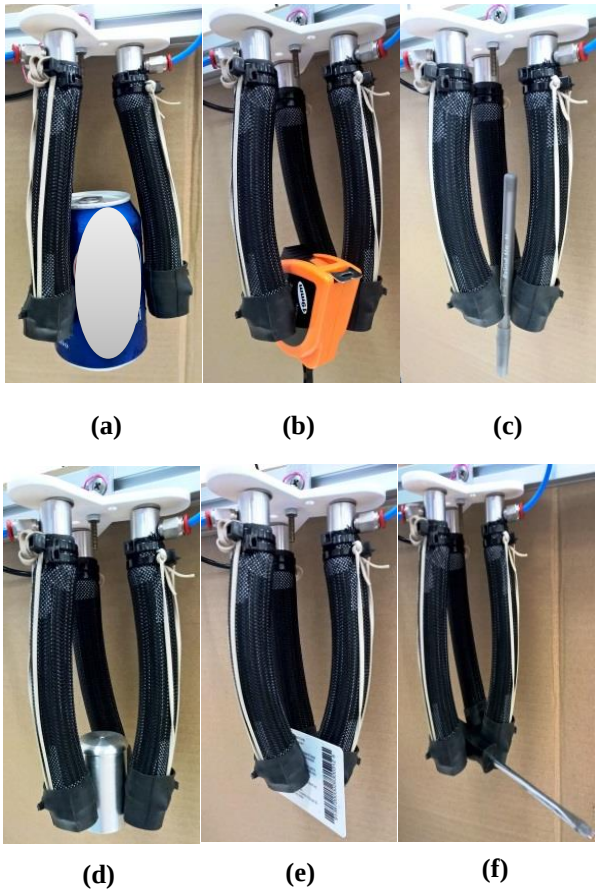

Figure 7.6 Multiple objects grasped by the proposed gripper. (**a**) 500 g Cola can. (**b**) A measuring tape. (**c**) Pen. (**d**) 2.5 cm (diameter) cylinder object. (**e**) 5x7 cm business card. (**f**) A screwdriver

7.2.1 Increment of grasping points

To increase the grasping force of the proposed gripper, three more fingers are added to the design, but the finger lengths are less. This modification provides six grasping points of two groups of three. The length of the long fingers is 14 cm, while the length of the others is 9 cm. Therefore, the objects will be grasped by six points as shown in Figure **7.7**.

Figure **7.7** illustrates that the long fingers grasp an object of up to 20 cm in dimension and the small group can start grasping from 14 cm. A similar experiment for the three-finger gripper was also done to find the maximum grasping payload for cylindrical objects of 14 cm diameter, which represents shapes of the maximum dimension to be grasped by the six fingers. The results show that the maximum grasping payload is 3.6 kg and the maximum bending angle of the small finger is 26^0. The weight of the new gripper is 0.34 kg, while it provides 2.57 times of the previous gripper, which represents 7.2 times that of RBO hands.

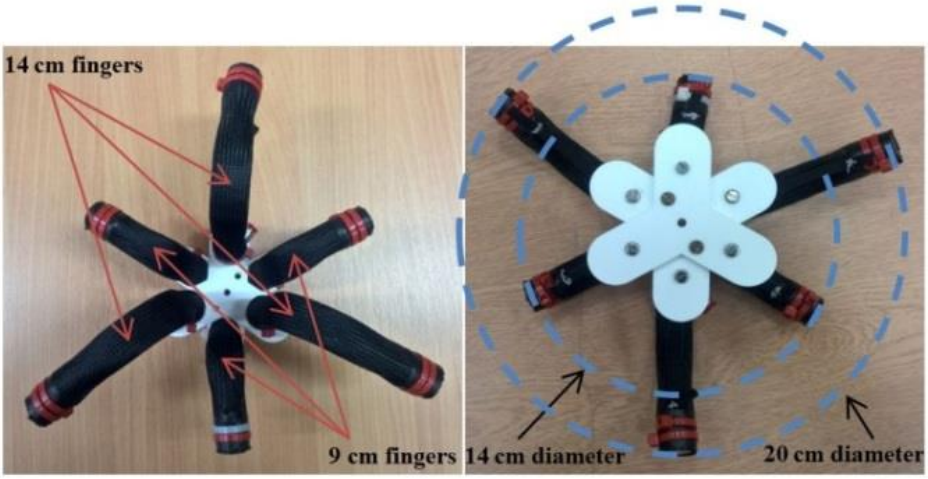

Figure 7.7 The layout of the six bending fingers.

7.2.2 The grasping control of different loads

The grasping control of different objects is a challenge for this type of soft gripper. In this section, the proposed control system PNNP in section 5.5 is used to control the grasping force. Figure 7.8 shows the block diagram of the control system.

In this control system, a 10 kg load cell has been used and the weight scale is designed as shown in Figure 7.10.a. The designed weight scale is used as a base for the object and it

provides the force (F) to the controller via Arduino Mega 2560 and multiplies it by a safety factor (s); the resulting force is a set point (F_s). While the feedback force (F_f) is provided by a force sensitive resistance (FSR-402), which is mounted on the fingertip of one finger, the diameter of the active area for this sensor is 12.5 mm and the output force is multiplied by 3 to give the sum of the force of the gripper. According to the error sign between F_s and F_f, the controller will activate either the filling part or the venting part by sending the appropriate duty cycle of the pulse width modulation (PWM) to control the solenoid valve.

An approximate relationship between the force and the duty cycle is used to train the NN controller as:

$$y = \frac{17.85 \times u}{98} \tag{7.2}$$

Where y is the gripper force in (N), the number "17.85" represents the maximum force produced from the gripper in (N), u is the controlled duty cycle and the "98" refers to 98% of the maximum duty cycle for the control signal to avoid the continued supply to the solenoid valve. The controller is validated by applying sinusoidal and step set signals at 0.25 and 0.5 Hz as shown in Figure 7.9.

Figure 7.9 illustrates that the controller is accurate enough to be used for different object weights. The sinusoidal response shows that the signal of the force sensor tries to track the input signal with a constant error due to the continuous changing.

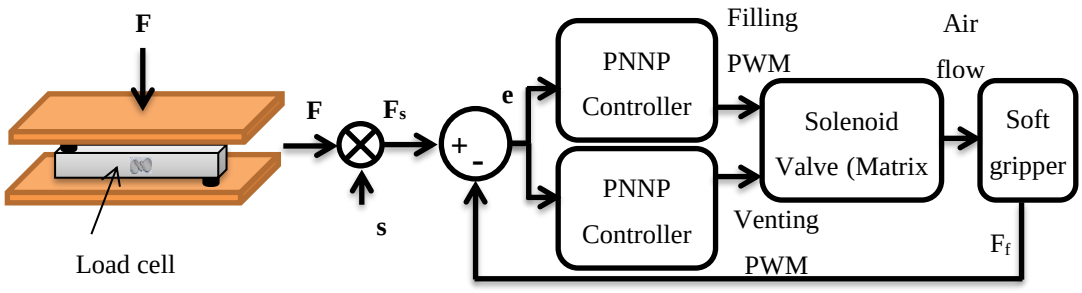

Figure 7.8 The full block diagram of the grasping force control system.

Moreover, the step response has a zero steady state error because of its constant values at zero and 1000 g.

On the other hand, the time of release is higher than at the time of grasping because the time of grasping because the time needed to vent the muscle is more than the time needed to fill it. This occurs for two reasons: the hysteresis of the PMA and the difference between the air pressure inside the actuator and the outside air pressure.

To examine the effectiveness of the proposed gripper and the control system, an adjustable weight cylinder object is used for three different load values (500 g, 1000 g and 1400 g). Figure 7.10 shows the object and the control performance.

Figure 7.10.b shows that the steady-state error is zero for different load values. The maximum pressure for this process is 110 kPa, 240 kPa and 390 kPa for the object loads 500 g, 1000 g and 1400 g, respectively. Moreover, the safety factor is set to 1.3 to prevent slipping during the grasping process.

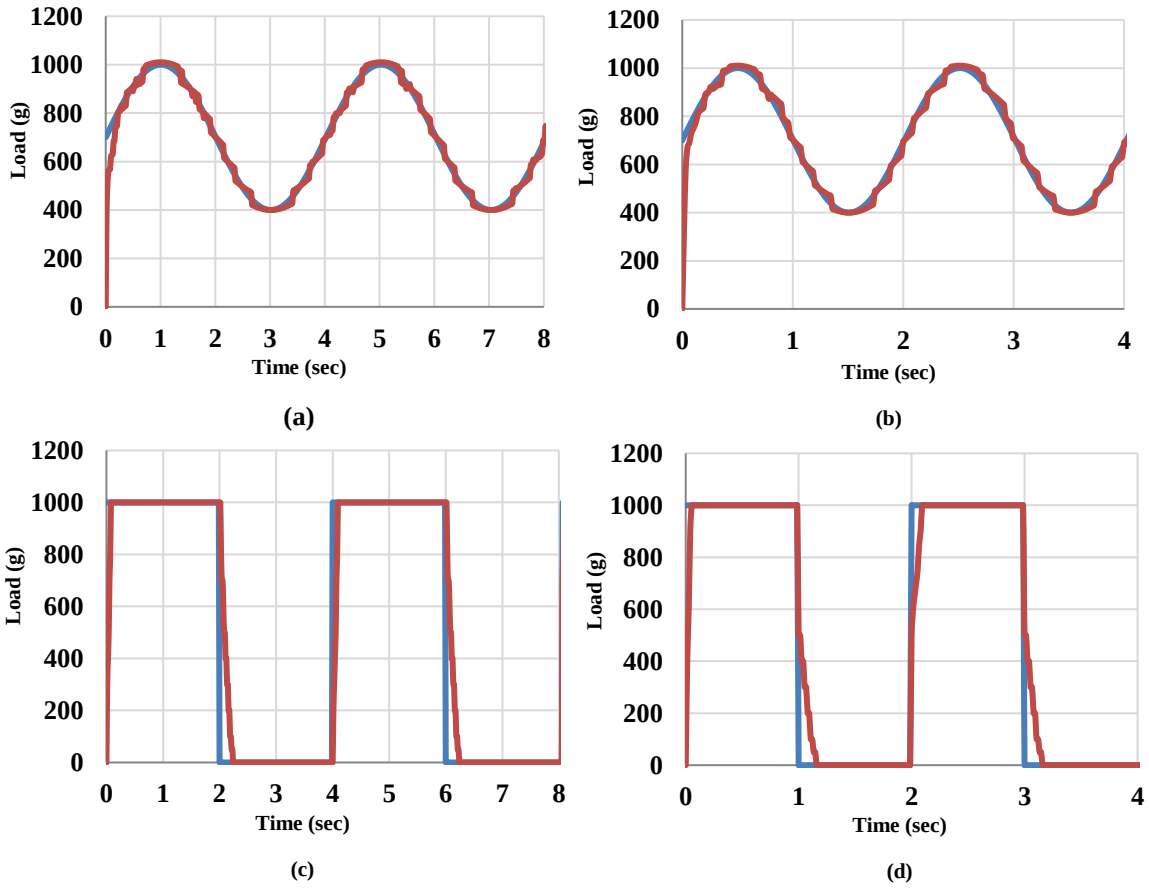

Figure 7.9 The controller response for the three finger gripper. (**a**) The sinusoidal response at 0.25 Hz, (**b**) The sinusoidal response at 0.5 Hz, (**c**) The step response at 0.25 Hz and (**d**) The step response at 0.5 Hz.

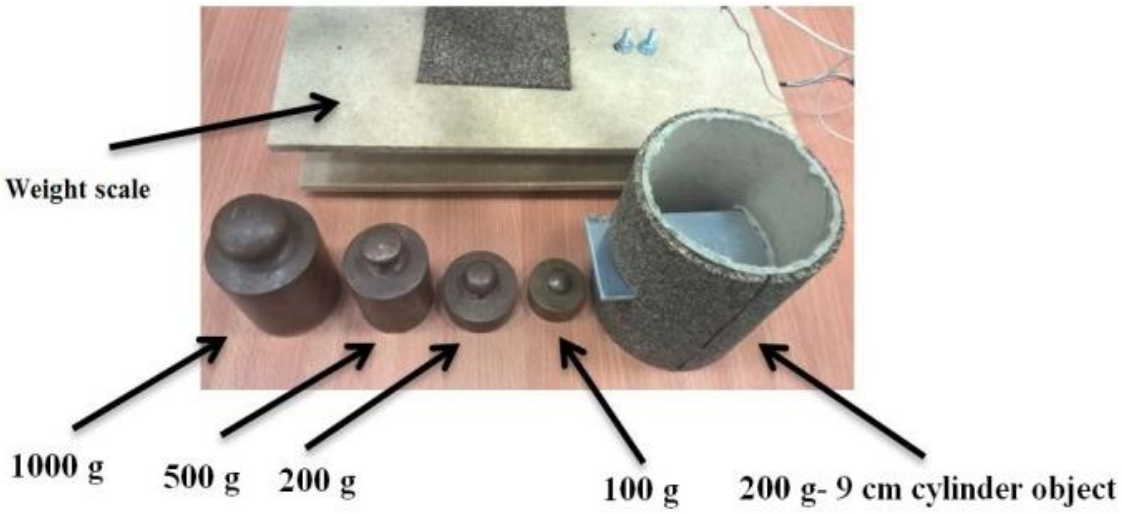

(a)

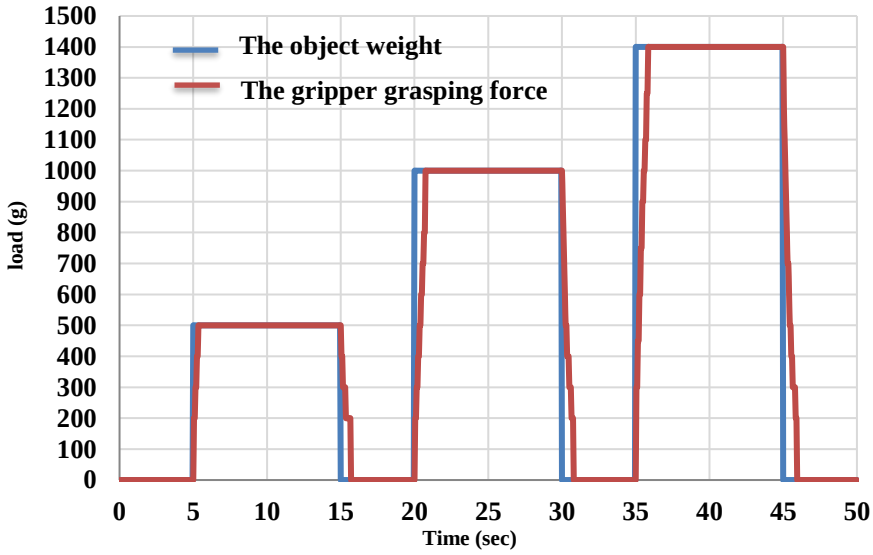

(b)

Figure 7.10 The grasping force control. (**a**) The weight scale and the object. (b) The response of the gripper due to different load values.

An experiment has been done to validate the high repetition level of the proposed gripper to grasp a 1.0 kg object by the three-finger gripper for 30 times. The results show that the maximum error in grasping force is 20 g and the MSE for the process of 30 times is 0.000122. This result shows the high reliability of the gripper and the control system.

7.3 Extension-circular gripper

A novel soft gripper is proposed in this section by using the extensor and the CPMA. Figure 7.11 illustrates the structure of this gripper, which is built using three 18 cm extensor actuators and one CPMA.

The extensor actuators provide an ability to extend and bend in addition to increasing the gripper's stability, while the grasping occurs due to the circular actuator, which is made as a 30 cm simple contractor muscle. The maximum inner diameter for the gripper is 7.8 cm.

Experiments have been done to define the performance of the proposed gripper. Air pressure is applied by using a solenoid valve to the extensor actuators, which changes the length of the gripper. The length of the gripper changes with pressure until it reaches the maximum length of 24 cm at 500 kPa with an extension ratio of 33%. Then pressure is applied to the CPMA and the inner diameter is reduced to the minimum of 4.45 cm at 400 kPa. Fig. 18 shows the diameter and the length as a function of pressure. Further air pressure is added to the CPMA, but the inner diameter remains constant because the contractor muscle reaches its maximum contraction ratio so that the percentage of the diameter reduction after the 400 kPa can be ignored.

Figure 7.11 The structure of the extension-circular gripper.

The diameter reduction ratio (DRR) can be calculated from (7.3) and it is equal to 43% for the presented gripper.

$$DRR = \frac{D_0 - D}{D_0} \tag{7.3}$$

Where: D_0 is the diameter at zero pressure and D is the diameter at pressurised condition.

The extension-circular gripper has an advantage over multi-finger grippers due to an infinite number of contact points between the inner surface of the CPMA and the object to be handled. This preference increases the applied force and provides a significant grasping stability. On the other hand, pressurising the extensor PMAs simultaneously results in increasing the gripper length, as shown in Figure 7.12, while different pressure amounts in each actuator lead to moving the circular actuator in multiple directions. The maximum angle is 61^0 in relation to its original position and can be achieved by applying air pressure to one actuator. These performances increase the efficiency of the gripper by adding the bending behaviour.

To explain the pressure-payload characteristic for this gripper, an experiment has been done by selecting multi-weight cylindrical objects of 6 cm diameter. The load starts at 0.5 kg and is then increased by 0.5 kg steps. At each step, the applied air pressure is raised to prevent slipping. Figure 7.13 illustrates the experimental results and shows that the maximum payload for the presented gripper is 10.9 kg for the 6 cm object and the payload–pressure characteristic is linear above the 1.5 kg load. The parameter to be controlled for the extension-circular gripper is the air pressure in the circular actuator, which provides an easy strategy for achieving the grasping operation.

Objects of various shapes can be grasped; however, their size must be limited to no more than 3.9 cm between the object's centre and its edge. **Error! Reference source not f ound.** shows the grasping of different objects using the extension-circular gripper. Different object shapes and weights require different grasping force; however, the proposed gripper provides equal grasping force for all contact points between the objects and the CPMA. The direction of these forces is toward the centre of the circle.

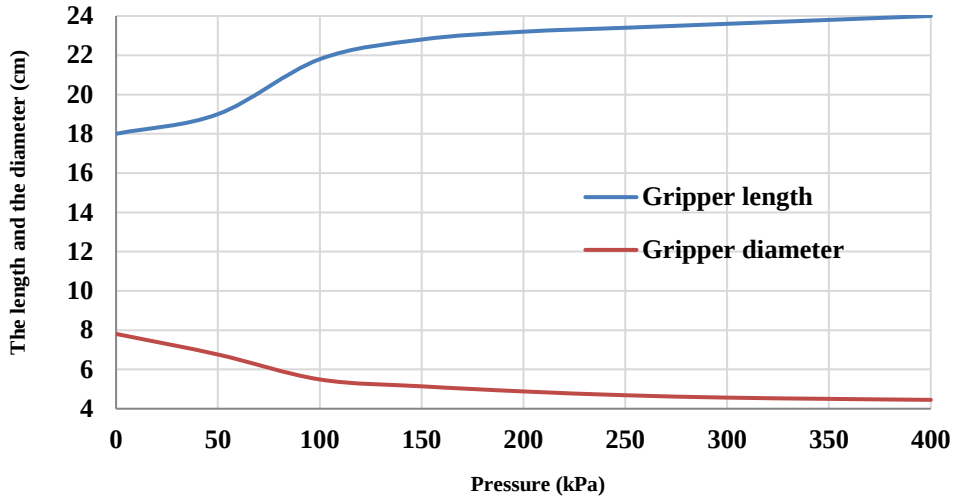

Figure 7.12 Variation of the length and the diameter for the extension-circular gripper

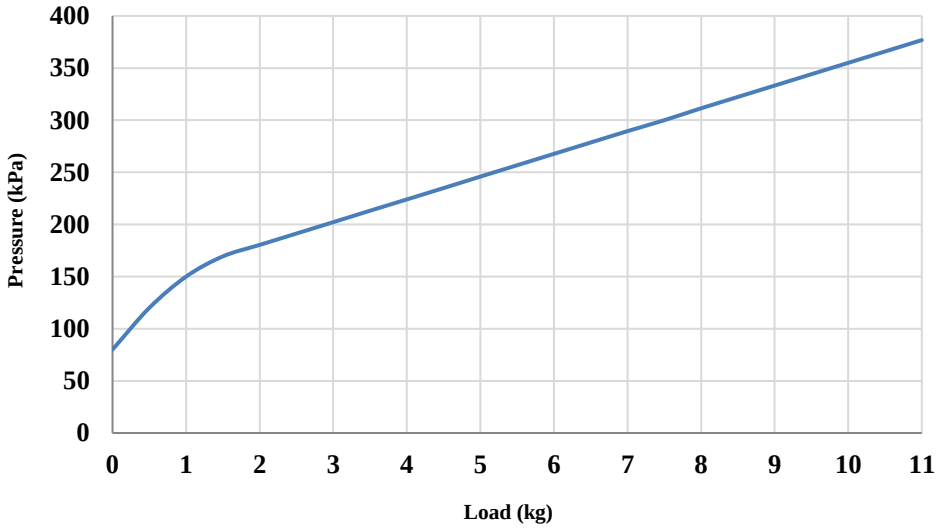

Figure 7.13 The payload –pressure characteristics for the extension-circular gripper.

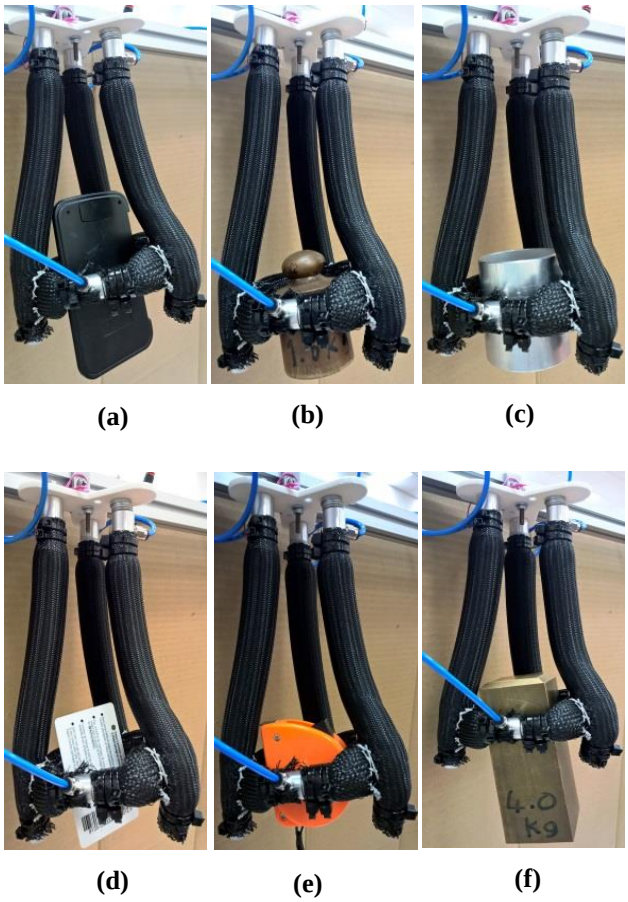

Figure 7.14 Multiple objects grasped by the extension-circular gripper. (**a**) 7x12 cm calculator. (**b**) 1.0 kg weight. (**c**) 6 cm (diameter) cylinder object. (**d**) 5x7 cm business card. (**e**) A measurement tape. (**f**) 4.0 kg rectangular object

7.3.1 Three CPMAs gripper

In this section the extensor-circular gripper is redesigned by increasing the number of CPMAs to three to increase the grasping payload. In this design, the length of the gripper at zero pressure is 27 cm and it is increased to 38.1 cm at 500 kPa. From (7.4) the extension ratio for the extensor muscles is 41%. The diameter for each CPMA is from 8 cm to 4.3 cm for the maximum pressure of 400 kPa. The diameter reduction ratio for these circular actuators is 46%. Figure 7.15 illustrates the three CPMAs gripper and its performances are illustrated in Figure 7.16.

$$\acute{\varepsilon} = \frac{L - L_0}{L_0} \tag{7.4}$$

A similar experiment in section 7.3 is used to define the grasping load of the three CPMAs gripper. For a cylindrical object with a 6 cm diameter the gripper can grasp up to 40 kg while it weight is 0.8 kg.

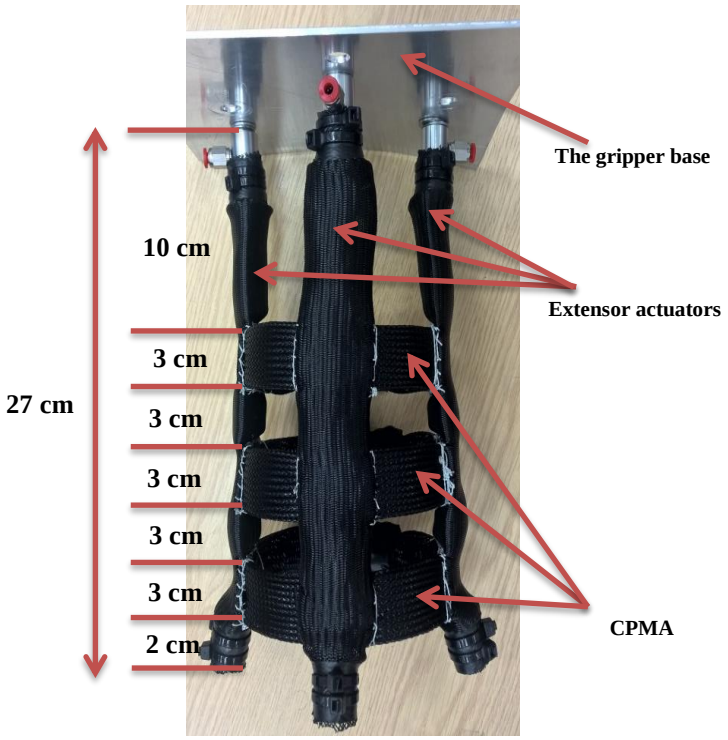

Figure 7.15 The dimensions and the structure of the three CPMAs gripper.

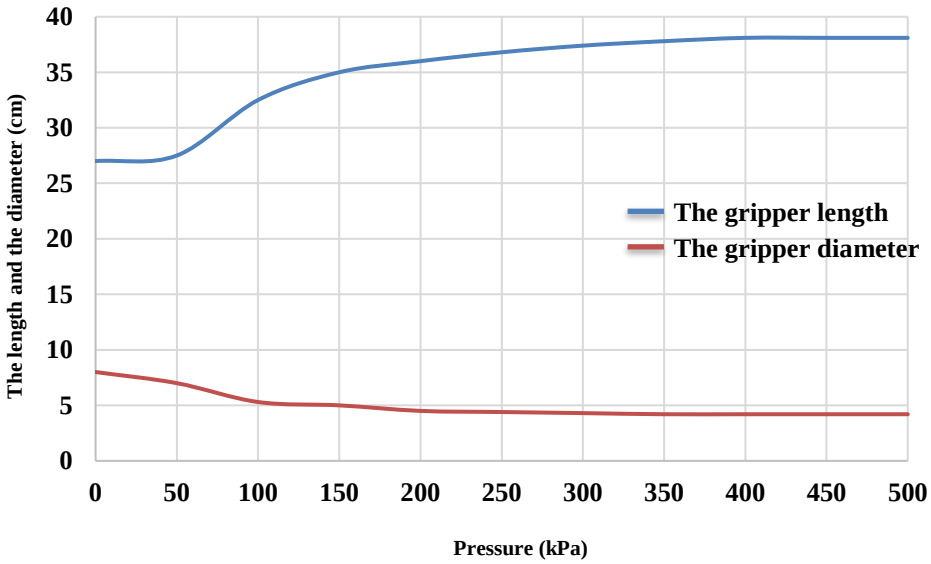

Figure 7.16 Variation of the length and the diameter for the three CPMs gripper.

7.3.2 The control system of the CPMAS gripper

A similar control system for the finger gripper is used in this section but we changed the load cell maximum load to 40 kg. A 6 cm diameter of adjustable weight cylindrical object has been used to validate the grasping performances of the extensor-circular gripper of one and three CPMAs, respectively. Figure 7.17 shows the controller results for both grippers at different object loads. Figure 7.18 shows grasping examples of the three CPMAs gripper at different loads.

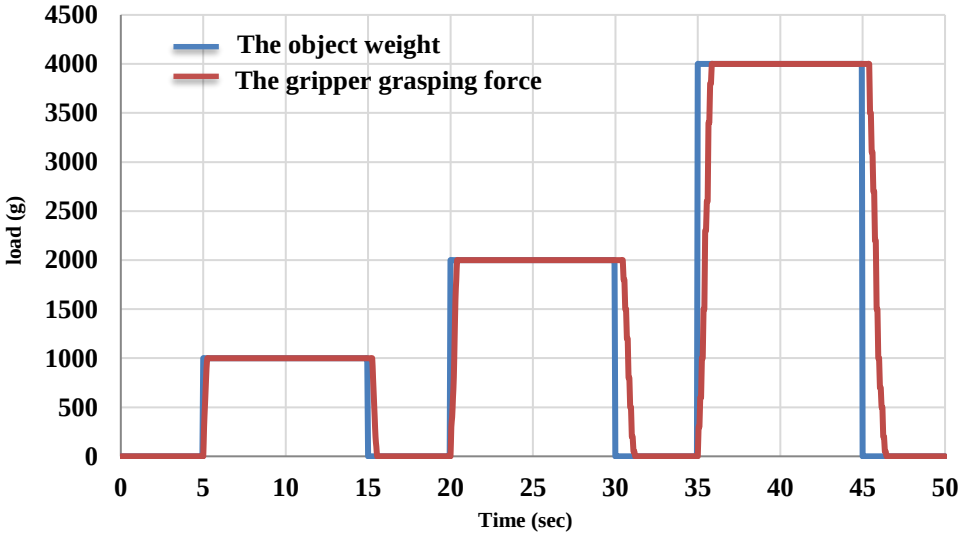

(a)

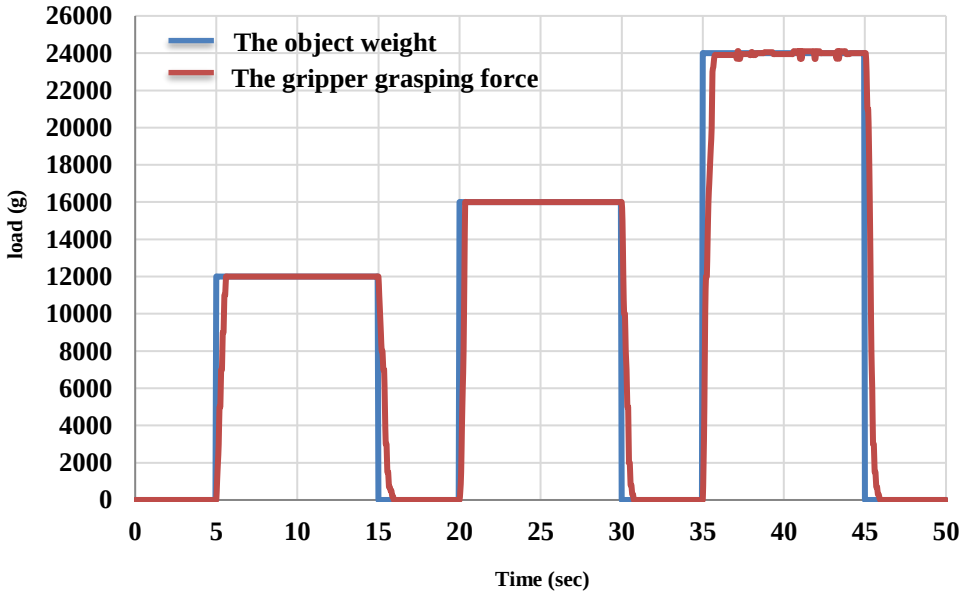

(b)

Figure 7.17 The grasping force control. (**a**) The grasping control results for the one CPMA gripper at three different loads (**b**) The grasping control results for the three CPMAs gripper at three different loads

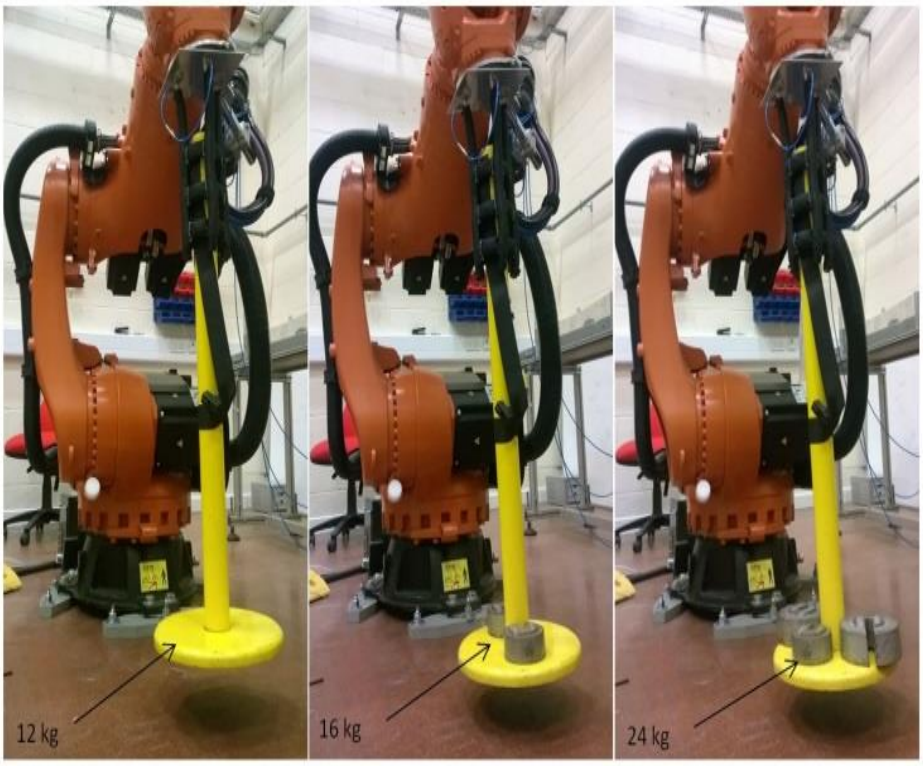

Figure 7.18 The grasping examples for the three CPMAs gripper at three different loads

7.4 Summary

Grasping and safe handling of objects is a very important issue in robotic application. The end effector is a part of the robot that has direct contact with the object. Different object dimensions, shapes, materials and weights require different and complex designs of end effectors. The complexity of the design can, in turn, lead to the need for a complex control system.

The chapter presented two soft gripper designs that use PMAs; a three finger gripper based on a bending contraction PMA and an extension-circular gripper. The physical structure of each gripper is described individually, and the grasping performance assessed experimentally.

The first gripper has been shown to provide a wide range of grasping sizes for different object shapes and dimensions and has been demonstrated to have grasp strength sufficient to hold a 1.4 kg mass. Controlling the air pressure inside the fingers leads to closing of the

fingers, the soft nature of the fingers means that they can conform to the shape of the object being grasped without the need for any complex control system or grasp planning.

The extension-circular gripper has two main features; it can extend in length, allowing the main grasping contact area to be appropriately positioned on the object to be grasped. The second feature is a circle shape PMA which, when pressurised, reduces in diameter allowing it to grasp an object placed at its centre. The gripper has been shown experimentally to be capable of lifting loads up to 10.9 kg.

A modification is done to the two grippers to increase their performances and the control system is designed for each gripper to evaluate the design efficiencies.

Chapter Eight:

8. Novel Design and Position Control Strategy of a Soft Robot Arm

8.1 Introduction

This chapter presents a novel design of a continuum arm, which has the ability to extend and bend efficiently by using the contraction, extension and the SBCA actuators. Two different position control strategies are presented, arising from the results of the soft robot arm experiment. A cascaded position control is applied to control the position of the end effector of the soft arm at no load by efficiently controlling the pressure of all the actuators in the continuum arm. A new algorithm is then proposed by distributing the x, y and z-axis to the actuators and applying an effective closed-loop position control to the proposed arm at different load conditions.

8.2 Design and Construction of the Soft Arm

In this section, we have designed a new continuum arm based on the pneumatic muscle actuator, which has the ability to extend and bend. The proposed soft arm has been designed and built to provide multiple degree of freedoms (DoF) and performances based on the knowledge we have obtained from the designs and results in Section 2. It is designed to operate close to humans due to its softness and safe operation performances.

Designing any robot arm is subject to project requirements. The main objective of this project is to get a robot arm to pick up an object from the ground and move it to any position within 360º of the vertical robot arm axis. To achieve this objective, the following performances are required:

- The ability for length increment.
- The ability to bend in all directions.
- The arm force is big enough to pick up different objects.

Five extensor PMAs have been used to build the top section of the soft robot arm. The suggested structure of the top section provides a bending performance (as explained in chapter 4), in addition to the elongation behaviour of the proposed arm.

The second section is made from five contractor actuators which offer a high tensile force and a contraction of about 30% of the reset length in addition to the bending behaviour. The full design of the two sections of the proposed soft arm is illustrated in Figure 8.1.

Using five actuators instead of three (Walker et al., 2005) increases the force of the robot arm for similar diameters. The high-tension thread used to connect the corner actuators with the centre PMA longitudinally, performs the bending behaviour. The bending payload along the *x*-axis and along the *y*-axis is performed by two actuators that increase the bending force due to the parallel structure, as previously shown in chapter 4.

The extension segment has been made from identical 25 cm extensor PMAs, while the lower section is made from 30 cm contractor actuators. The length of the soft arm, including the fixed, the mid end, the free end and the end-effector bracket, is 72 cm. The cross section appears as a square of 10 cm in length, which represents the dimensions of the fixed and free ends.

The actuator's caps are made from aluminium and the fixed, mid and free ends have been designed by Solidworks 2016 and built by a 3D printer using plastic material (see Figure 8.1.a). The proposed continuum arm achieves the requirements above by reaching 12 cm elongation (elongation by increasing 48%) and a 117-degree full bending angle using both sections at no load. The weight of the contractor section is 0.2 kg and the weight of the end-effector support is 0.3 kg.

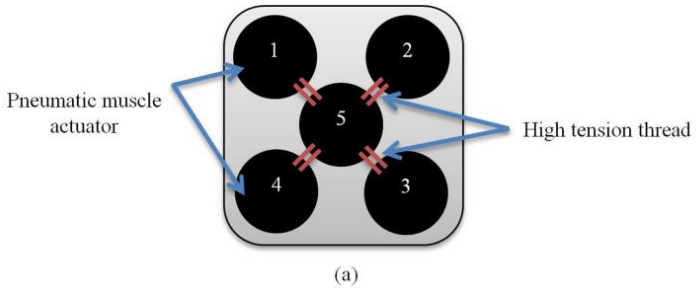

(a)

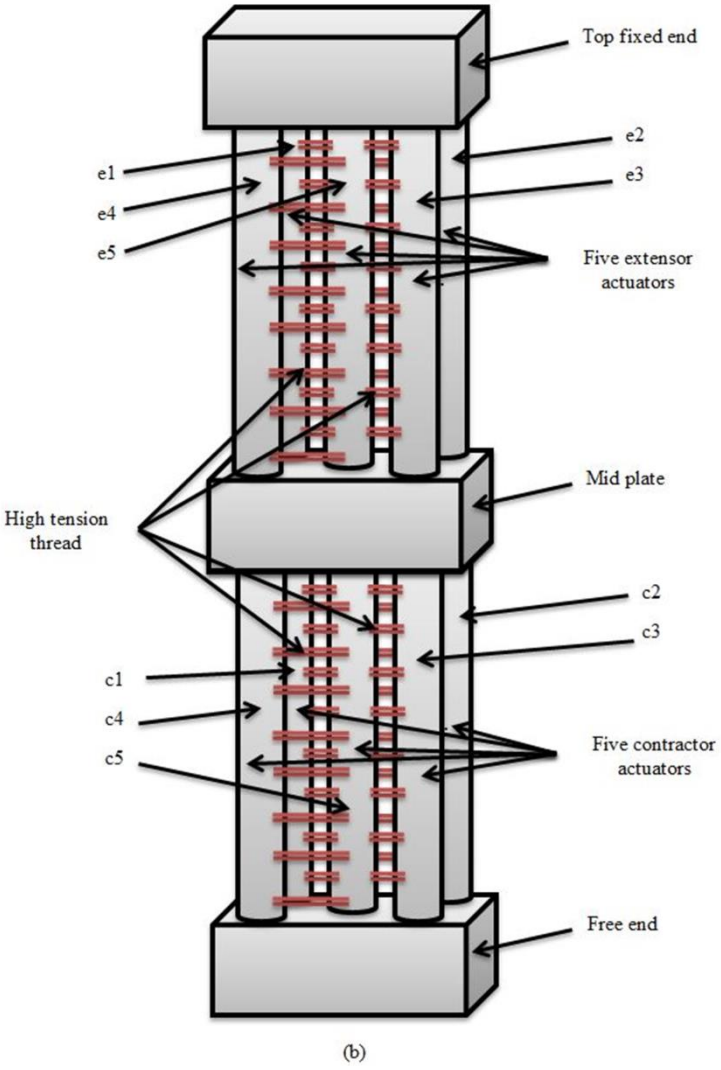

Figure 8.1 The proposed soft arm. (**a**) The layout of actuator distributions. (**b**) The structure of the entire arm.

8.2.1The Bending and Displacement Test of the Soft Arm

The bending performance of the proposed soft arm can be achieved by either pressurising one actuator (but not the centre PMA because the thread prevents its bending) in the top section, one in the bottom section or both. Other possibilities of bending could be achieved through a combination of either two, three or more PMAs, in both the top and the bottom sections. Referring to Figure 4a, the probable bending performances can be

explained in Figure 8.2, where (E) refers to the extensor actuator and (C) refers to the contractor actuator. Figure 8.3 illustrates the bending angle of the free end in three patterns.

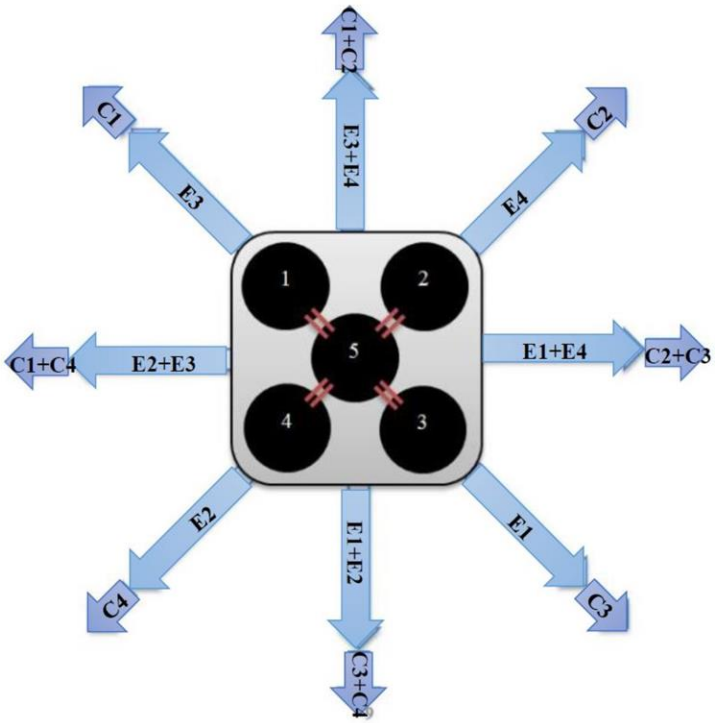

Figure 8.2 Possible direction movements by pressurising one or two actuators in each section.

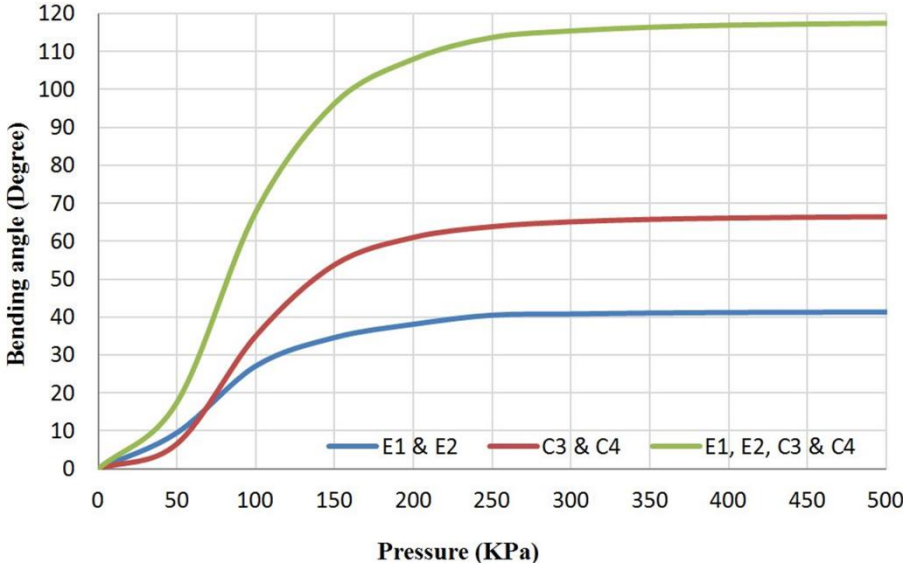

Figure 8.3 The bending angle of the proposed soft arm due to three different pressurise patterns.

A pressure sensor (0–500 kPa) and an MPU 6050 sensor have been used to record both the air pressure and the bending angle at different air pressure values from zero to 500 kPa for three repetitions. The MPU 6050 sensor has been mounted onto the free end of the arm to measure the bending angle. The experiment is set by applying an air pressure via solenoid valve (Matrix MK754.8E1D2XX) by (MATRIX, Italy) by steps of 50 kPa which is controlled by microcontroller (Arduino mega 2560) by (Arduino, Italy).

In Figure 8.3, the bending angle of the extension segment is lower than the angle of the contraction segment due to the weight of both the bottom section and the end effector support, in addition to the reverse bending behaviour of the contraction part because of its material. On the other hand, the bending behaviour of the contraction part is similar to the bending of the contraction arm (Figure 4.12) at a 0.3 kg load, which represents the weight of the end-effector bracket. Pressurising two actuators in both the extension and the contraction sections simultaneously, produces a bending angle that is more than the summation of the separated operations.

Furthermore, activate the two sections simultaneously increases the displacement into *x* and *y* directions in addition to *z*, which increases with the bending.

8.3 The Modified Design of the Proposed Arm

In order to increase both the bending and the payload of the robot arm, we have used the self-bending contraction actuator (SBCA) (see section 6.2) instead of the simple contraction PMA. The bending angle for this type is more than the bending angle of the contraction section of the proposed robot arm. Furthermore, the weight of the bottom section will be reduced by removing the centre actuator; this also decreases the controller parameters. The bending muscles are positioned to bend into the corners of the square plate. Figure 8.4 shows the new design of the proposed continuum arm with an ability to extend longitudinally and bend in all direction, and Figure 8.5 illustrates the bending of the new design by activating the same actuators as in Figure 8.3.

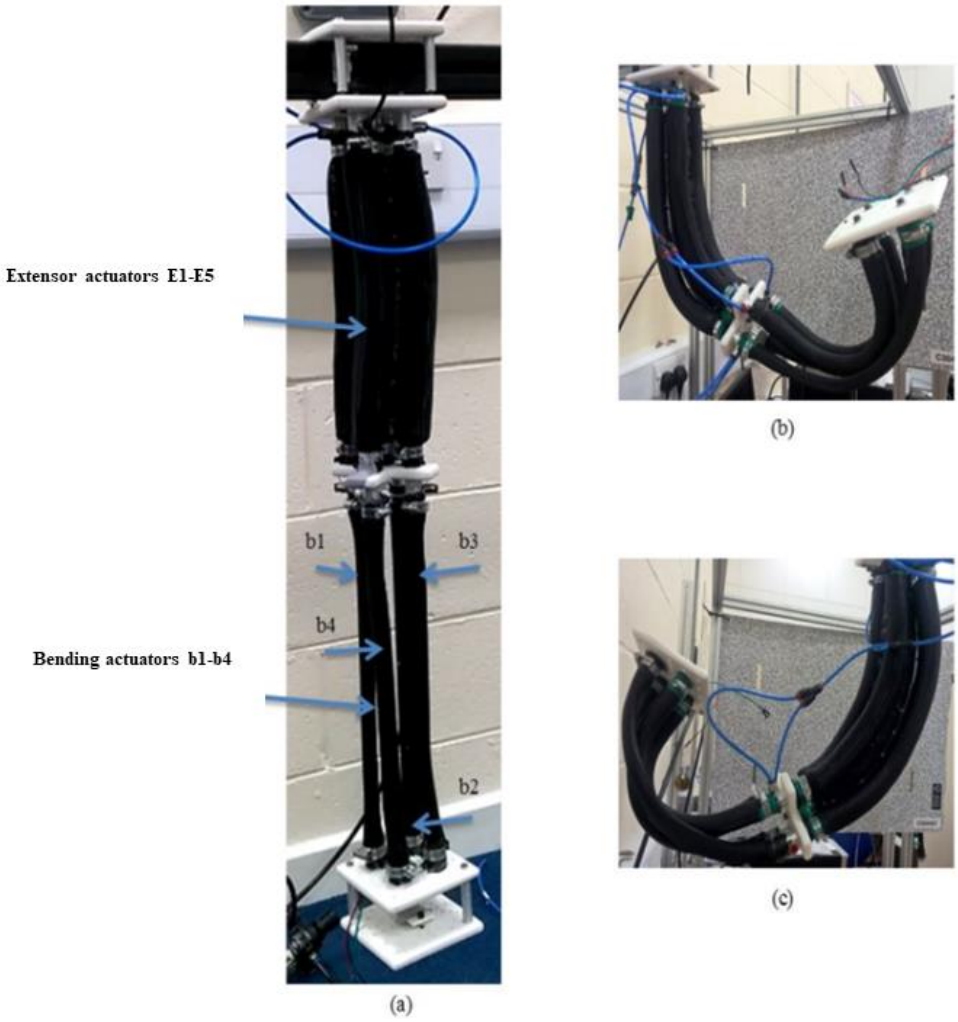

Figure 8.4 The modified version of the proposed soft arm. (**a**) The arm at no pressure. (**b**) and (**c**) represent two different bending possibilities.

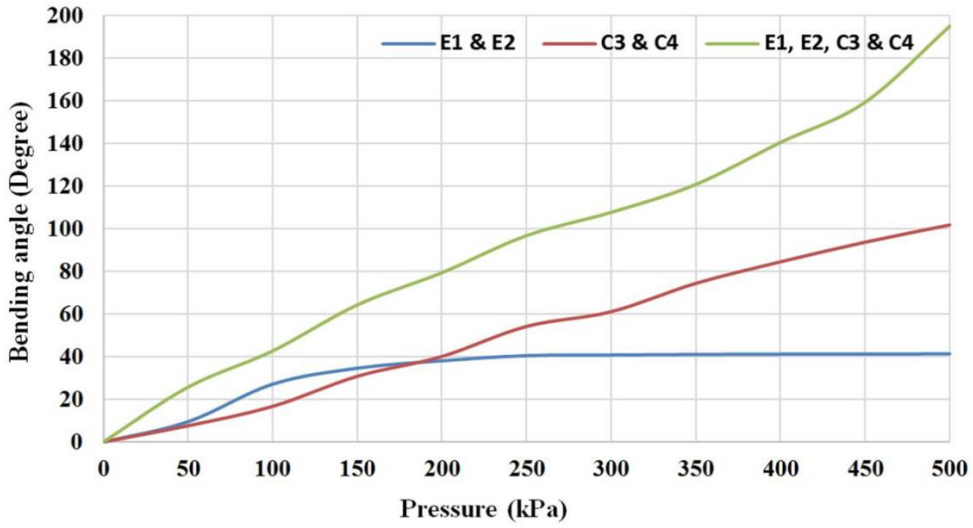

Figure 8.5 The bending angle of the modified soft arm due to three different pressurised patterns.

8.4 Controlling the Presented Soft Arm

Controlling a system such as a soft continuum robot arm is a challenge due to: (i) the various motions performed, such as contraction, extension and bending; (ii) the nature of the material properties, including hysteresis and the viscos elastic behaviour; (iii) the unique performances for each design (George Thuruthel, Ansari, Falotico, & Laschi, 2018). To control the presented continuum robot arm, two different strategies are applied.

8.4.1 Cascaded Position Control

The no-load position control of the free-end has been set by mapping the Cartesian coordinates of the end effector as a function of the air pressure in the five extensor PMAs and four SBCAs. Numerous patterns are applied in this experiment by pressurising one actuator at a time, or two actuators or more, until all of the actuators in the robot arm have been pressurised. The patterns are selected to cover all the probabilities by 50 kPa steps and for three repetitions. Each time the air pressure is increased from zero to 500 kPa, the position of the free-end is recorded.

In this experiment, two cameras (Pixy CMUcam5) by (CMUcam, Amazon, UK) have been used to track the 3D position of the arm. An Arduino MEGA 2560) by (Arduino, Italy) is also used in addition to the nine pressure sensors (0–500 kPa) and three Solenoid Valves (Matrix MK754.8E1D2XX) by (MATRIX, Italy).

The Pixy camera only tracks x and y positions for a predefined object. To solve this issue, two cameras have been used in two positions to get a 3D reading of the tracking object. A blue ball has been chosen as a tracking object and it is attached to the end of the robot arm so as to be seen as a blue circle at all times. Figure 8.6 explains the layout of the cameras and the ball.

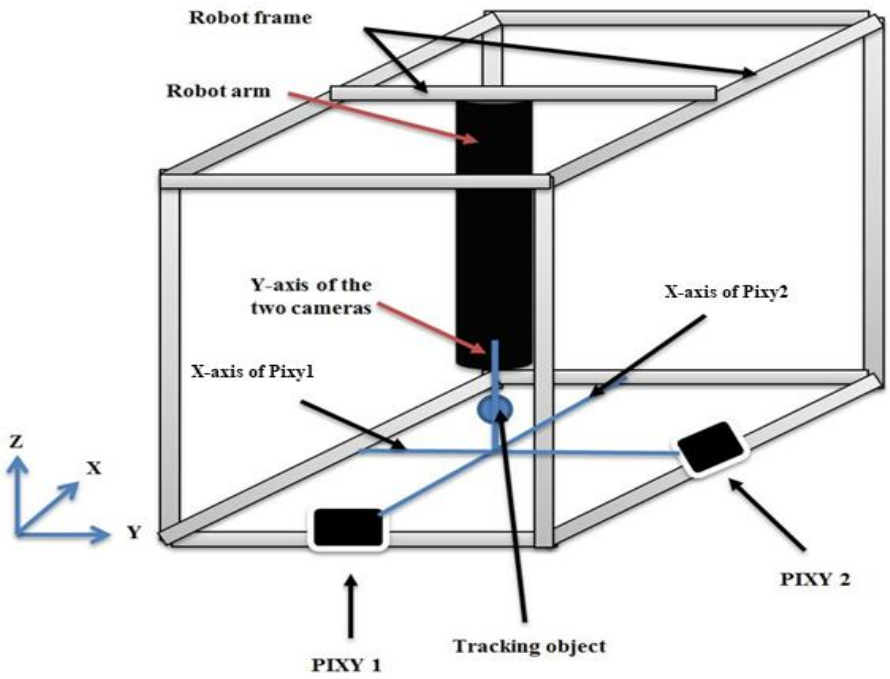

Figure 8.6 The layout of the robot arm and the camera system.

The X-axis of Pixy1 and the X-axis of Pixy2 have been set at the Y-axis and X-axis of the robot arm, respectively. Meanwhile, the Y-axis of the two cameras has been set as the Z-axis of the robot arm by calculating the average value of both Y-positions, with the reference point at no pressure set to (0, 0, −720) mm.

The vision system provides 3D position data for mapping the robot's movements and this data is used to train a neural network (NN) with 3-inputs and 9-outputs and 8 neurons in one hidden layer at mean square error (MSE) equal to 8.69×10^{-8}. The tangent function is selected as a fitting function for the hidden neurons. The NN configuration is implemented in Matlab tool (2016a) and it provides the reverse information of the robot (inverse kinematics), where the inputs are the position of the robot and the outputs are the air pressures in the nine actuators.

The mapping data of x-y, x-z and y-z are illustrated in Figure 8.7.a-c for different pressurising patterns in the nine actuators at pressure steps from 0 to 500 kPa. The results show non-symmetrical movements due to the difficulties of build a symmetrical continuum arm and the friction between the parallel actuators.

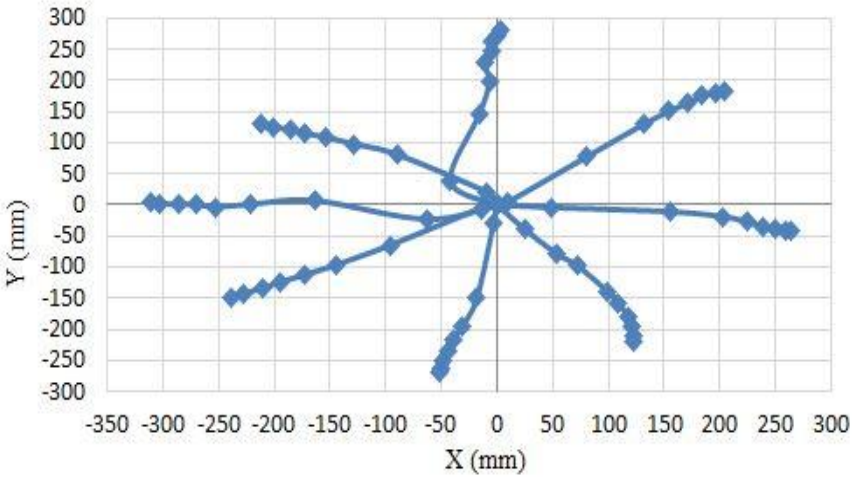

(a)

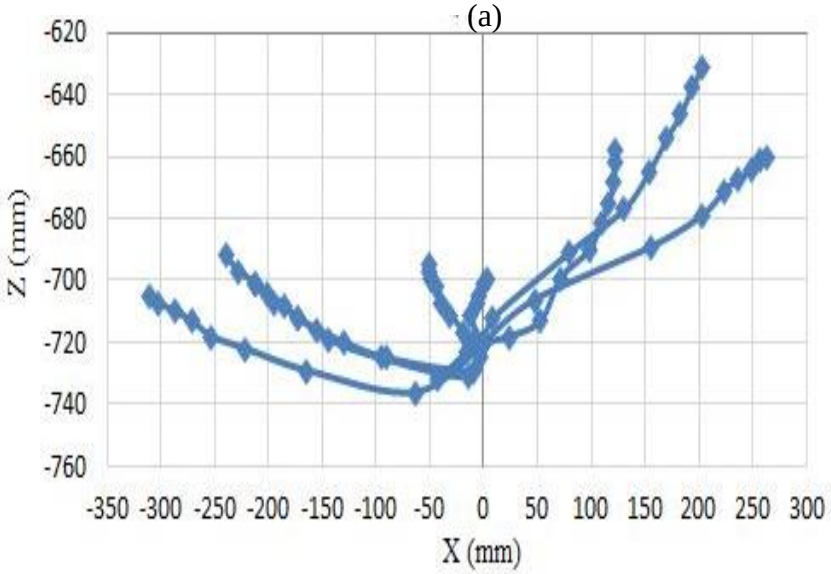

(b)

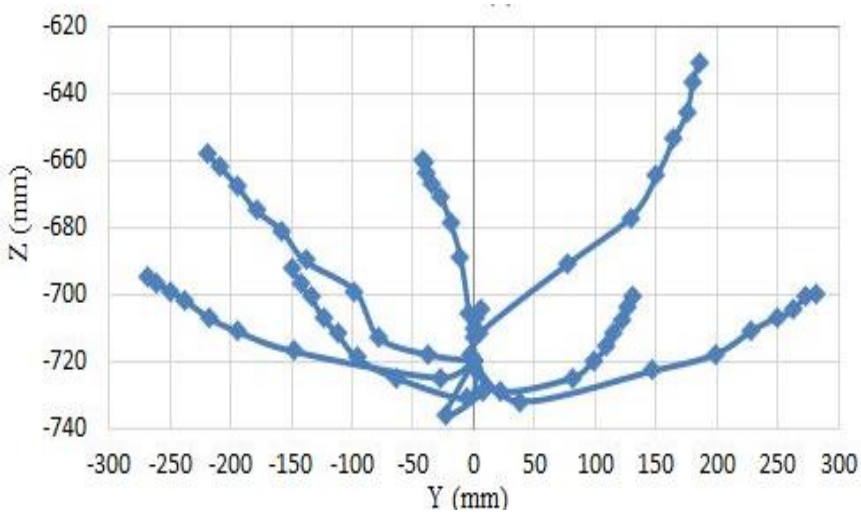

(c)

Figure 8.7 Mapping of the movement data. (**a**) X-Y mapping. (**b**) X-Z mapping. (**c**) Y-Z mapping.

The pressure control has been applied to control the offline position of the soft arm at no load. Nine pairs of NN controllers are used to control the pressure in the nine actuators, where each pair contains two controllers for filling and venting the PMA, respectively. In each pair, the individual controller work depends on the error of air pressure. Figure 8.8 illustrates the flowchart of each pair.

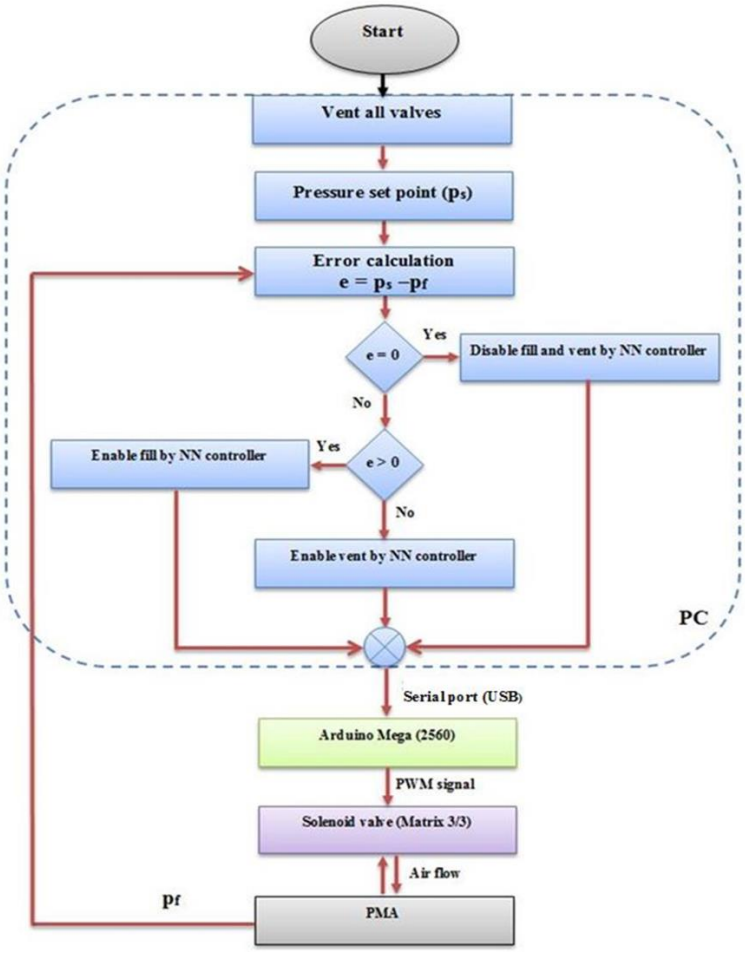

Figure 8.8 The flowchart of single pair of neural network controllers.

The NN controller has been designed as the specification in chapter 5 to fill or vent the actuator depending on the error of the pressure, and the model used in this system is the approximate relationship between the duty cycle of the controller output and the air pressure in the PMA as in (8.1), during 0.5 (sec) steps.

$$y = \frac{500\ (kPa) \times u}{98} \tag{8.1}$$

Where y is the pressure in kPa, the number (500) represents the maximum air pressure in kPa, u is the controlled duty cycle and the (98) refers to 98% of the maximum duty cycle for the control signal to avoid the continuous supply to the solenoid valve.

Using (8.1) as a model to train the NN controller instead of the trend line of the actual data does not affect the plant output, therefore, the approximate equation has been used.

The full block diagram of the cascaded position control system is shown in **Error! R eference source not found.** and a random pattern of movement is selected to validate the cascaded control system, as shown in Figure 8.10, starting from the initial point (0, 0, −720) mm. The pneumatic muscles for both sections are called PMA1 to PMA9 for the extensor muscles (e1, e2, e3, e4 and e5) and the bending muscles (b1, b2, b3 and b4) (see Figure 8.1 and Figure 8.4).

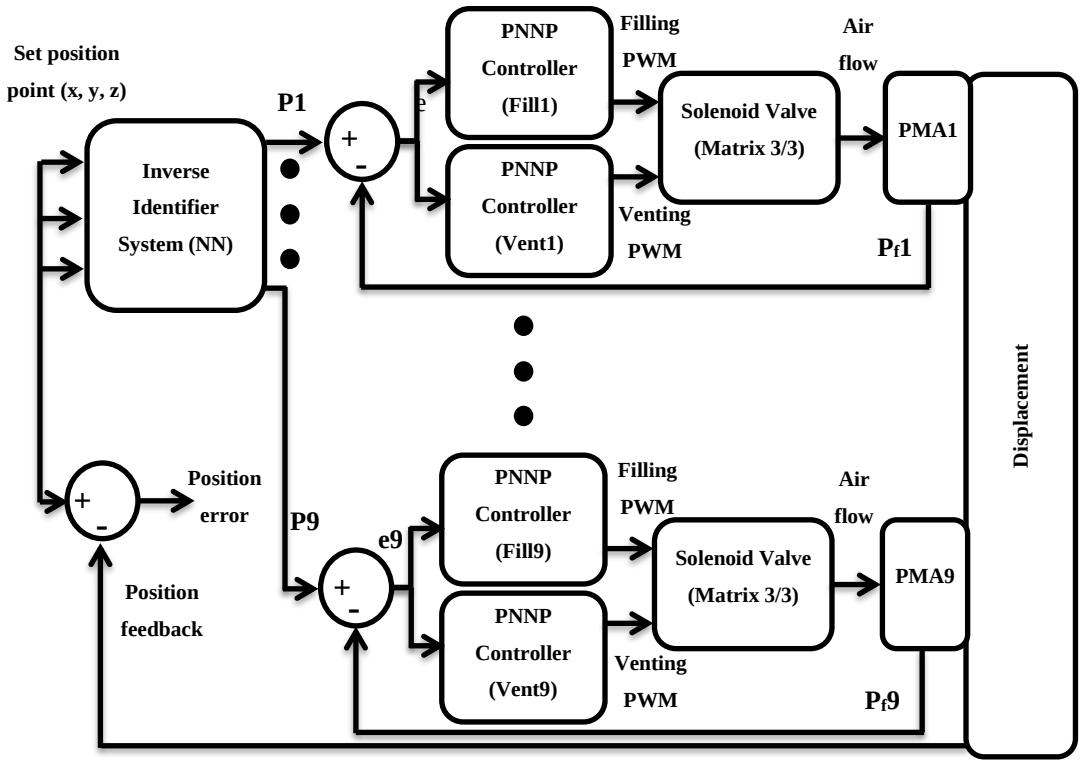

Figure 8.9 The full block diagram of the cascaded position control system.

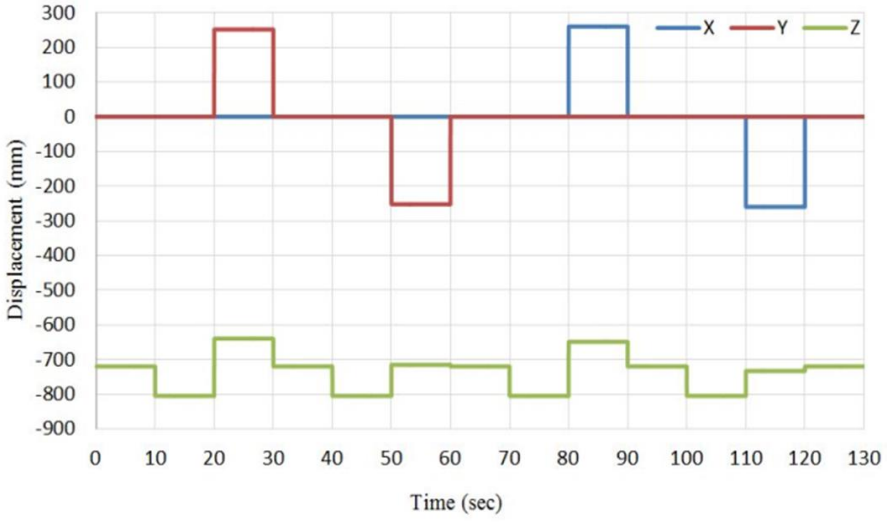

Figure 8.10 A random pattern to validate the cascaded position control system.

In this pattern, we wanted to get movement along the *X*-axis by 260 mm and *Y*-axis by 252 mm; the *z* displacement is the result of these two actions. Therefore, the control system which is described in **Error! Reference source not found.** will control the pressure in all a ctuators to track the desired position pattern. The pressure outputs from the inverse kinematics system and their feedback values have been illustrated in Figure 8.11, while Figure 8.12 shows the position set point and the position feedback at no-load, and Figure 8.13 shows the position error.

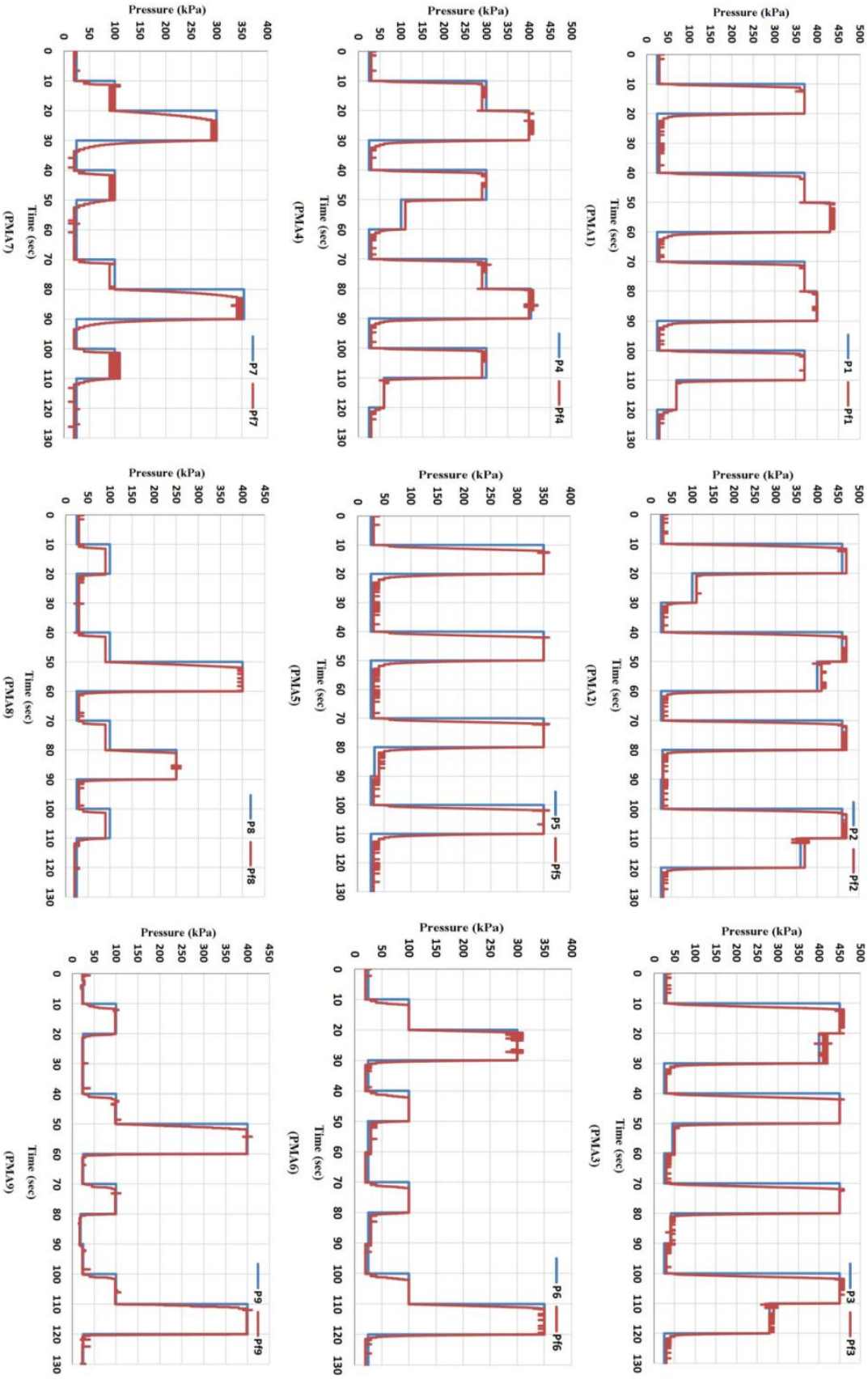

Figure 8.11 The output and feedback air pressure for the nine actuators, which have been programmed to control the position of the multi-function soft arm at no-load by using the cascaded control system.

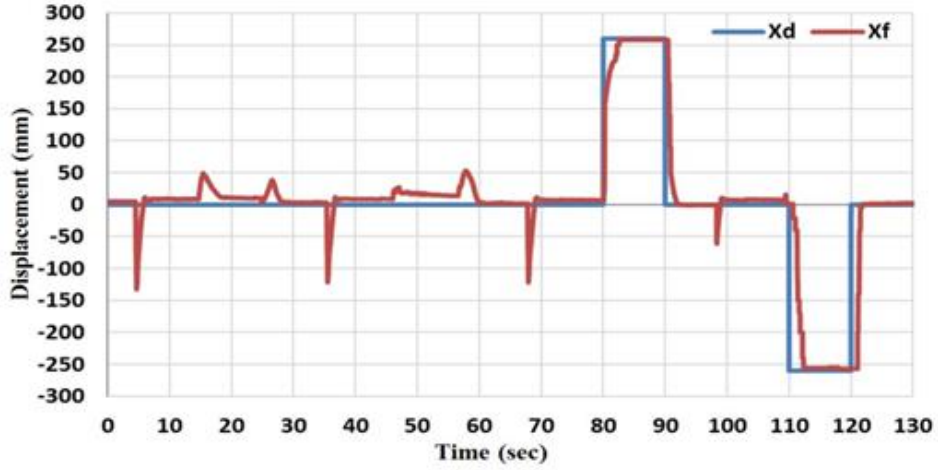

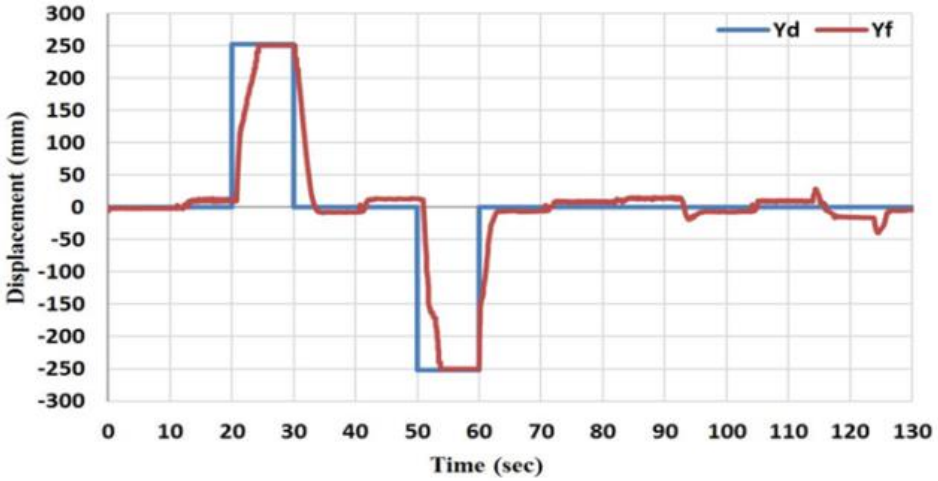

(**b**)

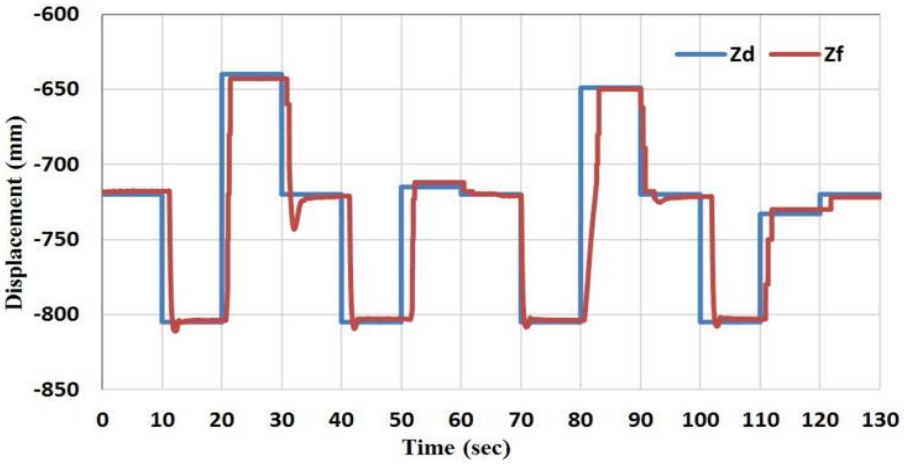

(**c**)

Figure 8.12 The desired feedback position for the multi-function soft arm by the cascaded control system. (**a**) The x position. (**b**) The y position and (**c**) is the z position.

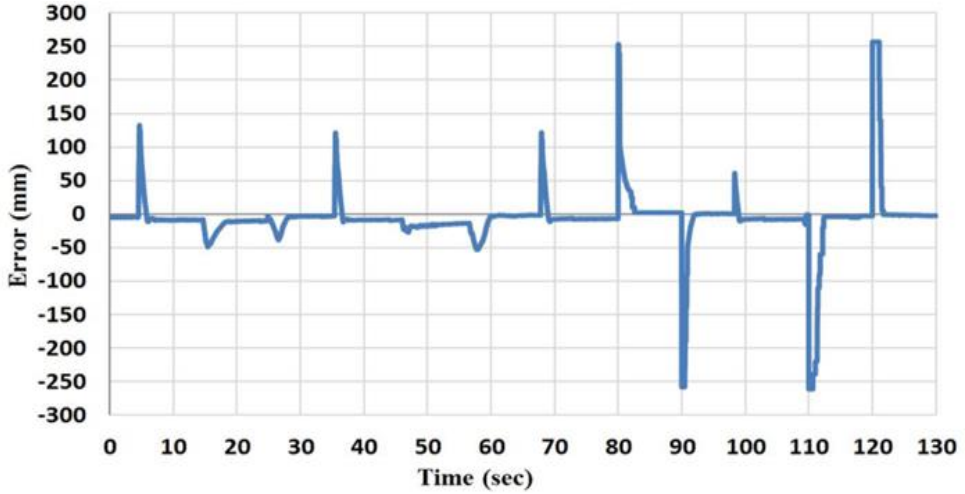

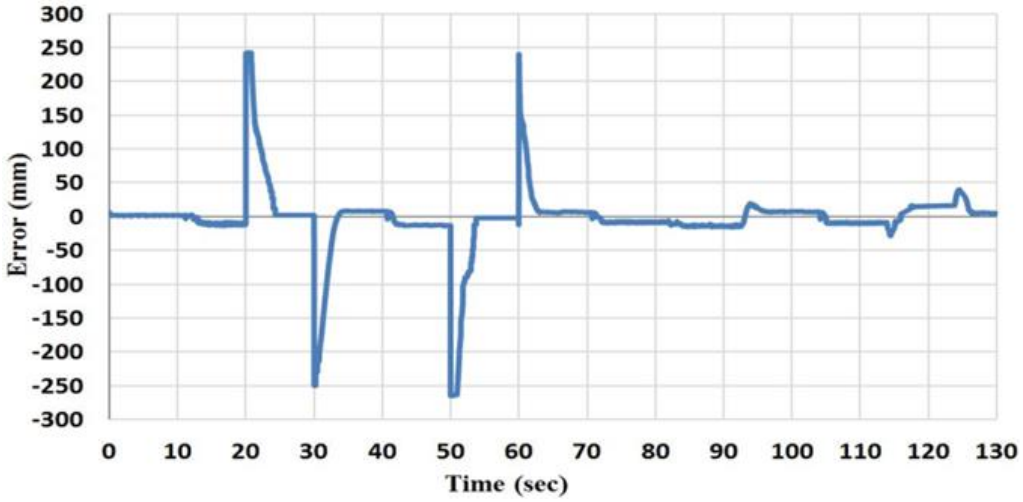

(**b**)

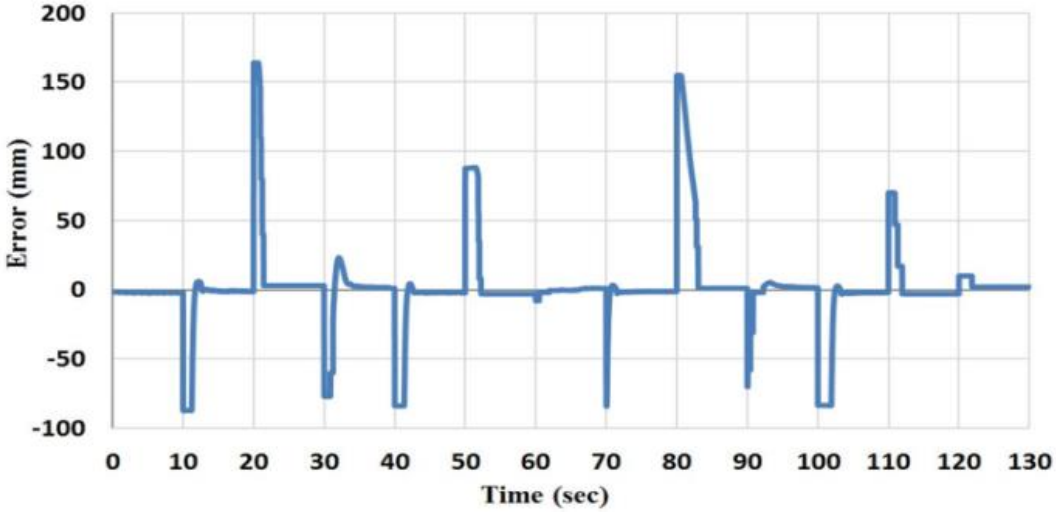

(**c**)

Figure 8.13 The error of x, y, z displacements, respectively (**a**) The x position error. (**b**) The y position error and (**c**) is the z position error.

According to Figure 8.11, the pressure control has been fulfilling the controller requirements, where the error is set to be (± 5 kPa) to increase the stability of the controller system by increasing the gap between the filling and venting controllers for each actuator. According to the sign of the pressure error, a switch is designed to select either the filling or venting controller. While the air pressure is under the closed loop control, the position in this cascaded system is under an open loop control system.

Figure 8.12 and Figure 8.13 show the desired x, y and z displacements and the feedback data from the cascaded control system at no-load and the error, respectively. It is clear that there is no correction to y when the x changes, and vice versa. Furthermore, in a load condition, the pressure control will work properly while the position will present a high error.

8.4.2 Closed-Loop Position Control of the Two-Segments Soft Arm

A large amount of data has been used to map the movement of the soft arm by pressurising the 9-actuators into different patterns and repeating these values several times. Due to the softness, nonlinearity and hysteresis of the PMA, the positions at similar pressure patterns differ each time, and that makes the inverse identifier system not accurate enough, which causes an error in position even at no-load.

Due to the unique design of the proposed soft arm, the pressure in each muscle effects the position of the end effector significantly. Consequently, a suitable control algorithm has to be applied to solve the position control under load conditions.

According to Figure 8.2 and Figure 8.7, the movement of the extension section covers 360° at displacement up to an average of 260 mm in all directions, which can represent a base joint for the robot arm. On the other hand, pressurising the bottom section causes a movement toward the *z*-axis by about 150 mm (see Figure 8.2, Figure 8.5 and Figure 8.7).

An infinitive degree of freedom and the numbers of base joints make the motion planning for the robot arm quite difficult since the search space will be large, as it is exponential in the number of robot joints [48]. To reduce these difficulties, another classification might be present for the arm joints according to the active actuator in section one.

At the beginning, a certain task is asked of the robot arm, such as grasping objects of different weights each time and moving them to a specific position in space by selecting a suitable path. This plane can be generated and then executed by applying a suitable control system [49].

In the case of the proposed continuum arm, both the joint classification and the motion plan have been explained in Figure 8.14, which only shows the motion by the extension section.

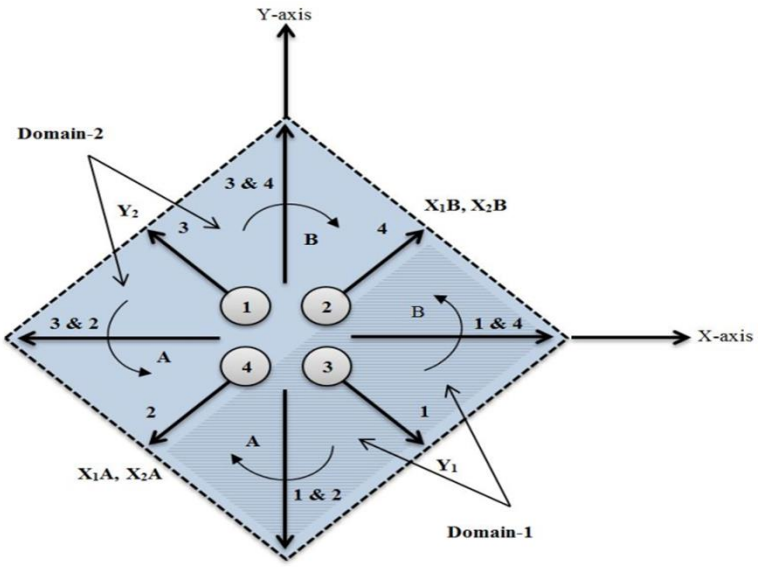

Figure 8.14 Joints and motion of the extension section.

Assuming that each muscle represents a joint, the robot arm will move towards the arrows (1, 2, 3 and 4) when one actuator (single joint) has been activated. The motion starts from the initial point P_0 (0, 0) into points P_1 (125, −229), P_2 (−249, −157), P_3 (−224, 135) and P_4 (213, 189) (see Figure 8.7) by an approximately straight line, and its displacement depends on the amount of air pressure, which varies from 0 kPa to 500 kPa.

Referring to Figure 8.14, domain-1 illustrates the motion of the continuum arm by activating the actuators 1, 2 and 4 (joints 1, 2 and 4), which represents 50% of the full motion of the robot arm due to the top section. Domain-2 shows the motion due to the extension actuators 3, 2 and 4 (joints 3, 2 and 4), and that is the other half of the robot motion. Figure 8.15 shows the movement of the three joints in domain-1, according to the explanation above.

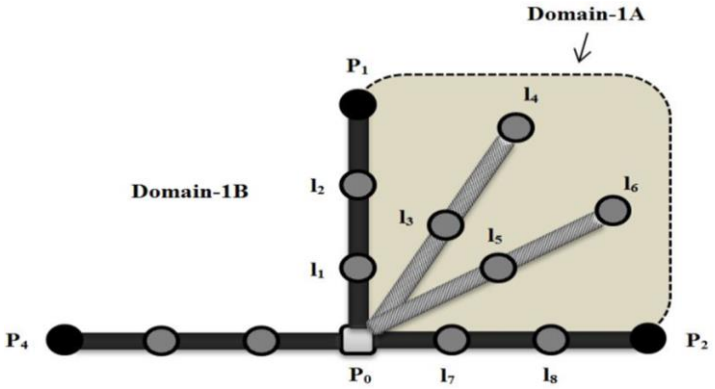

Figure 8.15 The top view of the three joint movements of actuators 1, 2 and 4 at x-y plan.

Applying air pressure to the extensor PMA1, drawing a path from P_0 to P_1 through l_1 and l_2 at zero pressure in PMA2 and PMA4 while pressurising PMA2, leads to moving the robot arm toward P_2 through l_7 and l_8. The rest of the l-points refer to the other locations of the robot arm due to different pressurising conditions for PMA1 and PMA2.

According to Figure 8.14 and Figure 8.15, the following position control algorithm is proposed for the soft robot arm under study:

Assign y-axis to actuators 1 and 3 as follows:

- Actuator 1 covers y values at domain-1 and defines as Y_1.
- Actuator 3 covers y values at domain-2 and defines as Y_2.
- If the desired position point locates under Y_1; the PMA2 and PMA4 define as:
- Actuator 2 covers x-values at domain-1A and defines as X_1A.
- Actuator 4 covers x-values at domain-1B and defines as X_1B.
- If the desired position point locates under Y_2; the PMA2 and PMA4 define as:
- Actuator 2 covers x-values at domain-2A and defines as X_2A.
- Actuator 4 covers x-values at domain-2B and defines as X_2B.

While the bottom section is built from bending-contraction actuators which provide bending behaviour effects directly to the z-direction of the robot arm, these PMAs have been classified into two pairs to work together and control the z-position as the following:

- If the desired position point locates under Y_1, bending-actuator3 and bending-actuator4 pressurise simultaneously.
- If the desired position point locates under Y_2, bending-actuator1 and bending-actuator2 pressurise simultaneously.

The length's increment of the proposed soft arm is considered to be a special motion at the origin of the x-y plan. To achieve this movement the controller applies equally suitable values of air pressure to all 5- actuators in the extension section at the same time.

The layout of the soft robot arm and the pixy cameras have been used (see Figure 8.6) to control the position of the end-effector according to the block diagram in Figure 8.16.

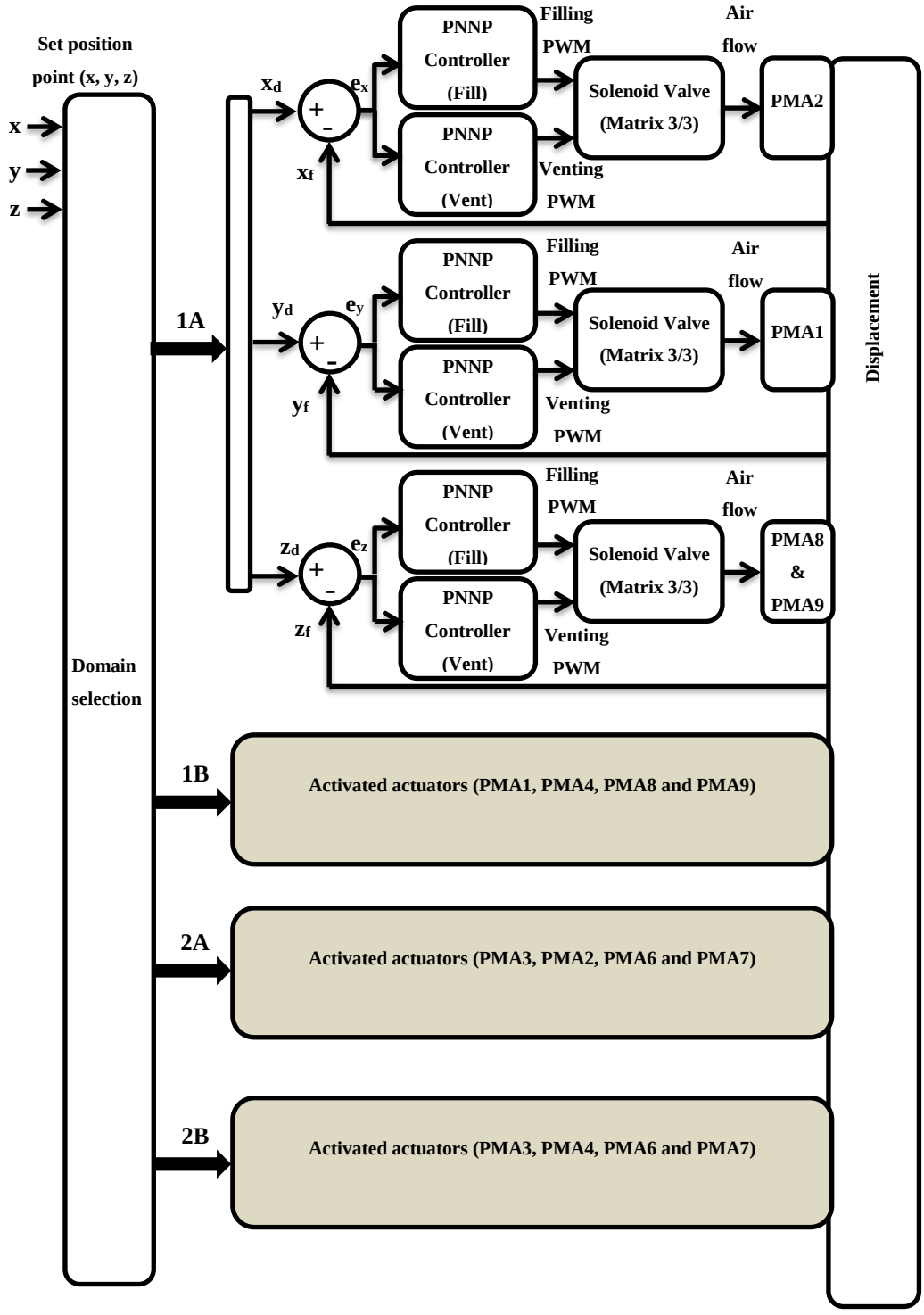

Figure 8.16 The full block diagram of the closed loop position control system.

The algorithm distributes the axes to the actuators and provides an easy and effective strategy to control the position of the soft robot arm at any load condition. The controller system in Figure 20 has been applied to an example of movement from the initial point (0, 0, −720) to the target point (−30, −120, −650) at three load conditions (no-load, 300 g and 500 g) and for three repetitions at acceptable accuracy as in Figure 8.17. Moreover, this motion used four actuators (PMA1, PMA2, PMA8 and PMA9), while other motions could use other combinations of actuators but under the algorithm above.

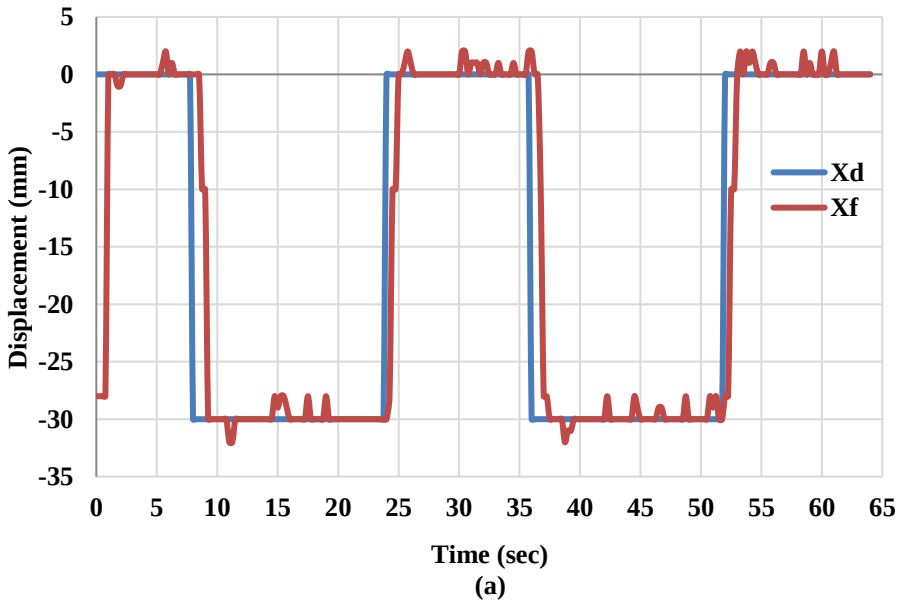

(a)

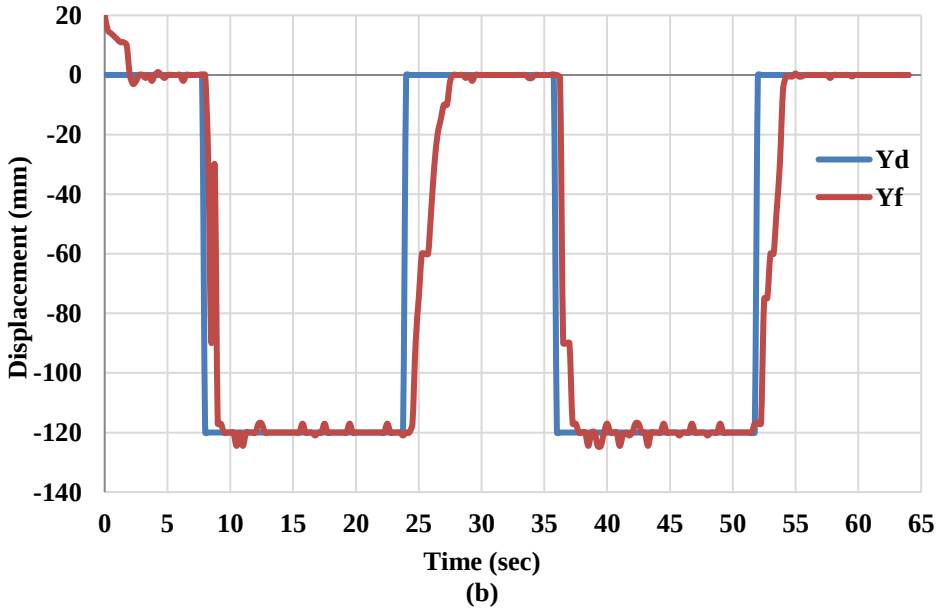

(b)

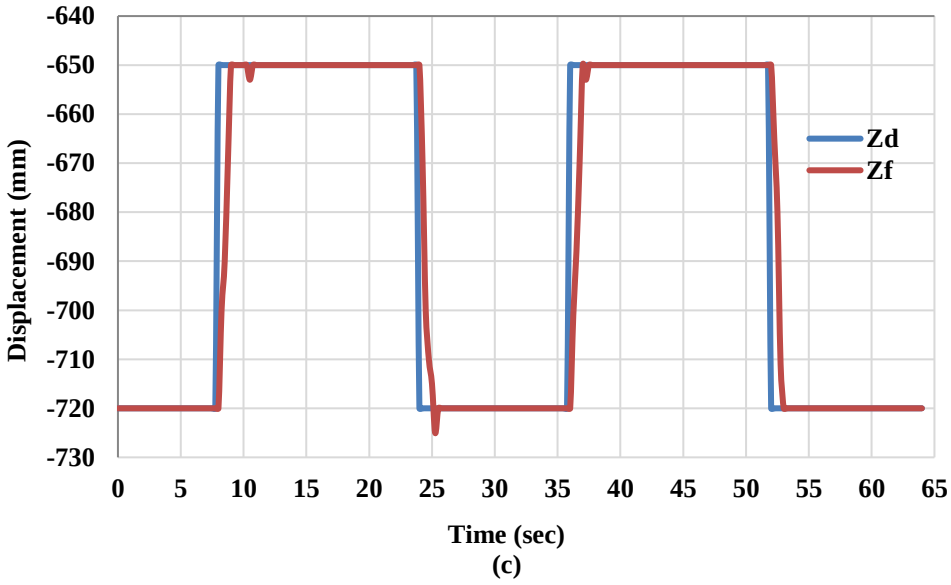

Figure 8.17 The reference and the feedback positions at 300 g. (**a**) Is the X and Xf position. (**b**) Is the Y and Yf position. And (**c**) Is the Z and Zf position.

The results of this experiment have been illustrated in Figure 8.17 and Figure 8.18, and since changing the air pressure in PMA1, not only affects the *y*-position but also both the *x* and *z* positions. Therefore, each time the controller of PMA1 tries to track the desired position on y, the controller of PMA2 changes the pressure of the (x) actuator to track x and the controller of the bending actuators adjusts the pressure of the (z) actuators to correct the z-position.

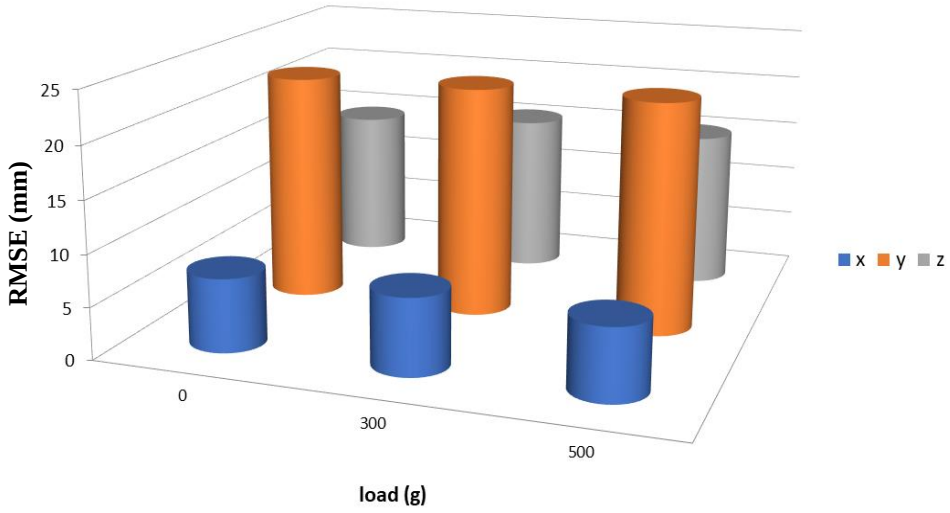

Figure 8.18 The RMSE for the position control at three different load conditions.

This is useful if the x-controller will first affect the y and z positions, and the z-controller affects the x and y controller.

The maximum air pressure in the activated actuators is listed in Table 2 at different load conditions and it is clear that the air pressure is increased when the load is increased.

Figure 8.17 shows the tracking of x, y and z at 300 g with low steady state error, which proves the quality of the presented algorithm and the closed loop controller. The root mean square error (RMSE) for no-load, 300 g, and for 500 g is shown in Figure 8.18. While the maximum applied air pressure has been listed in Table 8.1, it rises with the increment in load to increase the payload for the soft robot arm.

Table 8.1 The maximum pressure in kPa in the activated actuators at different load values.

Load (g)	PMA1	PMA2	PMA8 & PMA9
0	140	70	320
300	310	130	450
500	500	176	500

8.5 Summary

A new continuum arm structure is proposed by using both types of actuators as two sections of the soft robot arm. The first section has been made from five extensor PMAs while the bottom section is made from five contractor air actuators. This design provides special performances of this type of robot arm, such as elongation, contraction, bending by single or both sections towards all directions.

A modified design of the presented continuum arm has been implemented by replacing the five (simple) contraction actuators in the bottom section with four self-bending contraction actuators (SBCA) to reduce the number of actuators and enhance the bending performance. A full mapping of its movement is then illustrated. A cascaded position control has been applied by using inverse model identification and a valuable closed-loop neural network (NN) controller for air pressure. This method shows the ability to achieve a specific position in the space at no load of the proposed soft arm.

A new position control algorithm has been proposed from the mapping data and moving performances of the presented continuum arm. This algorithm distributes the *x*-axis and *y*-

axis on corner actuators of the top section and the z-axis on the two pairs of the bending-contraction actuators in the bottom section.

A specific layout of two PIXY cameras is explained to get three-dimensional data from the free-end of the continuum arm by using the two-dimensional output of the camera. The proposed algorithm and the feedback from the vision system are used to design and apply an efficient closed-loop position control of the presented continuum arm at different load conditions.

Numerous applications can be achieved by using the proposed continuum arm in its modified version, such as manufacture food processing and as a classification robot arm, can pick up objects and move them depending on their colour, weight or shape by using specific end-effectors and sensors.

Chapter Nine:

9. Multiple Robot System

9.1 Introduction

Several combinations of collaborative robot system could be applied as mentioned in chapter 3. In this chapter, a task sharing is produced for two and three continuum arms respectively (R-R). Then, a collaborative between a human and a single soft robot arm (R-H) is proposed by three configurations.

9.2 Robot-Robot (R-R) Collaborative System

9.2.1 Single bending continuum arms

In this section, two identical 30 cm length and 1.7 cm diameter SBCAs are built to form a bending continuum arm and an end-effector of three fingers (Section 7.2) made from SBCA of 10 cm length and 1.7 cm diameter for each arm as shown in Figure 9.1.

Figure 9.1 A 30 cm bending continuum arm and the three fingers gripper

The proposed continuum arms have a single bending direction controlled by a PNNP controller system. They laid out to bend toward each other to perform a simple task as shown in Figure 9.2. The controller system applied an air pressure to the gripper of the arm *A* (left) to grasp the object then both arms bend to 90°. At this point, the gripper of the Arm *B* (right) is activated while the gripper of the arm *A* is released. The PNNP controller system then forces both arms to 0°, and release the second gripper.

Figure 9.2 The proposed continuum arms at 90 degree.

The NN controller for the bending process has been trained by the approximation relationship between the duty cycle and the bending angle as in (9.1):

$$\beta = \frac{215\ (degree) \times u}{98} \tag{9.1}$$

Where: β is the bending angle, (215°) is the maximum bending angle of the 30 cm SBCA (see 6.2.2) at no-load, and u is the duty cycle.

While, the NN controller for the grasping process is trained by using the approximation function between the grasping force and the duty cycle similar to (7.2).

The PNNP controller is configured from 8-sub controllers, two (fill & vent) for each variable (bend & grasp) per arm.

An experiment has been done to validate the high repetition level of the unidirectional continuum arm to bend up to 90° for 30 times. The results show that the maximum error in bending angle is 0.5° and the MSE for the process of 30 times is 0.070077. This result shows the high reliability of the continuum arm and the PNNP control system.

9.2.2 Multiple bend continuum arms

This section presents a collaborative control system by using unidirectional and bidirectional continuum arms. The collaborative system consists from two tasks: (i) R-R and (ii) R-R-R as follows:

9.2.2.1 Two continuum arms collaborative system

As explained in section 4.2.3, the structure of the PMA affects its force. Therefore, a large size of SBCA is designed to increase the bending payload. An inner rubber tube of 26.5 mm inner diameter and stuffiness of 545 N/m is used to build a 60 cm reset length continuum arm with end effector of four 13 cm reset length fingers gripper (using 4 instead of three is to increase the grasping force, see section 7.2.1). Table 9.1 lists the full specification of the continuum arm and Table 9.2 shows the specification of the fingers. While the proposed continuum arm and the end effector is shown in Figure 9.3.

Table 9.1 The specifications of the continuum arm.

L_0 (m)	**Rubber thickness (m)**	**Braided thickness (m)**	**Rubber diameter (m)**
0.6	1.1×10^{-3}	0.5×10^{-3}	26.5×10^{-3}
Rubber stiffness(N/m)	**Rod length (m)**	**Rod thickness (m)**	**Rod width (m)**
545	0.6	0.003	0.025

Table 9.2 The specifications of the bending finger.

L_0 (m)	**Rubber thickness (m)**	**Braided thickness (m)**	**Rubber diameter (m)**
0.13	1.1×10^{-3}	0.5×10^{-3}	12×10^{-3}
Rubber stiffness(N/m)	**Rod length (m)**	**Rod thickness (m)**	**Rod width (m)**
363	0.13	0.002	0.008

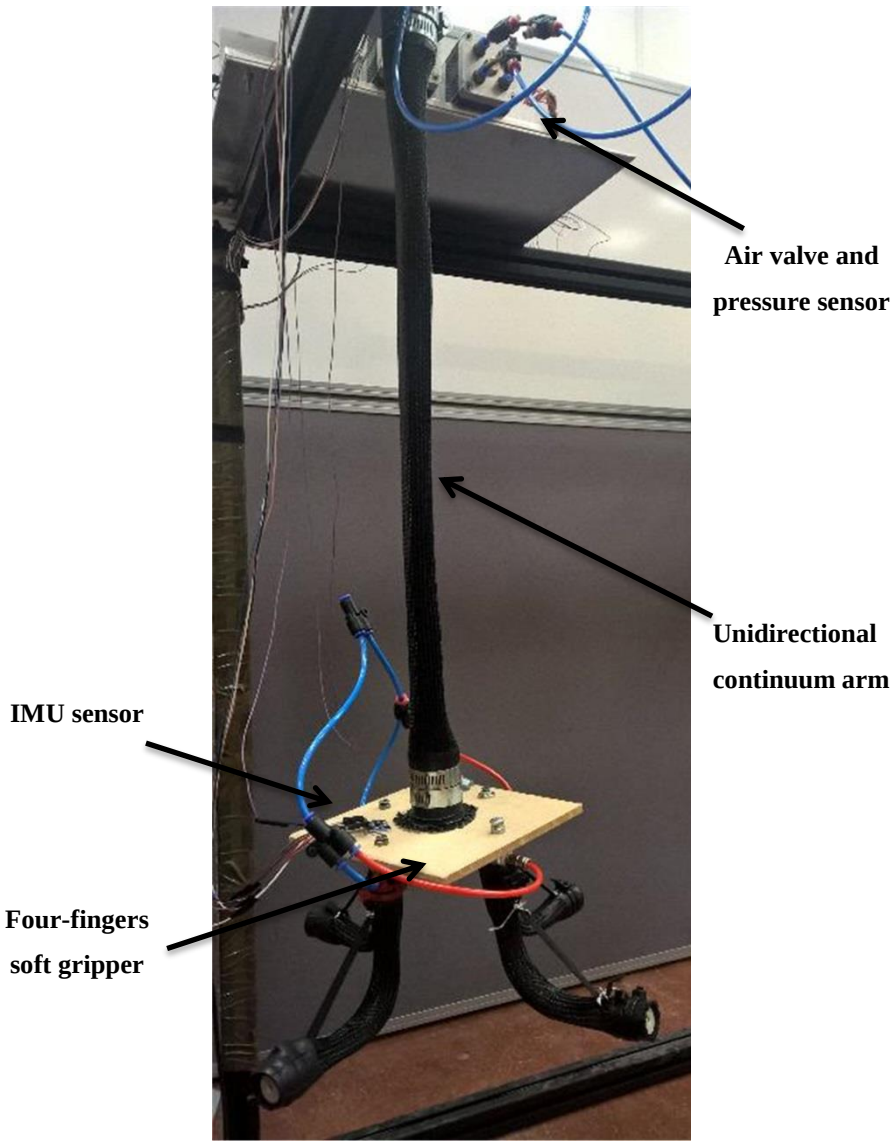

Figure 9.3 The proposed unidirectional continuum arm and the end effector.

The second arm is constructed centre SBCA as in Table 9.1 to bend in one direction and two identical SBCAs for the specifications similar to that in Table 9.2, but, the initial and the rod lengths are 60 cm each. These two actuators laid in the left and the right of the first SBCA to bend in opposite direction. This structure provides balance to the end effector. The extension-circular gripper (section 7.3) is used for this arm. Figure 9.4 shows the bidirectional continuum arm and the end effector. On the other hand, the bending direction of the bidirectional continuum arm is shown in Figure 9.5.

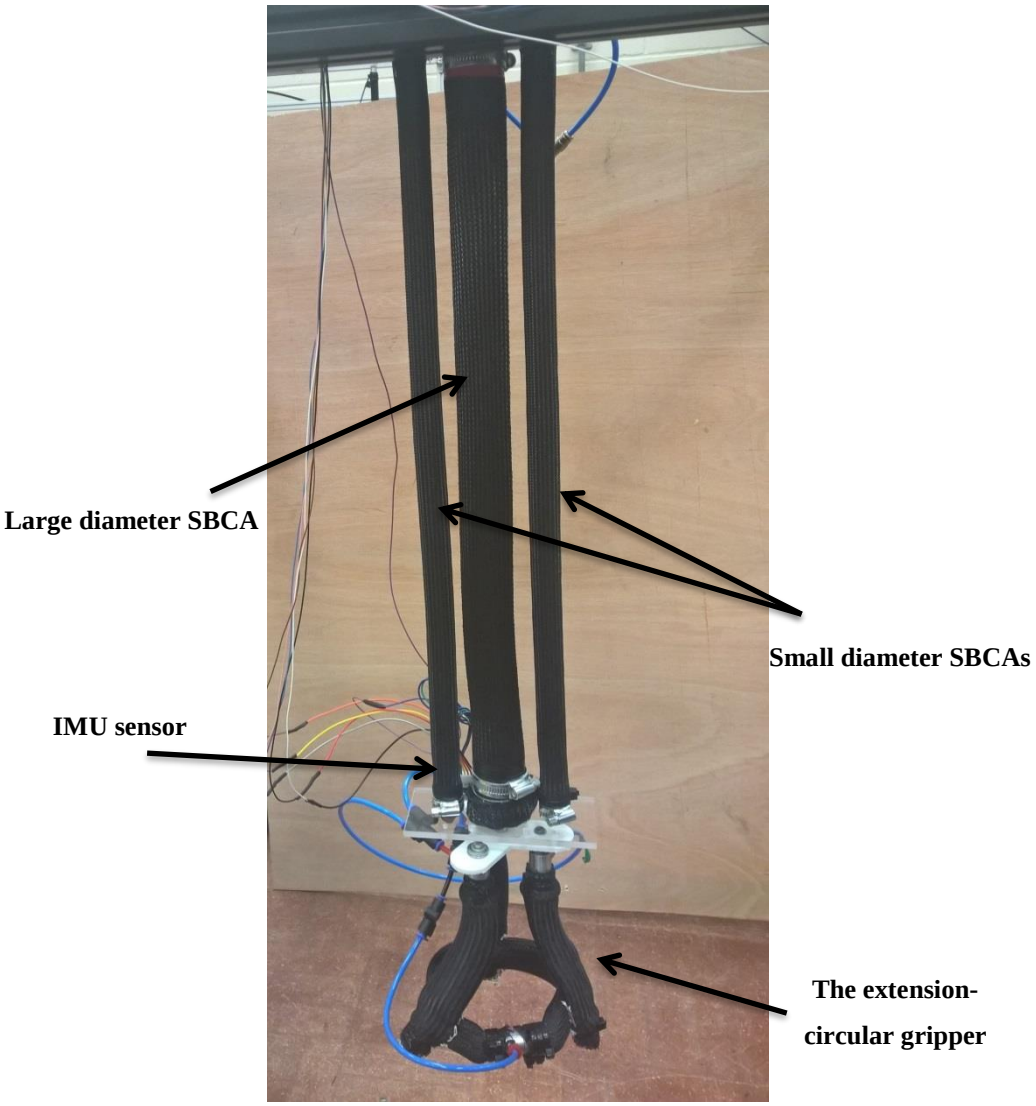

Figure 9.4 The bidirectional continuum arm and the soft gripper.

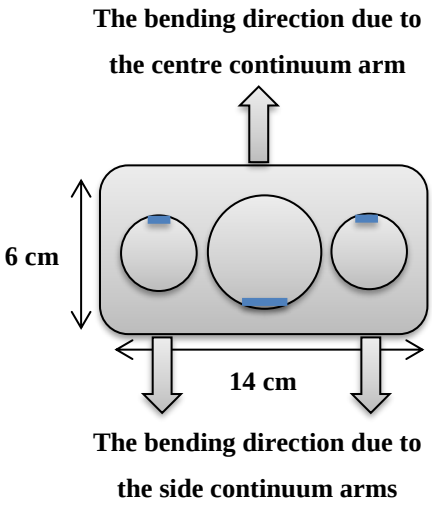

Figure 9.5 The bending direction of the bidirectional continuum arm.

Similar task for the previous section is used but the grasping process is started from the bidirectional soft arm first. The bidirectional continuum arm has the ability to bend in two directions together with bending ability of the extension-circular gripper (section 7.3). And that provides an additional advantage by grasping an object that even does not in the centre of the arm. Figure 9.6 and Figure 9.7 illustrate several shifted bending examples. Figure 9.8 shows the two arms at 90°.

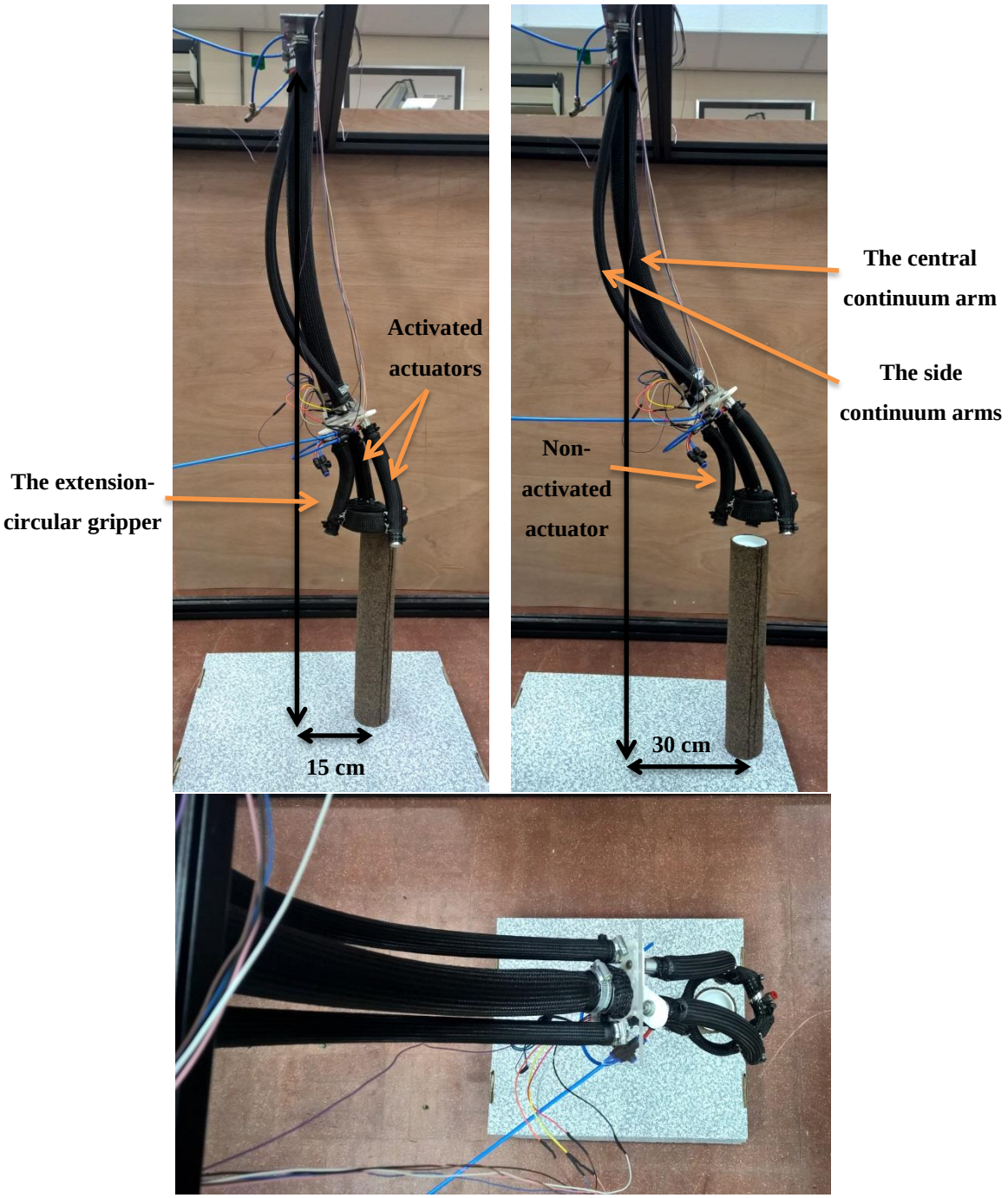

Figure 9.6 The bidirectional continuum arm at different right-shift bending examples.

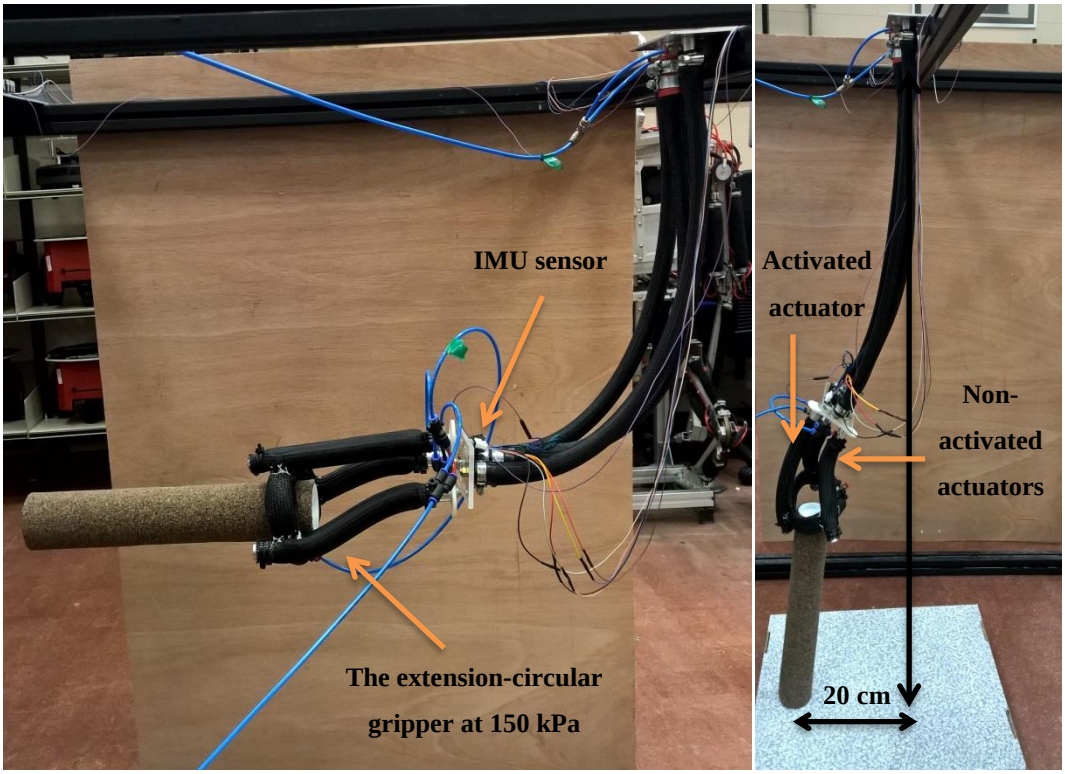

Figure 9.7 The bidirectional continuum arm at different left-shift bending examples.

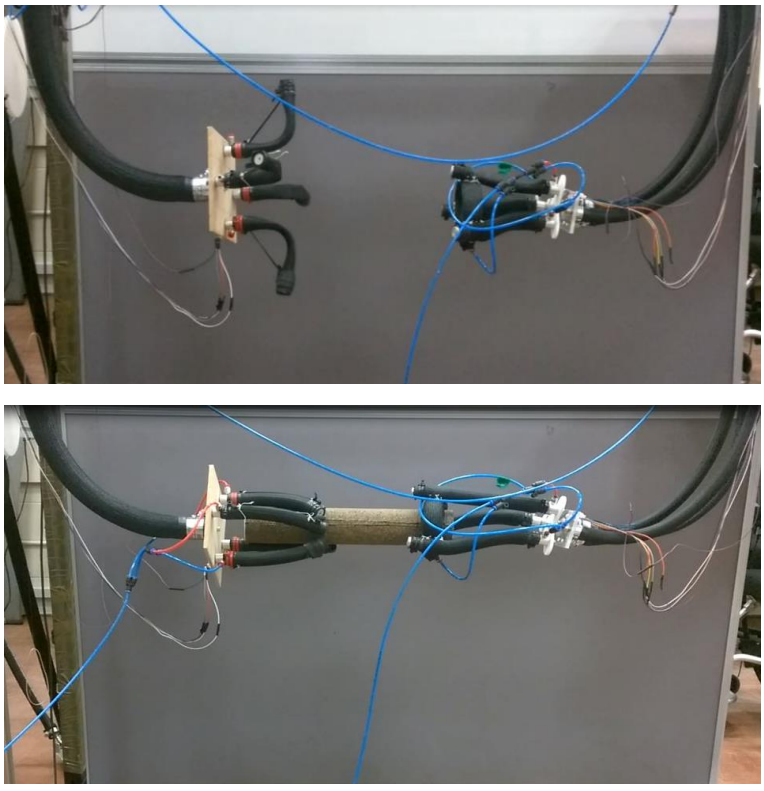

Figure 9.8 90° bending angle of the both arms

9.2.2.2 Three continuum arms collaborative system

In this section, three continuum arms are involved in a collaborative task. Two unidirectional arms on the both sides of a centre bidirectional continuum arm. The previous designs for both arms are used as shown in figure 9.9.

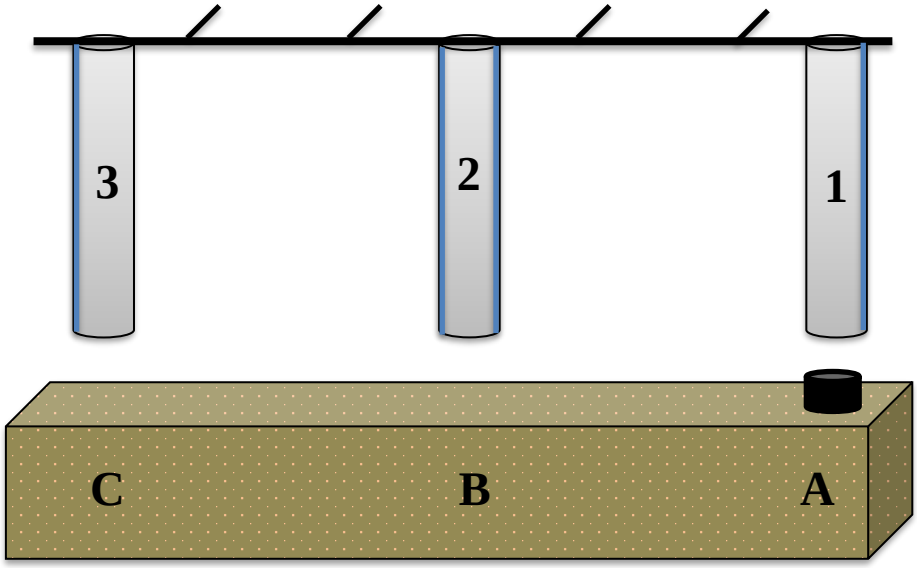

(a)

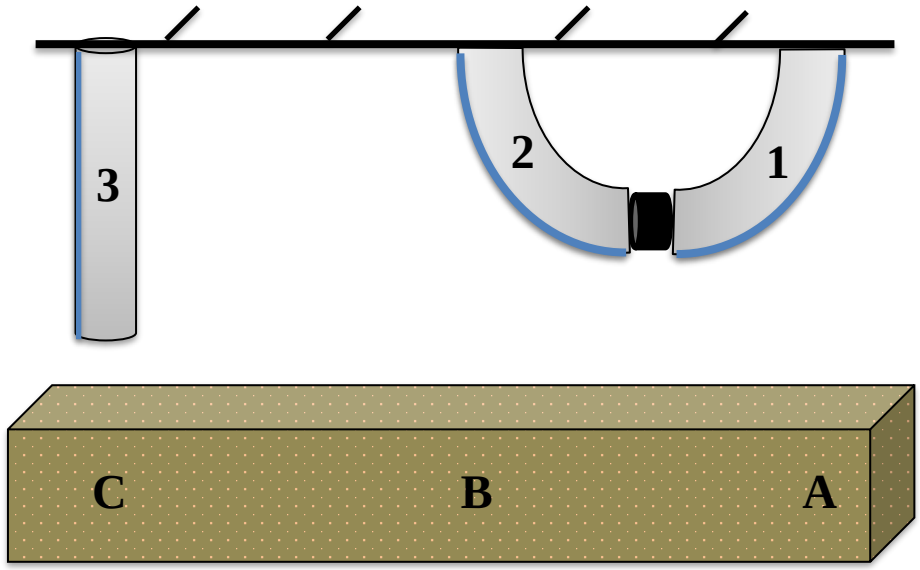

(b)

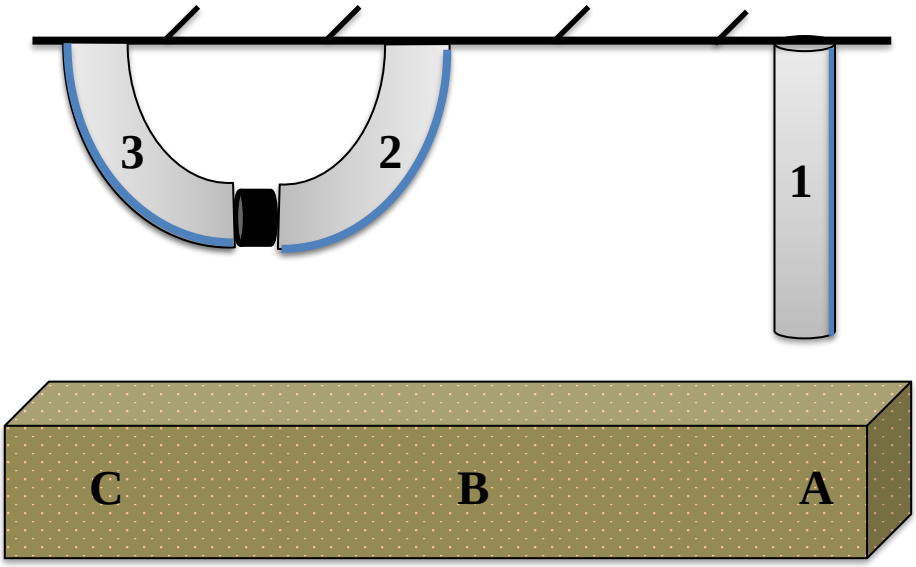

(c)

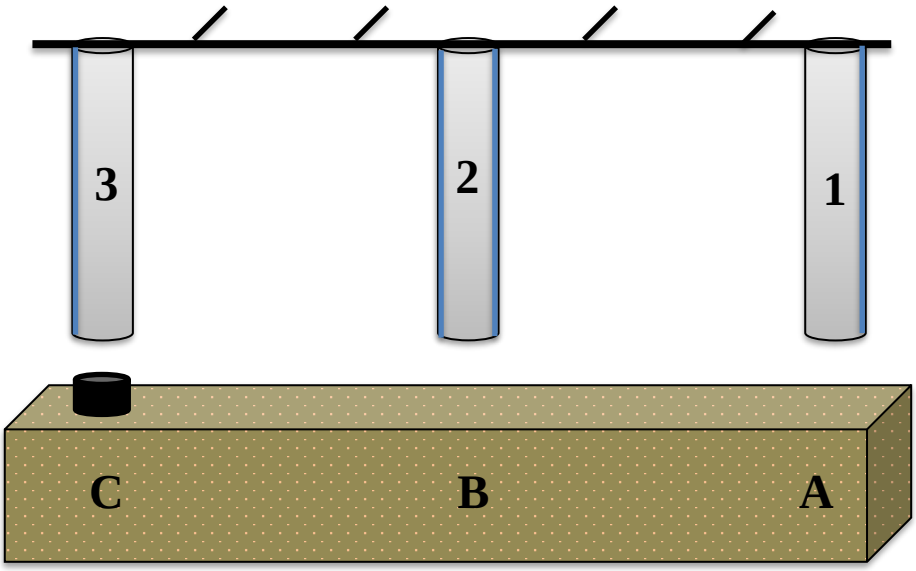

(d)

Figure 9.9 The layout of the continuum arms and moving process of an object from position A to position C. (**a**) the object at position A. (**b**) activating arm1 and arm2. (**c**) activating arm2 and arm3. and (**d**) the object at position C.

The PNNP controller system for this task contains 16-sub controller divided by eight pairs. Two controllers are used for each bending direction and that equal to eight, two for each finger-gripper, and four for the extension-circular gripper.

Similar layout in Figure 9.9 is used again, nevertheless, the task starts from the centre bidirectional continuum arm. A colour detection sensor is added to the extension-circular gripper to classify the objects into two groups. Then the arm passes the objects either to the left arm or to the right arm (see Figure 9.10).

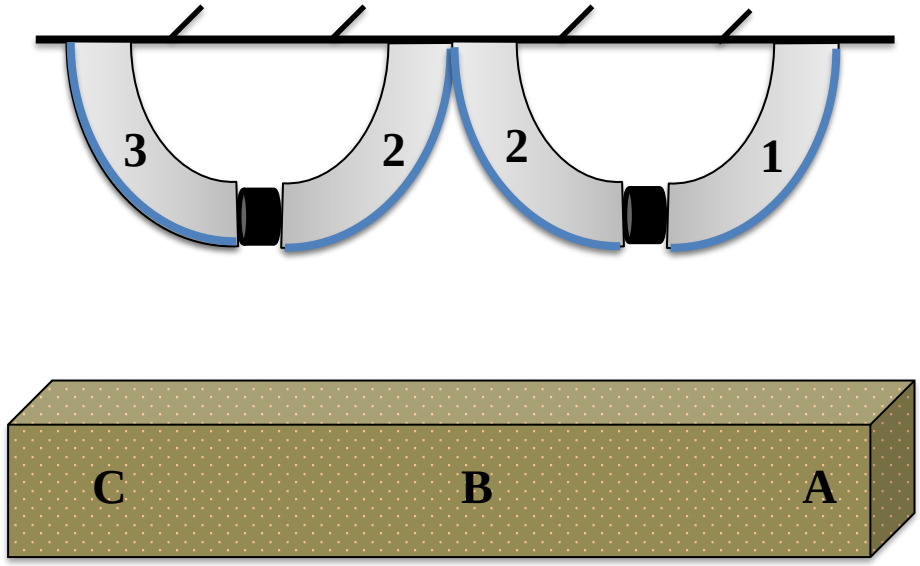

Figure 9.10 Colour classification task

9.3 Human-Robot Interaction (HRI)

A task has been done to show the HRI by using similar unidirectional continuum arm above. Furthermore, the DB-PMA (section 6.3) is used to construct a single-actuator continuum arm, using its performances of moving vertically and horizontally.

9.3.1 Sharing control of HRI

Unsafe workspace for individuals forces them to work from a split-site. In this section, a single direction continuum arm and a four finger-gripper (see Figure 9.3) is used to work in a workspace consider to be unsafe for human being. A MPU and a pressure sensor are used to measure the bending angle of the continuum arm and the air pressure in the finger-gripper respectively. On the other hand, the MPU sensor and the flex sensor are worn by a human hand as shown in Figure 9.11.

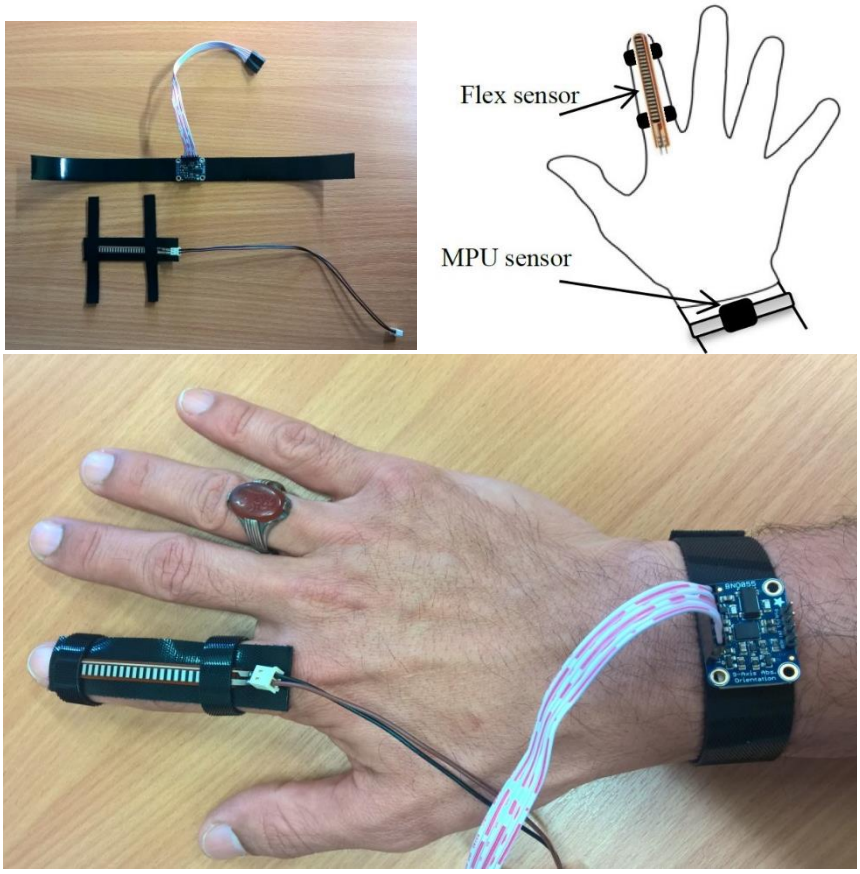

Figure 9.11 The wearable sensors to control the bending angle and grasping force

The wearable MPU sensor is used to send the set bending angle to the PNNP controller to adjust the bending angle of the continuum arm; and the flex sensor control the grasping fore of the finger-gripper by converting the resistance to a pressure. The controller system controls the air pressure in the fingers to control the grasping process.

In this process, the human sends a variable reference bending and grasping force to the controller via Arduino Mega 2560, and the controller adjusts both of them on the continuum arm. Figure 9.12 shows the bending angle for the both the human hand and the continuum arm at two different loads.

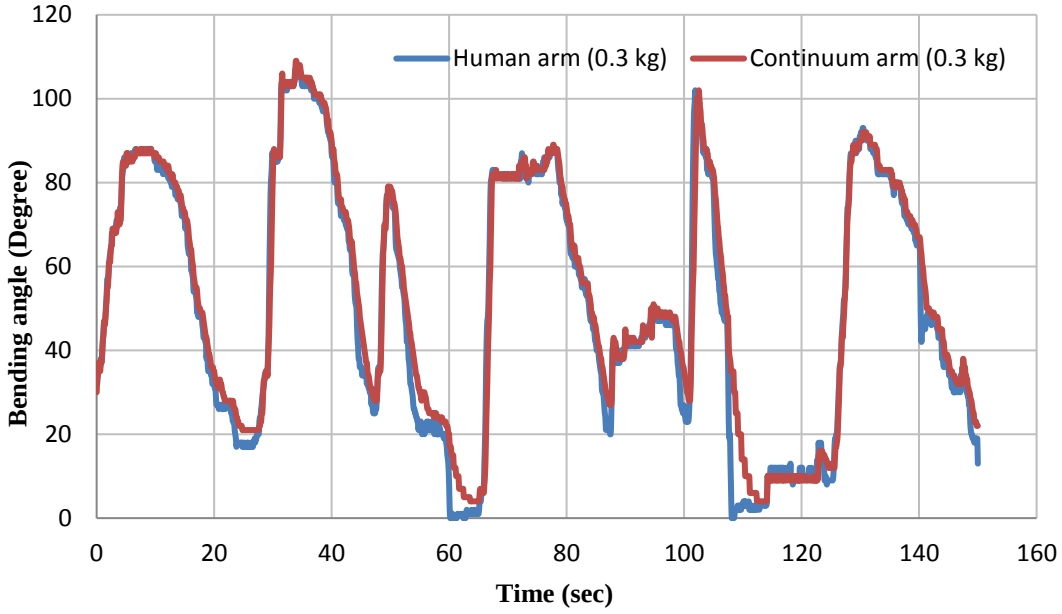

(a)

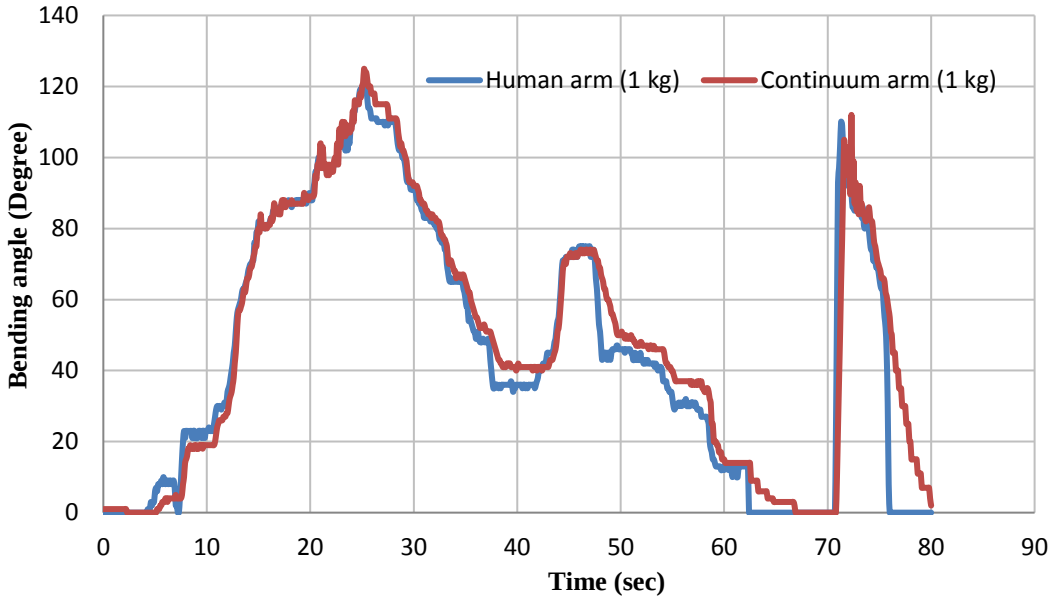

(b)

Figure 9.12 The bending angle for both the human hand and the continuum arm at 0.3 and 1 kg.

Figure 9.12 illustrates the efficiency of the PNNP controller, which provides a precise tracking for the bending angle of human arm. As previous mentioned, the tracking error for the filling process is less than the error of venting process due to the difference between the air pressure in the air muscle and the environment. Figure 9.13 shows the human and the continuum arms at certain bending angle and grasp force.

Figure 9.13 the human and the continuum arms at certain bending angle and grasp force

9.3.2 Continuum arm by DB-PMA

The double-bend PMA (section 6.3) is used with a gripper of two fingers based on SBCA to form a continuum arm work together with a human. Figure 9.14 illustrates the gripper and the proposed continuum arm is illustrated in Figure 9.15 at different pressurised conditions.

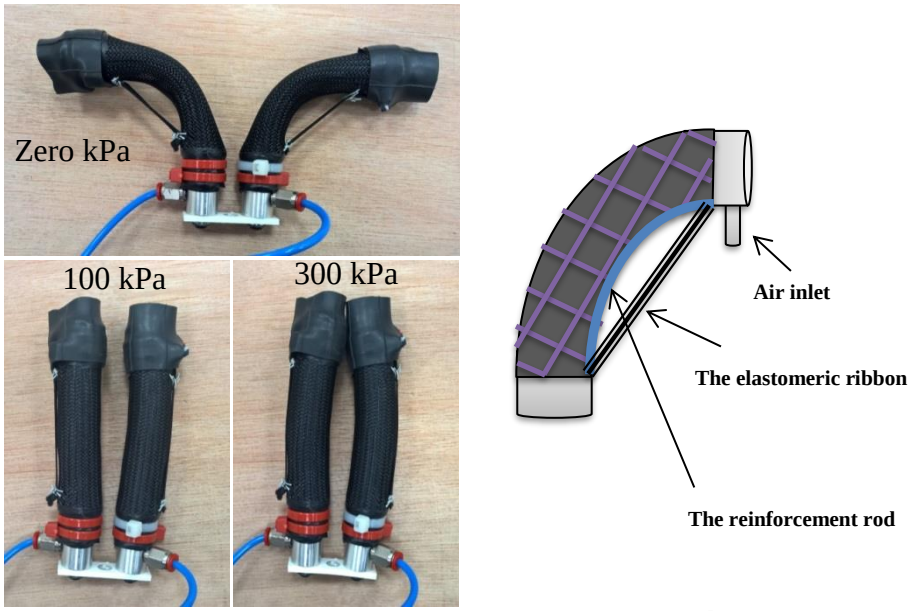

Figure 9.14 The two-fingers soft gripper based on self-bending contraction actuators (SBCA). (**a**) The soft gripper at different air pressures. (**b**) The schematic design of the soft finger.

Figure 9.15 The proposed continuum arm at different pressurised conditions.

Again, the PNNP controller is used in this section to control the horizontal movement (L_h) of the robot arm by using an ultrasound sensor (HC-SR04) to measure the horizontal length. Figure 9.16 shows the flowchart of the controller system, and the NN is trained by the approximation function as in (9.2).

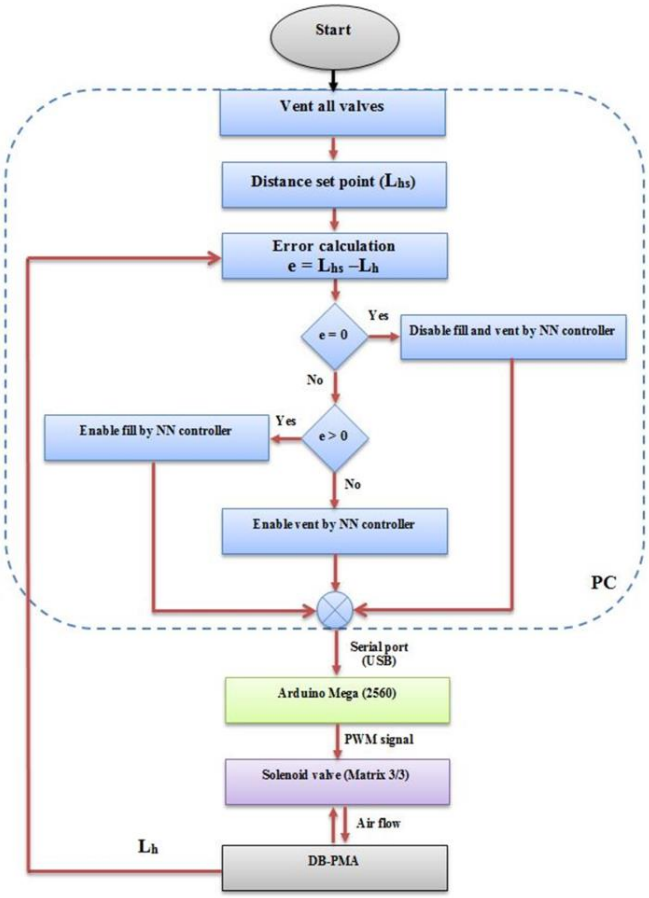

Figure 9.16 The flowchart of the control system and the continuum arm.

$$L_h = \frac{0.5L_0 \times u}{98} \tag{9.2}$$

where: L_h is the horizontal distance between the initial position (relaxed condition) and the new position (pressurised condition), u is the controlled duty cycle of the pulse width modulation (PWM) signal, L_0 represents the initial length, the number 98 refers to the 98% of the maximum duty cycle for the control signal to avoid continuous supply to the air valve, and 0.5 is the maximum horizontal distance L_{hmax} (50%) for special case 2 (section 6.3.34).

Step and sinusoidal signals were applied to the controller system at 0.5 Hz, and the response for the horizontal moving process is illustrated in Figure 9.17.

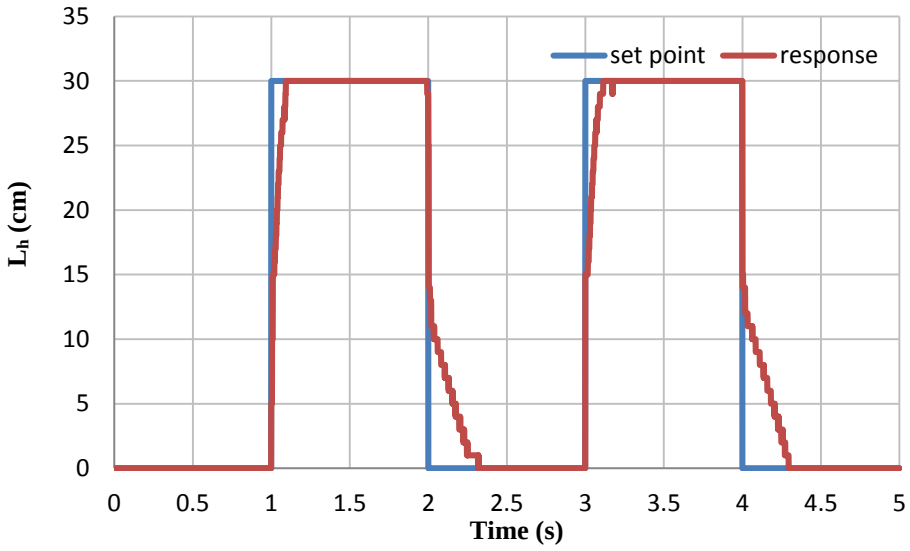

(a)

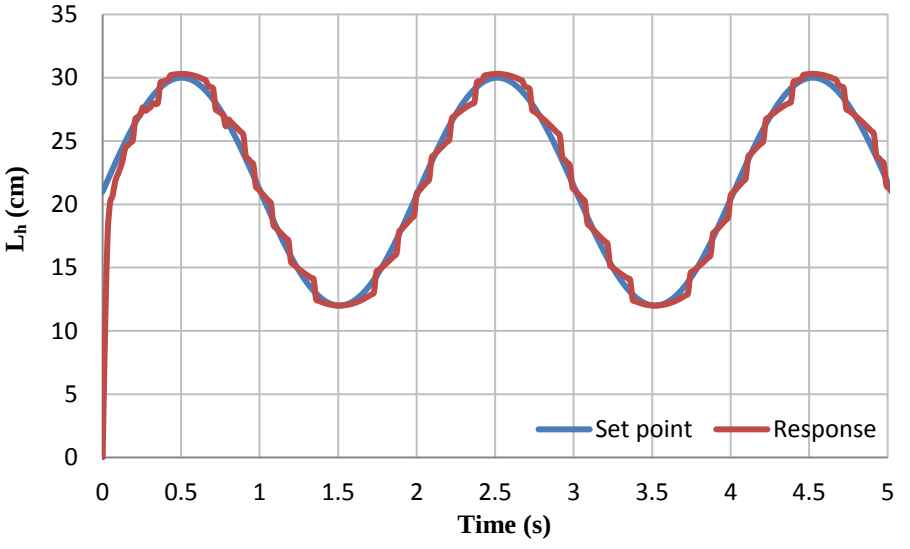

(b)

Figure 9.17 (**a**) The step response of the horizontal distance at 0.5 Hz. (**b**) The sinusoidal response of the horizontal distance at 0.5 Hz.

Figure 9.17 shows that the contraction time was more than the elongation time due to the hysteresis of the actuator material and the pressure difference between the actuator and

the outside pressure. The sinusoidal response shows that the L_h is tracking the input signal with low error values.

This process illustrates the ability to use a single soft actuator as an effective robot arm for specific applications at zero or minimum loads. The second half, the gripper and the object, represents a load on the first half (upper-half). This accumulative load reduces the bending angle of the upper-half and places the end of the DB-PMA not in the vertical direction. Two options were possible to overcome the effect of the load condition: either the length of the reinforcement rod increases to increase the bending angle of the upper-half (Table 9.3) or two identical SBCAs in series are used instead of a single DB-PMA.

Table 9.3 The maximum bending angle for the three different self-bending contraction actuators (SBCAs) at 500 kPa.

Length of the Actuator and Reinforcement Rod (cm)	Maximum Bending Angle
10	25°
20	135°
30	215°

Figure **9.18** shows the new horizontal moving continuum arm using the SBCA. This modification ensures the horizontal motion of the continuum robot arm by applying different air pressure.

Using two SBCAs instead of the DB-PMA increased the controlled variables; however, the features were improved. Since each bending actuator is controlled individually, the soft robot arm shows different shapes and performances.

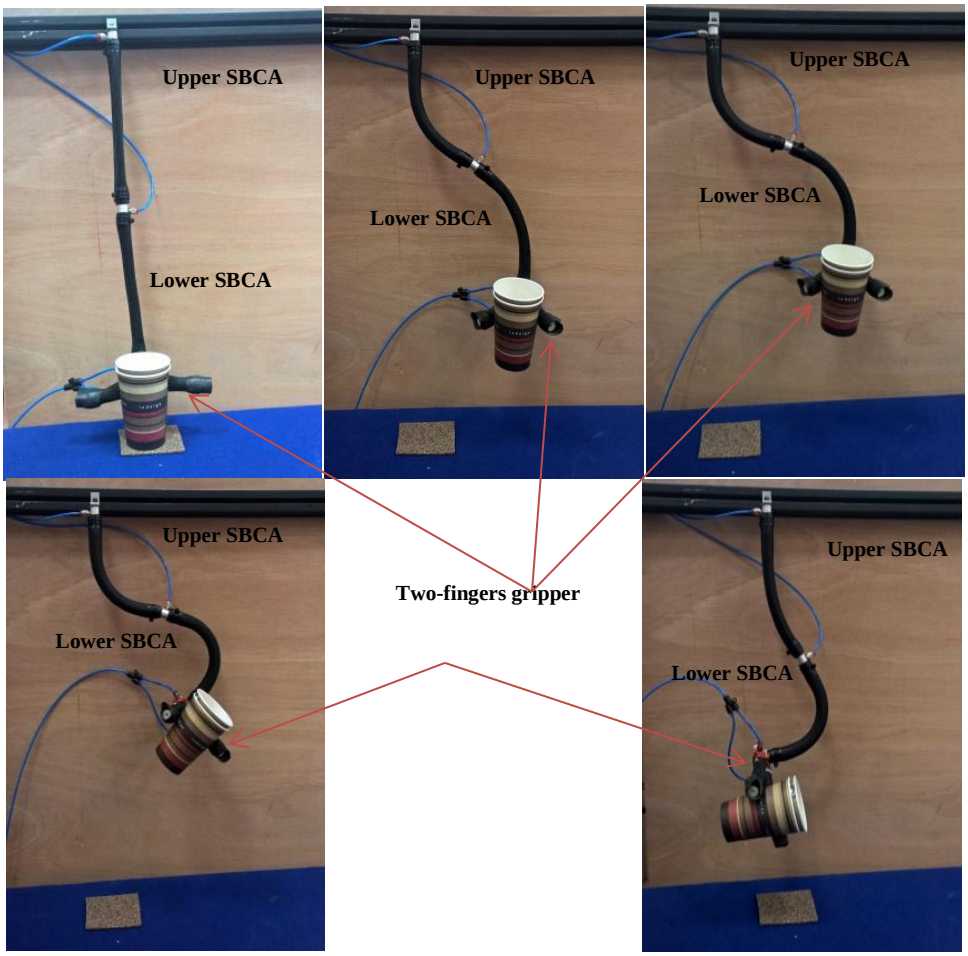

Figure 9.18 The horizontal moving arm of two SBCAs at different pressurising conditions.

Chapter Ten:

10. Summary and Future Work

10.1 Summary

A collaborative robot system and multi robots involves number of challenges and difficulties including the best design, optimal physical construction, efficient control, and safe human interaction. This thesis discussed the main types of actuators used in robots and the advantages and the drawbacks of each kind, then the case for using the pneumatic muscle actuator (PMA) has been argued in detail. The different types of the PMA and their performance are studied, the most common force models are overviewed, and the control strategies used are presented.

Furthermore, the safety factors and parameters are explained in chapter two in order to design a safer robot for human interaction. The main types of the collaboration systems are illustrated in chapter three.

Using the PMA for designing the entirely soft robot arm leads to the building of a new generation of robot system. This system has the advantages of soft actuators and soft material and overcomes the main disadvantages of rigid actuators as well as rigid material. On the other hand, the high level of nonlinearity is the greatest challenge of this type of robot. Moreover, the optimal models of actuator length and force have not yet been achieved, which lead to a complicated control process. These difficulties double when the continuum arm is constructed from multi PMAs.

In chapter four we proposed a mathematical model for the actuator length, then the modification of the Tondu and Lopez (2000) contraction force formula is introduced. Moreover, the new formula is adapted to fit with the extensor PMA. Many schemes are discussed for a multi PMAs configuration including soft arms. Then length, force and bending are tested. The free end angle is modelled mathematically for no load and load conditions. New structure-based formulas are presented in this chapter for the contraction PMA. The contributions in chapter four have been published in several journal and conference papers (See the publication list (1, 2, 4, 5 and 7)).

Chapter five presents a novel design of the neural network controller in parallel with the proportional controller (PNNP). This controller system provides a high precision and fast control performances to the single and multiple actuators as well as to the position control system, grasping and multiple robot system.

Chapter six presents three novel pneumatic actuators. Self-bending contraction actuator SBCA, which provides an efficient bending angle and bending payload. The second actuator is the double-bend pneumatic muscle actuator DB-PMA. The opposite bending behaviour of the DB-PMA in its two halves provide displacement in the horizontal and vertical directions. The circular pneumatic muscle actuator CPMA is the third novel actuator in this chapter and it is inspired by the human facial muscles. The CPMA provides an efficient grasping force compare with its weight.

Active soft grippers are presented in chapter seven. Two different designs are contributed in this chapter by using the extension, the SBCA and the CPMA. The contributions in chapter six and chapter seven have been published in several journal and conference papers (See the publication list (3, 7, 8 and 9)).

In chapter eight, novel multi-degree of freedom continuum arm is proposed. This arm is made from two sections to provide extension behaviour by using extensor PMAs in section one and an infinite direction bending by the bending-actuators in section two. Two position control strategies have been applied to this soft arm. A cascaded control system is applied first by mapping the moving data and then applied a pressure control at no-load. A closed loop control system then applied to control the position of the end-effector in space at different load conditions by using a control strategy depends on the structure and the mapping data. The contributions in this chapter are published in two papers (See the publication list (10 and 7)).

Chapter nine present different designs of continuum arms and collaboration tasks by using two or three continuum arms together and a robot- human interaction. Part of the contributions in this chapters are published (See the publication list (3 and 11)).

The proposed models showed a significant matching between the experimental and the theoretical data. On the other hand, the designs and the controllers show new and efficient performances of the soft robot.

10.2 Future work

The enhanced and the new models for the single and multiple pneumatic muscle contraction and extension actuators can be used for further research as a high accuracy mathematical models to design, built, and control the pneumatic muscle actuator (PMA).

Different structures of the continuum arms can be built by using the presented actuators by this thesis for different applications. Achieving a high bending continuum arm is being possible by using the self-bending contraction actuator (SBCA), which provides high bending performances in terms of bending angle and force. The novel circular pneumatic muscle actuator (CPMA) with its kinematics is suitable to many applications such as grasping due to its high radial force. Furthermore, the double-bend pneumatic muscle actuator (DB-PMA) can be used as a single continuum arm to move and object up and side simultaneously. Large scales of the presented actuators provide more force and displacement performances make them suitable for the industrial applications. On the other hand, small scales are also possible for limited work-space or for medical applications.

Further research is still needed to enhance the length, force, and bending angle formulas for the different types of the pneumatic muscle actuators. On the other hand, the contraction ratio for the single PMA can be enhanced by decreasing the rest braided angle, as well as increasing the braided angle will improve the extension ratio for the extensor PMA.

The parallel neural network-proportional (PNNP) controller provides high level of accuracy and rapid response due to the combination and the structure of the neural and proportional controllers. This PNNP controller is can be used to control the dynamic for the pneumatic system. Furthermore, the axes distribution algorithm offers an efficient strategy to control the position of the multiple directional soft continuum arms. On the other hand, the presented actuators and continuum arms together with PNNP controller can be used for different collaborative systems such as human-Robot interaction.

References

Adorno, B. V., Fraisse, P., & Druon, S. (2010). *Dual position control strategies using the cooperative dual task-space framework.* Paper presented at the 2010 IEEE/RSJ International Conference on Intelligent Robots and Systems (IROS), .

Al Abeach, L. A., Nefti-Meziani, S., & Davis, S. (2017). Design of a variable stiffness soft dexterous gripper. *Soft robotics, 4*(3), 274-284.

Albu-Schäffer, A., Wolf, S., Eiberger, O., Haddadin, S., Petit, F., & Chalon, M. (2010). *Dynamic modelling and control of variable stiffness actuators.* Paper presented at the 2010 IEEE International Conference on Robotics and Automation (ICRA), .

Amend, J., Cheng, N., Fakhouri, S., & Culley, B. (2016). Soft robotics commercialization: Jamming grippers from research to product. *Soft robotics, 3*(4), 213-222.

Andrikopoulos, G., Nikolakopoulos, G., & Manesis, S. (2014). Advanced Nonlinear PID-Based Antagonistic Control for Pneumatic Muscle Actuators. *IEEE Transactions on Industrial Electronics,, 61*(12), 6926-6937.

Anh, H. P. H. (2010). Online tuning gain scheduling MIMO neural PID control of the 2-axes pneumatic artificial muscle (PAM) robot arm. *Expert Systems with Applications, 37*(9), 6547-6560.

Bajo, A., Goldman, R. E., & Simaan, N. (2011). *Configuration and joint feedback for enhanced performance of multi-segment continuum robots.* Paper presented at the Robotics and Automation (ICRA), 2011 IEEE International Conference on.

Bartow, A., Kapadia, A., & Walker, I. (2013). *A novel continuum trunk robot based on contractor muscles.* Paper presented at the Proceedings of the 12th WSEAS International Conference on Signal Processing, Robotics, and Automation.

Bechar, A., & Edan, Y. (2003). Human-robot collaboration for improved target recognition of agricultural robots. *Industrial Robot: An International Journal, 30*(5), 432-436.

Berman, S., Halász, Á., Hsieh, M. A., & Kumar, V. (2009). Optimized stochastic policies for task allocation in swarms of robots. *IEEE transactions on robotics, 25*(4), 927-937.

Bicchi, Tonietti, G., Bavaro, M., & Piccigallo, M. (2005). *Variable stiffness actuators for fast and safe motion control.* Paper presented at the Robotics research. The eleventh international symposium.

Bicchi, A., & Tonietti, G. (2004). Fast and soft arm tactics: dealing with the safety–performance tradeoff in manipulators design and control. *IEEE Robotics and Automation Magazine, Special Issue on 'Safety Among Us, 11*, 22-33.

Bowler, C. J., Caldwell, D. G., & Medrano-Cerda, G. (1996). *Pneumatic muscle actuators: Musculature for an anthropomorphic robot arm.* Paper presented at the Actuator Technology: Current Practice and New Developments., IEE Colloquium on (Digest No: 1996/110).

Burgard, W., Moors, M., Fox, D., Simmons, R., & Thrun, S. (2000). *Collaborative multi-robot exploration.* Paper presented at the Proceedings. ICRA'00. IEEE International Conference on Robotics and Automation, 2000. .

Cai, D., & Yamaura, H. (1996). *A robust controller for manipulator driven by artificial muscle actuator*. Paper presented at the Proceedings of the 1996 IEEE International Conference on Control Applications, 1996., .

Camarillo, D. B., Carlson, C. R., & Salisbury, J. K. (2009). *Task-space control of continuum manipulators with coupled tendon drive.* Paper presented at the Experimental Robotics.

Carbonell, P., Jiang, Z.-P., & Repperger, D. (2001). *Nonlinear control of a pneumatic muscle actuator: backstepping vs. sliding-mode.* Paper presented at the Proceedings of the 2001 IEEE International Conference on Control Applications, 2001.(CCA'01). .

Catalano, M. G., Grioli, G., Garabini, M., Bonomo, F., Mancini, M., Tsagarakis, N., & Bicchi, A. (2011). *Vsa-cubebot: A modular variable stiffness platform for multiple degrees of freedom robots.* Paper presented at the 2011 IEEE International Conference on Robotics and Automation (ICRA),.

Cervantes, I., & Alvarez-Ramirez, J. (2001). On the PID tracking control of robot manipulators. *Systems & control letters, 42*(1), 37-46.

Choi, H., & Koc, M. (2006). Design and feasibility tests of a flexible gripper based on inflatable rubber pockets. *International Journal of Machine Tools and Manufacture, 46*(12), 1350-1361.

Chou, C.-P., & Hannaford, B. (1996). Measurement and modeling of McKibben pneumatic artificial muscles. *IEEE Transactions on robotics and automation., 12*(1), 90-102.

Davis, S., & Caldwell, D. G. (2006). Braid effects on contractile range and friction modeling in pneumatic muscle actuators. *The International Journal of Robotics Research, 25*(4), 359-369.

Davis, S., Tsagarakis, N., Canderle, J., & Caldwell, D. G. (2003). Enhanced modelling and performance in braided pneumatic muscle actuators. *The International Journal of Robotics Research, 22*(3-4), 213-227.

Deimel, R., & Brock, O. (2013). *A compliant hand based on a novel pneumatic actuator.* Paper presented at the Robotics and Automation (ICRA), 2013 IEEE International Conference on.

Deimel, R., & Brock, O. (2016). A novel type of compliant and underactuated robotic hand for dexterous grasping. *The International Journal of Robotics Research, 35*(1-3), 161-185.

Doumit, M., Fahim, A., & Munro, M. (2009). Analytical modeling and experimental validation of the braided pneumatic muscle. *IEEE Transactions on Robotics,, 25*(6), 1282-1291.

Dudek, G., Jenkin, M., & Milios, E. (2002). A taxonomy of multirobot systems. *Robot teams: From diversity to polymorphism*, 3-22.

Ende, T., Haddadin, S., Parusel, S., Wüsthoff, T., Hassenzahl, M., & Albu-Schäffer, A. (2011). *A human-centered approach to robot gesture based communication within collaborative working processes.* Paper presented at the 2011 IEEE/RSJ International Conference on Intelligent Robots and Systems (IROS), .

Erkmen, I., Erkmen, A. M., Matsuno, F., Chatterjee, R., & Kamegawa, T. (2002). Snake robots to the rescue! *IEEE Robotics & Automation Magazine, 9*(3), 17-25.

Fantoni, G., Santochi, M., Dini, G., Tracht, K., Scholz-Reiter, B., Fleischer, J., . . . Franke, J. (2014). Grasping devices and methods in automated production processes. *CIRP Annals-Manufacturing Technology, 63*(2), 679-701.

Faudzi, A. A. M., Razif, M. R. M., Nordin, I. N. A. M., Suzumori, K., Wakimoto, S., & Hirooka, D. (2012). *Development of bending soft actuator with different braided angles.* Paper presented at the 2012 IEEE/ASME International Conference on Advanced Intelligent Mechatronics (AIM).

Fryman, J., & Matthias, B. (2012). *Safety of industrial robots: From conventional to collaborative applications.* Paper presented at the Robotics; Proceedings of ROBOTIK 2012; 7th German Conference on.

Fryman, J., & Matthias, B. (2012). *Safety of industrial robots: From conventional to collaborative applications.* Paper presented at the Conference on Robotics; Proceedings of ROBOTIK 2012; 7th German

Gadd, C. W. (1966). *Use of a Weighted-Impulse Criterion for Estimatéjlnjury Hazard.* Paper presented at the Proc. 10th Stapp Car Crash, New York.

Gao, D., & Wampler, C. W. (2009). Head injury criterion. *Robotics & Automation Magazine, IEEE, 16*(4), 71-74.

George Thuruthel, T., Ansari, Y., Falotico, E., & Laschi, C. (2018). Control Strategies for Soft Robotic Manipulators: A Survey. *Soft robotics*.

Gerkey, B. P., & Matarić, M. J. (2004). A formal analysis and taxonomy of task allocation in multi-robot systems. *The International Journal of Robotics Research, 23*(9), 939-954.

Giannaccini, M. E., Georgilas, I., Horsfield, I., Peiris, B., Lenz, A., Pipe, A. G., & Dogramadzi, S. (2014). A variable compliance, soft gripper. *Autonomous Robots, 36*(1-2), 93-107.

Giannaccini, M. E., Xiang, C., Atyabi, A., Theodoridis, T., Nefti-Meziani, S., & Davis, S. (2018). Novel design of a soft lightweight pneumatic continuum robot arm with decoupled variable stiffness and positioning. *Soft robotics, 5*(1), 54-70.

Gieras, J. F. (2008). *Advancements in electric machines*: Springer Science & Business Media.

Giorelli, M., Renda, F., Calisti, M., Arienti, A., Ferri, G., & Laschi, C. (2015). Learning the inverse kinetics of an octopus-like manipulator in three-dimensional space. *Bioinspiration & biomimetics, 10*(3), 035006.

Giorelli, M., Renda, F., Calisti, M., Arienti, A., Ferri, G., & Laschi, C. (2015). Neural network and jacobian method for solving the inverse statics of a cable-driven soft arm with nonconstant curvature. *IEEE transactions on robotics, 31*(4), 823-834.

Giorelli, M., Renda, F., Ferri, G., & Laschi, C. (2013). *A feed-forward neural network learning the inverse kinetics of a soft cable-driven manipulator moving in three-dimensional space.* Paper presented at the Intelligent Robots and Systems (IROS), 2013 IEEE/RSJ International Conference on.

Gleeson, B., MacLean, K., Haddadi, A., Croft, E., & Alcazar, J. (2013). *Gestures for industry: intuitive human-robot communication from human observation.* Paper presented at the Proceedings of the 8th ACM/IEEE international conference on Human-robot interaction.

Godage, I. S., Branson, D. T., Guglielmino, E., & Caldwell, D. G. (2012a). *Pneumatic muscle actuated continuum arms: Modelling and experimental assessment.* Paper

presented at the Robotics and Automation (ICRA), 2012 IEEE International Conference on.

Godage, I. S., Branson, D. T., Guglielmino, E., & Caldwell, D. G. (2012b). *Pneumatic muscle actuated continuum arms: Modelling and experimental assessment.* Paper presented at the 2012 IEEE International Conference on Robotics and Automation (ICRA), .

Godage, I. S., Branson, D. T., Guglielmino, E., Medrano-Cerda, G. A., & Caldwell, D. G. (2011). *Dynamics for biomimetic continuum arms: A modal approach.* Paper presented at the 2011 IEEE International Conference on Robotics and Biomimetics (ROBIO), .

Godage, I. S., & Walker, I. D. (2015). *Dual Quaternion based modal kinematics for multisection continuum arms.* Paper presented at the 2015 IEEE International Conference on Robotics and Automation (ICRA), .

Goodmurphy, C. W., & Ovalle, W. K. (1999). Morphological study of two human facial muscles: orbicularis oculi and corrugator supercilii. *Clinical Anatomy, 12*(1), 1-11.

Gravagne, I. A., Rahn, C. D., & Walker, I. D. (2003). Large deflection dynamics and control for planar continuum robots. *IEEE/ASME Transactions on Mechatronics, 8*(2), 299-307.

Gudiño-Lau, J., & Arteaga, M. A. (2005). Dynamic model and simulation of cooperative robots: a case study. *Robotica, 23*(05), 615-624.

Guo, J., Elgeneidy, K., Xiang, C., Lohse, N., Justham, L., & Rossiter, J. (2018). Soft pneumatic grippers embedded with stretchable electroadhesion. *Smart Materials and Structures*.

Haddadin, S., Albu-Schäffer, A., & Hirzinger, G. (2007a). *Dummy crash-tests for the evaluation of rigid human-robot impacts.* Paper presented at the International Workshop on Technical Challenges for dependable robots in Human Environments.

Haddadin, S., Albu-Schäffer, A., & Hirzinger, G. (2007b). *Safety Evaluation of Physical Human-Robot Interaction via Crash-Testing.* Paper presented at the Robotics: Science and Systems.

Haddadin, S., Albu-Schäffer, A., & Hirzinger, G. (2010). Safe physical human-robot interaction: measurements, analysis and new insights *Robotics research* (pp. 395-407): Springer.

Hannan, M. W., & Walker, I. D. (2003). Kinematics and the implementation of an elephant's trunk manipulator and other continuum style robots. *Journal of robotic systems, 20*(2), 45-63.

Hassan, T., Manti, M., Passetti, G., d'Elia, N., Cianchetti, M., & Laschi, C. (2015). *Design and development of a bio-inspired, under-actuated soft gripper.* Paper presented at the Engineering in Medicine and Biology Society (EMBC), 2015 37th Annual International Conference of the IEEE.

Heyer, C. (2010). *Human-robot interaction and future industrial robotics applications.* Paper presented at the 2010 IEEE/RSJ International Conference on Intelligent Robots and Systems (IROS), .

Hirose, S., & Yamada, H. (2009). Snake-like robots [tutorial]. *IEEE Robotics & Automation Magazine, 16*(1), 88-98.

Homberg, B. S., Katzschmann, R. K., Dogar, M. R., & Rus, D. (2015). *Haptic identification of objects using a modular soft robotic gripper.* Paper presented at the Intelligent Robots and Systems (IROS), 2015 IEEE/RSJ International Conference on.

Hopkins, J. K., Spranklin, B. W., & Gupta, S. K. (2009). A survey of snake-inspired robot designs. *Bioinspiration & biomimetics, 4*(2), 021001.

IFR International Federation of Robotics. (2015). World Robotics 2015 Industrial Robots. Retrieved from http://www.ifr.org/industrial-robots/statistics/

Ilievski, F., Mazzeo, A. D., Shepherd, R. F., Chen, X., & Whitesides, G. M. (2011). Soft robotics for chemists. *Angewandte Chemie, 123*(8), 1930-1935.

Jamwal, P. K., & Xie, S. Q. (2012). *Artificial Neural Network based dynamic modelling of indigenous pneumatic muscle actuators.* Paper presented at the 2012 IEEE/ASME International Conference on Mechatronics and Embedded Systems and Applications (MESA), .

Kaipa, K. N., Morato, C., Liu, J., & Gupta, S. K. (2014). *Human-robot collaboration for bin-picking tasks to support low-volume assemblies.* Paper presented at the Human-Robot Collaboration for Industrial Manufacturing Workshop, held at Robotics: Science and Systems Conference (RSS 2014).

Kamrani, A. K., & Nasr, E. S. A. (2008). *Collaborative Engineering*: Springer.

Kang, B.-S., Kothera, C. S., Woods, B. K., & Wereley, N. M. (2009). *Dynamic modeling of Mckibben pneumatic artificial muscles for antagonistic actuation.* Paper

presented at the IEEE International Conference on Robotics and Automation, 2009. ICRA'09. .

Kang, R., Branson, D. T., Zheng, T., Guglielmino, E., & Caldwell, D. G. (2013). Design, modeling and control of a pneumatically actuated manipulator inspired by biological continuum structures. *Bioinspiration & biomimetics, 8*(3), 036008.

Kang, R., Guglielmino, E., Branson, D. T., & Caldwell, D. G. (2013). *Kinematic model and inverse control for continuum manipulators.* Paper presented at the 2013 10th IEEE International Conference on Control and Automation (ICCA), .

Kang, R., Guo, Y., Cheng, K., & Chen, L. (2014). *Design and control of a soft actuator driven by pneumatic muscles.* Paper presented at the 2014 International Conference on Industrial Automation, Information and Communications Technology (IAICT), .

Kapadia, A., & Walker, I. D. (2011). *Task-space control of extensible continuum manipulators.* Paper presented at the Intelligent Robots and Systems (IROS), 2011 IEEE/RSJ International Conference on.

Kapadia, A. D., Fry, K. E., & Walker, I. D. (2014). *Empirical investigation of closed-loop control of extensible continuum manipulators.* Paper presented at the Intelligent Robots and Systems (IROS 2014), 2014 IEEE/RSJ International Conference on.

Kapadia, A. D., Walker, I. D., Dawson, D. M., & Tatlicioglu, E. (2010). *A model-based sliding mode controller for extensible continuum robots.* Paper presented at the Proceedings of the 9th WSEAS international conference on Signal processing, robotics and automation.

Katzschmann, R. K., Marchese, A. D., & Rus, D. (2015). Autonomous object manipulation using a soft planar grasping manipulator. *Soft robotics, 2*(4), 155-164.

Kelasidi, E., Andrikopoulos, G., Nikolakopoulos, G., & Manesis, S. (2011). *A survey on pneumatic muscle actuators modeling.* Paper presented at the 2011 IEEE International Symposium on Industrial Electronics (ISIE), .

Kosuge, K., Yoshida, H., Taguchi, D., Fukuda, T., Hariki, K., Kanitani, K., & Sakai, M. (1994). *Robot-human collaboration for new robotic applications.* Paper presented at the 20th International Conference on Industrial Electronics, Control and Instrumentation, 1994. IECON'94., .

Krüger, J., Lien, T. K., & Verl, A. (2009). Cooperation of human and machines in assembly lines. *CIRP Annals-Manufacturing Technology, 58*(2), 628-646.

Krüger, J., Schreck, G., & Surdilovic, D. (2011). Dual arm robot for flexible and cooperative assembly. *CIRP Annals-Manufacturing Technology, 60*(1), 5-8.

Küçük, S. (2012). *Serial and Parallel Robot Manipulators: Kinematics, Dynamics, Control and Optimization*: InTech.

Leephakpreeda, T. (2011). Fuzzy logic based PWM control and neural controlled-variable estimation of pneumatic artificial muscle actuators. *Expert Systems with Applications, 38*(6), 7837-7850.

Liu, J.-F., & Abdel-Malek, K. (2000). Robust control of planar dual-arm cooperative manipulators. *Robotics and Computer-Integrated Manufacturing, 16*(2), 109-119.

Maghooa, F., Stilli, A., Noh, Y., Althoefer, K., & Wurdemann, H. A. (2015). *Tendon and pressure actuation for a bio-inspired manipulator based on an antagonistic principle.* Paper presented at the Robotics and Automation (ICRA), 2015 IEEE International Conference on.

Manti, M., Cacucciolo, V., & Cianchetti, M. (2016). Stiffening in soft robotics: a review of the state of the art. *IEEE Robotics & Automation Magazine, 23*(3), 93-106.

Martell, J., & Gini, G. (2007). Robotic hands: Design review and proposal of new design process. *Image, 180*, 9270.

Martini, F., Timmons, M. J., & Tallitsch, R. B. (2008). *Human anatomy* (6th ed.): San Francisco: Pearson Benjamin Cummings.

McMahan, W., Chitrakaran, V., Csencsits, M., Dawson, D., Walker, I. D., Jones, B. A., . . . Rahn, C. D. (2006a). *Field trials and testing of the OctArm continuum manipulator.* Paper presented at the Proceedings 2006 IEEE International Conference on Robotics and Automation, 2006. ICRA 2006.

McMahan, W., Chitrakaran, V., Csencsits, M., Dawson, D., Walker, I. D., Jones, B. A., . . . Rahn, C. D. (2006b). *Field trials and testing of the OctArm continuum manipulator.* Paper presented at the Robotics and Automation, 2006. ICRA 2006. Proceedings 2006 IEEE International Conference on.

McMahan, W., Jones, B. A., & Walker, I. D. (2005). *Design and implementation of a multi-section continuum robot: Air-Octor.* Paper presented at the 2005 IEEE/RSJ International Conference on Intelligent Robots and Systems, 2005.(IROS 2005). .

Melo, K., Garabini, M., Grioli, G., Catalano, M., Malagia, L., & Bicchi, A. (2014). *Open Source VSA-CubeBots for Rapid Soft Robot Prototyping.* Paper presented at the RoMa, Robot Makers Workshop in RSS2014, Robotics Science and Systems.

More, M., & Líška, O. (2013). *Comparison of different methods for pneumatic artificial muscle control.* Paper presented at the Proceedings of the IEEE 11th International

Symposium on Applied Machine Intelligence and Informatics (SAMI2013), January31–February2.

Mosadegh, B., Polygerinos, P., Keplinger, C., Wennstedt, S., Shepherd, R. F., Gupta, U., . . . Whitesides, G. M. (2014). Pneumatic networks for soft robotics that actuate rapidly. *Advanced functional materials, 24*(15), 2163-2170.

Nakamura, T., & Shinohara, H. (2007). *Position and force control based on mathematical models of pneumatic artificial muscles reinforced by straight glass fibers.* Paper presented at the 2007 IEEE International Conference on Robotics and Automation, .

Natarajan, E., Faudzi, M., Athif, A., Jeevanantham, V. M., Razif, M., Rusydi, M., . . . Aimi, I. N. (2014). *Numerical Dynamic Analysis of a Single Link Soft Robot Finger*. Paper presented at the Applied Mechanics and Materials.

Neppalli, S., Jones, B., McMahan, W., Chitrakaran, V., Walker, I., Pritts, M., . . . Grissom, M. (2007). *Octarm-a soft robotic manipulator*. Paper presented at the Intelligent Robots and Systems, 2007. IROS 2007. IEEE/RSJ International Conference on.

Neppalli, S., & Jones, B. A. (2007). *Design, construction, and analysis of a continuum robot.* Paper presented at the Intelligent Robots and Systems, 2007. IROS 2007. IEEE/RSJ International Conference on.

Nguyen-Tuong, D., & Peters, J. (2011). Model learning for robot control: a survey. *Cognitive processing, 12*(4), 319-340.

Niiyama, R., Sun, X., Sung, C., An, B., Rus, D., & Kim, S. (2015). Pouch motors: Printable soft actuators integrated with computational design. *Soft Robotics, 2*(2), 59-70.

Nordin, I. N. A. M., Razif, M. R. M., Natarajan, E., Iwata, K., & Suzumori, K. (2013). *3-D finite-element analysis of fiber-reinforced soft bending actuator for finger flexion.* Paper presented at the Advanced Intelligent Mechatronics (AIM), 2013 IEEE/ASME International Conference on.

O'Halloran, A., O'malley, F., & McHugh, P. (2008). A review on dielectric elastomer actuators, technology, applications, and challenges. *Journal of Applied Physics, 104*(7), 071101.

Ozparpucu, M. C., Haddadin, S., Albu-Schäffer, A., & Center, G. A. (2014). *Optimal control of variable stiffness actuators with nonlinear springs.* Paper presented at the Proceedings. IFAC 2014, World Congress.

Pinterest. (2019, June 14). Pinterest. Retrieved from https://www.pinterest.co.uk/pin/334181234847005306/?autologin=true

Poole, A., & Booker, J. (2011). Design methodology and case studies in actuator selection. *Mechanism and Machine Theory, 46*(5), 647-661.

Pratt, G. A., & Williamson, M. M. (1995). *Series elastic actuators.* Paper presented at the 1995 IEEE/RSJ International Conference on Intelligent Robots and Systems 95.'Human Robot Interaction and Cooperative Robots', Proceedings. .

Ranjan, R., Upadhyay, P., Kumar, A., & Dhyani, P. (2012). Theoretical and Experimental Modeling of Air Muscle. *International Journal of Emerging Technology and Avanced Engineering, 2*(4), 112-119.

Rateni, G., Cianchetti, M., Ciuti, G., Menciassi, A., & Laschi, C. (2015). Design and development of a soft robotic gripper for manipulation in minimally invasive surgery: a proof of concept. *Meccanica, 50*(11), 2855-2863.

Razif, M., Rusydi, M., Elango, N., Nordin, M., Aimi, I. N., Faudzi, M., & Athif, A. (2014). *Non-linear finite element analysis of biologically inspired robotic fin actuated by soft actuators.* Paper presented at the Applied Mechanics and Materials.

Razif, M. R. M., Bavandi, M., Nordin, I. N. A. M., Natarajan, E., & Yaakob, O. (2014). *Two chambers soft actuator realizing robotic gymnotiform swimmers fin.* Paper presented at the Robotics and Biomimetics (ROBIO), 2014 IEEE International Conference on.

Renda, F., Giorelli, M., Calisti, M., Cianchetti, M., & Laschi, C. (2014). Dynamic model of a multibending soft robot arm driven by cables. *IEEE transactions on robotics, 30*(5), 1109-1122.

Robinson, D. W. (2000). *Design and analysis of series elasticity in closed-loop actuator force control.* Massachusetts Institute of Technology.

Robinson, G., & Davies, J. B. C. (1999). *Continuum robots-a state of the art.* Paper presented at the Robotics and Automation, 1999. Proceedings. 1999 IEEE International Conference on.

Rolf, M., & Steil, J. J. (2014). Efficient exploratory learning of inverse kinematics on a bionic elephant trunk. *IEEE transactions on neural networks and learning systems, 25*(6), 1147-1160.

Roy, N., & Dudek, G. (2001). Collaborative robot exploration and rendezvous: Algorithms, performance bounds and observations. *Autonomous Robots, 11*(2), 117-136.

Sárosi, J., Bíró, I., Németh, J., & Cveticanin, L. (2015). Dynamic modeling of a pneumatic muscle actuator with two-direction motion. *Mechanism and Machine Theory, 85*, 25-34.

Schiavi, R., Grioli, G., Sen, S., & Bicchi, A. (2008). *VSA-II: a novel prototype of variable stiffness actuator for safe and performing robots interacting with humans.* Paper presented at the IEEE International Conference on Robotics and Automation, 2008. ICRA 2008. .

Severinson-Eklundh, K., Green, A., & Hüttenrauch, H. (2003). Social and collaborative aspects of interaction with a service robot. *Robotics and autonomous systems, 42*(3), 223-234.

Shan, Y., & Koren, Y. (1993). Design and motion planning of a mechanical snake. *IEEE transactions on systems, man, and cybernetics, 23*(4), 1091-1100.

Shawyer, B. (2010). *Explorations in geometry*: World Scientific Publishing Company.

Shi, J., Jimmerson, G., Pearson, T., & Menassa, R. (2012). *Levels of human and robot collaboration for automotive manufacturing.* Paper presented at the Proceedings of the Workshop on Performance Metrics for Intelligent Systems.

Shimoga, K. B. (1996). Robot grasp synthesis algorithms: A survey. *The International Journal of Robotics Research, 15*(3), 230-266.

Shintake, J., Rosset, S., Schubert, B., Floreano, D., & Shea, H. (2016). Versatile soft grippers with intrinsic electroadhesion based on multifunctional polymer actuators. *Advanced Materials, 28*(2), 231-238.

Stilli, A., Wurdemann, H. A., & Althoefer, K. (2014). *Shrinkable, stiffness-controllable soft manipulator based on a bio-inspired antagonistic actuation principle.* Paper presented at the Intelligent Robots and Systems (IROS 2014), 2014 IEEE/RSJ International Conference on.

Su, Y., Duan, B., & Zheng, C. (2004). Nonlinear PID control of a six-DOF parallel manipulator. *IEE Proceedings-Control Theory and Applications, 151*(1), 95-102.

Su, Y., Sun, D., & Duan, B. (2005). Design of an enhanced nonlinear PID controller. *Mechatronics, 15*(8), 1005-1024.

Szepe, T. (2011). *Accurate force function approximation for pneumatic artificial muscles.* Paper presented at the 2011 3rd IEEE International Symposium on Logistics and Industrial Informatics (LINDI), .

Takosoglu, J. E., Laski, P. A., Blasiak, S., Bracha, G., & Pietrala, D. (2016). Determining the static characteristics of pneumatic muscles. *Measurement and Control, 49*(2), 62-71.

Tatlicioglu, E., Walker, I. D., & Dawson, D. M. (2007). *Dynamic modelling for planar extensible continuum robot manipulators.* Paper presented at the 2007 IEEE International Conference on Robotics and Automation,.

Thanh, T. D. C., & Ahn, K. K. (2006). Nonlinear PID control to improve the control performance of 2 axes pneumatic artificial muscle manipulator using neural network. *Mechatronics, 16*(9), 577-587.

Tinós, R., Terra, M. H., & Ishihara, J. Y. (2006). Motion and force control of cooperative robotic manipulators with passive joints. *IEEE Transactions on Control Systems Technology,, 14*(4), 725-734.

Tondu, B. (2012). Modelling of the McKibben artificial muscle: A review. *Journal of Intelligent Material Systems and Structures, 23*(3), 225-253.

Tondu, B., & Lopez, P. (2000). Modeling and control of McKibben artificial muscle robot actuators. *Control systems, IEEE, 20*(2), 15-38.

Tonietti, G., Schiavi, R., & Bicchi, A. (2005). *Design and control of a variable stiffness actuator for safe and fast physical human/robot interaction.* Paper presented at the Proceedings of the 2005 IEEE International Conference on Robotics and Automation, 2005. ICRA 2005.

Transeth, A. A., Pettersen, K. Y., & Liljebäck, P. (2009). A survey on snake robot modeling and locomotion. *Robotica, 27*(7), 999-1015.

Trivedi, D., Lotfi, A., & Rahn, C. D. (2008). Geometrically exact models for soft robotic manipulators. *Robotics, IEEE Transactions on, 24*(4), 773-780.

Trivedi, D., Rahn, C. D., Kier, W. M., & Walker, I. D. (2008). Soft robotics: Biological inspiration, state of the art, and future research. *Applied Bionics and Biomechanics, 5*(3), 99-117.

Tsagarakis, N., & Caldwell, D. G. (2000). *Improved modelling and assessment of pneumatic muscle actuators.* Paper presented at the IEEE International Conference on Robotics and Automation, 2000. Proceedings. ICRA'00. .

Tsagarakis, N. G., Sardellitti, I., & Caldwell, D. G. (2011). *A new variable stiffness actuator (CompAct-VSA): Design and modelling.* Paper presented at the 2011 IEEE/RSJ International Conference on Intelligent Robots and Systems (IROS),.

Vanderborght, B., Albu-Schäffer, A., Bicchi, A., Burdet, E., Caldwell, D. G., Carloni, R., . . . Ganesh, G. (2013). Variable impedance actuators: A review. *Robotics and autonomous systems, 61*(12), 1601-1614.

Wakimoto, S., Ogura, K., Suzumori, K., & Nishioka, Y. (2009). *Miniature soft hand with curling rubber pneumatic actuators.* Paper presented at the Robotics and Automation, 2009. ICRA'09. IEEE International Conference on.

Walker, I. D. (2013). Continuous backbone "continuum" robot manipulators. *ISRN Robotics, 2013*.

Walker, I. D., Dawson, D. M., Flash, T., Grasso, F. W., Hanlon, R. T., Hochner, B., . . . Zhang, Q. M. (2005). *Continuum robot arms inspired by cephalopods.* Paper presented at the Defense and Security.

Wang, B., Aw, K. C., Biglari-Abhari, M., & McDaid, A. (2016). *Design and fabrication of a fiber-reinforced pneumatic bending actuator.* Paper presented at the Advanced Intelligent Mechatronics (AIM), 2016 IEEE International Conference on.

Wang, B., McDaid, A., Giffney, T., Biglari-Abhari, M., & Aw, K. C. (2017). Design, modelling and simulation of soft grippers using new bimorph pneumatic bending actuators. *Cogent Engineering, 4*(1), 1285482.

Wettels, N., Parnandi, A. R., Moon, J.-H., Loeb, G. E., & Sukhatme, G. S. (2009). Grip control using biomimetic tactile sensing systems. *IEEE/ASME Transactions On Mechatronics, 14*(6), 718-723.

Wickramatunge, K. C., & Leephakpreeda, T. (2010). Study on mechanical behaviors of pneumatic artificial muscle. *International Journal of Engineering Science, 48*(2), 188-198.

Wolf, S., & Albu-Schaffer, A. (2013). *Towards a robust variable stiffness actuator.* Paper presented at the 2013 IEEE/RSJ International Conference on Intelligent Robots and Systems (IROS), .

Wright, C., Buchan, A., Brown, B., Geist, J., Schwerin, M., Rollinson, D., . . . Choset, H. (2012). *Design and architecture of the unified modular snake robot.* Paper presented at the Robotics and Automation (ICRA), 2012 IEEE International Conference on.

Wright, C., Johnson, A., Peck, A., McCord, Z., Naaktgeboren, A., Gianfortoni, P., . . . Choset, H. (2007). *Design of a modular snake robot.* Paper presented at the Intelligent Robots and Systems, 2007. IROS 2007. IEEE/RSJ International Conference on.

Yamakita, M., Yamada, T., & Tanaka, K. (2003). *Control of snake like robot for locomotion and manipulation.* Paper presented at the Proc. Int. Symp. on Adaptive Motion of Animals and Machines, WeP-III.

Yanco, H. A., & Drury, J. L. (2004). *Classifying human-robot interaction: an updated taxonomy.* Paper presented at the SMC (3).

Zheng, T., Branson, D. T., Kang, R., Cianchetti, M., Guglielmino, E., Follador, M., . . . Caldwell, D. G. (2012). *Dynamic continuum arm model for use with underwater robotic manipulators inspired by octopus vulgaris.* Paper presented at the Robotics and Automation (ICRA), 2012 IEEE International Conference on.

Zheng, T., Branson III, D. T., Kang, R., Cianchetti, M., Guglielmino, E., Follador, M., . . . Caldwell, D. G. (2012). *Dynamic continuum arm model for use with underwater robotic manipulators inspired by octopus vulgaris.* Paper presented at the 2012 IEEE International Conference on Robotics and Automation (ICRA), .

Zinn, M., Roth, B., Khatib, O., & Salisbury, J. K. (2004). A new actuation approach for human friendly robot design. *The International Journal of Robotics Research, 23*(4-5), 379-398.

Zlot, R., & Stentz, A. (2005). *Complex task allocation for multiple robots.* Paper presented at the Robotics and Automation, 2005. ICRA 2005. Proceedings of the 2005 IEEE International Conference on.

A. Appendix

Table A.1 Experiment results of a 20 cm PMA.

P (kPa)	L (cm)	Ĺ (cm)	Length difference (%)	θ (degree)	D (cm)	ε
0	20	19.7	1.15	31.35196	1.767	0.011
50	19.48	19.0	4.65	34.53823	1.989449	0.046
100	16.82	16.3	18.1	44.96463	2.479712	0.181
150	15.56	15.3	23.45	48.59935	2.632123	0.234
200	14.9	14.8	26	50.26118	2.698315	0.26
250	14.7	14.6	26.95	50.87006	2.722002	0.269
300	14.52	14.4	27.9	51.47372	2.745183	0.279
350	14.2	14.1	29.075	52.21343	2.773172	0.290
400	14.08	14.0	29.6	52.54155	2.785439	0.296
350	14.17					
300	14.32					
250	14.52					
200	14.7					
150	15.06					
100	15.94					
50	18.66					
0	19.54					

Table A.2 Experiment results of a 30 cm PMA.

P (kPa)	L (cm)	Ĺ (cm)	Length difference (%)	θ (degree)	D (cm)	ε
0	30	30	0	30.02661	1.752	0
50	29.9	29.89	0.366667	30.38815	1.771211	0.0036
100	27.9	27.57	8.1	37.28242	2.120968	0.081
150	25.7	25.48	15.06667	42.66416	2.372918	0.1506
200	24.4	24.26	19.13333	45.56276	2.500084	0.1913
250	23.7	23.62	21.26667	47.0268	2.561903	0.2126
300	23.2	23.16	22.8	48.05785	2.604437	0.228
350	22.8	22.84	23.86667	48.76536	2.633137	0.2386
400	22.6	22.59	24.7	49.31282	2.655069	0.247
450	22.4	22.39	25.36667	49.74756	2.672313	0.2536
500	22.1	22.18	26.06667	50.20105	2.690137	0.2606
450	22.3					
400	22.5					
350	22.8					
300	23.0					
250	23.5					
200	24.0					
150	25.2					
100	27.1					
50	29.8					
0	30					

Table A.3 Experiment results of a 40 cm PMA.

P (kPa)	L (cm)	Ĺ (cm)	Length difference (%)	θ (degree)	D (cm)	ε
0	40	39.99	0.025	30.285803	1.764	0.000
50	39.7	39.55	1.125	31.348494	1.821585	0.011
100	36.6	36.3	9.25	38.386876	2.174273	0.092
150	33.9	33.53	16.175	43.612765	2.415219	0.161
200	32.0	31.91	20.225	46.446253	2.537587	0.202
250	31.1	30.95	22.625	48.063716	2.604676	0.226
300	30.4	30.39	24.025	48.988482	2.642104	0.240
350	29.9	29.91	25.225	49.770919	2.673235	0.252
400	29.6	29.61	25.975	50.255376	2.692261	0.259
450	29.4	29.38	26.55	50.624497	2.706628	0.265
500	29.0	29.08	27.3	51.103047	2.725086	0.273
450	29.3					
400	29.5					
350	29.8					
300	30.3					
250	30.8					
200	31.7					
150	33.0					
100	35.9					
50	39.4					
0	39.9					

P (kPa) / W (kg)	150	200	250	300	350	400
0	15.7	15.2	14.8	14.6	14.15	14.2
0.5	16.1	15.5	15.2	14.8	14.5	14.3
1	16.4	15.6	15.4	15.1	14.8	14.4
1.5	16.7	15.8	15.5	15.2	14.9	14.5
2	17	15.9	15.6	15.3	15	14.6
2.5	17.2	16.2	15.9	15.4	15.1	14.7
3	17.5	16.4	16.1	15.5	15.2	14.8
3.5	17.7	16.55	16.3	15.6	15.3	15
4	17.9	16.75	16.4	15.7	15.4	15.1
4.5	18	16.8	16.5	15.8	15.5	15.2
5	18.3	17	16.7	15.9	15.7	15.25
5.5	18.6	17.2	16.9	16.1	15.9	15.4
6	18.8	17.4	17.1	16.2	16.1	15.5
6.5	19.1	17.6	17.2	16.3	16.2	15.6
7	19.3	17.7	17.3	16.4	16.3	15.7
7.5	19.4	17.9	17.4	16.45	16.35	15.8
8	19.5	18.1	17.5	16.5	16.4	15.9
8.5	19.6	18.3	17.6	16.7	16.5	16.1
9	19.7	18.5	17.7	16.75	16.6	16.2
9.5	19.8	18.7	17.8	16.8	16.65	16.3
10	19.9	18.8	17.9	16.85	16.7	16.4

Table A.5 Length of a 30 cm contractor PMA due to the change in weight and pressure.

P (kPa) / W (kg)	150	200	250	300	350	400	450	500
0	25.4	24.2	23.5	23.15	22.8	22.6	22.4	22.1
0.5	25.5	24.2	23.6	23.15	22.9	22.6	22.5	22.2
1	25.8	24.3	23.8	23.18	23	22.6	22.6	22.25
1.5	26.1	24.4	23.95	23.2	23.1	22.7	22.7	22.3
2	26.4	24.6	24.1	23.3	23.2	22.75	22.8	22.4
2.5	26.7	24.8	24.2	23.45	23.3	22.8	22.8	22.5
3	26.9	25.1	24.4	23.6	23.4	23	22.9	22.6
3.5	27.2	25.3	24.6	23.7	23.6	23.1	23	22.7
4	27.5	25.5	24.7	23.9	23.7	23.2	23.1	22.8
4.5	27.8	25.7	24.9	24	23.8	23.3	23.2	22.9
5	28	26	25.1	24.2	23.9	23.4	23.3	22.95
5.5	28.4	26.3	25.4	24.3	24.2	23.5	23.4	23
6	28.7	26.5	25.5	24.4	24.4	23.6	23.5	23.1
6.5	28.9	26.8	25.7	24.6	24.5	23.7	23.6	23.3
7	29.1	27	25.9	24.8	24.6	23.8	23.7	23.4
7.5	29.3	27.2	26	25	24.7	23.9	23.8	23.5
8	29.4	27.4	26.2	25.3	24.8	24.1	23.9	23.6
8.5	29.6	27.6	26.4	25.5	24.9	24.3	24	23.7
9	29.7	27.8	26.6	25.7	25	24.4	24.1	23.8
9.5	29.8	28	26.8	25.8	25.1	24.5	24.2	23.9
10	30	28.2	26.9	26	25.2	24.7	24.4	24

Table A.6 Length of a 40 cm contractor PMA due to the change in weight and pressure.

P (kPa) / W (kg)	150	200	250	300	350	400	450	500
0	33.53	31.91	30.95	30.39	29.91	29.61	29.38	29.08
0.5	34.9	32.5	31.3	30.8	30.3	30	29.6	29.5
1	35.1	32.9	31.6	31.1	30.5	30.1	29.7	29.6
1.5	35.5	33.2	31.8	31.3	30.6	30.3	29.9	29.8
2	35.8	33.5	32.2	31.5	30.8	30.4	30	29.9
2.5	36.2	33.8	32.4	31.7	31	30.5	30.2	30
3	36.6	34.1	32.6	31.9	31.2	30.7	30.3	30.1
3.5	37	34.3	32.8	32.1	31.3	30.8	30.4	30.2
4	37.3	34.6	33.1	32.3	31.5	31	30.5	30.4
4.5	37.6	34.9	33.4	32.5	31.7	31.2	30.7	30.5
5	38	35.3	33.6	32.7	31.8	31.3	30.8	30.6
5.5	38.3	35.8	33.8	33	32	31.5	31	30.8
6	38.7	36	34	33.2	32.2	31.7	31.1	31
6.5	39	36.4	34.3	33.4	32.3	31.8	31.2	31.1
7	39.2	36.6	34.6	33.6	32.5	32	31.4	31.2
7.5	39.4	36.9	34.8	33.8	32.7	32.2	31.5	31.3
8	39.7	37.2	35	34	32.9	32.3	31.7	31.4
8.5	39.85	37.5	35.3	34.2	33.1	32.4	31.8	31.5
9	40	37.7	35.5	34.4	33.3	32.6	31.9	31.6
9.5	40.2	38	35.8	34.6	33.4	32.7	32.1	31.8
10	40.5	38.3	36	34.8	33.6	33	32.3	31.9

Table A.7 Experiment results of a 22 cm PMA.

P	L	Ĺ (cm)	Length difference	θ	D (cm)	έ
0	22	22.34	0	70.21748	2.99984	0.0154
50	24.	26.34	19.72727	66.4806	2.923135	0.1972
100	30.	30.8	40	62.18369	2.819594	0.4
150	31.	31.67	43.95455	61.3263	2.797016	0.4395
200	31.	32.11	45.95455	60.89001	2.785287	0.4595
250	32.	32.35	47.04545	60.65125	2.7788	0.4704
300	32.	32.6	48.18182	60.40194	2.771974	0.4818
350	32.	32.72	48.72727	60.28206	2.768674	0.4872
400	32.	32.8	49.09091	60.20206	2.766464	0.4909
350	32.					
300	32.					
250	32.					
200	32.					
150	31.					
100	31.					
50	27.					
0	22.					

Table A.8 Experiment results of a 32 cm PMA.

P	L	Ĺ (cm)	Length difference	θ	D (cm)	έ
0	32	32.02	0	71.51493	3.003456	0.0006
50	32.	32.5	1.5625	71.22751	2.998381	0.0156
100	44.	45.01	40.65625	63.5317	2.834889	0.4065
150	47.	47.51	48.46875	61.93577	2.794477	0.4846
200	48.	48.83	52.59375	61.08356	2.772008	0.5259
250	49.	49.64	55.125	60.55714	2.757821	0.5512
300	50.	50.23	56.96875	60.17197	2.747294	0.5696
350	50.	50.75	58.59375	59.83127	2.737879	0.5859
400	51.	51.15	59.84375	59.56839	2.730548	0.5984
450	51.	51.49	60.90625	59.34438	2.724255	0.6090
500	51.	51.84	62	59.11325	2.717719	0.62
450	51.					
400	51.					
350	50.					
300	50.					
250	49.					
200	49.					
150	47.					
100	46					
50	32.					
0	32.					

Table A.9 Experiment results of a 42 cm PMA.

P	L	Ĺ (cm)	Length difference	θ	D (cm)	ε
0	42.0	42.25	0.616786	71.8020	3.0039	0.006
50	42.8	43.35	3.228929	71.3122	2.9954	0.032
100	55.5	56.68	34.96893	65.2322	2.8712	0.349
150	59.3	59.71	42.18929	63.8095	2.8374	0.421
200	60.6	60.98	45.19571	63.2120	2.8227	0.451
250	61.6	61.71	46.94536	62.8629	2.8140	0.469
300	62.2	62.20	48.10357	62.6311	2.8081	0.481
350	62.6	62.73	49.36036	62.3791	2.8017	0.493
400	63.0	63.07	50.17357	62.2158	2.7975	0.501
450	63.3	63.39	50.9375	62.0621	2.7935	0.509
500	63.7	63.75	51.8	61.8883	2.7890	0.518
450	63.4					
400	63.1					
350	62.8					
300	62.2					
250	61.8					
200	61.2					
150	60.1					
100	57.8					
50	43.9					
0	42.5					

Table A.10 Length of a 22 cm extensor PMA due to the change in weight and pressure.

P (kPa) / W (kg)	100	150	200	250	300	350	400
0	30.1	31.4	32.11	32.35	32.6	32.72	32.8
0.5	31.2	32.4	32.8	33	33	33	33.1
1	32.6	33.2	33.4	33.4	33.2	33.2	33.2
1.5	34.1	34	34	33.8	33.6	33.5	33.5
2	35.4	34.8	34.4	34.2	33.9	33.8	33.7
2.5	36.7	35.7	34.9	34.6	34.2	34.1	34
3	38.1	36.5	35.5	35	34.6	34.4	34.2
3.5	39.4	37.2	36	35.4	34.9	34.6	34.4
4	40.6	38.1	36.5	35.8	35.2	34.9	34.7
4.5	41.7	39	37	36.2	35.6	35.2	34.9
5	42.8	39.7	37.5	36.6	35.9	35.5	35.2
5.5	44	40.5	38	36.9	36.3	35.8	35.4
6	44.9	41.3	38.5	37.3	36.6	36.1	35.7
6.5	45.8	42	39	37.7	36.9	36.4	35.9
7	46.3	42.7	39.5	38.1	37.2	36.6	36.2
7.5	47.4	43.3	40	38.5	37.6	36.9	36.4
8	48.2	43.9	40.5	38.9	37.9	37.2	36.7
8.5	49	44.6	40.9	39.2	38.2	37.4	36.9
9	49.5	45.2	41.4	39.6	38.5	37.7	37.15
9.5	50.5	45.7	41.8	40	38.9	38	37.3
10	51.1	46.2	42.2	40.3	39.2	38.3	37.6

Table A.11 Length of a 32 cm extensor PMA due to the change in weight and pressure.

P (kPa) / W (kg)	100	150	200	250	300	350	400	450	500
0	45.01	47.51	48.83	49.64	50.33	51	51.45	51.89	52
0.5	45.8	48.3	50.2	50.8	51.4	51.9	52.3	52.5	52.7
1	47.4	49.4	51.1	51.5	52.1	52.4	52.7	52.9	53.1
1.5	49	50.5	52	52.2	52.6	52.8	53.1	53.3	53.4
2	50.4	51.7	52.8	52.9	53.2	53.3	53.5	53.6	53.7
2.5	51.8	52.7	53.5	53.5	53.6	53.7	53.8	53.9	54
3	53.3	53.5	54.2	54	54.1	54.2	54.2	54.2	54.3
3.5	54.6	54.7	54.8	54.6	54.6	54.6	54.6	54.5	54.6
4	55.9	55.6	55.6	55.2	55.2	55	55	54.9	54.9
4.5	57	56.5	56.3	55.7	55.6	55.4	55.3	55.2	55.2
5	58	57.3	57	56.3	56.2	55.8	55.6	55.5	55.4
5.5	59.2	58.5	58	57.1	56.6	56.1	56	55.7	55.7
6	60.5	59.5	58.7	57.7	57	56.6	56.4	56.2	56
6.5	61.8	60.2	59.5	58.2	57.5	57	56.8	56.5	56.2
7	63	60.7	60	58.7	57.9	57.4	57.2	56.8	56.5
7.5	63.7	61.2	60.4	59.3	58.4	57.7	57.5	57.1	56.7
8	64.5	61.7	60.8	59.9	58.9	58.3	57.8	57.5	57
8.5	65.3	62.5	61.4	60.4	59.3	58.7	58.2	57.8	57.2
9	66	63.2	61.8	60.7	59.8	59.1	58.5	58.2	57.5
9.5	66.7	63.9	62	61.1	60.1	59.4	58.8	58.5	57.9
10	67.8	64.2	62.2	61.5	60.5	60	59.2	58.8	58.2

P (kPa) / W (kg)	100	150	200	250	300	350	400	450	500
0	52.5	57.7	60.7	61.5	62.2	62.6	63	63.2	63.4
0.5	55.5	58.9	62	62.2	63.1	63.5	63.6	63.7	63.9
1	58.5	61.5	62.9	63.4	63.7	64	64	64.2	64.3
1.5	61.1	63.2	63.9	64.2	64.3	64.5	64.5	64.5	64.6
2	63.5	64.5	65	65	65	64.9	65	64.9	65
2.5	65.5	66.1	65.8	65.7	65.5	65.4	65.4	65.3	65.3
3	67.6	67.5	66.8	66.4	66.1	65.9	65.8	65.7	65.6
3.5	69.4	68.8	67.7	67.2	66.8	66.4	66.3	66.2	66
4	70.8	70.1	68.6	67.8	67.4	66.9	66.7	66.5	66.4
4.5	72.2	71.6	69.6	68.6	68	67.4	67.2	66.9	66.8
5	73.8	72.8	70.5	69.4	68.6	68	67.6	67.3	67.1
5.5	75.2	74	71.4	70	69.4	68.5	68	67.8	67.6
6	76.6	75.2	72.2	71	69.9	69	68.5	68.2	67.9
6.5	77.6	76.4	73.1	71.6	70.4	69.5	69	68.6	68.3
7	78.5	77.4	73.8	72.2	71	69.9	69.4	69	68.6
7.5	80.5	78.4	74.7	72.7	71.5	70.4	69.8	69.4	69
8	81.5	79.5	75.5	73.5	72	70.8	70.2	69.7	69.4
8.5	82.5	80.4	76.3	74.1	72.5	71.2	70.6	70	69.6
9	84	81.3	77	74.6	73.2	71.6	71	70.4	69.9
9.5	85.2	82.2	77.7	75.4	73.7	72.1	71.4	70.8	70.2
10	86.5	83	78.5	76	74.2	72.6	71.8	71.1	70.5